HIGH FIELD COMPACT TOKAMAK REACTOR (HFCTR) CONCEPTUAL DESIGN

Archival copy - not to be removed
from the library

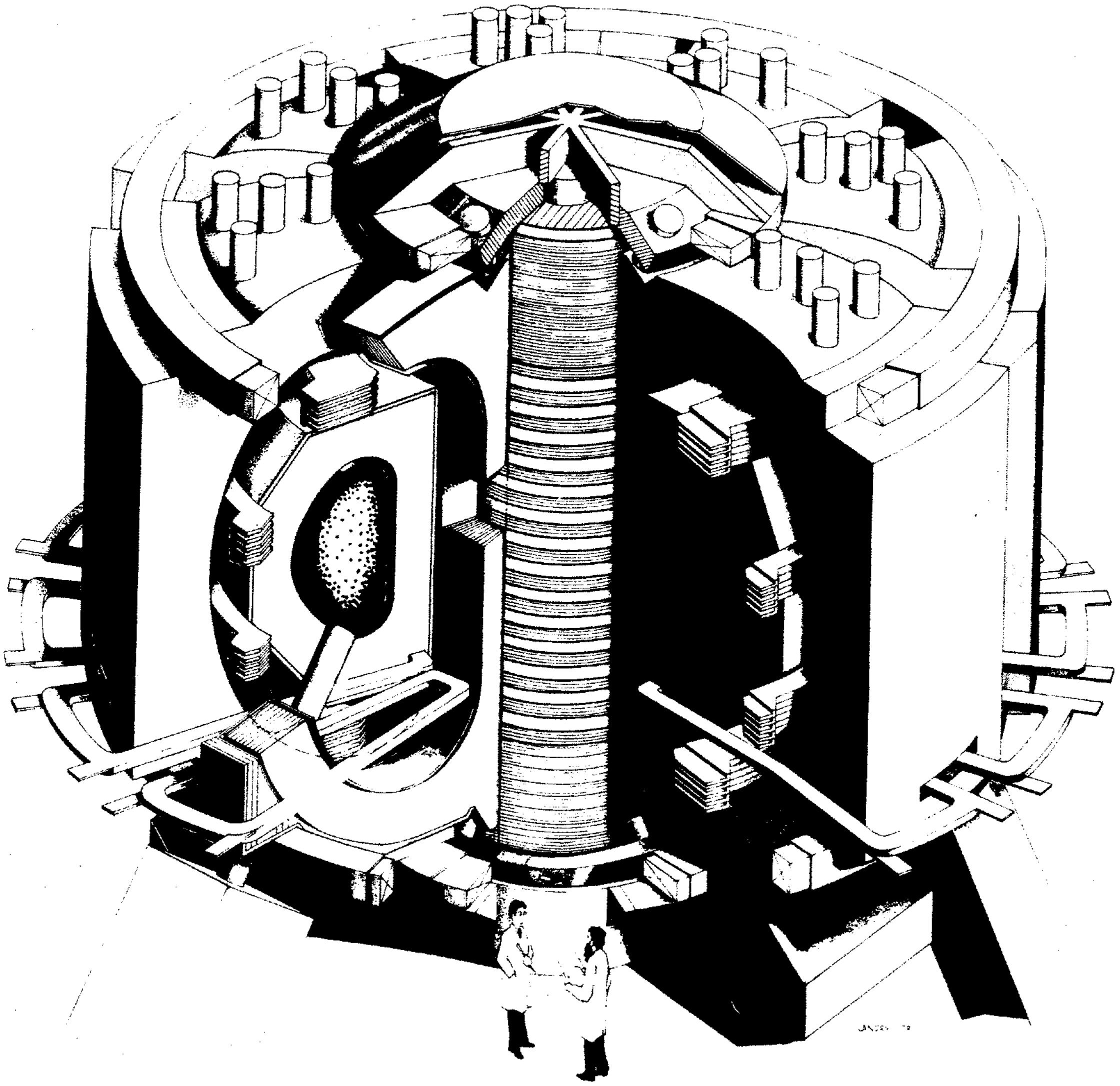

Final Report
January 1979

M.I.T. Plasma Fusion Center
Research Report RR-79-2

HIGH FIELD COMPACT TOKAMAK REACTOR (HFCTR)

CONCEPTUAL DESIGN †

Final Report - January 1979

D.R. Cohn[M] - Project Manager
J.H. Schultz[W] - General Editor

L. Bromberg[M]
F. Chang[C]
D.L. Cook[M]
M. Culbert[W]
J. Fisher[C]
D. Hackworth[W]
R.D. Hay[M]
D.L. Jassby[P]
D.L. Kaplan[M]
K.E. Kreischer[M]
L.M. Lidsky[M]
F. Malick[W]
T. McManamy[M]
K. Molvig[M]
J. Murphy[W]
M. Okabayashi[P]
D.O. Overskei[M]
M. Sniderman[W]
W. Stephany[M]
H.H. Towner[P]
J.E.C. Williams[M]

M MIT Plasma Fusion Center* & Francis Bitter National Magnet Laboratory††
P Princeton Plasma Physics Laboratory
W Westinghouse Electric Corporation
C Charles Stark Draper Laboratory

† Work supported by U.S. Department of Energy Contract #EG-77-S-02-4183
* Supported by U.S. Department of Energy
†† Supported by National Science Foundation

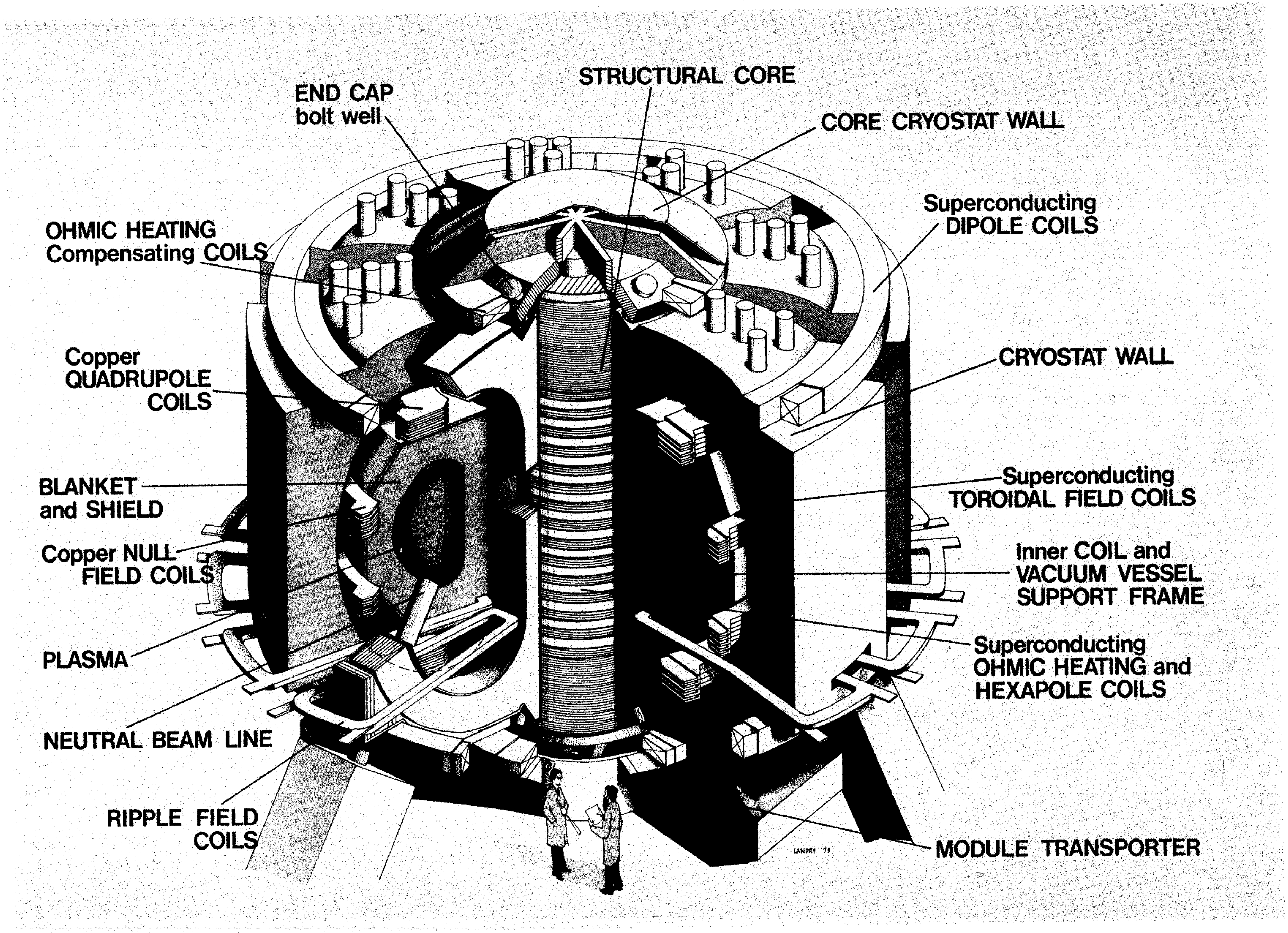
STRUCTURAL CORE
END CAP bolt well
CORE CRYOSTAT WALL
Superconducting DIPOLE COILS
OHMIC HEATING Compensating COILS
CRYOSTAT WALL
Copper QUADRUPOLE COILS
BLANKET and SHIELD
Superconducting TOROIDAL FIELD COILS
Copper NULL FIELD COILS
Inner COIL and VACUUM VESSEL SUPPORT FRAME
PLASMA
Superconducting OHMIC HEATING and HEXAPOLE COILS
NEUTRAL BEAM LINE
RIPPLE FIELD COILS
MODULE TRANSPORTER
LANDRY '79

ABSTRACT

A conceptual design has been developed for a compact (R_o = 6.0 m) high field (B_T = 7.4 T) tokamak demonstration power reactor which can produce fusion power densities as high as 10 MW/m^3 with a spatially averaged value of toroidal beta of less than 5%. The HFCTR design is based upon minimal extrapolation from experimentally established plasma confinement and MHD stability in tokamak devices. A unique design for the NB_3Sn toroidal-field magnet system reduces the stress in the high-field trunk region and allows the achievement of high fields with a small radial build. An integrated system of automated actuators, vacuum and current-carrying mechanical joints and flexible cryostats allow total modularization of the reactor, including the coil systems. A detailed estimate of maintenance operation time indicated the possibility of very high plant availability. The modest value of toroidal beta permits a simple plasma-shaping coil system, located inside the TF coil trunk. Heating of the central plasma is attained by the use of ripple-assisted injection of 120-keV D^o beams, which is also used for dynamic control of the plasma temperature during the burn period. A FLIBE-lithium blanket is designed especially for high-power-density operation in a high-field environment, and gives an overall tritium breeding ratio of 1.05.

TABLE OF CONTENTS

1. EXECUTIVE SUMMARY

1.1 INTRODUCTION

This report describes the conceptual design of a high-field ($B_T = 7.4$ T) compact ($R = 6.0$ m) tokamak reactor (HFCTR) which can produce fusion power densities as high as 10 MW/m^3 with a spatially averaged value of toroidal beta of less than 5%. Thermal power levels as high as 3,300 MW can be obtained. Ignition can be obtained with a toroidal beta as low as 2.5% and the reactor can be operated at ignition at power levels as low as 1,000 MW. Total modularization of the tokamak, including both the toroidal and poloidal system leads to significantly improved plant availability. An advanced toroidal field coil design allows all reactor subsystems other than the TF coil to have approximately the same size and specific power as those in higher beta (8-10%) designs operated at lower field with more conventional magnet systems.

The HFCTR conceptual design has the following new features:

(1) <u>High Plasma Density Operation ($n_o \simeq 5 \times 10^{20}$ m^{-3}); Minimum Extrapolation of Experimentally Established Results for Transport and MHD Stability</u>.

Based upon the "empirical scaling law" for energy confinement time [1,2] ($\tau_E \sim na^2$), high density operation permits a reduction in the plasma size required for ignition. High fusion power density, P_f, is achieved because $P_f \sim n^2$. High n is also known to result in relatively small impurity content [3].

High field operation allows the achievement of ignition and high fusion power density in a relatively compact reactor at moderate values of plasma total beta.

(2) Diametrically Reacting, High JB, Niobium Tin TF Coils

The tensile stress in the trunk of the niobium tin (Nb_3Sn) magnet system at 13.1 T is reduced by load sharing with the core and by reaction between diametrically opposite D coils [4]. The operation of the Nb_3Sn coils at high values of JB permits the generation of high fields with minimum increase in the size of the magnet system.

(3) Total Modularization of Tokamak System

The tokamak is divided into 8 modules which can be rapidly and automatically connected and disconnected and removed for replacement by a spare module. It has been estimated that all mechanical operations in a module replacement can be performed in two days. Although one other demo reactor design [5] has enunciated a method for rapid, automatic replacement of a blanket and first wall module, this is the first design to incorporate a method for the rapid replacement of a complete 45° sector which includes the TF coils. This approach removes the need to assume that the coil systems will be failsafe and need not be serviceable. It also permits periodic annealing of defects in the matrix of the superconducting cable. The success of an experimental program to establish the reliability of the joining concepts in this design (described in 1.8) could demonstrate that the tokamak is a topologically acceptable configuration for maintenance in a utility environment.

(4) Simple, Modularized Plasma Shaping-Coil System

The plasma elongation requirements for achieving the 4% plasma beta ($b/a \simeq 1.6$) are relatively modest, allowing a simple plasma-shaping coil system. A superconducting hexapole field plasma shaping coil is located in the core, thereby eliminating the need for placement of relatively inaccessible copper coils on the inboard side of the vacuum chamber. The copper coils located inside the TF modules are segmented with electrical connections formed by pressure contacts.

(5) Pulsed Nulling-Field Coils

The principal equilibrium-field coils are superconducting, unpulsed and operated continuously, while a separate copper nulling coil system provides the necessary field change during start-up [4]. This nulling coil system greatly minimizes the pulsed power and stored energy requirement as only the vertical field in the volume immediately surrounding the plasma is pulsed.

(6) Ripple-Trapping Beam Injection

The use of conventional neutral beam injection would require a D^o neutral beam voltage in excess of 250 keV in order to obtain adequate penetration. In order to remove the requirement for high beam voltage a controlled toroidal-field ripple is used to enhance the penetration of energetic ions formed by near-vertical injection of 120 keV D^o beams. [6].

(7) FLIBE-Lithium Blanket

The blanket coolant is FLIBE, which is characterized by high density and low electrical conductivity, thus minimizing the pumping power requirements at high neutron wall loadings in a high magnet field environment in a small-size blanket. Slowly pumped, nearly stagnant lithium is used for tritium breeding, giving an overall breeding ratio of 1.05. This blanket system obviates the need for high flow rates of high temperature lithium and is therefore less susceptible to accidents due to high circulating pressure.

1.2 THREE FIGURES OF MERIT FOR A DEMONSTRATION POWER REACTOR

A figure of merit can be roughly defined as a parameter of a system which causes the profitability of the system to increase as the figure increases over a broad range of possible design space for the system. Figures of merit can be of significant benefit to the conceptual design of commercial tokamak reactors because the systems are so complex, the design space so bread and the design goal so far in the future that numerical costing methods provide limited guidance. Considerable emphasis has been placed upon using the total beta of the plasma as a figure of merit. While beta and other plasma parameters are important, it has become increasingly clear that additional basic figures of merit should be developed to guide conceptual design studies toward the commercialization of pure fusion tokamaks. Fusion technology assessment papers [7] have argued that technological limitations may make fusion inherently less economical than fission. For example, if first wall neutron loading is limited by thermal, mechanical and high vacuum conisderations to less than 1 MW/m^2, then a tokamak fusion reactor of a given electrical output must be larger, more complex and more expensive than a fission reactor, even if plasma beta equals one. In this section we will identify and discuss the existence of three overall reactor (as opposed to plasma) figures of merit.

Two figures of merit associated with reactor design have previously achieved general acceptance -- wall loading on the plasma first wall (P_W) and plant availability (p.a). In addition, we propose that the product of the average current density in the inner leg of the toroidal field magnet and the maximum field at the toroidal field coil, $\bar{J}\ B_{MAX}$, is a fundamental figure of merit.

It can be suggested that the combination of the following three figures of merit:

(a) P_W

(b) P_W x p.a.

(c) $\bar{J}\ B_{MAX}$

form a complete set of figures of merit for a tokamak reactor. That is, a conceptual reactor design which increases all three parameters simultaneously, (assuming moderate good sense regarding the avoidance of very rare or expensive materials) should improve the commercializability of tokamak fusion reactors.

The argument that $\bar{J}\ B_{MAX}$ is a fundamental figure of merit is given in Appendix K. The result of the argument is that the only way to achieve first-order improvements in any figure of plasma performance is either to increase reactor size or to increase $\bar{J}\ B_{MAX}$. For example, total fusion power, with β_T proportional to ε, the inverse aspect ratio, is

$$P_T \sim (\bar{J}\ B_{MAX})^2\ C^6\ \varepsilon^4\ R_o^5 \tag{1.1}$$

where C is a measure of how close the TF coil is to the plasma magnetic axis and $C^6\ \varepsilon^4$ has an optimum value for any value of major radius R_o. The wall loading, with β_T proportional to ε, is

$$P_W \sim (\bar{J}\ B_{MAX})^2\ C^6\ \varepsilon^3\ R_o^3 \tag{1.2}$$

where $C^6\ \varepsilon^3$ $_o$has an optimum value for any R_o. While JB and P_W are functionally related, they are still independent.

To consider whether three independent figures of merit taken together are good indicators of commercializability, consider the following correspondences:

(1) $m^2 \Leftrightarrow \$$

(2) $MW \Leftrightarrow kWe$

(3) $MW \cdot (p.a.) \Leftrightarrow kWh$

The latter two correspondences are dimensionally obvious. While the dependence of reactor cost on the square of linear dimension is a reasonable fit to the relations found in numerical cost analyses, the actual relation is unimportant to this argument, as will be shown. When the terms on each side of the correspondences are combined we can obtain:

(1) $P_W^{-1} \Leftrightarrow \$/kWe$

(2) $(P_W \cdot (p.a.))^{-1} \Leftrightarrow \$/kWh$

and (3) $(J \times B)^{-1} \Leftrightarrow (\$/kWe) * \$$

Apart from important social costs, such as safety and environmental hazards, the only three financial cost figures related to commercialization are cost, cost per kilowatt and cost per kilowatt-hour. Assuming that first cost is proportional to the square of linear dimensions gives a particularly simple set of correspondences. However, any positive exponent will give the result that, if all three reactor figures of merit are increased, all three financial cost figures should decrease.

The three figures of merit indicate a direction for commercial reactor design studies to take and which we have attempted to take in the HFCTR study. In this study, we present a reactor design which significantly increases the

$\bar{J} \times B_{MAX}$ of previous reactor designs (as shown in Figure 1-1), equals the wall-loading and increases the plant availability over that in the previous generation of reactor designs.

J x B has been increased by the following methods:

(1) Use of Nb_3Sn superconductor. We have also examined the consequences of using a more advanced superconductor, such as $Nb_3(Sn_{1-x} Ga_x)$.

(2) Use of vertical reactions through the reactor central column to reduce tensile stress in the inside legs of the TF coils.

(3) Use of additional plate material in the "knee of the D" along with external horizontal reactions to reduce bending-induced stresses.

(4) Use of new experimental information to derive a new and encouraging correlation for the Nusselt number for multi-stranded cable in supercritical helium.

(5) Use of lattice-braided superconducting cable for even flow of helium coolant to each conductor strand.

(6) Use of well-characterized design techniques and experimental information developed through Westinghouse participation in the Large Coil Program.

First-wall thermal loading (MW/m^2) has been increased by the following methods:

(1) Use of a high heat capacity, low pumping power coolant, such as FLIBE.

(2) Use of a high maximum temperature structural material, such as TZM.

TOKAMAK	B_{MAX}	$\bar{J}$	$\bar{J}B_{MAX}$
UWMAK I	8.7 T	8.05 MA m^{-2}	69.7
UWMAK II	8.3 T	7.39 MA m^{-2}	61.3
UWMAK III	8.75 T	8.77 MA m^{-2}	76.7
GA EPR	8.0 T	12.7 MA m^{-2}	101
NUWMAK	11.9 T	11.7 MA m^{-2}	138
HFCTR	13.1 T	12.2 MA m^{-2}	160

Figure 1-1 Force Densities in Conceptual Superconducting Toroidal Field Coil Designs for Tokamak Power Reactors.

(3) Use of a thick copper coating on the first-wall coolant tubes to reduce thermal stresses.

(4) Use of bracketed thin tubes, unconstrained along their axes as the first wall facing the plasma.

(5) Use of a double vacuum vessel. The structural wall holding the first wall coolant tubes separates the medium vacuum blanket region from the high vacuum plasma region.

High plant availability, compatible with a high wall-loading and frequent need for replacement of a module, is achieved by the following methods:

(1) Total modularization. Every subsystem included in a 45° modular sector can be rapidly and automatically removed and replaced, not just the blanket and first wall.

(2) Use of flexible cryostats. TF dewars can collapse and form a monolithic toroidal structure with the central cylinder and each other on energization of the TF coils.

(3) Use of flat multilam copper joints, allowing zero-insertion force formation of inside joints in poloidal field coils.

(4) Use of double vacuum wall and mechanical vacuum seals.

(5) Replacement of manipulator-based maintenance by automatic actuator-based maintenance techniques.

1-3. PLASMA CHARACTERISTICS

The "empirical scaling" relation for the energy confinement time was used as a guideline for determining the plasma halfwidth needed to ensure ignition. The scaling relation is $\tau_E = 3.2 \times 10^{-21} q^{1/2} \bar{n}_L a^2$ [1,2] where all quantities are in MKS units, $\bar{n}_L$ is the line average density and a is the plasma radius. Reference [2] summarizes the experimental data on which this scaling relation is based. The plasma halfwidth was chosen to be as small as possible, consistent with insuring a reasonable margin of safety (MS) for the attainment of ignition. The margin of safety for a given Z_{eff} is defined as $MS \equiv (n\tau_E)_{emp}/(n\tau_E)_{ign}$, where $(\bar{n}\tau_E)_{emp} \sim n^2 a^2 \sim \beta_T^2 B_T^4 a^2/T^2$ is the value of $(n\tau_E)_{emp}$ at the reactor reference operating point, obtained from the empirical scaling law, and $(\bar{n}\tau_E)_{ign}$ is the value of $\bar{n}\tau_E$ needed for ignition. The maximum permitted values of $(\bar{n}\tau_E)_{emp}$ are limited by the requirement that $(\tau_E)_{emp}$ be less than $(\tau_E)_{nc}$ where $(\tau_E)_{nc}$ is the energy confinement time obtained from neoclassical scaling. For $Z_{eff} = 1.2$, MS = 2.4; while for $Z_{eff} = 1.5$, MS = 1.2. A further lower limit on the plasma halfwidth is set by the aspect ratio becoming so large that the plasma beta is unacceptably small. Based upon these consideration, the plasma halfwidth was chosen to be 1.2 m.

Reference base case operating parameters for the HFCTR are listed in Table 1-I. Figure 1-2 shows the possible range of density, temperature and average wall loading for the HFCTR. The upper limit on density and temperature is determined by the plasma pressure limit. The lower limit is determined by the requirement for ignition with a margin of safety of 1. Within this range the thermal power production can vary from ~1000 MW_{th} to 3300 MW_{th}.

TABLE 1 - I

REFERENCE HFCTR PARAMETERS

Machine Parameters	
Major radius, R_o (m)	6.0
Plasma halfwidth, a(m)	1.2
Aspect ratio	5.0
Plasma shape factor, S	1.5
Field at plasma, B_T(T)	7.4
Maximum field at winding, B_{T_o}(T)	13.1
Plasma volume, V_p(m^3)	317
First wall area, A_W(m^2)	475
Plasma Parameters	
Safety factor at $r = a$, $q(a)$	3.0
Average toroidal beta, $<\beta_T>$	0.04
Plasma current, (MA)	6.7
Electron density, n(m^{-3})	$5.2 \times 10^{20}(1 - \frac{r^3}{a^3})$
Electron ion temp, T (keV)	$12.4\ (1 - \frac{r^2}{a^2})$
Z_{eff} (Helium + Mo)	1.2
$(\bar{n}\tau_E)_{emp}/(\bar{n}\tau_E)_{ign}$	2.4
Beam Power, P_b(MW)	100
Beam Energy, W_b(keV)	120
Power Production	
Av. fusion power density, $\bar{P}_f$(MW/m^3)	7.7
14-Mev neutron wall loading, P_W(85% duty, MW/m^2)	3.4
Total fusion power, $\bar{P}_f V_p$	2440
Av. thermal power, P_{th} (85% duty, MW)	2470

TABLE 1 - I

REFERENCE HFCTR PARAMETERS (CONT.)

Machine Parameters	
Gross electric power, P_g (35% efficiency, MW)	870
Net electric power, P_n (MW)	775
Plant efficiency, η_p (%)	31

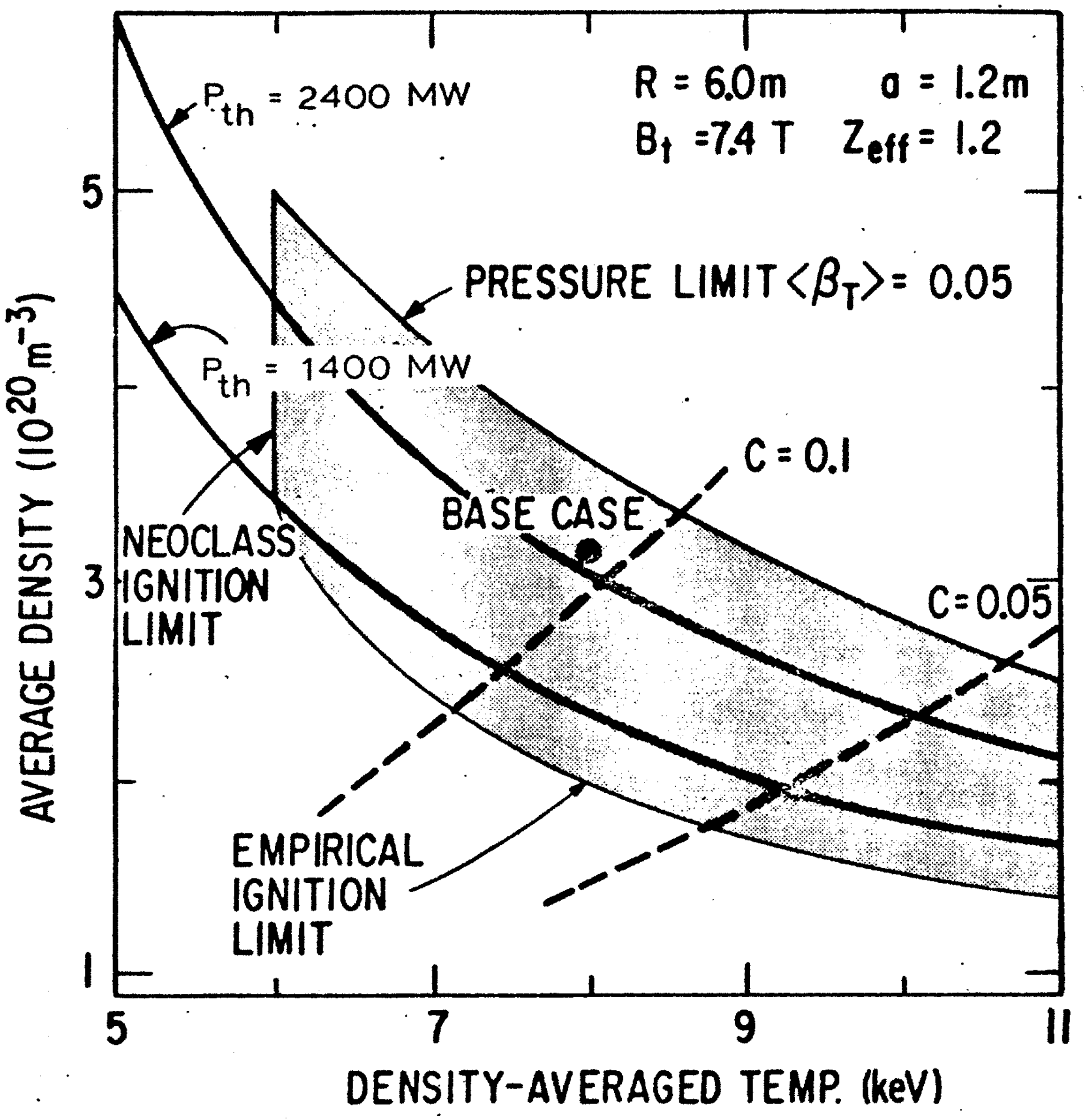

Figure 1-2 Shaded area is the permissible range of reactor operation for the parameters shown. Ignition limits for both empirical and neoclassical scaling laws are indicated. C ≡ plasma collisionality.

The neutron wall loading would vary from 1.4 MW/m^2 to 4.5 MW/m^2. In addition, it may be desirable that the collisionality (C) of the plasma be greater than ~0.1. The collisionality is defined as $C = \nu_{ei}A/\omega_{be}$, where ν_{ei} is the electron-ion-collision frequency, ω_{be} is the electron bounce frequency, and A is the aspect ratio. This value of collisionality is well within the range characteristic of present devices, where the empirical scaling law is known to be valid. Contours for collisionality equal to 0.1 and 0.05 are shown in Figure 1-1.

1.4 MAGNET DESIGN

The design of a magnet system to attain the highest practical toroidal field in a compact tokamak requires the integration of a number of different objectives. The aspect ratio and the ratio of toroidal field on axis to the field in the magnet windings are determined by the need to deal with large forces associated with high field operation and by the requirement of a satisfactory blanket thickness. In addition it is desirable to modularize the construction to facilitate disassembly for maintenance. Further practical constraints are the need to minimize pulse power requirements, to limit steady state power dissipation in copper coils and to reduce refrigeration losses in superconducting coils.

The coil configuration shown in Figure 1-3 has been developed to fulfill the objectives within the inherent constraints. Table 1-II lists the principal characteristics of the magnet systems. Figure 1-4 shows the basic TF sector module.

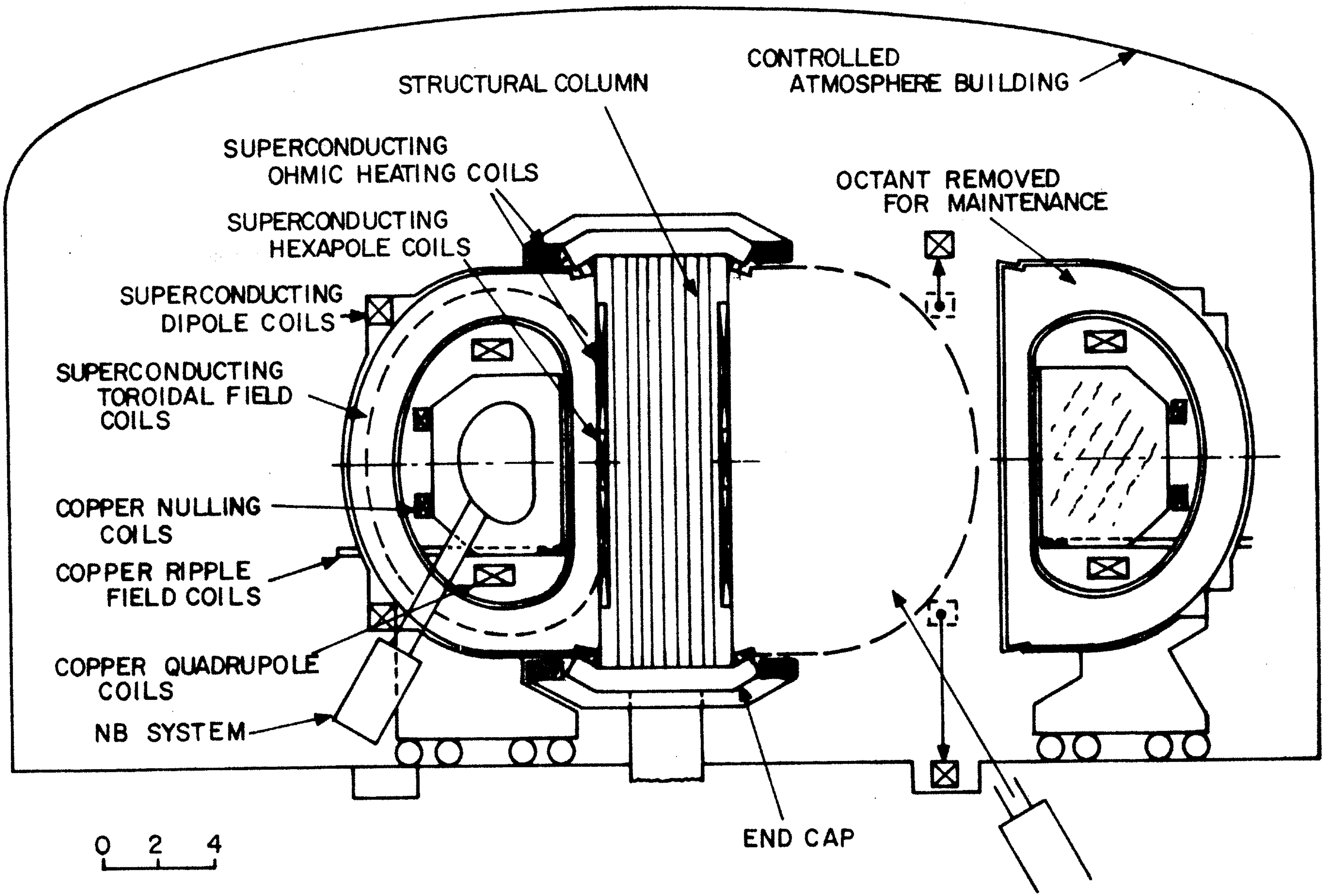

Figure 1-3 Elevation view of HFCTR showing all magnet systems.

TABLE 1 - II

HFCTR MAGNET SYSTEM PARAMETERS

TF Coils	
Number of coils	16
Current in each coil	13.9 MA
Field at $R_o = 6$ m	7.4 T
Maximum field in coil at R = 3.4 m	13.1 T
Inside aperture	6.5 m wide 10.5 m high
Ripple at outside plasma surface	1% max.
Maximum stress in winding structure	210 MPa (0.1% strain)
Stored energy	40 GJ
Weight of each coil assembly	425 tonnes
VF Coils	
Superconducting dipole coils	-21.2 MA
Copper quadrupole coils	6.4 MA
Copper null-field coils	6.4 MA pulsed
Copper null-field stored energy	500 MJ
Superconducting hexapole coils	-8.0 MA
VF Stored energy	2 GJ
OH Coils	38 MA total
OH Field	4.1 T max.
OH Stored energy (fast and slow pulsed)	1 GJ
Magnet System	
Peak power input (5 sec start-up)	565 MW
Average power input (500 sec burn)	80 MW
Startup flux requirement	120 Wb
Burn flux requirement	60 Wb

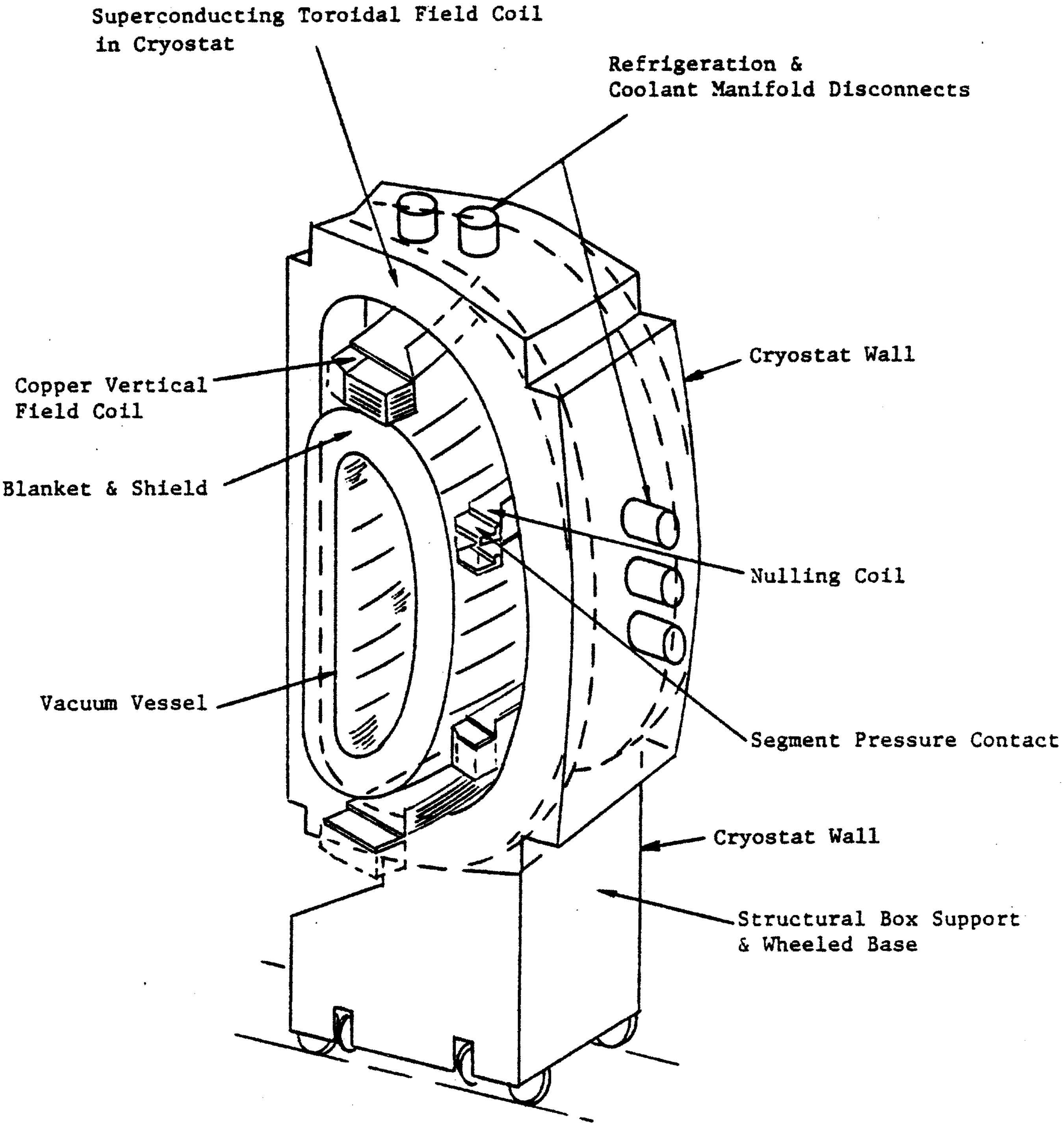

Figure 1-4 TF Sector Module

The reactor is designed so that the exchange of a module is accomplished by built in automatic devices. There are no time consuming hand operations that must be performed with manipulators. All power and coolant connections are made by remotely actuated quick disconnects and only those connections are actuated that are on the module which is to be moved.

A unique design for toroidal field coil tensile force containment uses circular end caps as in Figure 1-3 at the top and bottom to support a portion of the outward forces developed in the outer arc of opposed D coils [4]. In addition, end caps are fastened to the structural core so that vertical forces are carried by the entire central column. As a result, the tensile stresses on the center straight sections of the toroidal field coils are reduced.

The structural plates which carry the superconductor contain slots in which the insulated superconductor is inserted. The reinforcing structure shown separately for emphasis in Figure 1-3 is built into the plates in Figure 1-5 to limit the tensile stress in the outer arc of the conductor rings to 210 MPa, a strain of 0.1% in stainless steel.

The plan view in Figure 1-5 shows the basic features of the demountable sectored toroidal field coils. Two independent coils are mounted with a modular octant of the blanket and shield system on a common wheeled base. A major maintenance operation involves the replacement of one complete octant section. The cryostat walls surrounding the mating sides of the TF coil trunk straight section and the cryostat walls surrounding the core column are moveable, so that in the energized state a high-pressure solid contact is made. Conversely, when separated the cryostat vacuum walls will distend to limit thermal conduction and radiation, allowing the internal structure to

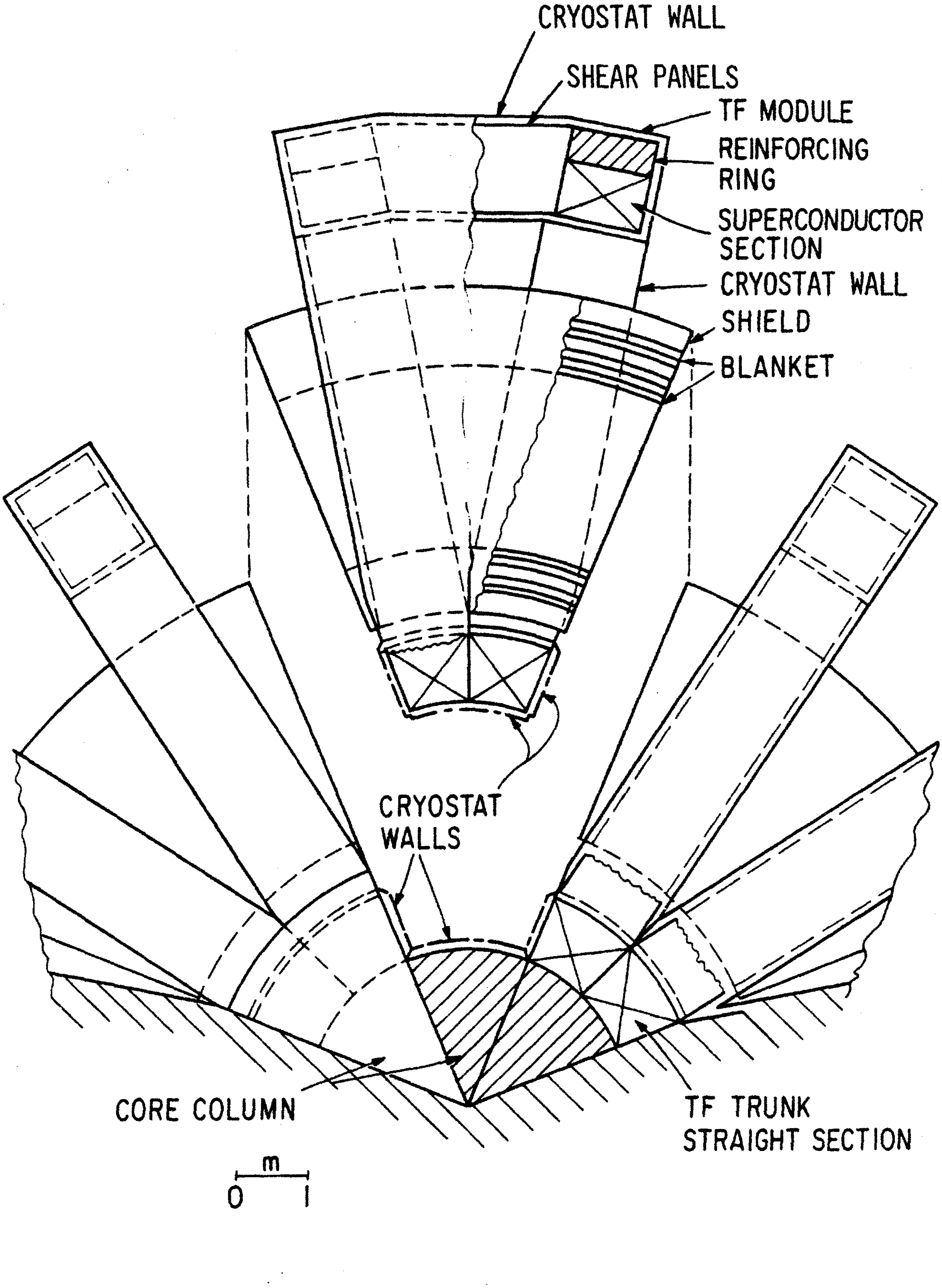

Figure 1-5 Plan view of toroidal magnet system with a two coil module demounted.

remain cold. This design avoids the necessity of warming the entire magnet system to service one module. The reference helium atmosphere around the entire magnet system eliminates air condensation on the cold surfaces which are accessible through "cracks" between the moveable cryostat walls.

The removal of a module is further simplified by the use of mechanically actuated vacuum seals instead of welds on the vacuum vessel flanges, and by the use of a method of support for out-of-plane forces which does not require the use of shear panels between modules.

The equilibrium field system is chosen to maximize the flexibility of coil location and to reduce the pulsed energy requirement. The main equilibrium field system consists of a superconducting dipole coil outside the toroidal field coils and a DC copper quadrupole coil inside. A nulling field coil, placed inside the toroidal field coils, is driven to oppose the DC vertical field [4]. It is regulated to provide the correct equilibrium field during start-up. The nulling-coil field is decreased as the plasma current increases, simultaneously providing the correct equilibrium field and about half of the required 120 Wb of fast flux. The energy transfer of 500 MJ in this system is only 1/4 that of the total equilibrium field. Figure 1-6 shows the time dependent magnetic flux transfer and the buildup of plasma current.

The copper coils which are located in the TF coil bore, are segmented to permit the withdrawal of a module. Supporting these segments on the blanket and shield structure to eliminate hoop tension makes possible the design of an intersegment connector which can operate at a current density consistent with those to be used in the coils. This connector which is of the zero insertion force type, will accept the position misalignments which are likely to occur between the segment ends and it will have an acceptable life when

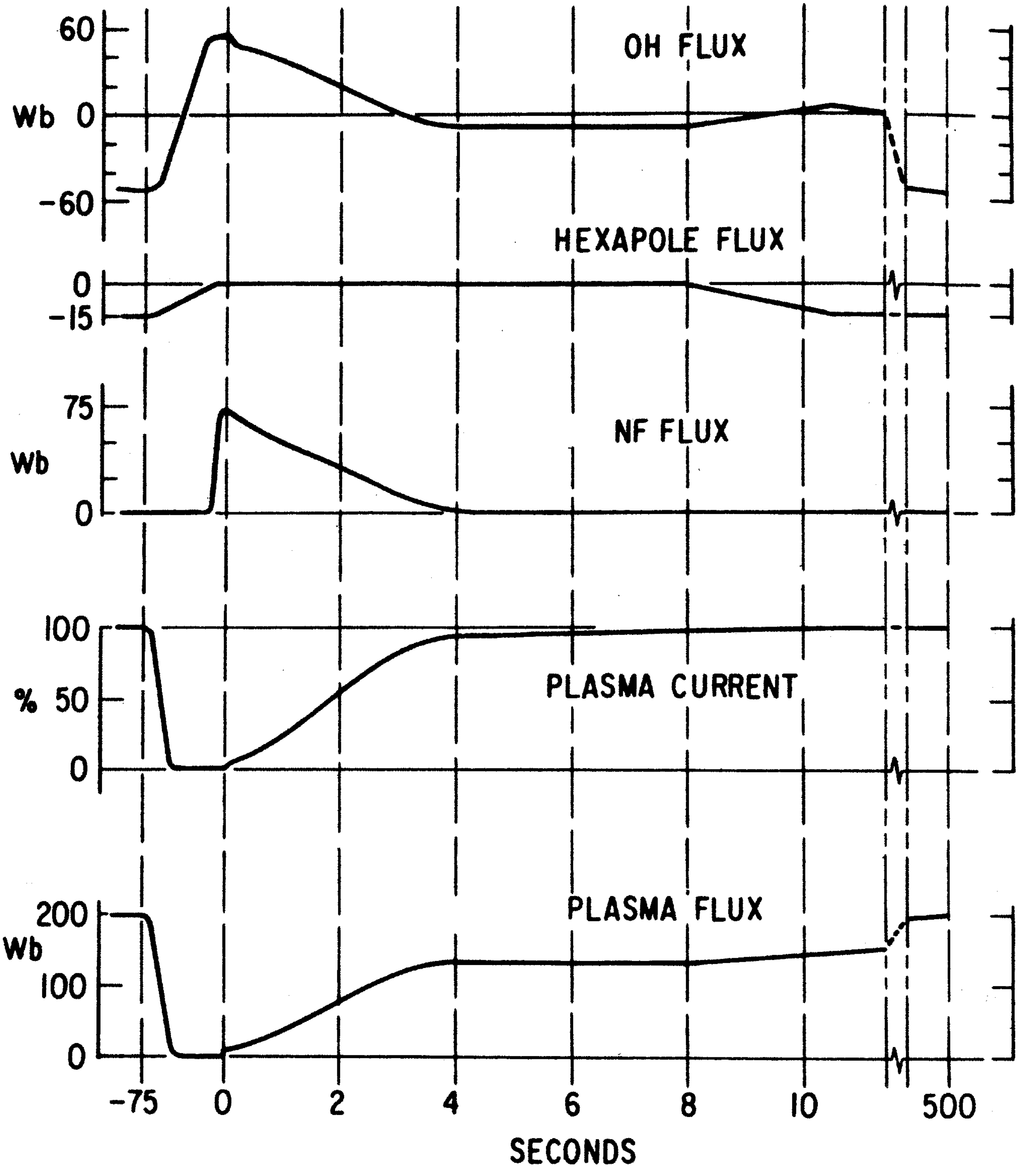

Figure 1-6 Waveforms of magnetic flux and plasma current.

operated with the small movements which occur at each pulse.

The superconducting hexapole coil is located in the throat and is independent of the toroid modules. This coil provides the field gradient needed to make the D-shaped plasma.

The additional flux needed for start-up and for maintaining the burn is supplied by a superconducting ohmic heating coil in the core. Supplementary compensating coils above and below the toroid modules are adjusted to make this field as small as possible at the plasma. To limit the maximum field and stored energy, the OH coils are driven from 4.1 T through zero to -4.1 T for a total flux transfer of about 120 Wb. The pulsed-coil conductor is made from a niobium titanium (NbTi) superconducting composite.

The imposition of an external field pulse on a superconductor greatly complicates the conductor design, especially at high fields. The average field increment imposed on the TF coil from the vertical field pulse and the induced plasma current is < 1 T. The energy dissipated by eddy currents in the twisted superconductor and stabilizer from the varying field is estimated to be < 3 kW per TF coil. As the critical temperature of Nb_3Sn is near 7 K at 13 T, there is a margin for thermal diffusion of the energy dissipated during the field pulse. Further refinement of the vertical field coil design should result in a substantial decrease in the pulsed losses.

1.5 PLASMA HEATING AND TEMPERATURE CONTROL

Conventional neutral-beam injection requires beam energies of about 400 keV D^{o} in order to ensure penetration of the fast neutrals into the central plasma region at the highest densities of interest ($\sim 5 \times 10^{20}$ m^{-3})

and correspondingly the highest margins of safety. In order to reduce the beam voltage requirement so as to permit use of state-of-the-art D° beams, the reference heating scheme in the present design makes use of the ripple-trapping injection method [6], for which 120 keV D° beams are adequate. This injection technique is not essential in the operation of the HFCTR and it would be possible to use conventional neutral injection if adequate negative ion beam technology is available. Eight beam injectors, each delivering 12.5 MW at 120 keV, are installed for near-vertical injection, as indicated in Figure 1-3. The required access area constitutes about 1% of the torus wall area. A toroidal field ripple with significant top-bottom asymmetry is produced by special ripple-inducing coils located in the horizontal plane 3.0 m below the magnetic axis, inside each of the eight TF modules. The eight sets of ripple coils produce alternate maxima and minima in the toroidal field, with the injectors located at the 8 minima. Energetic ions formed from the neutral beams are trapped in the ripple magnetic well, and drift upward to the central plasma region where the ripple becomes small (< 1%) and the ions are detrapped. The coils are activated during the 4 second higher-density period of the start-up stage. Each single turn ripple coil carries 1.8 MA, and the pulsed Joule heating in the eight coils is 130 MW. The power consumed is 1 MW when averaged over the burn time of 500 seconds.

Fusion alpha particles begin to contribute significantly to plasma heating when T_i reaches about 5 keV. The vertically asymmetric ripple causes a fast radial drift of the banana-trapped alphas (about one-third of the total alpha population), so that only about 70% of the alpha energy is deposited in the plasma [6]. Once ignition is attained, the ripple coils are deactivated.

If the empirical confinement scaling remains valid at the operating temperature, then the equilibrium operating point is unstable to temperature perturbations. It may then become possible, by activating one or more pairs of ripple coils during the burn, to vary the fraction of confined alpha particles in response to temperature perturbations [8].

Even without active thermal stabilization, an upper limit to a temperature runaway would probably be set by the onset of MHD ballooning modes [9] when the plasma beta exceeds 5%. These modes are expected to result in enhanced radial heat diffusion, effectively introducing an unfavorable temperature dependence of confinement time.

In the event that $n\tau_E$ at the steady-state ignited operating point turns out to be several times the value needed for equilibrium ignition, a fixed amount of radiating high-Z gas (e.g. xenon) can be added to provide an equilibrium operating point. Less than 0.1% of xenon is required.

1.6 BLANKET AND SHIELD

The basic concept behind the blanket design is to use lithium as the breeding material while cooling the blanket with the molten salt, FLIBE ($2\ \mathrm{LiF \cdot BeF_2}$). This blanket is designed specifically for use at high neutron wall-loadings in intense magnet fields in a compact device. The requirement of small blanket thickness demands that a fairly dense coolant be used. The liquid metals would require unacceptable pumping power levels because of MHD effects in the high magnetic field, and pressurized gases - even at 50 atm - are not compatible with minimum blanket thickness. FLIBE is attractive because it is characterized by high density and good heat-transfer properties, while having a relatively low electrical conductivity [10].

It is chemically stable, is relatively noncorrosive and is neutronically favorable. In this arrangement FLIBE is used primarily for cooling the first wall and blanket. The total pumping power requirement for the blanket in the reference design of the HFCTR is about 10 MW during operation.

The molybdenum alloy TZM (99.39% Mo, 0.5% Ti, 0.08% Zr, 0.03% C) may be an appropriate structural material choice. It can be utilized at the relatively high temperatures required for molten salt operation and is chemically compatible with FLIBE. The problem of fabrication associated with TZM has been alleviated as much as possible by a modular blanket design which allows sections of the blanket to be fabricated at the point of manufacture, where good quality control is feasible. The design also allows for the primary vacuum seals to be made with stainless steel in the moderator/reflector region.

A diagram of the "outboard" blanket and shield is shown in Figure 1-7. The first surface seen by the plasma consists of a set of tubes which are convectively cooled by FLIBE passing through them. These tubes intercept all the alpha power (~ 1 MW/m^2 as a surface heat load). Further into the blanket there are a number of molten lithium breeding regions (95% Li - 5% Mo) which are cooled by FLIBE flowing in tubes. The lithium is essentially stagnant, flowing only fast enough to maintain a low tritium inventory (cycle time $\sim$ 1 day). Beyond the breeding regions is the two part graphite and stainless-steel moderator/reflector and composite stainless steel and boron carbide shield. Additional shielding on the outboard side is placed just inside the TF coil cryostat wall.

The "inboard" blanket/shield thickness is approximately 1.0 meter, while the "outboard" blanket/shield serves mainly as a shield with minimal breeding. Neutronic analysis shows that the tritium breeding ratio of the "outboard"

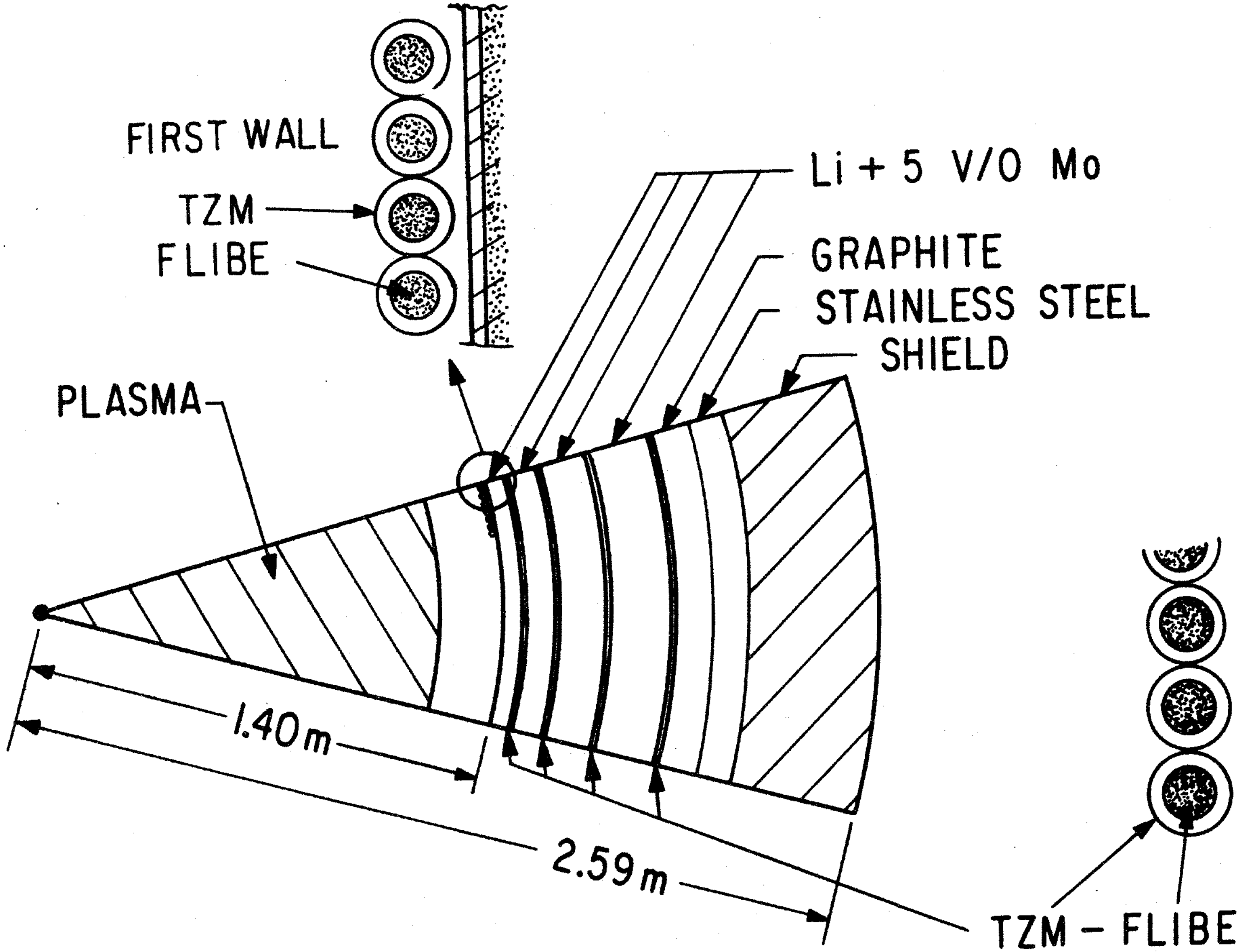

Figure 1-7 Section diagram of outboard blanket and shield.

blanket/shield is 1.23. The net tritium breeding ratio for the entire blanket is about 1.05. Decay analysis and radiological hazard evaluation were not treated in this study.

1.7 BURN TIME

The tokamak burn time has a direct effect on several reactor properties: the fatigue to failure time of the first wall, the energy multiplication factor, and the duty cycle. These factors bear directly on the overall reactor economics.

In the HFCTR, as in all tokamak designs, the burn time is limited either by the available volt-seconds needed to sustain the plasma current or by the impurity buildup. In this context, impurities refer to the alpha ash plus the sputtered first wall material. Whether impurities quench the plasma before the volt-seconds are expended depends on the influx and efflux of the various impurity species as well as the effectiveness with which they can be removed from the plasma. At present, relatively little is known about impurity behavior in a thermonuclear reactor. However, valuable impurity information should become available with experiments proposed for the 1980's. Earlier information about impurity behavior at reactor temperatures is expected from the ISX-B and PDX experiments.

If the ignited plasma is not quenched by impurities, then a burn time of 500 seconds or longer is anticipated. This is based on 60 volt-seconds or more being available during the burn period. These volt-seconds come from the OH coils located in the core. Throughout this report a base case burn time of 500 seconds is assumed.

The dwell time (cycle time minus burn time) for the base case HFCTR is estimated to be 20 seconds. This is based on a shutdown time of $\sim$ 4 seconds, a pumpout and recharge time of $\sim$ 7 seconds, and a start-up time of $\sim$ 8 seconds. With a relatively long HFCTR burn time of $\sim$ 500 seconds and a dwell time of $\sim$ 20 seconds, the problems associated with a pulsed reactor are mitigated. That is, the fatigue to failure time is long, the energy multiplication factor is large, and the duty factor is close to unity.

If the burn period is short (i.e., τ_b < 100 seconds), then the HFCTR, as presently designed, is unlikely to be economical. Besides resulting in low energy multiplication factors and short first wall lifetimes, the OH and TF coil refrigeration requirments could become unacceptably large.

For the HFCTR to avoid impurity quenching, adequate impurity control must be provided. The incorporation of a divertor for this purpose adds to the complexity of the HFCTR and could have a significant detrimental impact on the ease of maintenance. As a result, impurity control is provided by a combination of a plasma-gas blanket and a limiter that facilitates alpha ash pumping. Plasma-gas blankets, as presently observed in high density experiments, reduce the neutral efflux. This should minimize first wall sputtering and limit the amount of molybdenum that gets into the plasma. The limiter-pumping scheme prevents the alpha ash from accumulating to unacceptable levels. If relatively little molybdenum gets into the plasma, then considerable levels of alpha ash can be tolerated (i.e., $n \sim 10^{20}\ m^{-3}$) and the effectiveness of the limiter-pumping scheme can be reduced.

1.8 IMPLICATIONS FOR THE NEXT STEP REACTOR

The next step tokamak fusion reactor should be designed to resolve as many of the questions related to the commercialization of fusion power as possible. Several important features, such as plasma ignition, long pulses, superconducting coils and divertors have been incorporated into the design of various proposed next step reactors. We believe that the design of HFCTR has sufficiently sharpened our vision of the commercial fusion reactor to suggest several new features which merit technology tests and are attractive for incorporation into a next step reactor. These are listed below:

(1) Flexible cryostats. The next-step reactor might be modularized. One module could include a flexible cryostat and be capable of being rapidly removed and replaced by an automated remote handling system. Some concepts for rapid sublimation of frozen air, such as resistive bellows heaters, could also be incorporated.

(2) Poloidal field coil joints. All reactor concepts could be improved if reliable, remotely connectable poloidal field coils, outside the toroidal field coils, were included to permit reactor operation in the case of joint failure.

(3) Actuators and quick-disconnect joints for remote disassembly. One module could be completely equipped with all of the fully automated features which would be desirable in a commercial reactor. All automatic assembly/disassembly procedures could be demonstrated before D-T operation. Manipulators would be used to disassemble the rest of the reactor (and the automated module in case of quick-disconnect equipment failure).

(4) Mechanical vacuum joints. One module of the plasma vacuum vessel could include mechanical joints, both in the high-vacuum plasma-containing vessel and in the medium-vacuum, atomospheric pressure-withstanding vacuum vessel. Both flange designs could incorporate the possibility of welding the vessels shut if the mechanical joints are inadequate.

(5) Fast reestablishment of high vacuum. Methods of rapidly reestablishing high vacuum, after a module has been exposed to air or a helium environment could be demonstrated.

(6) Fast detritiation. Definitive experiments on the permeation of tritium through candidate first wall materials could be performed. A fast method of first wall detritiation, prior to opening up a module, should be demonstrated, if possible.

(7) Frictional support of overturning forces. One two-coil module would not have shear panels between itself and adjacent modules.

(8) Material limiter with vacuum pump. A material limiter with associated vacuum pumps could be evaluated as an alternative to a divertor, under reactor-like conditions, in a machine which includes a divertor.

(9) Ripple coils. One module could incorporate a ripple coil to assist neutral beam penetration.

1.9 DIRECTIONS FOR FURTHER DESIGN STUDY WORK

The major direction of further work should be to demonstrate the feasibility of a tokamak fusion reactor with higher values of the engineering figures of merit. In accordance with this goal, work should be begun on the preconceptual design of a reactor which doubles the fusion power of the present reference design, without changing the major dimensions. One measure of progress in the conceptual design fusion reactors has been a steady reduction of the major radius (e.g. UWMAK I, II, III). However, at this point it is more advantageous to demonstrate conceptual progress by holding the major reactor dimensions constant while improving plant availability and increasing the output power. The specific design studies needed to achieve this goal include several new topics for investigation and more detailed studies of previous topics. The most important subjects for immediate investigation are listed below:

- Further work should be done to establish the feasibility of the remote maintenance procedures proposed here. This work includes quantifying the times necessary for detritiation prior to disassembly and the reestablishment of high vacuum after reassembly and the expected times for the formation of frozen air on the flexible cryostat and for the removal of frozen air in atmospheric air, helium and evacuated chambers. The costs associated with these three alternative reactor environments should be better quantified. A hardware survey should also be performed, in particular to permit a meaningful comparison between the HFCTR and Culham MK II approaches to reactor disassembly.

- Higher JB (> 200 MA-T m^{-2}) toroidal field coil designs should be developed.
- A study of the feasibility of mechanical limiters, supplemented by vacuum pumps, as an alternative to magnetic divertors should be initiated.
- A study of various means of alleviating problems resulting from the possibility of a short burn (t_b < 100 seconds) caused by alpha ash buildup.
- The compatibility of a bundle divertor with a high field tokamak power reactor should be studied.
- A practical mechanical design of a plasma first-wall and blanket for very high wall loading (P_w > 5 MW/m^2) should be developed. High-vacuum considerations in the plasma chamber should be included.

REFERENCES - SECTION 1

[1] COHN, D.R., PARKER, R.R., and JASSBY, D.L., Nucl. Fusion 16 (1976) 31.

[2] JASSBY, D.L., COHN, D.R., and PARKER, R.R., Nucl, Fusion 16 (1976) 1045.

[3] PARKER, R.R., Trans. Am. Nucl. Soc., 26 (1977) 17; PLT group, 8th Eur Conf. on Controlled Fusion and Plasma Physics (Prague 1977), to be published.

[4] WILLIAMS, J.E.C., COHN, D.R., JASSBY, D.L. and PARKER, R.R., Trans. Am Nucl. Soc. 24 (1976) 44; COHN, D.R., JASSBY, D.L., PARKER, R.R., and WILLIAMS, J.E.C., The Technology of Controlled Nuclear Fusion, (Proc. 2nd Top. Mtg., Richland, WA. 1976) III, 931.

[5] MITCHELL, J.T.D., Proc 9th Symp on Fusion Technology, 1976.

[6] JASSBY, D.L. and GOLDSTON, R.J., Nucl. Fusion 16 (1976) 613.

[7] PARKINS, W.E., Science 199 (1978), 1403

[8] JASSBY, D.L. and TOWNER, H.H., Trans Am. Nucl. Soc. 24 (1976) 56.

[9] TODD, A.M. et.al., Phys Rev. Lett. 38 (1977) 826.

[10] GRIMES, W.R. and CANTOR, S., The Chemistry of Fusion Technology (Plenum Press, N.Y., 1973) 161.

2. PLASMA CHARACTERISTICS

One of the principal goals of the present study is to determine the range of parameters achievable when the confinement scaling currently observed in tokamak experiments ($\tau_E \propto na^2$, where n is the electron density) is extrapolated to the reactor regime. The range of characteristics which "empirically-scaled" plasmas might have is presented in the detailed plasma parameteric study described in Section 2.1.

The particular assumptions which lead to the HFCTR and the resultant HFCTR plasma characteristics are presented in Section 2.2. In this section, results of the parametric study are extensively used.

Section 2.3 presents a comprehensive discussion of the method of executing a low density start-up which minimizes the equilibrium field control and the neutral beam power.

Methods of impurity control and fueling applicable to a high density reactor are discussed in Section 2.4 and techniques for providing thermal stability of the plasma are presented in Section 2.5.

2.1 PLASMA PARAMETRIC STUDY USING THE EMPIRICAL SCALING LAW

Plasma parametric studies are, in general, very dependent on the scaling laws used for the description of the energy and particle confinement times. Previous studies have assumed various theoretical models for the energy confinement time [1,2]. The present study assumes that the energy confinement time is given by the empirical scaling law: [3,4]

$$\tau_E = 3.2 \times 10^{-21} \bar{n}_L q^{1/2} a^2 \text{ [sec]}$$

where $\bar{n}_L$ ≡ line-averaged electron density $[m^{-3}]$

q ≡ safety factor at $r = a$

a ≡ half-width of the plasma. [m]

The justification for this scaling law is given in Figure 2-1 [5-8], where τ_E divided by $\bar{n}_L q^{1/2}$ has been plotted for a number of ohmically heated tokamaks. The straight line is given by equation (2.1).

It is assumed that elongation (at constant halfwidth) does not increase the energy confinement time given by equation 2.1. Thus the above equation gives a conservative value for τ_E.

Recent results in ALCATOR A ($a = 0.09$ meter) have shown that the global energy confinement time follows this scaling to densities as high as $\bar{n}_L = 6 \times 10^{20}\ m^{-3}$. [9]. However, at these high densities there is some evidince that the local confinement time in the center of the plasma column is levelling off (at fixed B_T and I_P), probably due to the appearance of neoclassical ion thermal conductivity as a dominant transport mechanism. The implications of this classical saturation for the demonstration reactor are discussed below.

Throughout this section all quantities have MKS units with the exception of temperatures, which are in keV. All quantities are defined in Appendix A.

2.1.1 Calculational Model

Using a global energy balance similar to that employed by Stacey [10], a computer model was developed to study the parametric trade-offs. The model employed by Stacey was modified by making the following assumptions.

(1) Temperature equilibration: Because steady-state operation at high density ($n > 1 > 10^{20}\ m^{-3}$) is considered, the electron and ion

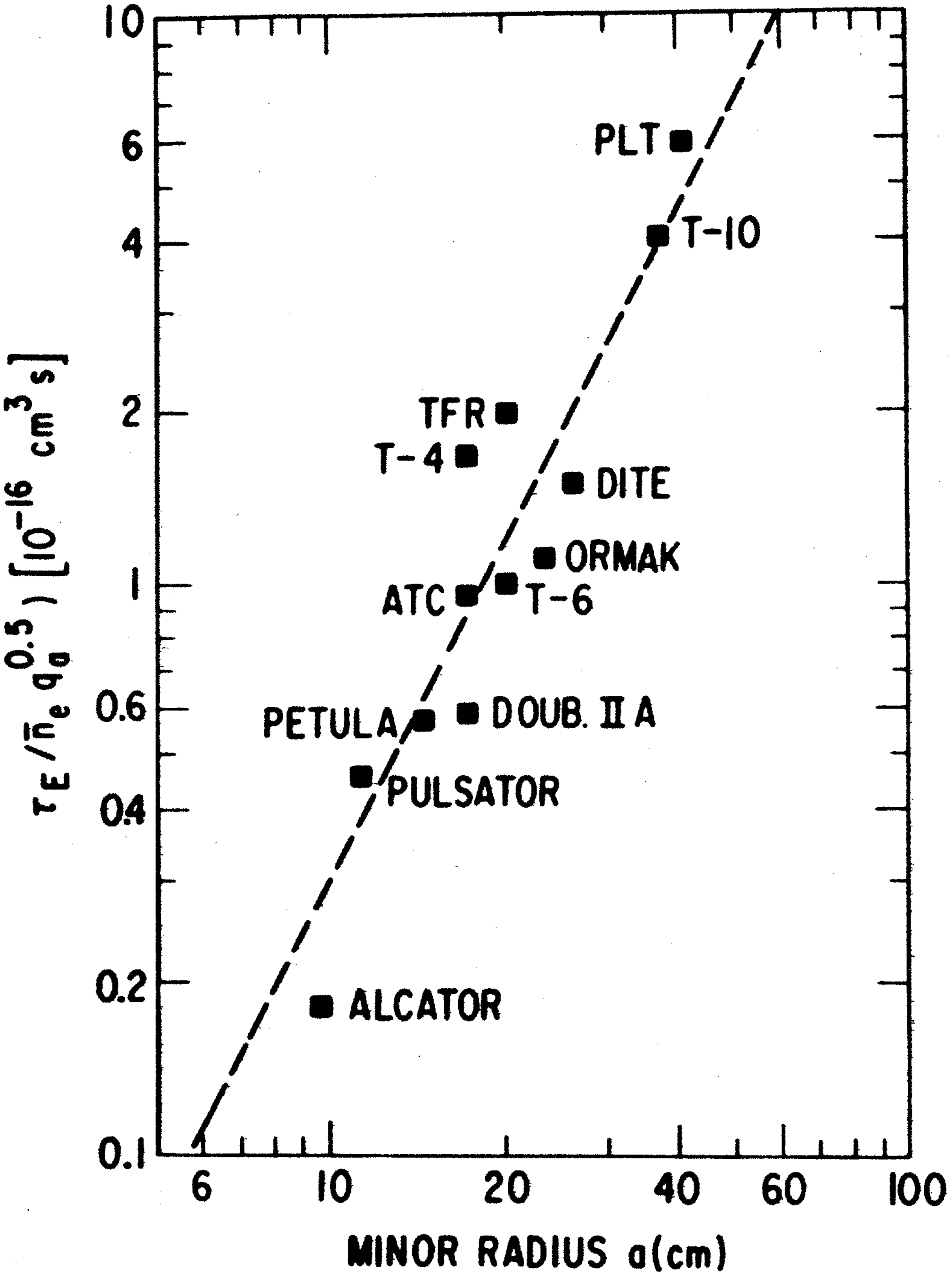

Figure 2-1 Energy confinement time $\tau_E = 1.5\ (n_eT_e + n_iT_i)\ \frac{dV}{P_{ohm}}$, normalized to $\bar{n}_e q^{0.5}$, for Ohmic-heated H or D tokamak plasmas. $\bar{n}_e$ is the line-averaged electron density and q_a is the safety factor at the limiter. From Ref [4]. The dashed line represents $\tau_E \sim a^2$. The best fit is obtained for $\tau_E \sim a^{2.2}$.

temperatures are assumed to have equilibrated: $T_e = T_i$.

(2) Equilibrium and ignition: The plasma is assumed to be ignited, that is, the alpha heating offsets the energy losses. Although the equilibrium operating point is unstable with respect to density and temperature fluctuations when empirical scaling is used, this point is assumed to be controllable (See Section 2.5), so that $\frac{d(nT)}{dt} = 0$.

(3) Energy and particle confinement: Equation (2.1) was used to describe both the energy and particle confinement; i.e., $\tau_P = \tau_E$. In actuality, τ_P might be somewhat larger.

(4) Radiation: A model for line-radiation based on the results of Post [11] and Hopkins [12] was used to account for the radiation losses due to high Z impurities. Assuming the high Z impurity is molybdenum, then the equation for this loss (assuming a strongly-favored $2_p - 2_S$ transition) is

$$P_L = 1.2 \times 10^{-32} n n_I \frac{S_x}{T^{1/2}} \frac{\text{watt}}{m^3} , \tag{2.2}$$

where

$$S_x \simeq -.5772 - \ln(-x) + \frac{x^2}{4} - \frac{x^3}{18} + \ldots,$$

$$x = 2 \times 10^{-3} \frac{(Z_I - 2)}{T}$$

and

n_I is the impurity ion density.

Although high toroidal fields are used in this study, the cyclotron radiation losses are expected to be inconsequential. This is examined further in Appendix B.

(5) Profiles: Recent studies have shown that the power balance is very sensitive to the radial profiles of density and temperature which are assumed [13]. In this study the density and temperature profiles are assumed to be given by

$$n(r) = n_o\left(1 - \frac{r^3}{\bar{a}^3}\right) \tag{2.3}$$

and

$$T(r) = T_o\left(1 - \frac{r^2}{\bar{a}^2}\right) \tag{2.4}$$

A slightly deformed plasma with a shape factor S = 1.5 is used. The mean halfwidth is therefore given by

$$\overline{a^2} = a^2(2S^2 - 1)^{1/2} \equiv \kappa a^2 \tag{2.5}$$

κ defined here in terms of the shape factor, is proportional to the ratio of plasma height to width (b/a). The radial dependences are eliminated by integrating over r and redefining quantities in terms of area averages:

$$\bar{f} \equiv \frac{1}{\pi\bar{a}^2}\int_0^{\bar{a}} f(r) \cdot 2\pi r dr \tag{2.6}$$

The only exception to this redefinition is the temperature, which is density-averaged so that $\bar{T}$ reflects the average energy per particle:

$$\bar{T} \equiv \frac{\int_0^{\bar{a}} T(r)n(r) \quad 2\pi r dr}{\int_0^{\bar{a}} n(r) \quad 2\pi r dr} \tag{2.7}$$

Figure 2-2 shows a comparison of the radial dependence of density, temperature, toroidal beta, and power density which results from the profile equations (2.3 and 2.4). Because of the simultaneous peaking of temperature and density in the center of the plasma column, the power output from plasmas with realistic profiles is higher than that from plasmas with flat profiles. Ignition is achieved more easily when profiles are taken into account.

(6) Deuterium/tritium ratio: The fuel composition is assumed to be 50% deuterium and 50% tritium to maximize the fusion power density.

(7) Plasma to TF coil distance: For the most efficient use of the toroidal field, the distance from the plasma to the TF coils should be minimized on the inboard side of the plasma. This distance is set at d = 1.4 meters, based on the shielding requirements described in Section 4.

(8) Safety Factor: The value of the safety factor at the limiter has been chosen to be 3.0.

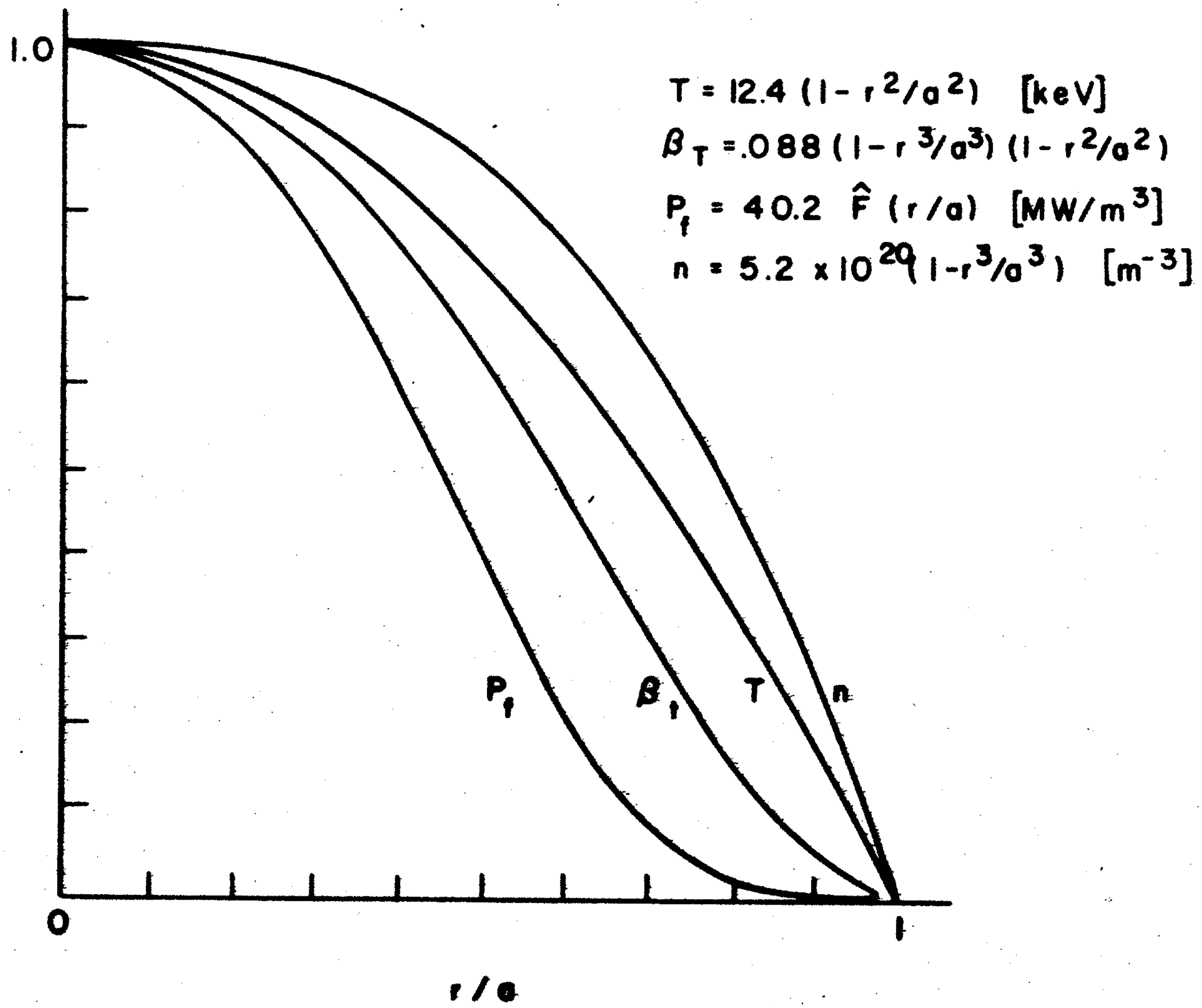

Figure 2-2 Normalized n,T, β_T, and P_f profiles.

2.1.2 Ignition Criteria

The criterion for ignition is that the plasma heating must equal the sum of the radiative, diffusive, and convective losses:

$$.25\ \overline{n^2 \langle \sigma_f v \rangle E_\alpha} = \overline{P_B} + \overline{P_L} + \frac{\overline{3nT}\ 1.6 \times 10^{-19}}{\tau_E} \tag{2.8}$$

where P_B is the bremsstrahlung radiation, P_L is the line radiation, $\langle \sigma_f v \rangle$ is the average of $\sigma_f v$ over a Maxwellian at T, $E_\alpha = 5.63 \times 10^{-13}$ Joules, and overhead bars denote area averages. In this equation it is implicitly assumed that the electron and ion densities are nearly equal. Furthermore P_B in equation (2.8) is given by [14]

$$P_B = 5.35 \times 10^{-37}\ Z_{eff}\ n^2 T^{1/2}\ \frac{\text{watt}}{\text{m}^3} \tag{2.9}$$

and P_L is given by Equation (2.2) where the product of the electron and impurity densities may be written as

$$n n_I = f(Z_I) n^2 \tag{2.10}$$

with

$$f(Z_I) = \frac{Z_{eff} - 1}{Z_I(Z_I - Z_{eff})} \times \left[1 + \frac{(Z_I - 2)(Z_{eff} - 1)}{Z_I(Z_I - Z_{eff})}\right]$$

Throughout this section the minimum Z_{eff} is assumed to be 1.1. This value is due to an alpha equilibrium density ≈ 0.05 n_e, obtained by assuming the thermalized alphas have the same particle confinement time as deuterium and tritium. Any additional contribution to Z_{eff} comes from the molybdenum impurity.

Equation (2.8) may be rewritten in the form of an $\bar{n}\tau$ criterion for ignition:

$$(\bar{n}\tau)_{ign} = \frac{3\ \bar{n}\ \overline{nT}\ 1.6 \times 10^{-19}}{0.25n^2\ <\sigma v>\ E_\alpha - K_B Z_{eff}^2 n^2 T^{1/2} - K_L f(Z_I) n^2 \frac{S_x}{T^{1/2}}} \qquad (2.11)$$

where $K_B = 5.35 \times 10^{-37}$ and $K_L = 1.2 \times 10^{-32}$. From Equation (2.11), it can be seen that $(\bar{n}\tau)_{ign}$ is independent of the magnitude of the density, but does depend on the density and temperature profiles.

By using Equations (2.1), (2.3), and (2.5), the value of $\bar{n}\tau$ given by the empirical scaling law may be written as:

$$(\bar{n}\tau)_{emp} = 4.0 \times 10^{-21}\ \bar{n}^2 a^2 q^{1/2} \qquad (2.12)$$

By setting $(\bar{n}\tau)_{emp} = (\bar{n}\tau)_{ign}$, the "empirical ignition criterion" may be found:

$$\bar{n}^2 a^2 = \frac{(\bar{n}\tau)_{ign}}{4.0 \times 10^{-21} q^{1/2}}$$

Using equation (2.11), the empirical ignition criterion is

$$\bar{n}a = \left[\frac{1.2 \times 10^5\ \bar{n}\ \overline{nT}}{1/4n^2 <\sigma_f v> E_\alpha - K_B Z_{eff}^2 n^2 T^{1/2} - K_L f(Z_I) n^2 \frac{S_x}{T^{1/2}}}\right]^{1/2} \qquad (2.13)$$

$$\equiv G(\bar{T},\ Z_{eff})$$

In the range of temperatures of interest (5 keV $< T <$ 12 keV), $G(\bar{T}. Z_{eff})$ is a decreasing function of temperature and an increasing function of Z_{eff}.

Equation (2.13) is plotted in Figure 2-4. In this graph $Z_{eff} = 1.1$ (i.e. no molybdenum, only the equilibrium alpha ash). Figure 2-4 therefore shows the empirical ignition curves under the most optimistic conditions. For example, the HFCTR ($a = 1.2$ m, $\bar{T} = 8$ keV) could achieve ignition with a density as low as 1.8×10^{20} m^{-3} if it is extremely clean. But it is highly improbable that a $Z_{eff} = 1.1$ plasma could be produced.

The important tradeoff to notice in Figure 2-4 is the inverse relationship between operation is necessary.

With the empirical scaling the product of plasma density and size, $\xi = \bar{n}a \equiv G(\bar{T}, Z_{eff})$, appears repeatedly. Equation (2.13) shows this to be a very important parameter. In addition to plotting the empirical ignition curves as $\bar{n}$ vs. a at fixed temperature and Z_{eff}, they may be plotted as ξ vs. temperature at various values of Z_{eff}. This is done in Figure 2-5. The numbers in parentheses are the concentration of molybdenum corresponding to each Z_{eff}. The importance of impurities in the ignition criterion is apparent. For example, at $\bar{T} = 8$ keV, ξ must increase from 2.1×10^{20} m^{-2} to 3.4×10^{20} m^{-3} if Z_{eff} changes from 1.1 to 1.5. For $a = 1.2$ meters, this represents a density increase from 1.7×10^{20} m^{-3} to 2.9×10^{20} m^{-3}. Note that if at $\bar{T} = 8$ keV, ignition cannot be achieved for $Z_{eff} > 1.7$, some combination of larger halfwidth, higher density, and higher temperature is needed to overcome a higher Z_{eff}.

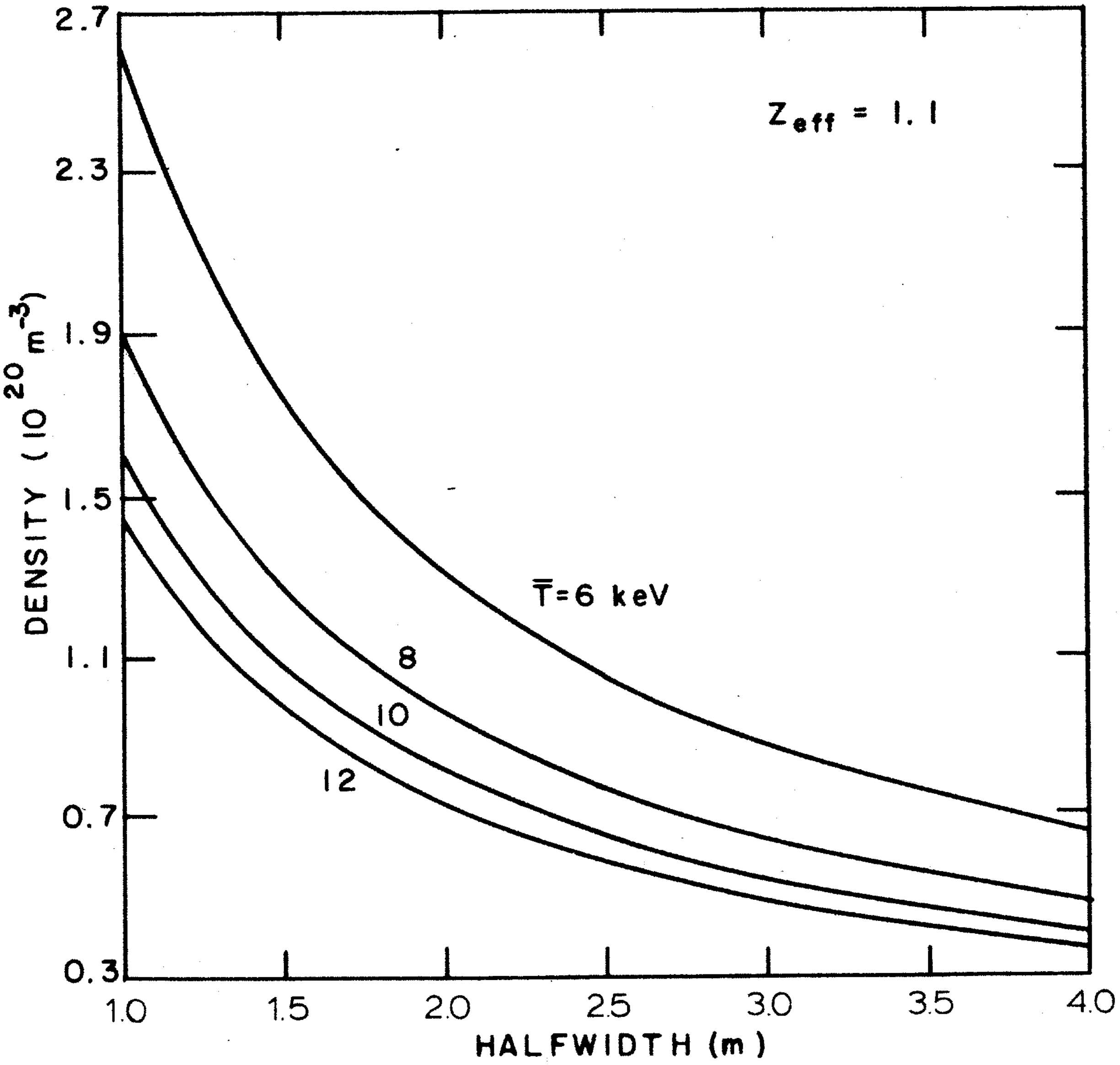

Figure 2-4 Empirical ignition curves plotted as n vs a.

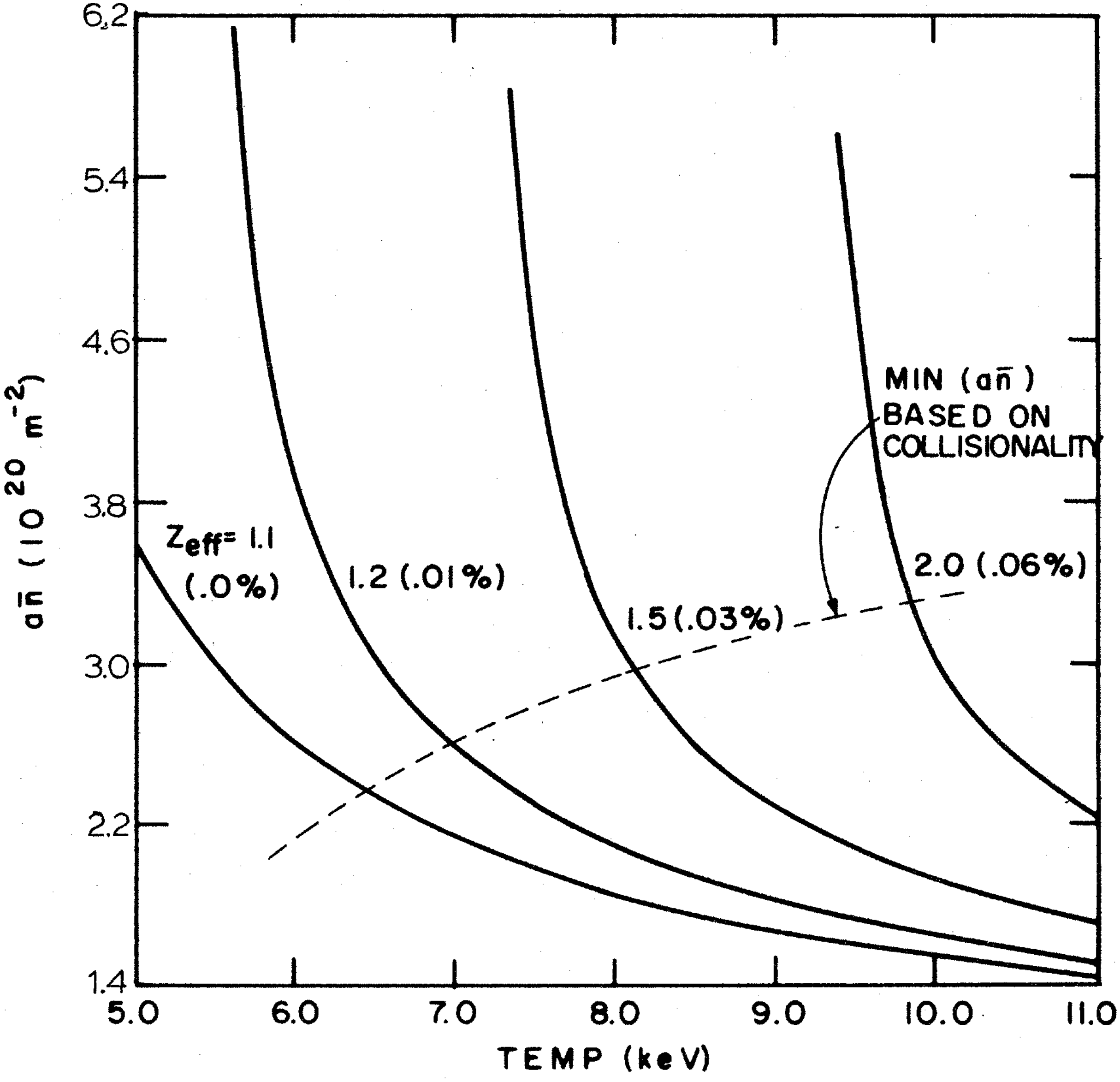

Figure 2-5 Empirical ignition curves plotted as $a\bar{n}$ vs. $\bar{T}$.

2.1.3 Collisionality Criterion

Most tokamak experiments, from which the empirical scaling law is obtained, operate in regimes of relatively large collisionality:

$$C \equiv \frac{\nu_{ei} A}{\omega_{be}} > 0.1$$

where ν_{ei} is electron-ion collision frequency, A is plasma aspect ratio, (throughout this section A = 5 will be used), and ω_{be} is electron bounce frequency. It may be written as

$$C = 6.0 \times 10^{-23} \frac{S\ q\ A^{2.5} Z_{eff} \xi}{\bar{T}^2} > 0.1 \tag{2.14}$$

Notice that the parameter $\xi = \bar{n}a$ also appears here. For the tokamaks listed in Figure 2-1, with the notable exception of PLT, the range of collisionality is between 0.1 and 1.5. Confidence in extrapolating the empirical scaling law to a power reactor increases if the collisionality is kept close to this range, i.e. $C \gtrsim 0.1$. In addition, theoretical considerations indicate that at lower collisionality a number of plasma instabilities may cause the confinement to deteriorate [16].

The minimum ξ which maintains C = 0.1 is given by

$$\xi_{min} = \frac{1.65 \times 10^{-21}\ \bar{T}^2}{S\ q\ A^{2.5} Z_{eff}} \tag{2.15}$$

Equation (2.15) is plotted with dashed lines in Figure 2-5. At $Z_{eff} = 1.1$, the minimum value of $\xi = \bar{n}a$ is 2.3×10^{20} m^{-2} and occurs at $\bar{T} = 6.4$ keV. If a were chosen to be 1.2 meters, the density which would satisfy both the ignition criterion, Equation (2.13), and the collisionality criterion, Equation (2.15), would be $\bar{n} = 1.9 \times 10^{20} m^{-3}$.

Because of the uncertainty involved in choosing a minimum value of C, and the expectation that the appearance of plasma instabilities will be gradual as C decreases, the requirement that $C \geq 0.1$ should not be considered as a sharp limit. Collisionality curves are given to indicate where highly collisional operating points might exist.

2.1.4 Neoclassical Limit

Although higher densities have led to better confinement in present tokamaks, the relation is expected to break down when the neoclassical limit is reached. At collisionality ≈ 0.1, the appropriate neoclassical scaling relation (banana regime) is given by [17].

$$\tau_{nc} = 8.8 \times 10^{6} \frac{\bar{T}^{1/2} A^{1/2} I_p^{\ 2}}{Z_{eff} S^{1/2}\ \bar{n}} \tag{2.16}$$

As opposed to the empirical scaling, the neoclassical confinement time varies inversely with plasma density. Figure 2-6 compares the neoclassical scaling law, Equation (2.16), with the empirical scaling law. As the density increases, the empirical curve is expected to be followed until the appropriate neoclassical limit is reached. The point of "turnover" represents the peak confinement time value achievable, and any further increase in density would lead to a deterioration in confinement as the neoclassical curve is followed. The density at which the peak confinement time occurs is found by setting $\tau_{emp} = \tau_{nc}$:

$$\bar{n}_{\tau_{max}} = \left[\frac{5.5 \times 10^{40}\ \bar{T}^{1/2}\ B_T^{\ 2}\ S^{7/2}}{A^{3/2}\ q^{5/2}\ Z_{eff}} \right]^{1/2} \tag{2.17}$$

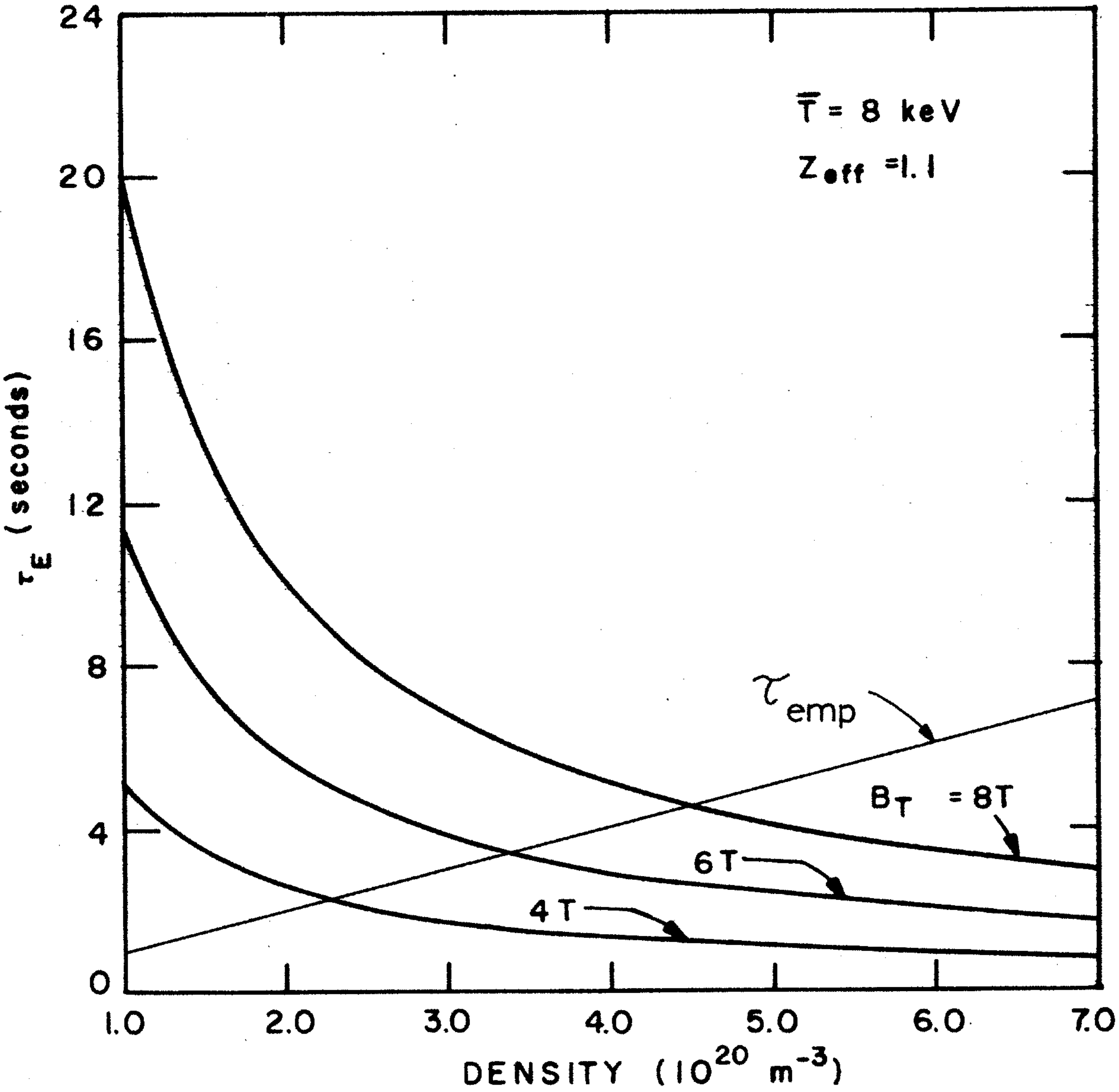

Figure 2-6 Neoclassical and empirical scaling laws for a = 1.2 m Note: For a fixed q(a) neoclassical scaling, unlike empirical scaling, depends on B_T.

$\bar{n}_{\tau_{max}}$ is independent of a and relatively insensitive to temperature. Figure 2-7 shows $\bar{n}_{\tau_{max}}$ as a function of B_T and Z_{eff}. In order to take full advantage of high density operation, which would lead to a small reactor, both cleanliness (low Z_{eff}) and high B_T are required. For example, at $Z_{eff} = 1.1$, $\bar{n}_{\tau_{max}} = 4.6 \times 10^{20}$ m^{-3} if $B_T = 8$ Tesla, and $\bar{n}_{\tau_{max}} = 2.2 \times 10^{20}$ m^{-3} if $B_T = 4$ Tesla.

2.1.5 MHD Stability Criteria

MHD equilibrium and stability constraints place an upper limit on the allowable toroidal plasma beta. Theoretical predictions indicate that plasma equilibria are possible for values of toroidal beta greater than 10% [18.19]. However, theory also predicts that internal ballooning modes could be excited at a lower beta value. β_c:

$$\beta_c = \frac{k_s}{Aq^2} \tag{2.18}$$

where k_s depends upon the plasma shape, S [20]. For a D-shape plasma with q = 3 and A = 5, a limiting toroidal beta of about 5% has been calculated using a computer code.

It is conceivable that other MHD modes (e.g. surface kink modes) might be excited at even lower beta values; however, for the purpose of this study, internal kink modes are assumed to limit the beta.

The lower limit on toroidal magnetic field may be determined by using the expected beta limit and the ignition criterion. Beta is defined as

$$\beta_T \equiv \frac{\sum_j n_j kT_j}{B_T^2/2\mu_e} \tag{2.19}$$

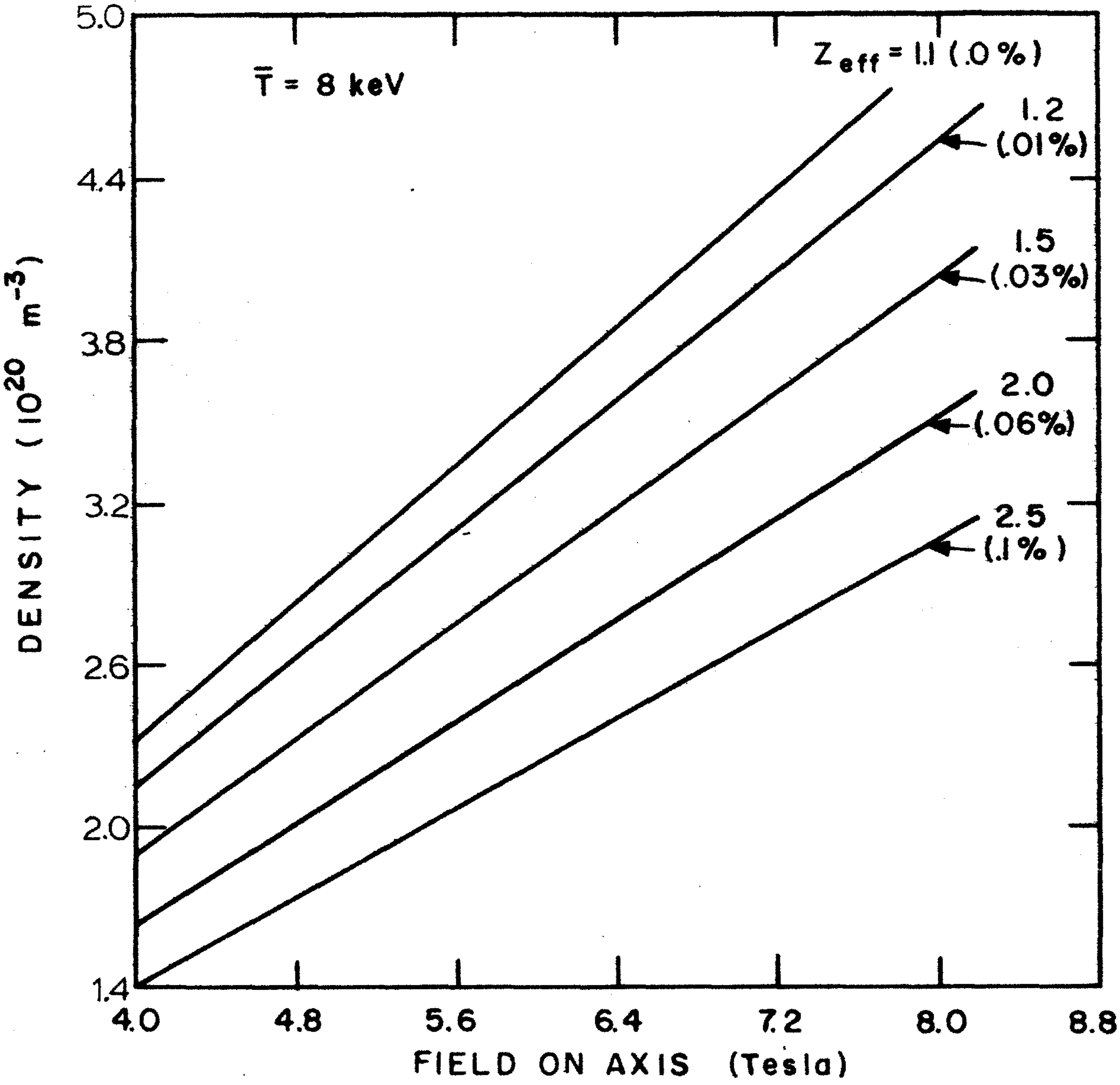

Figure 2-7 $\bar{n}_{\tau_{max}}$ vs. B_T

This can be expressed as

$$\bar{\beta}_T = 4.04 \times 10^{-22} \left[\frac{\bar{T}\,(\bar{n}_e + \bar{n}_i + \bar{n}_\alpha) + P_{SA}}{B_T^{\,2}} \right] \qquad (2.20)$$

where $\bar{n}_\alpha$ is the density of thermalized alphas, and P_{SA} is the nT product of suprathermal alphas.

The value of $\bar{\beta}_T$ is plotted as a function of B_T in Figure 2-8 for $\bar{T}$ = 8 keV and a = 1.2 meters. If values of $\beta_T \sim$ 6-8% can be reached, then toroidal fields less than 6 Tesla would be sufficient to allow a fairly clean ($Z_{eff} < 1.5$) plasma to reach ignition (looking at MS = 1 curves). The higher costs and stresses of high fields could then be avoided. If, however, the upper limit on $\bar{\beta}_T$ is 2-3%, then high fields (B_T > 7 Tesla) are required.

2.1.6 Magnetic Field Criteria

In reactor design, a limiting criterion is the maximum field allowable at the toroidal coils. The field at the plasma axis is related to the field at the coils, B_{To}, by

$$B_{To} = \frac{B_T}{1 - \frac{1}{A} - \frac{d}{Aa}} \qquad (2.22)$$

where d is the distance from the plasma edge to the toroidal coil on the small major-radius side of the plasma.

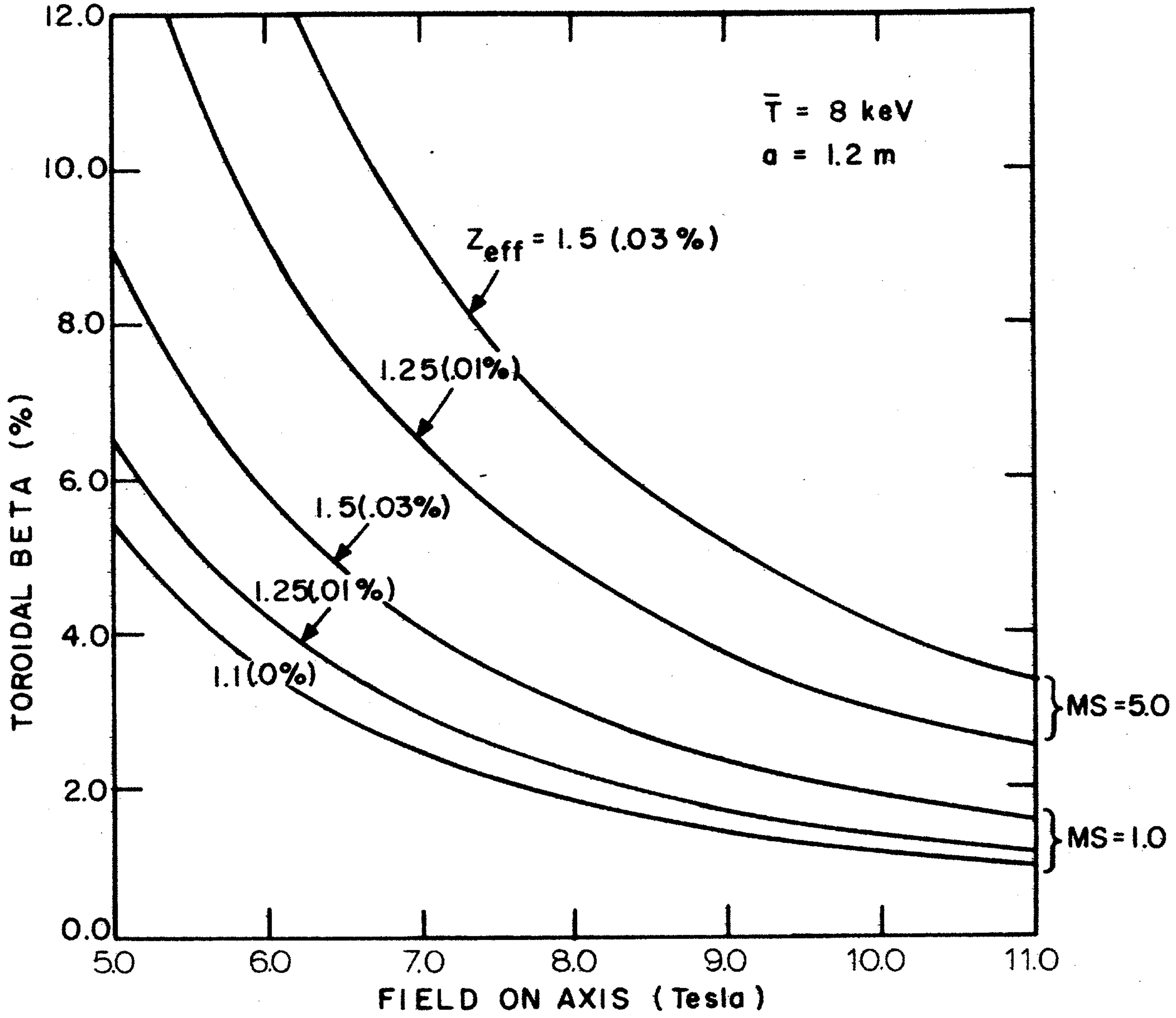

Figure 2-8 Empirical ignition curves plotted as B_T vs β_t.

By combining the ignition criterion, equation (2.13), with the definition of the toroidal beta, equation (2.20), the minimum toroidal field required for ignition may be written as a function of temperature, plasma halfwidth, and toroidal beta:

$$B_T = \left[\frac{8.9 \times 10^{-22}\ \bar{T}\ G(\bar{T},Z_{eff})}{a\bar{\beta}_T}\right]^{1/2} \tag{2.21}$$

where $G(\bar{T},Z_{eff})$ is the right hand side of Equation (2.13).

Now by combining Equations (2.21) and (2.22), an equation relating B_{To} to a and $\bar{\beta}_T$ is found:

$$B_{To} = \left[\frac{8.9 \times 10^{-22}\ \bar{T}\ G(\bar{T},Z_{eff})}{a\ \bar{\beta}_T(1 - \frac{1}{A} - \frac{d}{Aa})^2}\right]^{1/2} \tag{2.23}$$

For a given size reactor, B_{To} increases as $\bar{\beta}_T$ is lowered. If $\bar{\beta}_T$ is limited by ballooning modes to the value of 5%, Figure 2-9 indicates that the smallest plasma halfwidth for ignition at a coil field not exceeding 12 Tesla is about 0.8 meter. Also at a fixed value of $\bar{\beta}_T$, higher magnetic fields are required for ignition in smaller-size plasmas. By using equation (2.18), equation (2.23) may be rewritten:

$$B_{To} = \left[\frac{8.9 \times 10^{-22}\ \bar{T}\ G(\bar{T},Z_{eff})}{a(1 - \frac{1}{A} - \frac{d}{Aa})^2\ \frac{1}{A}\ \frac{k_s}{q^2}}\right]^{1/2} \tag{2.24}$$

This equation shows the advantages of elongation (S > 1) and small q.

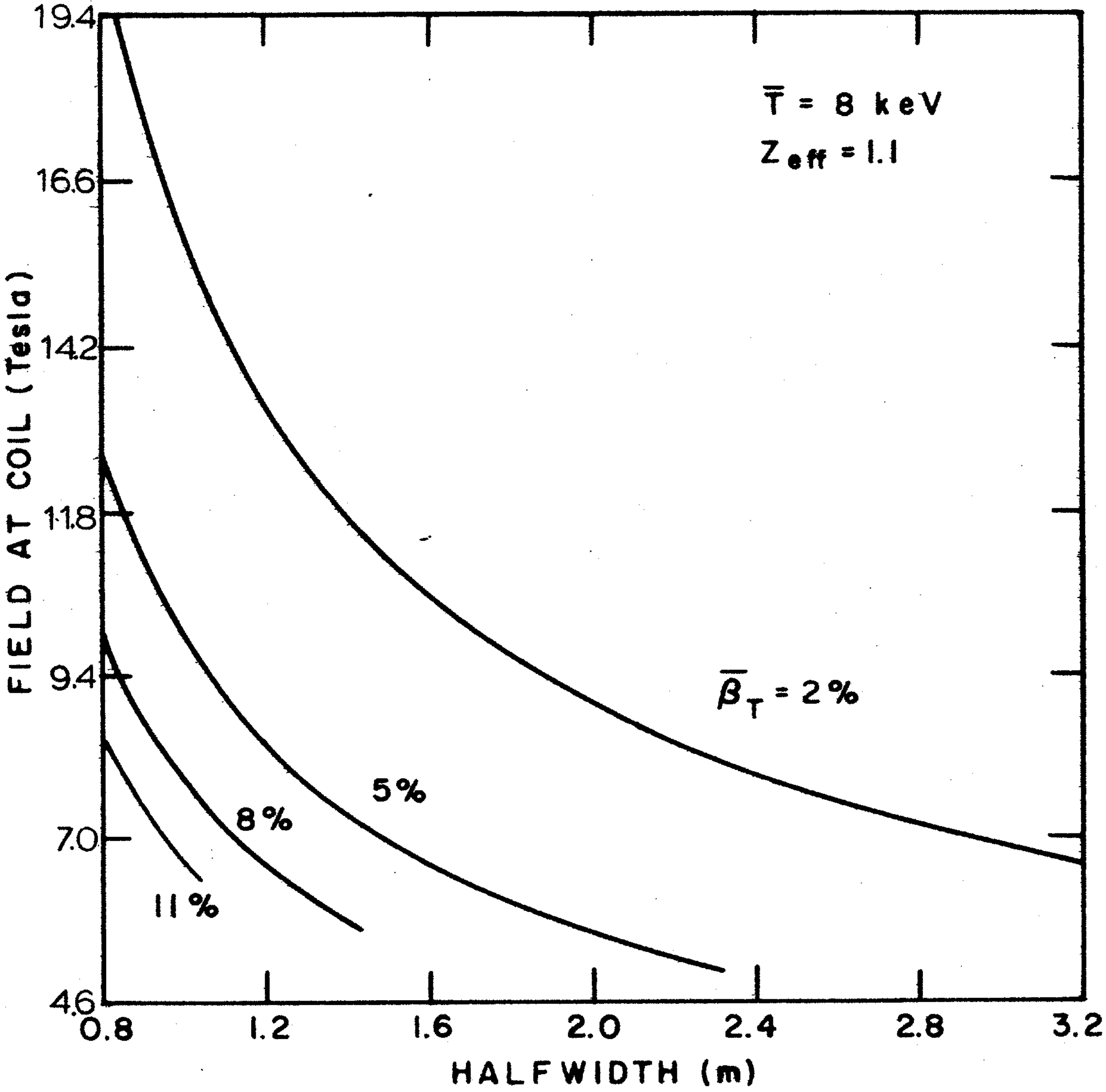

Figure 2-9 B_{To} vs. a.

2.1.7 Margin of Safety

Because of the present uncertainties concerning the confinement scaling and the maximum $\bar{\beta}_T$ achievable, a credible reactor design must include some "margin of safety". This quantity is defined as

$$MS \equiv \frac{(\bar{n}\tau)_{MIN}}{(\bar{n}\tau)_{ign}} \qquad (2.25)$$

where $(\bar{n}\tau)_{MIN}$ = Minimum $[(\bar{n}\tau)_{emp}, (\bar{n}\tau)_{nc}]$. This definition assumes that confinement cannot be better than that predicted by neoclassical scaling in equation (2.16). A value of $MS < 1$ would characterize a sub-ignition reactor.

Reasons for wanting a margin of safety greater than 1.0 are:

(1) confinement: the empirical scaling presently observed might deteriorate (possibly due to some unknown temperature dependence) before the neoclassical limit is reached.

(2) beta limitation: plasma deformation (e.g. a D-shape) may not significantly increase the toroidal beta limit. In addition, other MHD modes might be excited at lower beta values than the internal kink mode.

An increase in the concentration of the impurities in the plasma will adversely effect the MS. If impurity control proves to be difficult and the Z_{eff} cannot be reduced to low levels, then the MS will decrease due to an increase in $(\bar{n}\tau)_{ign}$.

Two methods of increasing the margin of safety are: (1) by increasing the plasma halfwidth which lowers the diffusive losses for both empirical and neoclassical scaling, (2) by increasing the toroidal field at a fixed value of $\bar{\beta}_T$ which allows higher density ($n^2 \sim \bar{\beta}_T^2 B_T^4$). In the neoclassical regime, higher fields improve confinement by permitting higher plasma current at fixed q.

Equations for the margin of safety may be developed for both the empirical and neoclassical confinement scaling laws. In the empirical regime

$$MS(emp) \equiv \frac{(\bar{n}\tau)_{emp}}{(\bar{n}\tau)_{ign}} \tag{2.26}$$

Using Equation (2.12) for $(\bar{n}\tau)_{emp}$ in combination with the definition of beta allows the margin of safety for empirical scaling to be written as

$$MS(emp) = 5.0 \times 10^{21} \frac{q^{1/2}\, \bar{\beta}_T^{\,2}\, B_T^{\,4}\, a^2}{\bar{T}^2 (\bar{n}\tau)_{ign}} \tag{2.27}$$

The tradeoff between small size and large margin of safety is easily seen. The sensitivity of MS(emp) to B_T and $\bar{\beta}_T$ is also evident. The tradeoffs between B_T and $\bar{\beta}_T$ are shown in Figure 2-8 for MS = 1 and MS = 5. For a given $\bar{\beta}_T$, the field must be increased by 50% to accomodate a change in the MS from 1 to 5.

In the neoclassical regime, the margin of safety is given by

$$MS(nc) \equiv \frac{(\bar{n}\tau)_{nc}}{(\bar{n}\tau)_{ign}} \tag{2.28}$$

Using Equation (2.16) for τ_{nc}, MS(nc) can be written as

$$MS(nc) = 8.8 \times 10^{6} \frac{I_P^{\,2}\ \bar{T}^{1/2}\ A^{1/2}}{Z_{eff}\ S^{1/2} (\bar{n}\tau)_{ign}} \tag{2.29}$$

The scaling of MS(nc) may be compared to that of MS(emp) by rewriting Equation (2.30)

$$MS(nc) = 2.2 \times 10^{20} \frac{a^2\ B_T^{\,2}\ \bar{T}^{1/2}\ S^{7/2}}{q^2\ Z_{eff}\ A^{3/2}\ (\bar{n}\tau)_{ign}} \tag{2.30}$$

In the neoclassical regime, a^2 again appears but the magnetic field strength is only raised to the second power.

In Figure 2-10, the margins of safety for empirical and neoclassical scalings are shown for several values of Z_{eff} as a function of temperature with B_T = 6.8 Tesla, a = 0.73 meter and $\bar{\beta}_T$ = 5%.

The empirical scaling values in Figure 2-10 can be scaled to other field strengths, halfwidths, and betas by using the relation

$$MS(emp) = MS(emp)_{GRAPH} \left(\frac{B_T}{6.8\ T}\right)^4 \left(\frac{a}{0.73\ m}\right)^2 \left(\frac{\bar{\beta}_T}{.05}\right)^2 \tag{2.31}$$

The neoclassical values can be scaled by using the relation

$$MS(nc) = MS(nc)_{GRAPH} \left(\frac{B_T}{6.8\ T}\right)^2 \left(\frac{a}{0.73\ m}\right)^2 \left(\frac{5.0}{A}\right)^{3/2} \tag{2.32}$$

Equation (2.25) may finally be written as

$$MS = \text{Minimum}\ (MS(emp),\ MS(nc)) \tag{2.33}$$

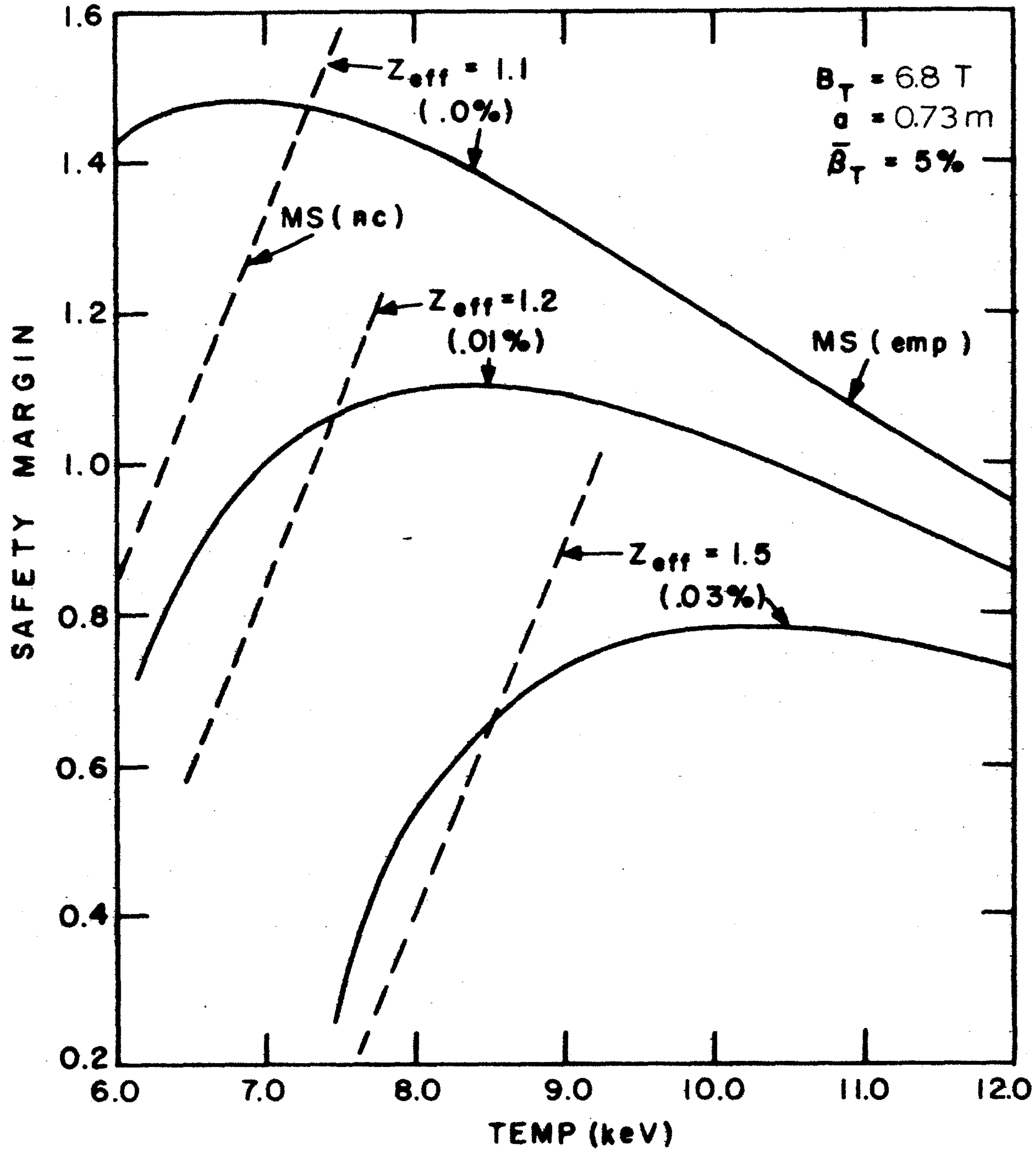

Figure 2-10 MS vs. T for empirical and neoclassical scaling.

again reflecting the belief that confinement cannot be better than that predicted by neoclassical scaling. Looking at Figure 2-10, one can see that operation in the temperature range where MS(nc) holds has an adverse effect on the MS for fixed $\bar{\beta}_T$, B_T, and a. Hence the margin of safety is optimized by operating in the empirical regime.

2.1.8 Power Production

The dependences of fusion power density (P_f), wall loading (P_w), and thermal power output (P_{th}) on density and size for MS(emp) = 1.0 are given by

$$P_f \sim MS\ \overline{n^2\langle\sigma v\rangle} \sim \frac{MS}{a^2}\ \overline{\langle\sigma v\rangle[G(\bar{T},Z_{eff})]^2} \qquad (2.34)$$

$$P_w \sim MS\ \overline{n^2\langle\sigma v\rangle} \left(\frac{a^2}{a + L_{SC}}\right) \sim \frac{MS}{a + L_{SC}}\ \overline{\langle\sigma v\rangle[G(\bar{T},Z_{eff})]^2} \qquad (2.35)$$

$$P_{th} \sim MS\ \overline{n^2\langle\sigma v\rangle}\ Aa^3 - MS\ \overline{\langle\sigma v\rangle[G(\bar{T},Z_{eff})]^2} \qquad (2.36)$$

Here L_{SC} is the "scrape-off" distance, i.e., the thickness of the plasma-gas blanket. From Equations (2.34) to (2.36), it can be seen that a smaller plasma halfwidth increases P_f and P_w, while decreasing P_{th}. Clearly, there is some optimum balance between high P_f, low P_{th}, and moderate P_w.

2.2 PLASMA PERFORMANCE ENVELOPE

2.2.1 HFCTR Parameter Choice

The parameters chosen for the HFCTR yield a small reactor characterized by high fusion power density, moderate values of wall loading and thermal output power, and substantial margin of safety in attaining ignition. The choice of the parameters is briefly described in this section.

Plasma Elongation

The value of the plasma shape factor has been chosen to be 1.5:

$$S \equiv \frac{\text{plasma circumference}}{2\pi a} = 1.5 \tag{2.39}$$

and the plasma is assumed to be D-shaped. The plasma stability is enhanced with increasing elongation, but the value of $S = 1.5$ is near the limit where the equilibrium-coil system and ripple-coil system begin to become complex and highly stressed.

Impurity Concentration

The zero-dimensional code used in the parametric study has shown that because of the presence of thermalized alphas, which are assumed to have the same particle confinement time as the fuel ions, the minimum achievable value of Z_{eff} in a reactor-grade plasma is 1.1. If proper precautions are taken in machine assembly and maintenance, and if the proposed impurity-control systems function properly, values of Z_{eff} near 1.1 should be attainable. For this study, a base case value of 1.2 has been chosen. The reactor can operate at higher Z_{eff} if impurity concentrations in the plasma cannot be reduced, but a corresponding reduction in the safety margin will occur.

Magnetic Field

It is expected that due to the ballooning mode instability, the toroidal beta for a tokamak reactor will be restricted to 3-6%. In order to satisfy the desired goal of compactness, high fields will be necessary for these values of β_T.

From Equation(2.21), Figure 2-11 is generated. Looking at this figure, one can see that in order to get $a \leq 1.2$ m for a reactor with MS = 2.1 operating at $\bar{T}_D = 8$ keV, a minimum $B_T = 6$ T is necessary for the optimistic choice of $\bar{\beta}_T = 6\%$. If the maximum toroidal beta drops to 3%, then a field on axis of 8 T will be needed.

In order to insure that a compact reactor will produce a reasonable total output power, a high fusion power density is desirable. Figure 2-12 shows P_f as a function of beta and toroidal field for $\bar{T} = 8$ keV. Again assuming that β_T will be restricted to the range 3-6%, this graph shows that 6 T is the minimum field needed in order to guarantee that P_f is greater than 7.5 MW/m^3 (for a reactor with a = 1.2 m and A = 5, this power density yields a $P_{th} \simeq 3000$ MW_{th}). If beta cannot be increased above 3%, the necessary field will be in excess of 8 T in order to achieve this fusion power density.

Based on these considerations, a range of 7-8 T has been chosen to characterize the field on axis for the HFCTR. For the base case, a value of 7.4 T has been selected based on stress levels on the inner sections of the toroidal coils.

Halfwidth

As has been mentioned repeatedly, compactness is an important objective of the HFCTR. The main incentive for this is to keep the total plant cost down while maintaining a competitive cost per kilowatt of electricity produced. A small reactor also simplifies the problem of incorporating a fusion power plant into the existing power grid [21].

Based on this reasoning, the minor radius should be made as small as possible. The minimum 'a' that can be tolerated is calculated based on the confinement of suprathermal alphas produced in the plasma. Using the results

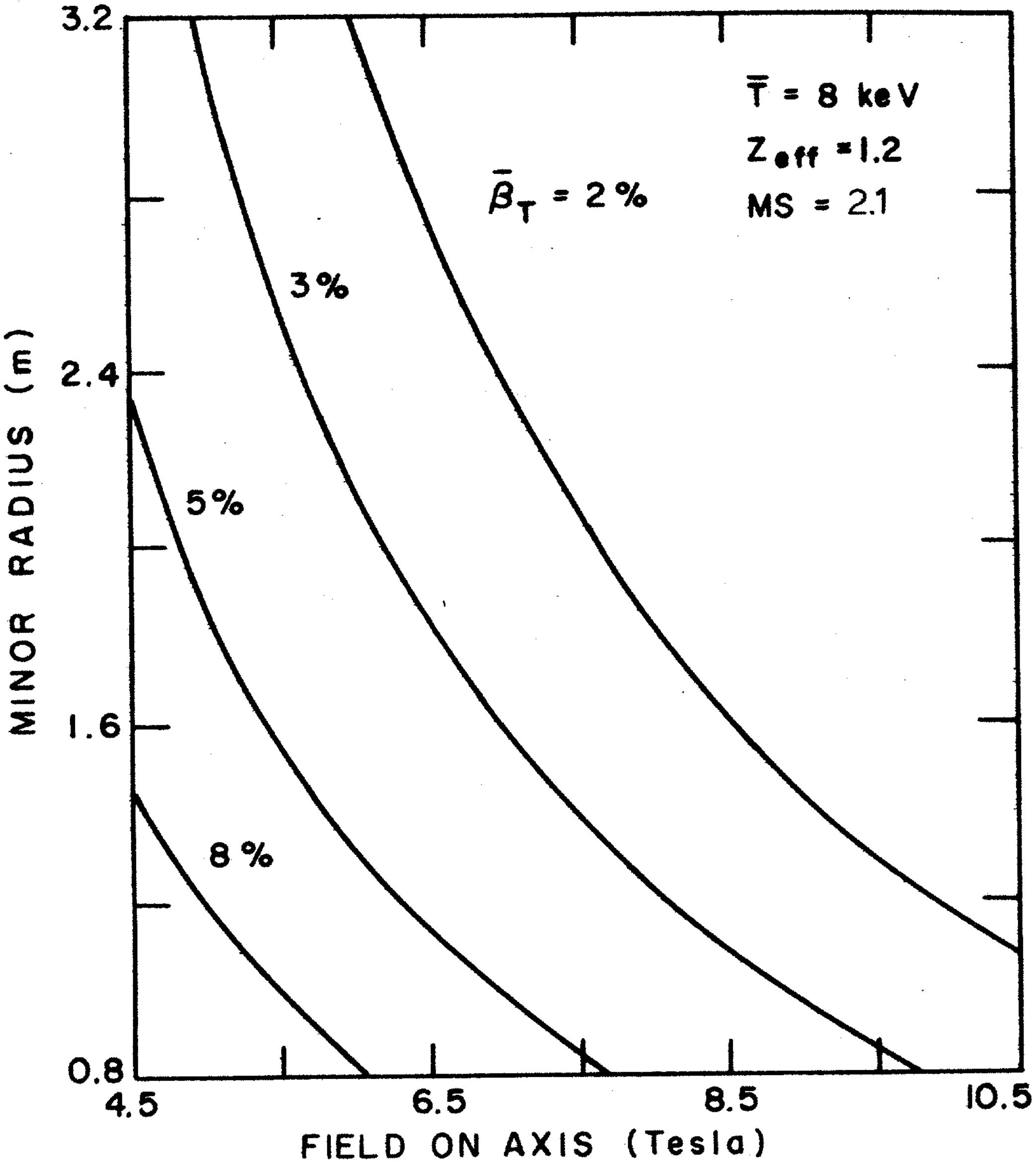

Figure 2-11 a vs. B_T.

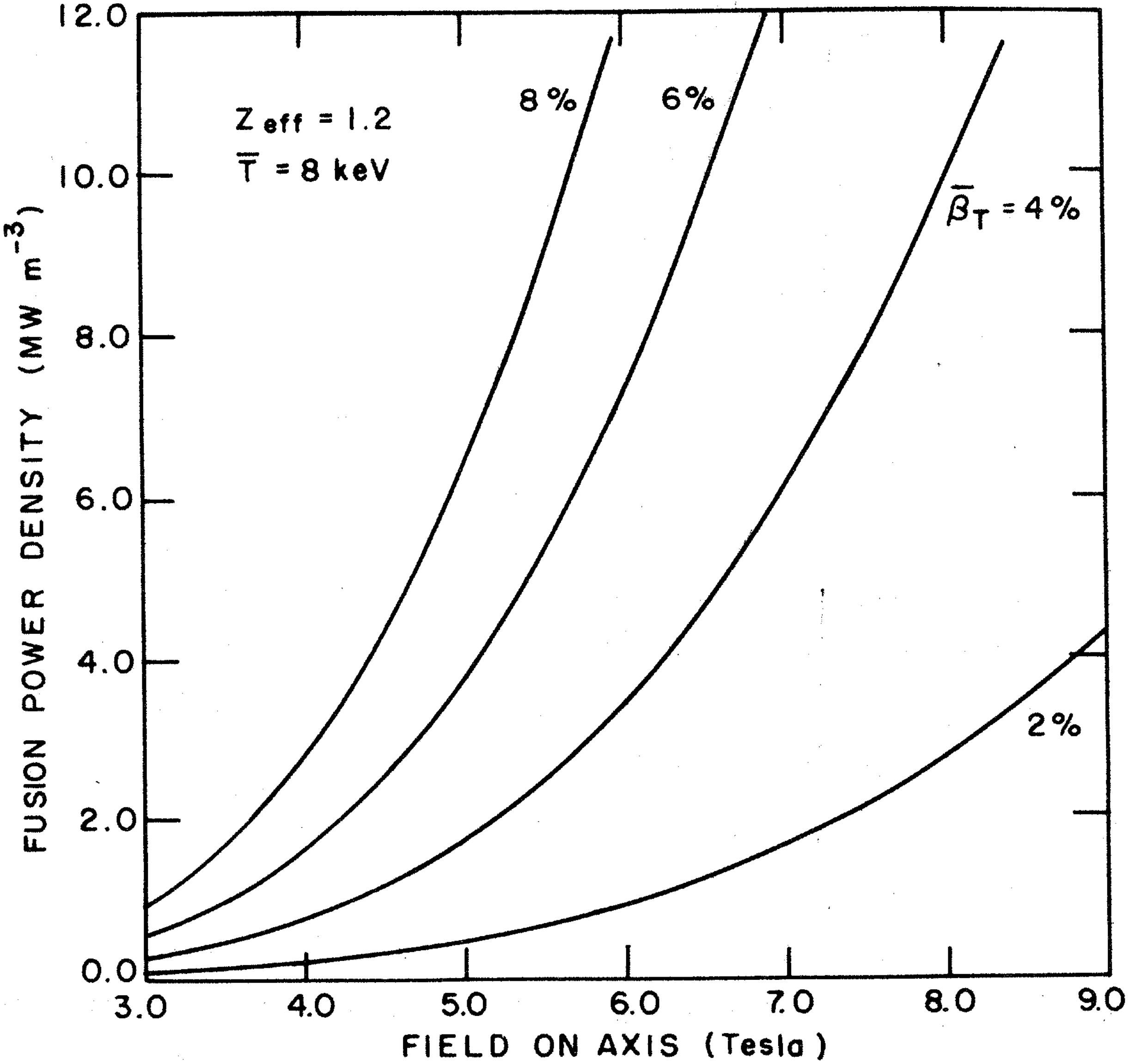

Figure 2-12 P_f vs. B_T.

of McAlees [22] $I_P > 4$ MA is sufficient to guarantee that more than 80% of these alphas will deposit their energy in the plasma. In addition, since

$$I_P \simeq \frac{5 \times 10^6 aS^2 B_T}{qA} > 4 \text{ MA} \tag{2.40}$$

it follows that for $A \simeq 5$:

$$a \geq .72 \text{ m} \tag{2.41}$$

This halfwidth is well above the value needed for ignition when $B_T = 7.4$ T and $\bar{\beta}_T \simeq 5\%$.

In actuality, although plasma physics predicts ignited operation with halfwidths as low as 72 cm, other considerations indicate that a somewhat higher value might be preferable. For example, a cost analysis of the HFCTR [23] found that the cost per kilowatt rises sharply for $a \lesssim 1.0$ m. This can be explained by noting that the total power output decreases as the minor radius is reduced ($P_{th} \sim a$) while the total plant cost is less sensitive to minor radius for $a \lesssim 1.0$ m.

In addition to cost, the need for a large margin of safety also encourages an increase in halfwidth. Equations (2.27) and (2.31) show that the MS scales as a^2 for both empirical and neoclassical energy confinement. Thus, a tradeoff between a smaller halfwidth and a larger safety margin exists, and one must decide what combination of 'a' and MS best satisfies the goals of the reactor. For example, if one requires that a reactor be able to ignite (i.e. MS = 1.0) even if $S > 1$ does not enhance beta (See Equation (2.18)), then ignition must be feasible with $\bar{\beta}_T$ as low as 2.2% for $A = 5$.

Equation (2.31) in conjunction with Figure 2-11 gives a minimum value for the halfwidth of (for $Z_{eff} = 1.1$)

$$a \gtrsim \left(\frac{1}{1.4}\right)^{1/2} \left(\frac{6.8}{7.4}\right)^2 \left(\frac{.05}{.022}\right) 0.73 \text{ m} \simeq 1.2 \text{ m} \qquad (2.42)$$

A final consideration in choosing an appropriate halfwidth is the need to keep the wall loading from becoming too large and thus necessitating frequent shutdowns for wall replacement. Using Equation (2.35) and noting that in the range of 8 to 20 keV, $<\sigma v>$ for fusion is approximately proportional to T^2, the wall loading can be written as a function of magnetic field, beta, and halfwidth:

$$P_w \sim \frac{n^2 <\sigma v> a^2}{(a + L_{SC})} \sim \frac{\bar{\beta}_T^2 \, B_T^4 \, a^2}{(a + L_{SC})} \qquad (2.43)$$

Thus, the selection of a maximum wall loading sets an upper limit on "a". For example, if the maximum $P_w = 4 \frac{MW}{m^2}$, for $\bar{\beta}_T \simeq 5\%$ and $B_T = 7.4$ T this gives $a \lesssim 1.35$ m.

In summarizing, the following is a list of restrictions described above that are important in choosing the appropriate minor radius:

(1)	keep cost per kilowatt competitive	$a > 1$ m
(2)	insure adequate suprathermal alpha confinement	$a > 0.75$ m
(3)	guarantee ignition even if plasma deformation does not enhance $\bar{\beta}_T$	$a > 1.2$ m
(4)	insure that the wall loading is within acceptable limits	$a \lesssim 1.35$ m

Based on these numbers, a halfwidth of 1.2 meters was chosen for the HFCTR.

Aspect Ratio

The choice of the aspect ratio is determined by the need to keep the field at the coil as small as possible, thus limiting the stresses in the TF coils. This reduces the amount of structural material needed to support the TF coil trunk. For a = 1.2 m, Figure 2-13 shows that the aspect ratio should fall in the range of 5 - 7, which gives a field at the coil of about 12 T. In line with the desire for compactness, the lower limit of this range was chosen, i.e., A = 5, for the HFCTR. This results in a major radius of 6 meters.

Temperature

Figure 2-10 shows the margin of safety for empirical confinement scaling as a function of the density-averaged temperature for $q = 3$, $S = 1.5$, and $A = 5$. Although the magnitude of the curves shown is for $B_T = 6.8$ T and $a = 0.73$ m, the maxima are unaffected by these particular choices. For $Z_{eff} = 1.2$, there is a broad maximum centered about $\bar{T}_D = 8$ keV. In order to maximize the margin of safety in attaining ignition, the nominal operating temperature of the plasma has been chosen to be 8 keV.

Density

The plasma density is determined by the values of toroidal beta, magnetic field, and plasma temperature which have been chosen. The maximum tolerable toroidal beta is determined by Equation (2.18), which gives a $\bar{\beta}_T$ of 5% for $A = 5$, $q = 3$, and $S = 1.5$. Since one wants to operate somewhat below this limit to provide room for density or temperature fluctuation, a $\bar{\beta}_T$ of 4% has been chosen for the HFCTR. Using Equation (2.20) with $\bar{T} = 8$ keV and $B_T = 7.4$ T yields an operating density of $\bar{n} = 3.1 \times 10^{20}$ m^{-3}.

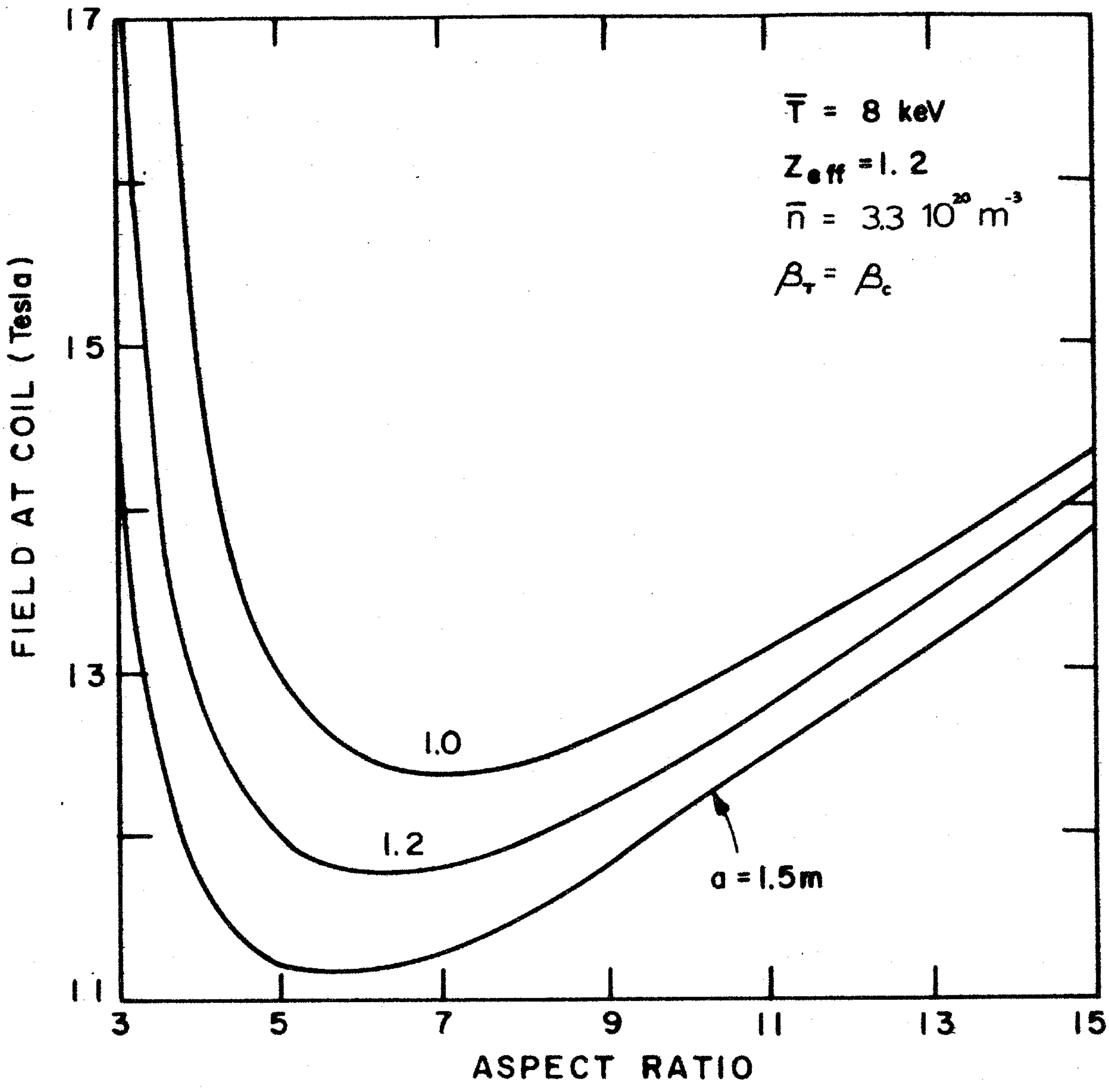

Figure 2-13 B_{To} vs. A.

2.2.2 Range of Operation

Although a specific operating temperature and density were chosen in the previous section based on the desire to maximize the safety margin, there is in actuality a range of $\bar{n}$ and $\bar{T}$ available for an ignited HFCTR. Once the size of a reactor plasma is determined (by fixing the halfwidth and aspect ratio), an operating area in density-temperature space is delineated by imposing the plasma physics constraints discussed in Section 2.1. This operating "window" defines the range of power levels attainable by the reactor. If, for example, a 1.2 meter plasma has an aspect ratio of 5, a central toroidal field of 7.4 Tesla, and $Z_{eff} = 1.2$, the constraints of ignition, collisionality ($C > .1$) and MHD stability will limit the range of allowable density-temperature combinations to the shaded area shown in Figure 2-14. In principle, with proper thermal stability control, the reactor can operate at any point within the shaded area.

The range of power densities attainable by a reactor is determined by the operating regime. Operation near the ignition curve results in low reactor power and low margin of safety, while operation near the MHD limit increases both the power level and the margin of safety. Figure 2-14 shows a number of curves of constant wall loading as a function of density and temperature for the HFCTR. Note that, for a given P_w, a wide range of temperatures and densities is available. In the case of the HFCTR, it is more desirable to operate at lower $\bar{T}$ and higher $\bar{n}$ in order to enhance collisionality. In this case, the lower temperature limit is set by the neoclassical ignition requirement. Figure 2-15 shows the safety margin for the HFCTR plotted as a function of Z_{eff} and temperature. Note that the choice of $\bar{T} = 7$ keV represents the lower limit of desired operation for $Z_{eff} = 1.2$. Operation

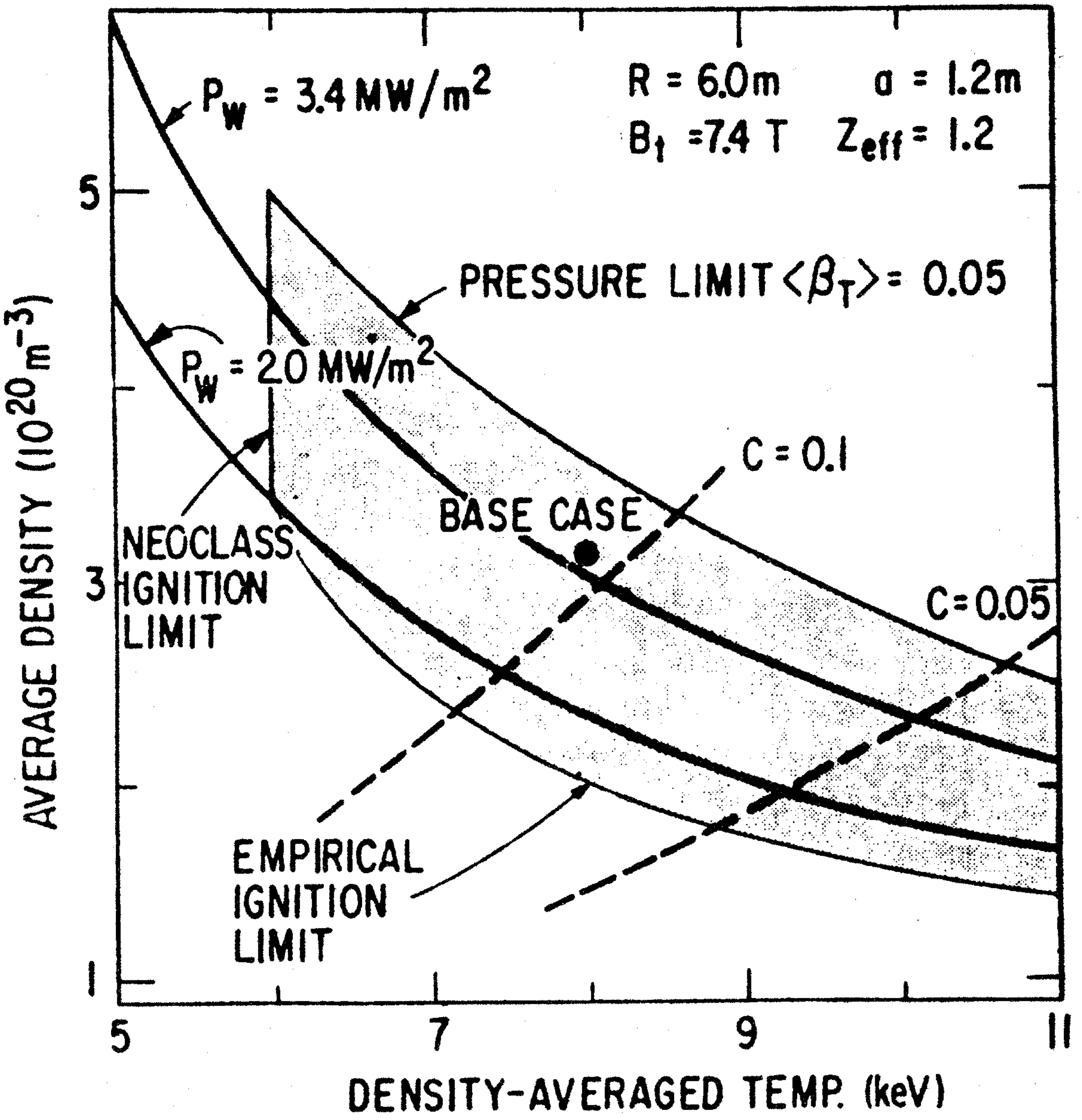

Figure 2-14 Shaded area is the permissible range of reactor operation for the parameters shown. Ignition limits for both empirical and neoclassical scaling laws are indicated. C= plasma collisionality.

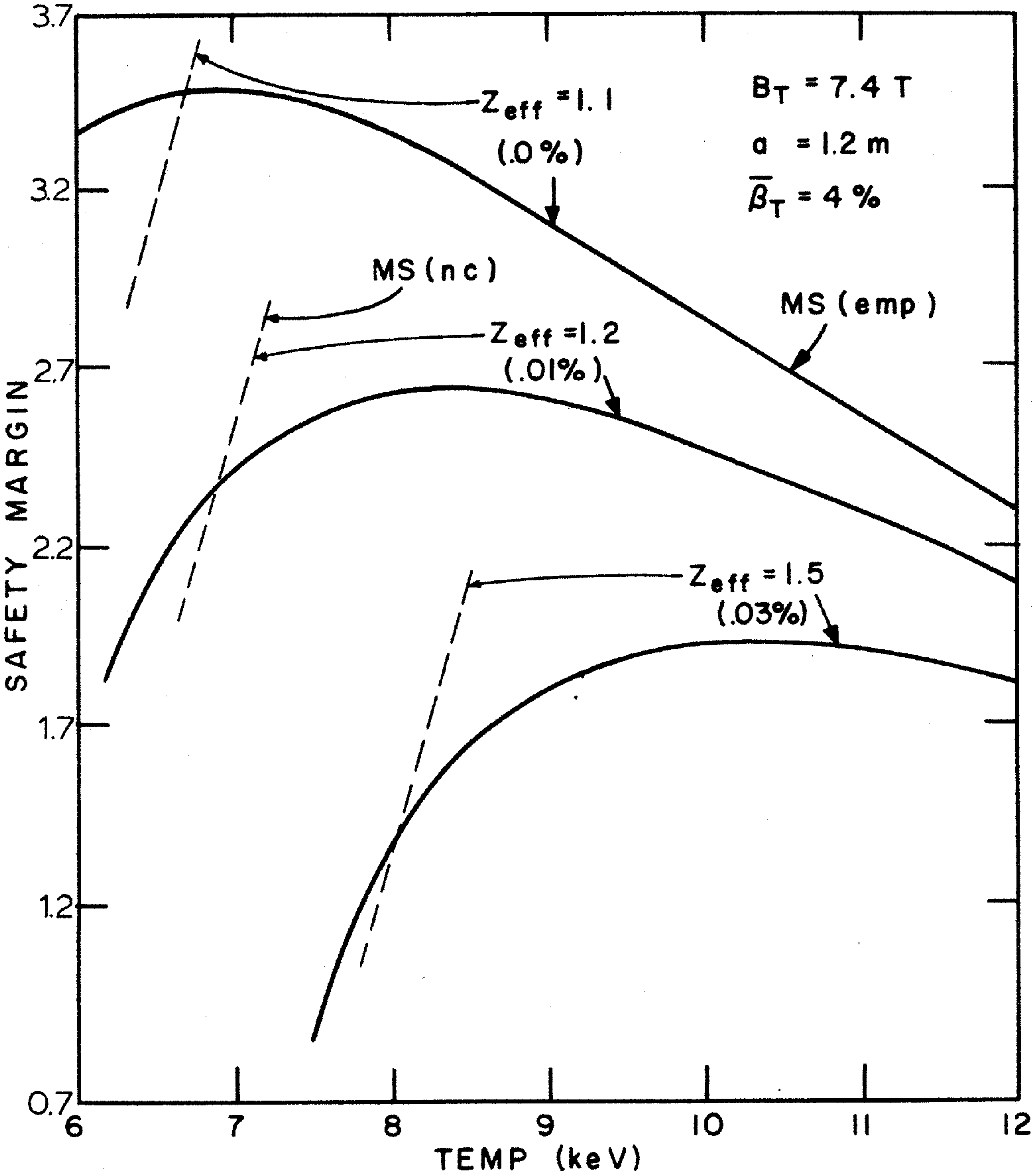

Figure 2-15 MS vs T for empirical and neoclassical scaling.

at a lower temperature results in a sharp deterioration of the margin of safety as the confinement changes from empirical to neoclassical.

In summary, the parameters chosen for the HFCTR yield a small reactor characterized by high fusion power density, moderate values of wall loading and thermal output power, and a substantial margin of safety in attaining ignition. A listing of the machine parameters, as well as the anticipated power ranges, is given in Table 2-I for the HFCTR base case.

2.3 START-UP

The manner in which the plasma is initiated, heated, and fueled is dependent on a number of constraints. These constraints delineate a fairly restrictive operating regime through which start-up must proceed. A discussion of these constraints, their implications to the start-up scenario, and a summary of the scenario are provided in this section.

The constraints are

(1) The power balance requirement

(2) The minimum tolerable safety factor

(3) The disruptive instability density limit

(4) The β_p requirements

(5) The applied-loop-voltage limit

(6) The runaway-electron limit

(7) The neutral beam requirements

(8) The limit on the flux change through the toroidal core

(9) The collisionality requirement

2.3.1 Start-up Sequence

Plasma start-up occurs in three phases: (1) the plasma initiation phase; (2) the plasma expansion phase; and (3) the beam heating phase. In the plasma initiation phase ($0 \text{ sec.} < t \lesssim 0.03 \text{ sec.}$) the plasma is broken down at an ion density of $n = 10^{19} \text{ m}^{-3}$ with a loop voltage of $V_{loop} = 250$ volts. Preionization may be required to assist in the breakdown. The minor radius is 0.25 meter, set by forcing the plasma center 0.25 meter from the limiter. An initial oxygen concentration of 0.8%, giving $Z_{eff} = 1.5$, is assumed. When oxygen line radiation becomes small, the density increases to $n = 3 \times 10^{19} \text{ m}^{-3}$ and the current density rises to $J = 410 \frac{\text{kA}}{\text{m}^2}$.

In the plasma expansion phase ($.03 \text{ sec.} < t < 2.0 \text{ sec.}$) the plasma minor radius is expanded from $a = 0.25$ meter to $a = 1.2$ meters by moving the plasma center away from the limiter while n and J are held constant. The plasma is then deformed slowly into an ellipse with a shape factor (circumference/$2\pi a$) of $S = 1.4$ and a cross-sectional area of 8.4 m^2.

In the first beam heating phase ($2.0 \text{ sec.} < t < 3.9 \text{ sec.}$) only one beam-line providing 12.5 MW is activated. While the ohmic and beam power continue to heat the plasma, the plasma current rises gradually to its final value of 6.7 MA. In the second beam heating phase ($3.9 \text{ sec.} < t < 8.4 \text{ sec.}$) the remaining beam-lines are then activated providing a total neutral beam power of 100 MW. The density is rapidly increased, and when n reaches $\sim 10^{20} \text{ m}^{-3}$, the ripple coils are employed to insure adequate beam penetration. The density continues to increase to $3.1 \times 10^{20} \text{ m}^{-3}$, with the temperature rising to the final operation value of 8 keV. When β_p is 50% to 75% of its final value, the hexapole field coils deform the ellipse into a D-shape of $S = 1.5$ while the plasma cross section remains at 8.4 m^2.

The start-up scenario results are presented at the end of this section. The density and electron temperature are shown as a function of time in Figure 2-16 ($T_e \approx T_i$; except early in the start-up when the density is low). The evolution of the current density is given in Figure 2-17. Curves of the power inputs and losses throughout start-up are presented in Figure 2-18. The values of applied loop voltage and integrated volt seconds as a function of time are given in Figures 2-19 and 2-20, respectively. Figure 2-21 shows the safety factor and the poloidal beta at the limiter. The temperature dependence of the line radiation is shown in Figure 2-22. Figure 2-23 shows the magnetic flux surfaces of the full-size D-shaped plasma.

2.3.2 Start-up Model

The quantitative results of the start-up scenario were generated by assuming flat temperature, density, and current density profiles (see Appendix C for details). This profile shape was used because of the uncertainty of the actual evolving shapes during start-up. The flat profile model requires higher average values of temperature and density for ignition than a peaked profile model, and thus the final results are somewhat conservative.

2.3.3 The Power Balance Requirement

The requirement that the power input exceed the power loss from the plasma is a very pervasive constraint. It directly affects the required applied loop voltage, the necessary neutral beam power, and the maximum fueling rate.

Because of the uncertainty surrounding impurity behavior in tokamaks, conservative assumptions regarding impurities were used in the determination

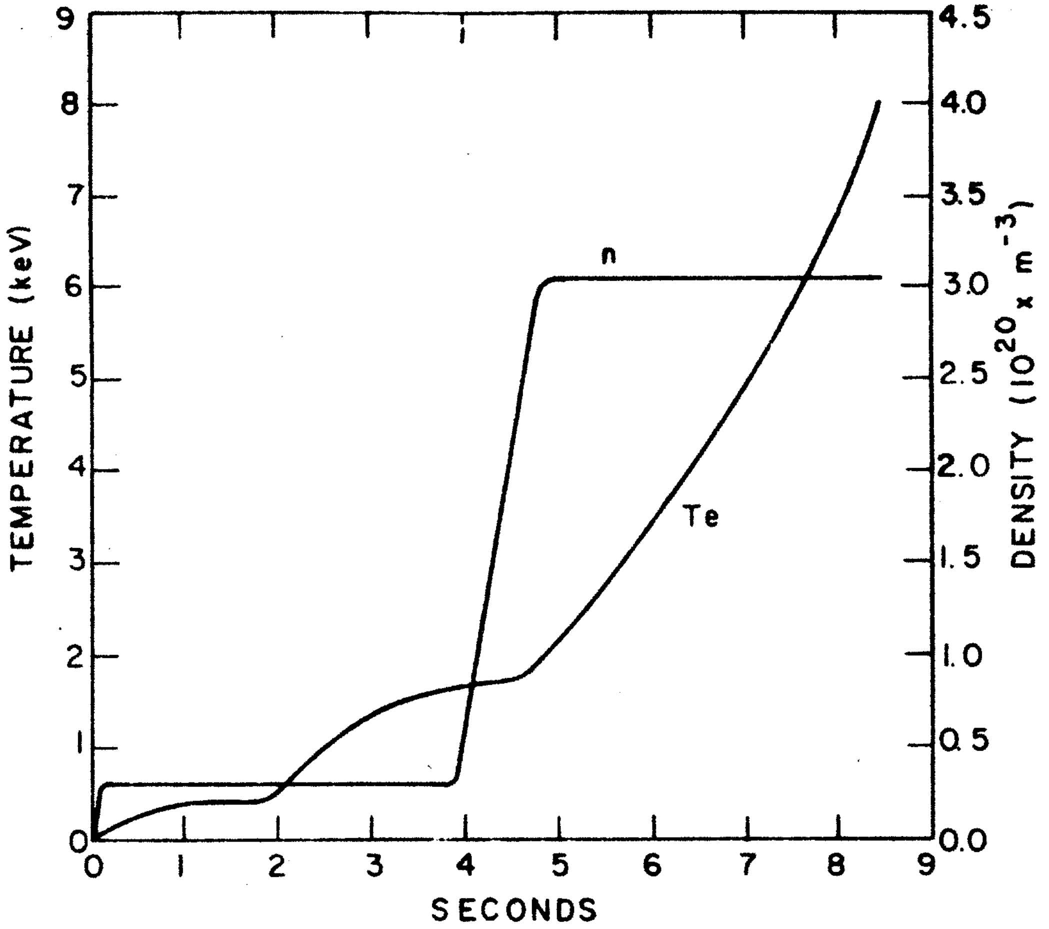

Figure 2-16 Temperature and density during start-up. Ripple coils are turned on at 4.1 seconds.

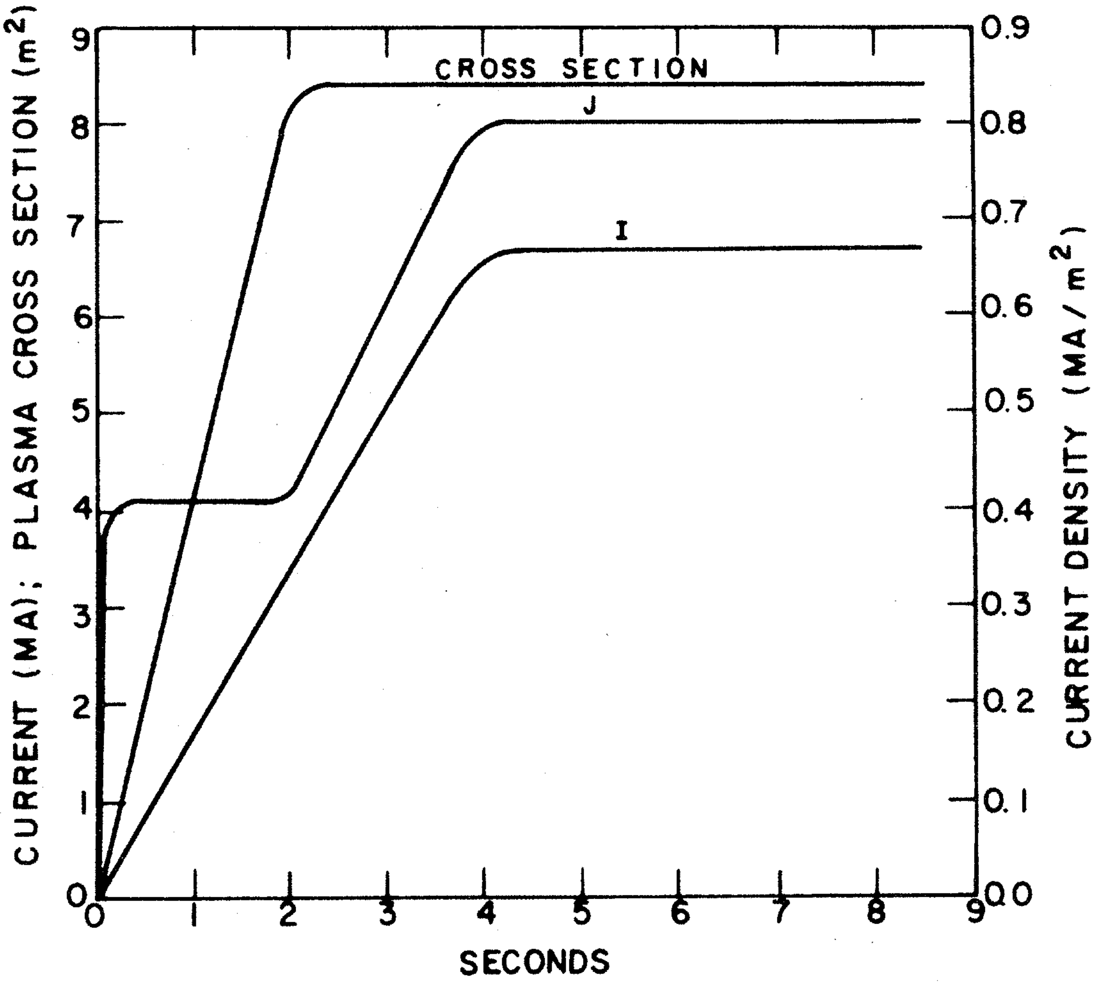

Figure 2-17 Current, current density, and plasma cross section development during start-up.

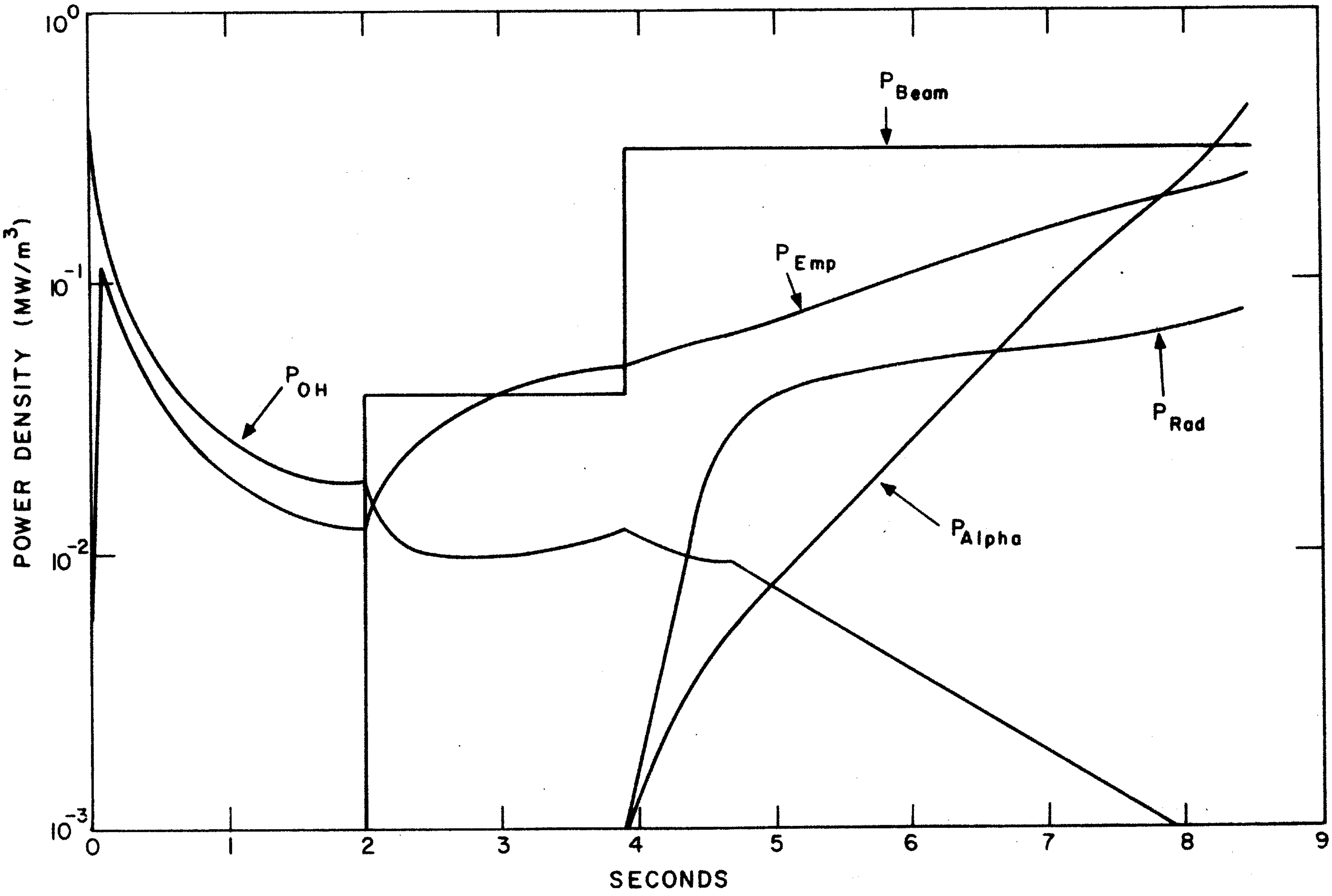

Figure 2-18 Power sources and sinks during start-up. (Note: Flat profiles considerably underestimate P_{alpha}).

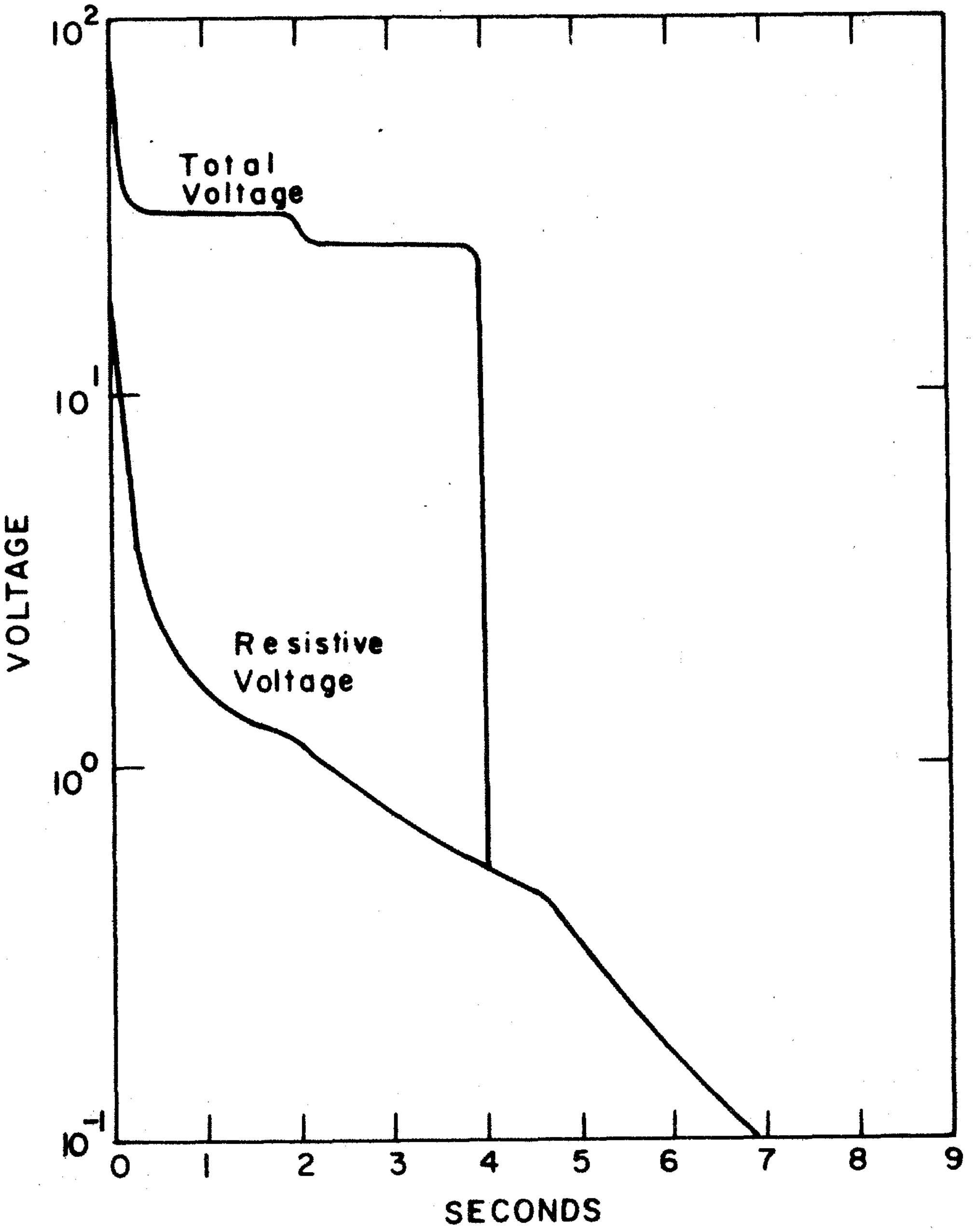

Figure 2-19 Voltage change during start-up.

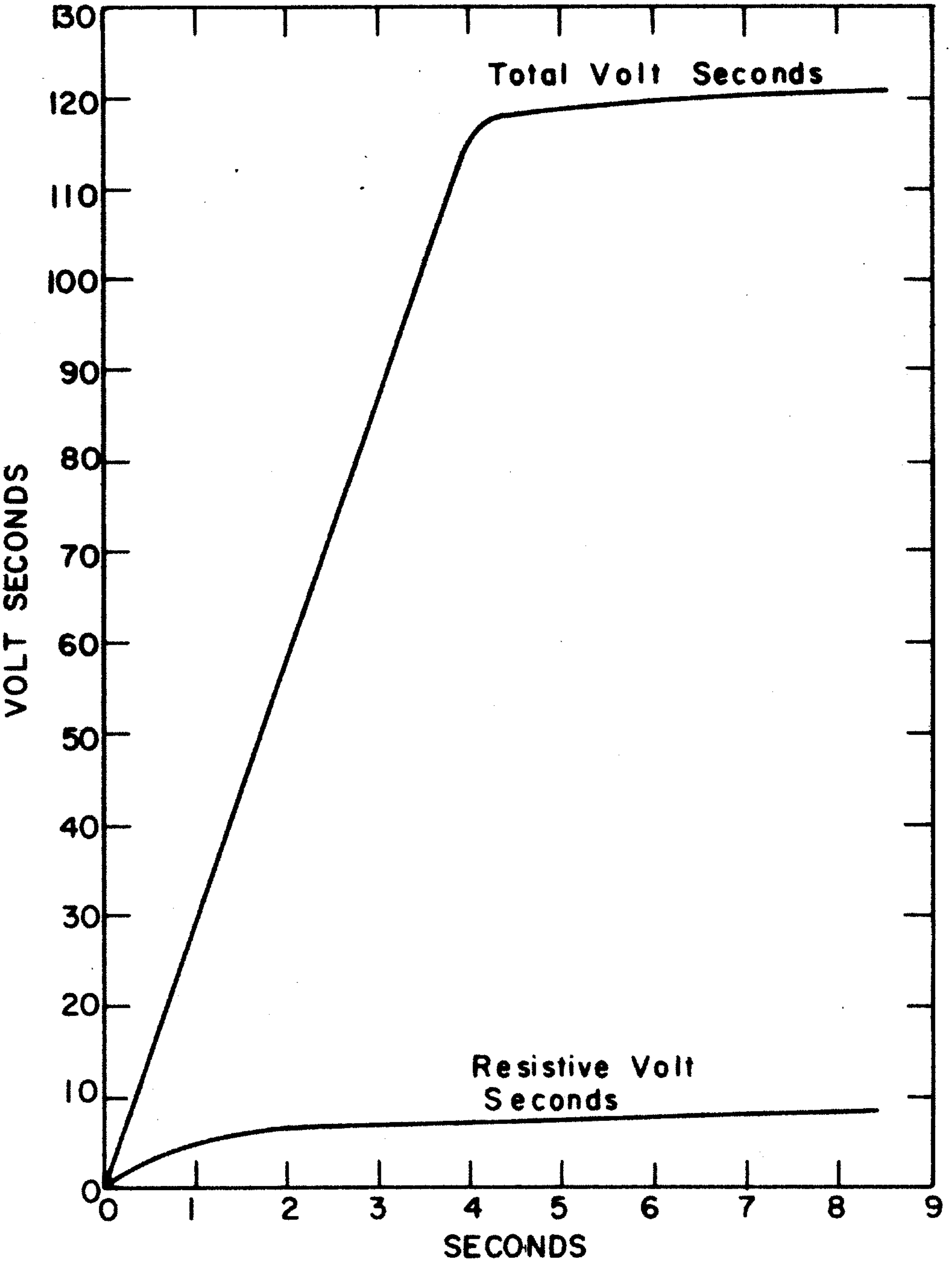

Figure 2-20 Volt-seconds requirement during start-up.

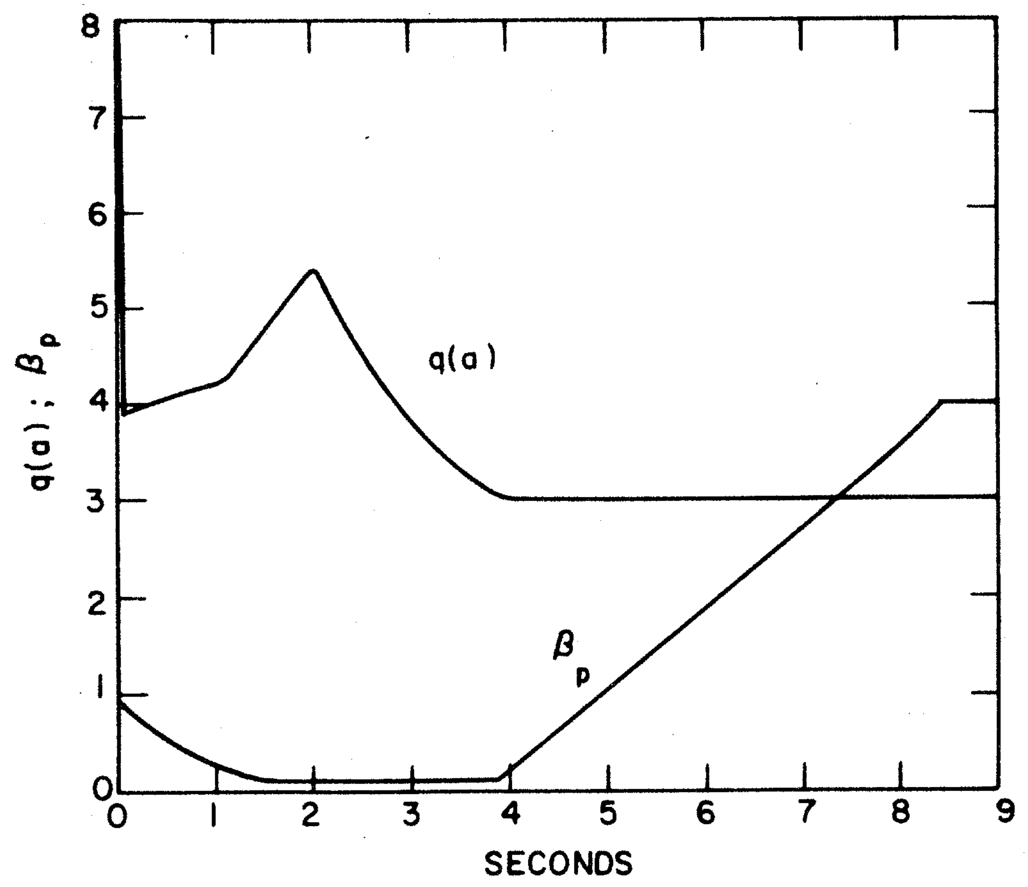

Figure 2-21 β_p and q during start-up.

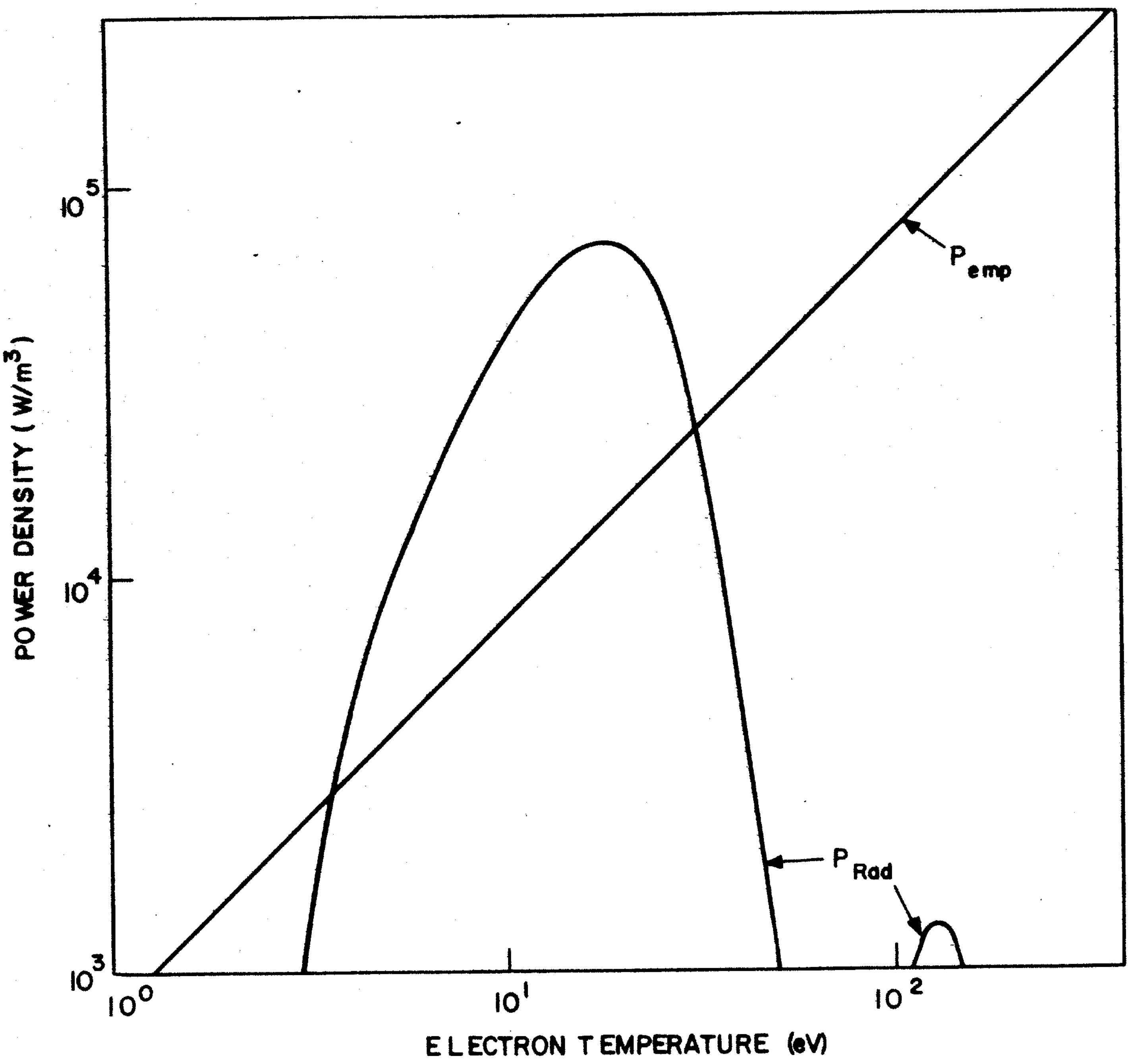

Figure 2-22 Comparing oxygen line radiation losses with empirical scaling losses for Z_{eff} = 1.5, n_{DT} = 1 × $10^{19}$$m^{-3}$, and a = .25 m. The radiation loss is taken from Ref. [1].

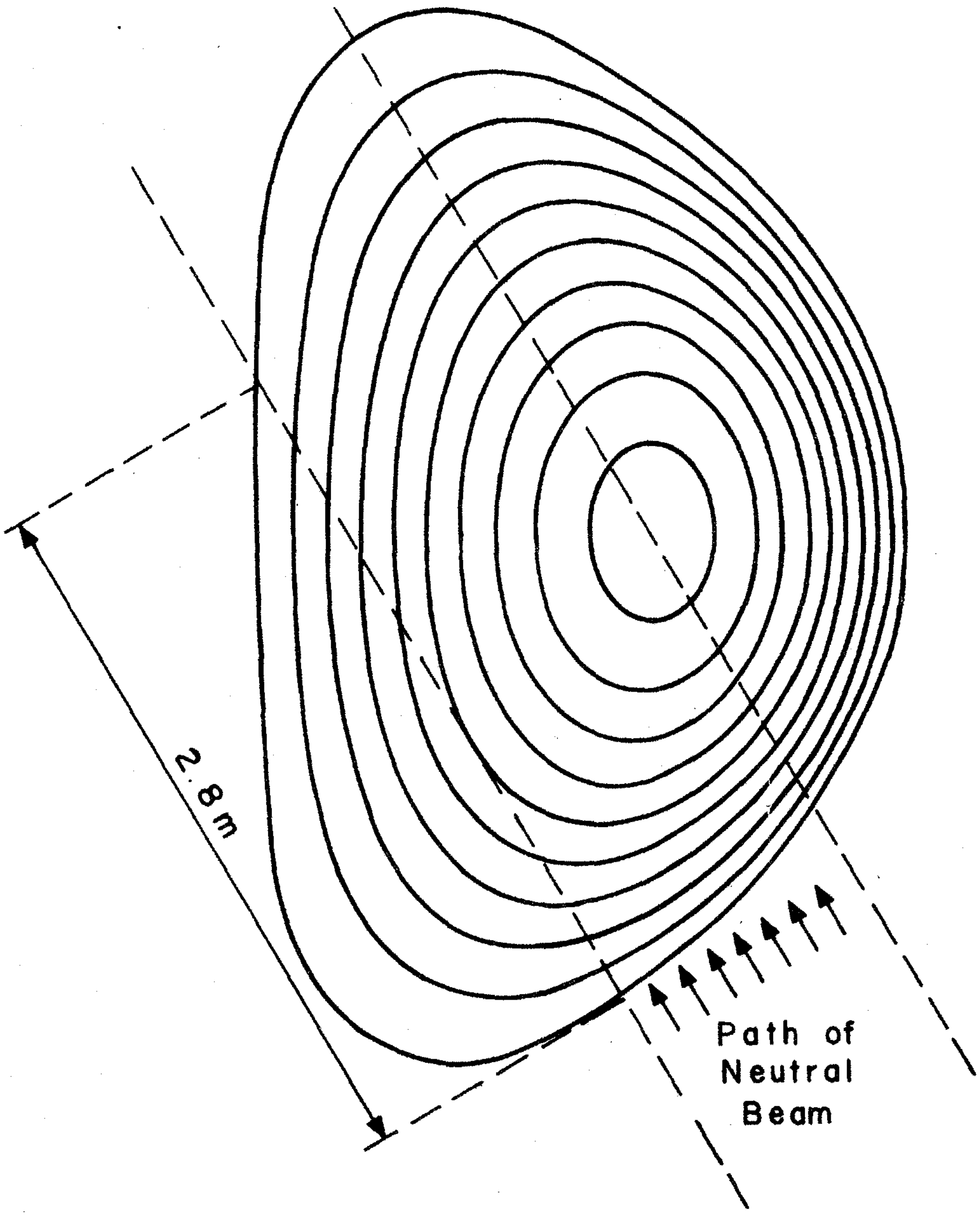

Figure 2-23 Determining the smallest plasma cord traversed by neutral beams.

of the power balance. In the start-up scenario, an initial oxygen concentration of 0.78% (Z_{eff} = 1.5) was assumed. This value of Z_{eff} appears close to the upper limit tolerable by demonstration-size machines during start-up. (Results from ALCATOR indicate clearly, however, that greater purity is attainable [24]). The line radiation resulting from such an initial oxygen concentration [25] and the energy needed to break down a gas suggest the strategy of using an initially low density and large applied loop voltage until $T_e \simeq 50$ ev. From Figure 2-22 it is seen that beyond this temperature the line radiation falls off rapidly, making it unnecessary to maintain a large ohmic power drive. Figure 2-19 shows the applied loop voltage dropping rapidly during the first 0.03 seconds.

During the expansion stage of start-up, the Z_{eff} is assumed likely to decline to $\sim$ 1.0 as injected fuel decreases the relative oxygen concentration. From Figure 2-16, it is seen that after the expansion stage when 12.5 MW of beam power is provided, T_e quadruples. This increased T_e will lead to additional sputtering of the first wall material, molybdenum, resulting in an increasing Z_{eff} (now due principally to Mo). This Z_{eff} is estimated to level off at 1.2 when the density has reached $3.1 \times 10^{20} m^{-3}$. This large density will greatly reduce the neutral efflux and the concomitant influx of impurities (see Section 2.4).

Figure 2-18 demonstrates that with a Z_{eff} of 1.2 the losses predicted by the empirical scaling law dominate during most of the start-up. The one exception is during the first 0.03 seconds when oxygen line radiation may dominate. (This radiation is not shown in Figure 2-18.)

From .03 to 2.0 seconds the losses predicted by empirical scaling decrease as the cross-sectional area of the plasma increases. During the remainder of the start-up sequence, these losses increase with increasing energy density. A total neutral beam power of 100 MW was found to be adequate for overcoming the combined losses and giving a reasonable start-up time of approximately 8.4 seconds.

2.3.4 The Minimum Tolerable Safety Factor

Present experimental results indicate that for peaked temperature profiles a safety factor at the plasma edge, q, greater than 3 might be needed to prevent MHD instabilities from disrupting the plasma. Since

$$q = \frac{B_T\ S}{B_p\ A} > 3 \tag{2.44}$$

this requirement will limit the maximum achievable plasma current. For the HFCTR, the limit for $B_T = 7.4$ T is 6.7 MA.

Figure 2-21 shows the effects of the plasma development on q. From t = .03 second to 1.1 seconds, q increases as the plasma major radius decreases and the minor radius increases. From about t = 1.1 seconds to 2.0 seconds, the plasma deformation (circular to elliptic) results in increasing q. After t = 2.0 seconds, the current density increases again, causing q to decline gradually to its final value of 3.

The above q behavior assumes that a classical 'skin effect' will not occur during the first 3.9 seconds of start-up. During this time the plasma parameters are similar to those of present experiments, for which flux conservation has not been observed.

2.3.5 The Disruptive Instability Density Limit

Tokamak experimentation has shown that a plasma column disruption occurs when some critical density, n_{ec}, is exceeded for an ohmically-heated hydrogenous plasma. The reason for this low-m-number MHD instability is not well understood. However, Murakami [26] has collected empirical evidence showing that

$$n_{ec} \sim \frac{B_T}{R_o} \tag{2.45}$$

The proportionality constant is $2.56 \times 10^{19}\ m^{-2}\ T^{-1}$ for discharges that have cold gas puffed in.

In addition, Gibson [27] has established a semi-empirical result which agrees well with experimental observation. He established that

$$n_{ec} \sim \left[6.7 \times 10^{26} \frac{Z_{eff}}{Z_{eff} - 1} \bar{T}_{OH}^{\ -3/2}\right]^{1/2} \bar{J} \tag{2.46}$$

where, for flat profiles,

$$\bar{T}_{OH} = T_e$$

and

$$\bar{J} = J$$

Both equations 2.45 and 2.46 are satisfied during start-up. As Figure 2-23 indicates, the density remains at $3 \times 10^{19}\ m^{-3}$ during the ohmic heating phase: thus insuring that Murakami's observed limit is not violated. During the first 30 milliseconds, the current density J is raised to 410 $\frac{kA}{m^2}$ and then held constant during the plasma expansion phase, as shown in Figure 2.24. This value is large enough to guarantee that the increasing temperature does not violate equation (2.45).

After neutral injection is initiated, the disruptive instability limit is less likely to be a problem [28]. The deposited beam power should tend to prevent the temperature and current density profiles from shrinking.

2.3.6 The β_p Requirement

Throughout start-up, β_p must be carefully controlled in order to avoid MHD instabilities. If the toroidal beta is limited by internal ballooning modes, then as described in Section 2.1.5

$$\beta_T \lesssim \beta_c = \frac{k_s}{Aq^2} \tag{2.18}$$

By combining equations (2.18) and (2.44) this limit can be rewritten as

$$\beta_p \lesssim \left[\frac{k_s}{S^2}\right] A \tag{2.47}$$

For the HFCTR the value of β_p should not exceed 5.0.

To minimize use of the hexapole field coils during start-up and to reduce the complexity of start-up, the outward shift of the magnetic flux surfaces should be delayed until the latter part of start-up. The outward shift of the magnetic flux surfaces is approximated by Ref. [29] as

$$\frac{\Delta}{a} = \frac{1 + 4\beta_p}{8A} \tag{2.48}$$

for a constant J profile and a parabolic pressure profile. This result suggests the strategy of keeping β_p small during most of start-up.

The behavior of β_p during start-up is seen in Figure 2-28. β_p remains low for the first 4.0 seconds of start-up and then rises rapidly, limited only by the available beam power. From 2.0 seconds to 4.0 seconds, a time during which the current nearly doubles, 12.5% of the available beam power is used. This insures a gradual plasma pressure increase and a correspondingly low $\beta_p \left(\beta_p \sim \frac{nT}{I^2}\right)$.

2.3.7 The Applied-Loop Voltage Limit

To minimize coil and power supply costs, the applied loop voltage should be as low as possible. This constraint, coupled with an intrinsically large plasma inductance ($L \simeq 1.7 \times 10^{-5}$ hy) and the requirement of a large initial $\frac{dJ}{dt}$, points to the desirability of an initially small plasma radius (i.e. $a \simeq 0.25$ meter). Were the plasma not small, a current density rise similar to that in ALCATOR $\left(\frac{3 \times 10^9 \text{ amp}}{m^2 - \text{sec}}\right)$ over an 8.4 m^2 plasma cross section would require a loop voltage in excess of 45 kV. Even if this number is off by a factor of several - possibly due to incorrect scaling of current density profiles - it is clear that a much-reduced initial plasma cross-sectional area is required. If $\frac{dJ}{dt}$ rises too slowly, then the required resistive volt-seconds and the runaway electron population could become excessive. An initially small plasma radius will also help insure proper current and temperature profile development in the event that a classical skin effect is observed.

In the start-up the maximum voltage, which occurs at breakdown, was taken to be $\sim$ 250 volts. This value seems to be a reasonable scale up from present experiments and is well within the 300 volt limit.

2.3.8 The Runaway-Electron Limit

Runaway electrons are a poorly understood phenomenon present in all tokamak experiments. The runaway rate depends sensitively on the values of T_e, n_e, and the applied loop voltage [30] and also on factors such as the amount of preionization and toroidal magnetic ripple [31].

As seen in Figure 2-16, the density rises rapidly prior to temperature increases at 0.03 seconds (initial heating after breakdown) and 3.9 seconds (second beam-heating phase). The applied loop voltage decreases from its initial value of 250 volts to below 30 volts before the temperature rises significantly. This is shown in Figure 2-19. These two actions serve to minimize the chances of creating a large runaway-electron population.

2.3.9 The Neutral Beam Requirements

In order to avoid the complexity associated with having energy dumps on the first wall opposite the beamlines, neutral beam injection should not occur before the plasma density has increased to a level sufficient to attenuate the neutrals by a large factor. In addition, the current must be large enough to prevent the banana orbits of the ionized beam neutrals from exceeding the dimensions of the plasma.

Thermal-hydraulic calculations indicate that an alpha wall loading of $\sim 1 \frac{MW}{m^2}$ on a 760°C first wall gives acceptable thermal stress levels and that the first wall temperature may drop by about 140°C between burn periods. At start-up, a wall loading of 2.0 $\frac{MW}{m^2}$ due to neutral-beam impact would raise the local wall temperature opposite the beam port by 100°C. The thermal stresses due to such a local hot spot appear to be acceptable.

In the present design, there are eight beamlines, each of which contains three 0.5 m × 1.0 m sources (see Section 5.2). The neutral beam power delivered by each source is 4.2 MW. From the geometry of the injection system, the highest possible wall loading opposite a beam port is due to two overlapping source beams, or 16.7 $\frac{\mathrm{MW}}{\mathrm{m}^2}$. In order to reduce this value to the 2.0 $\frac{\mathrm{MW}}{\mathrm{m}^2}$ level, the plasma must attenuate the neutrals by a factor of 8, allowing only 12% of the neutral beam power to strike the opposite wall. The requirement on the maximum mean-free-path for the neutrals is therefore given by

$$e^{-b/\lambda} \leq .12 \tag{2.49}$$

where b is the smallest plasma chord traversed by the overlapping beams, and λ is the mean-free-path against charge-exchange, ionization by ions, and ionization by electrons of a 120 keV neutral deuteron in the plasma. At 120 keV, the total trapping cross section (σ_{trap}) is about 3.09×10^{-20} m^2[32]. Since $\lambda = 1/n\sigma_{trap}$, the minimum density is given by

$$n_{min} = \frac{-\ln\ (.12)}{b\ \sigma_{trap}} \tag{2.50}$$

From Figure 2-23, the value of b is seen to be 2.8 meters. The minimum permissible density at the start of the beam injection phase is therefore 2.5×10^{19} m^{-3}.

The magnitude of the increased sputtering due to the 12% of the neutral beam current which is untrapped can be estimated. Taking the worst case (i.e. all 8 beamlines are activated), a 12% untrapped current would be $6.2 \times 10^{20} \frac{\text{neutrals}}{\text{sec.}}$. The sputtering coefficient for 120 keV deuterons on molybdenum is about 1.5×10^{-3} [33]. Combining these numbers indicate that the molybdenum buildup caused by the untrapped beam current is insignificant (i.e. $\sim 3.0 \times 10^{15} \frac{\text{Mo ions}}{\text{m}^3\text{sec}}$).

Since perpendicular beam injection is required, the banana width may be of the same order or larger than the plasma minor radius. In order to prevent this, a large plasma current is required before the neutrals are injected. The required current is determined by the condition

$$r_b \ll a \tag{2.51}$$

where r_b is the banana width.

Since

$$r_b = 2\rho_p/A^{1/2} \tag{2.52}$$

with ρ_p the poloidal gyroradii ($\rho_p \sim \frac{V_{th}\ aS}{I}$), the requirement for a 120 keV perpendicularly-injected beam is

$$\frac{3.8 \quad 10^5}{I} \ll a \tag{2.53}$$

or

$$I \gg 317 \text{ kA} \tag{2.54}$$

Figures 2-16 and 2-17 show that the density and current requirements are satisfied prior to beam injection (at t = 2.0 sec.). The density is $3 \times 10^{19}\ m^{-3}$ and the current is $\sim$ 3.5 MA when the beams are turned on.

2.3.10 The Limit on the Flux Change through The Toroidal Core

About 40 volt-seconds must be created by magnetic flux passing through the toroidal core. Too rapid a flux change will require uneconomical levels of refrigeration power. Therefore, a low applied loop voltage - about 25 volts - would be appropriate for much of start-up.

A low applied loop voltage affects start-up in a number of ways. It implies a relatively long start-up time - about 8.4 seconds - and a gradual current increase since most of the loop voltage is inductive. This is shown in Figure 2-19. The gradual current rise, in turn, requires that the plasma expand slowly since

$$\frac{dI}{dt} \approx J \frac{dA}{dt} \qquad (2.55)$$

during the plasma expansion phase. Finally, the plasma pressure must increase gradually so that the β_p limitations can be satisfied.

2.3.11 The Collisionality Requirement

With the exception of PLT, experiments from which the empirical confinement scaling ($\tau_E \approx na^2$) was established have operated in a regime of "collisionality" > 0.1, (see Section 2.1.3), i.e.

$$C \equiv \frac{A\ \nu_{ei}}{\omega_{be}} > 0.1 \qquad (2.56)$$

where ν_{ei} is the electron-ion collision frequency, A is the plasma aspect ratio and ω_{be} is the electron bounce frequency. In order to maintain the credibility of the scaling law in extrapolating to a large reactor, the value of collisionality should be greater than 0.1 during the start-up as well as the burn.

In the start-up scenario, the density is increased rapidly at the beginning of the second beam-heating phase, when 100 MW of beam power is injected. This density increase will prevent a rapid temperature rise which would lead to a collisionless plasma.

2.3.12 Summary of The Start-up Scenario

Start-up Sequence

(1) Initiation ($0 < t < 0.03$ sec.)

(a) Initially, $n = 10^{19}\ m^{-3}$, $a = 0.25$ m, $V_{loop} \simeq 250$ volts ('a' is set by centering the plasma 0.25 m from the limiter)

(b) When oxygen line radiation becomes small, n increases to $3 \times 10^{19}\ m^{-3}$ and J rises to $410\ \frac{kA}{m^2}$.

(2) Plasma Expansion (0.03 sec. $< t < 2.0$ sec.)

While keeping n and J constant, slowly expand the minor radius from 0.25 m to 1.2 m by moving the plasma center away from the limiter; then slowly deform the plasma into an ellipse with a shape factor (circumference/$2\pi a$) of $S = 1.4$, and cross-sectional area of 8.4 m^2.

(3) Beam Heating (2.0 sec. < t < 8.4 sec.)

  - (a) Using 12.5 MW of beam power the current rises gradually to its final value of 6.7 MA.
  - (b) When the current reaches 6.7 MA, 87.5 MW of additional beam power is used and the density is rapidly brought up to $3.1 \times 10^{20}\ m^{-3}$. When the density reaches $\sim 10^{20}\ m^{-3}$ the ripple coils are turned on to ensure beam penetration.
  - (c) With a constant density of $3.1 \times 10^{20}\ m^{-3}$ and a beam power of 100 MW, the temperature rises to the ignition value of 8.0 keV. When β_p is 50%-75% of its final value, the hexapole field coils deform the ellipse into a D-shape with $S = 1.5$ while the plasma cross section remains at $8.4\ m^2$.

Rationale for Start-up Sequence

(1) Initiation (0 < t < 0.03 sec.)

  - (a) The initial conditions will
    - (i) ensure that $T_e(t)$ and $I(t)$ increase for any realistic Z_{eff}
    - (ii) ensure an adequate $\frac{dJ}{dt}$ without an excessive V_{loop}.
  - (b) Increasing n to $3 \times 10^{19}\ m^{-3}$ and increasing J slowly to $410\ \frac{kA}{m^2}$ after T_e reaches 40 eV will
    - (i) decrease the chance of creating a large runaway-electron population
    - (ii) ensure that the density limit is not exceeded

(iii) help protect the first wall from neutral beam damage

(iv) limit the inductive voltage

(2) Plasma Expansion (0.03 sec. < t < 2.0 sec.)

Keeping n and J constant while the plasma grows gradually will

(i) minimize V_{loop}

(ii) help protect the wall from neutral beam damage.

(3) Beam Heating (2.0 sec. < t < 8.4 sec.)

A two-stage neutral beam heating phase will

(i) allow J to increase gradually to the final value while the plasma conductivity is low

(ii) decrease the chances of creating a large runaway-electron population

(iii) allow β_p to remain low during most of start-up, which leads to simplification of the field coil control system

(iv) ensure that the plasma remains collisional

(v) enable T_e to rise to the ignition value.

2.4 IMPURITY CONTROL AND THE BURN TIME

The commercial success of an ignited HFCTR depends largely on the length of the burn time and the fusion energy produced during the burn period. The burn time determines the frequency with which the first wall is thermally stressed, influencing the first wall lifetime. The burn time also directly affects the duty cycle. The energy output along with the burn time affects the energy multiplication factor.

The length of the HFCTR burn period is inextricably related to the question of impurity control. The rate at which alpha ash and impurities accumulate in the plasma determines whether the plasma quenches before the available volt-seconds are expended. For the HFCTR base case the burn period is assumed to be volt-second limited, with at least 60 volt-seconds available during this period. A burn time greater than 400 seconds results by assuming neoclassical resistivity along with a 60 volt-second availability. These volt-seconds come from OH coils located in the core. If the dwell time - cycle time minus burn time - is 20 seconds as is assumed for the base case, then many of the problems associated with pulsed operation are mitigated. That is; the duty cycle is near unity, the energy multiplication factor is large, and the first wall fatiguing is not severe. However, whether this base case scenario is feasible or not depends on the question of impurity control. This question is explored in greater detail below.

2.4.1 Impurity Control Without a Divertor

The application of a divertor to a conventional tokamak is a very difficult engineering problem which may require considerable compromise in cost, efficiency and size. The use of a plasma-gas blanket and an effectively designed limiter presents an alternative method for impurity control. The plasma-gas blanket would minimize the energetic neutral efflux that could bombard the first wall. This, in turn, would limit the first wall sputtering and the concomitant amount of high-Z impurities that accumulate in the plasma. The limiter would be used to deflect particles, especially alpha ash, out of the plasma and into a pumping port where they could be pumped away.

The Plasma-Gas Blanket

Whether an effective plasma-gas blanket will, in fact, be formed in a high density power reactor is still very much an open question. However, Alcator A does provide some encouraging results [34], routinely operating in a regime in which the energetic neutral efflux is small. This occurs when the neutral mean free path, ℓ_n, is much less than 'a'. When $\ell_n > a$, the following occurs:

(1) The background neutral density falls off rapidly from the first wall. This results in relatively few neutrals being near the hot core of the plasma.

(2) The energetic neutrals ionize or charge exchange before hitting the first wall.

In addition to experimental observation, first wall shielding is in qualitative agreement with neutral gas dynamics computations [35]. Furthermore the computational results shown in Figure 2-24 indicate that favorable first wall protection can be scaled up to reactor-type plasmas (also see Appendix D for a more detailed discussion).

A Limiter-Partical Removal Scheme

Using a limiter to remove particles, especially alpha ash, from the plasma is a concept requiring considerably greater research. The basic concept is to design a limiter that deflects particles into a pumping port where they can be pumped away. An interesting limiter design that utilizes this scattering concept has been proposed by Schivel [36]. At present the concept is very preliminary, and its effectiveness when scaled up to a power reactor is at least as speculative as that of a divertor. There are

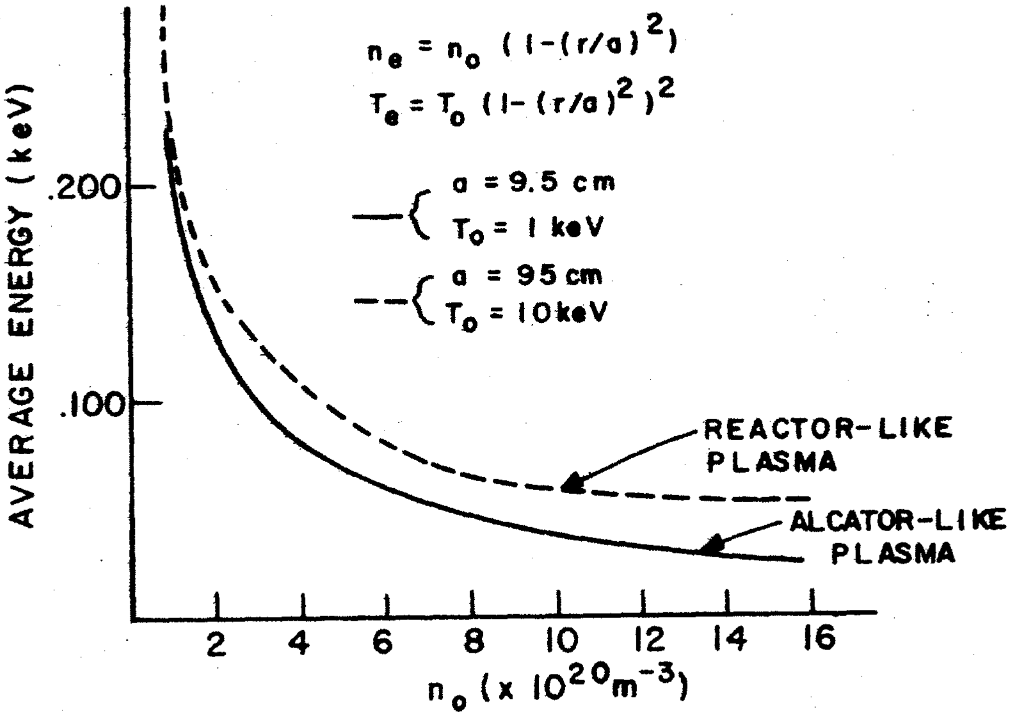

Figure 2-24 Mean energy of effluent, charge- exchanged neutral flux vs. central plasma density, n_o. (M. H. Hughes, private communication)

five primary questions that a limiter alpha removal scheme must address:

(1) Can the limiter be designed to remove the large heat flux impinging upon it?

(2) Can sputtering at the limiter be kept to small enough levels?

(3) What are the physical features of the plasma-gas blanket (e.g. will particles even diffuse out and if so then at what rate)?

(4) What pumping speed is required for acceptable impurity removal rates?

(5) How much first wall area must be used for pumping ports?

These questions are interrelated and will require additional research to be answered satisfactorily.

A limiter design very similar to the one proposed by Schivel and scaled up for use in the HFCTR is shown in Figure 2-25. If the scheme works properly ions will strike a neutralizer plate, scatter into a pumping system as neutrals, and be pumped away. In order for the concept to work, the limiter must deflect most of the scattered neutral particles into the pumping system, rather than back into the plasma. As is shown in Figure 2-25 the obtuse angle of the neutralizer plate and the small entry openings should help provide for a favorable deflection. In addition, the small dimensions of the limiter cause most ions to diffuse deeply into the "shadow" of the limiter before actually hitting the neutralizer plate. This should also decrease the chances of the alphas deflecting back into the plasma.

The applicability of Schivel's scheme or some variation of it to an HFCTR will probably depend upon whether the first two questions raised above can be affirmatively answered.

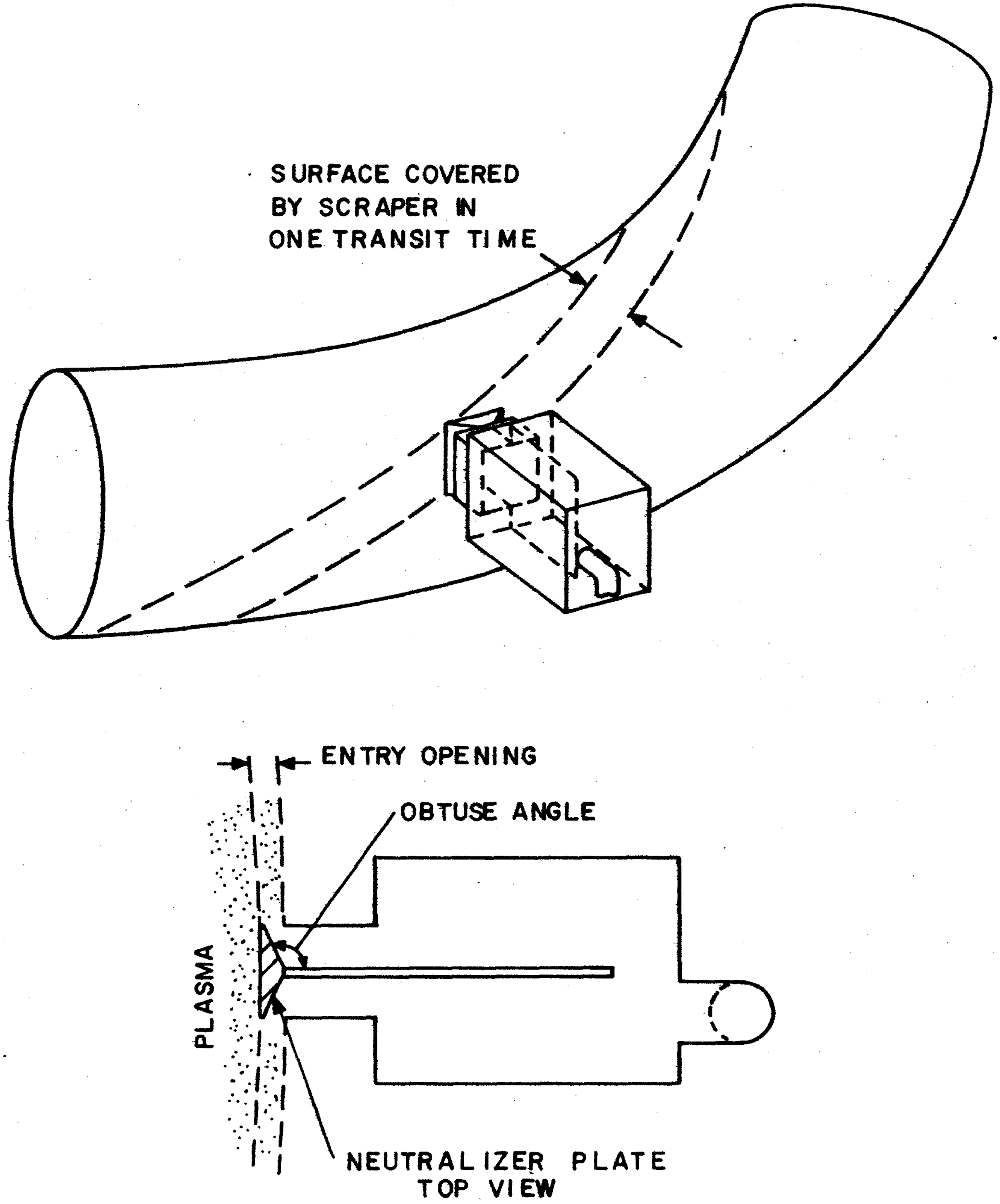

Figure 2-25 Limiter -alpha removal scheme adopted from Schivel [36].

2.4.2 How Effective Must Impurity Control Be?

Determining how effective the limiter and plasma-gas blanket must be in order to avoid a "premature" plasma quench is a difficult question because of the physics uncertainties. Nevertheless, a first cut is made at answering this crucial question.

As the alpha ash builds up in the plasma, creating an unwanted pressure, the D-T kinetic pressure must decrease to prevent the beta limit from being exceeded. In addition, the alpha ash and molybdenum accumulation causes the ignition curve on an n_{DT} - T graph to shift upward and to the right. From these two effects, it is clear that as the alpha ash and high-Z impurities accumulate, the available n_{DT} - T plasma operating regime gradually shrinks. This is shown schematically in Figure 2-26 Stages (I), (II), and (III) depict the temporal decrease of the available operating regime during the burn period.

Stage (III) is right at the point that the plasma is "forced" to quench. If this stage is surpassed before the volt-seconds are expended, then the burn period is necessarily impurity-limited. However, if the saturation density values, n_{Mos} and $n_{\alpha s}$, are such that

$$n_{Mos} < n_{MoIII} \tag{2.57}$$

and

$$n_{\alpha s} < n_{\alpha III} \tag{2.58}$$

then stage (III) need never be reached and a "premature" plasma quench can be avoided.

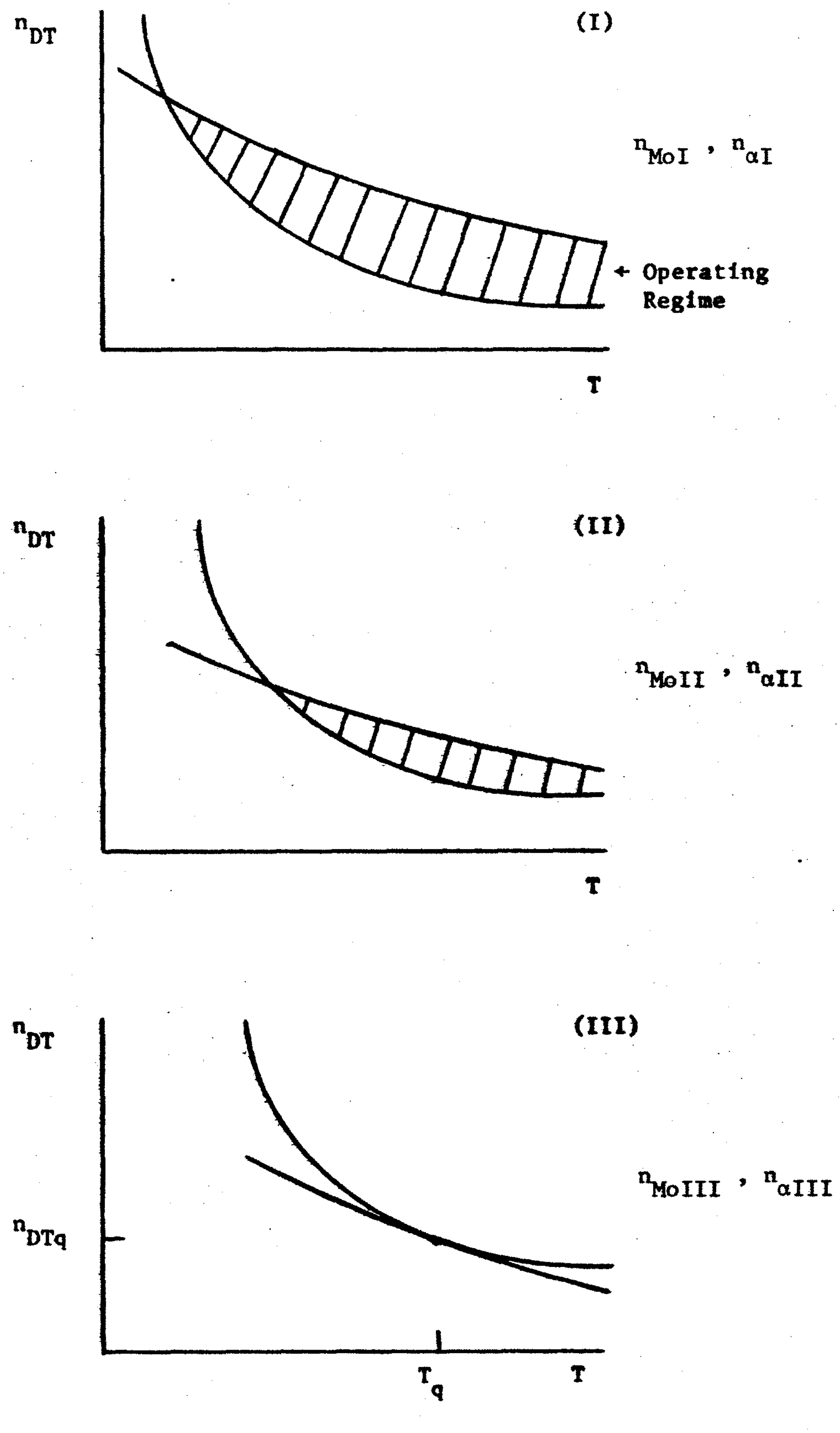

Figure 2-26 Temporal Decrease of the Available Operating Regime With $n_{MoI} < n_{MoII} < n_{MoIII}$ and $n_{\alpha I} < n_{\alpha II} < n_{\alpha III}$

Determining whether Equations (2.57) and (2.58) hold, requires finding n_{Mos} and $n_{\alpha s}$ as well as n_{MoIII} and $n_{\alpha III}$. n_{MoIII} and $n_{\alpha III}$ are related by some function, G. That is

$$G(n_{MoIII}) = n_{\alpha III} \tag{2.59}$$

where G is a monotonically decreasing function that must be determined numerically. $n_{\alpha s}$ can be estimated by using the simple rate equation

$$\frac{dn_{\alpha s}}{dt} = 0 = \frac{n_{DT}^2}{4} <\sigma v>_{DT} - \frac{n_{\alpha s}}{\tau_{p\alpha}} P \tag{2.60}$$

where $\tau_{p\alpha}$ is the alpha particle diffusion time and P_α is a measure of the probability of removing an alpha after it has diffused to the first wall. In other words, P_α is a measure of the effectiveness of the limiter-particle removal scheme. By rearranging Equation (2.60), $n_{\alpha s}$ can be written as a function of P_α. That is

$$n_{\alpha s} = \frac{\tau_{p\alpha}}{P\alpha}\left(\frac{n_{DT}^2}{4}\right)<\sigma v>_{DT} \tag{2.61}$$

Unfortunately because of physics uncertainties, there is no analogous equation that can be formulated for n_{Mos}.

By assuming that the impurity densities have the same profile shapes as the D-T density and that the $\tau_{p\alpha} = \tau_E$, it is possible to estimate whether a given P_α and n_{Mos} value will result in a prematurely (less than 500 s) quenched burn. By using Equations (2.57), (2.58), (2.59), and (2.61) Figure 2-27 is numerically generated. If the HFCTR impurity control is such that (P_α, n_{Mos})

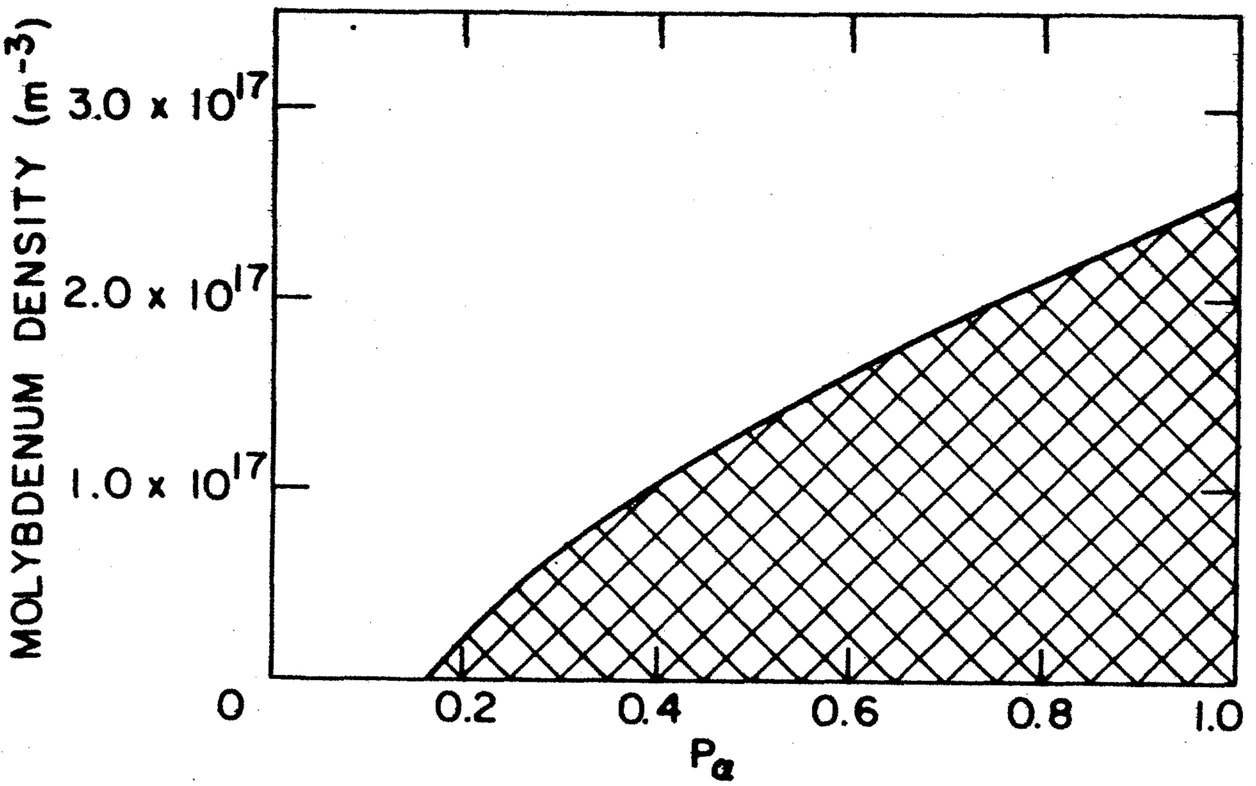

Figure 2-27 Maximum Molybdenum Density for Sustained Burn vs. Effectiveness of Alpha Removal

falls inside the cross-hatched area, then the reactor need not be impurity limited. Based on Figure 2-27 the following is apparent:

(1) If $n_{Mo} > 2.5 \times 10^{17}\ m^{-3}$, then the HFCTR plasma will quench irrespective of P_α. This implies that the plasma-gas blanket must be very effective, regardless of the efficacy of the limiter-particle removal scheme.

(2) The more effective the gas-blanket is, the less effective P_α needs to be. This result is in concurrence with one's intuition.

(3) If the plasma-gas blanket is very effective (i.e., $n_{Mo} \simeq 0$), then the limiter-particle removal scheme can be quite ineffective (i.e., $P_\alpha \simeq .17$).

2.5 THERMAL STABILITY AND REACTOR CONTROL

Figure 2-28 shows the confinement-temperature relation for equilibrium ignition. The equilibrium operating point occurs where the confinement-temperature characteristic of the plasma intersects curve L2. This equilibrium point is unstable if the slope of the plasma characteristic is greater than that of curve L2. The empirical scaling law used in this design study indicates that τ_E is independent of $T_i = T_e$, and it is also likely that n_e will be constant during a temperature perturbation. The plasma characteristic is then illustrated by line L1 in Figure 2-28. A small temperature perturbation causes the operating point to shift from point A to the right along line L1. With empirical scaling, all operating points on L2 are unstable at $T_i < 27$ keV, the minimum of the L2 curve.

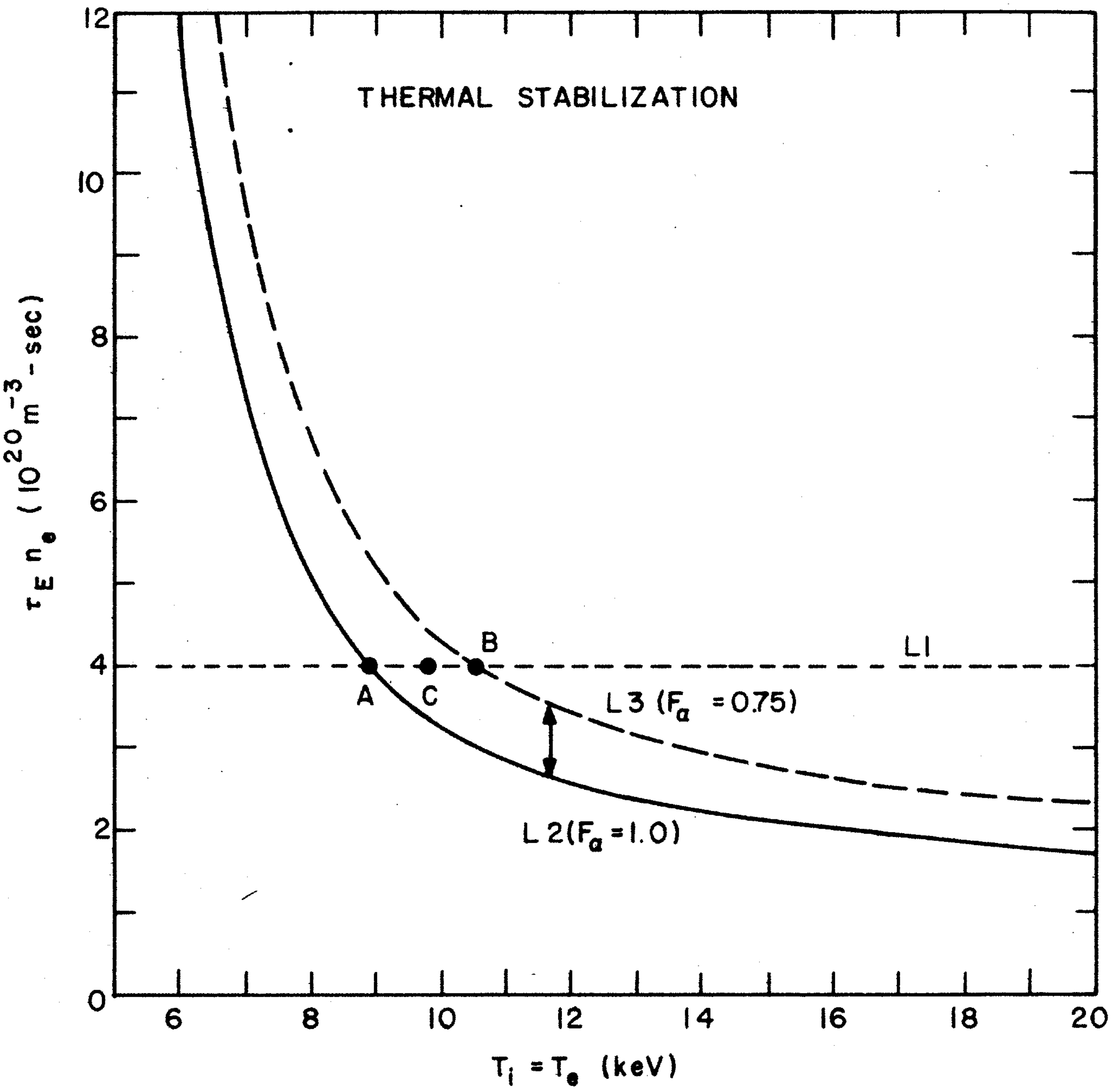

Figure 2-28 L2 and L3 are the equilibrium ignition conditions for different F_α. Flat density and temperature profiles are assumed.

2.5.1 Ripple Control

One way of regulating the plasma temperature at an unstable equilibrium point is by controlling the fraction of the energy of fusion alpha particles, F_α, that is deposited in the bulk plasma [37]. This control is achieved in the HFCTR by a vertically asymmetric toroidal-field ripple of controllable magnitude, which causes an enhanced outward drift of banana-trapped alpha particles [38]. The ripple is applied by means of the special ripple-inducing coils that are designed for ripple-injection heating (see Section 3.5).

If F_α can be reduced, the equilibrium ignition curve is raised upward to intercept L1 at point B. Provided that the interception is made before the plasma temperature reaches B, the thermal excursion is brought under control. The ripple field is then decreased, so that the equilibrium point shifts back to A. Another ripple-induced effect that can help control the plasma temperature is the enhancement of the radial diffusion of the reacting trail of the bulk-ion population [39]. This phenomenon can be important in reducing the plasma reactivity only when the plasma density is not too large; the alpha-ejection phenomenon seems likely to be the dominant control mechanism for the HFCTR.

In the following simplified analysis, bremsstrahlung radiation is ignored which is 15% or less of the alpha particle production rate, P_α, when $T > 8$ keV. The rate of change of temperature following a perturbation ΔT from unstable equilibrium is [40]

$$\frac{dT}{dt} = \frac{\Delta T}{\tau_E} \frac{20}{3} T^{-1/3} - 1 \qquad (2.62)$$

Here T is in keV, and the simplified low-temperature expression for $\langle \sigma v \rangle$ is used [41]. Provided that $T^{-1/3} \simeq$ constant, the rate of change of T is proportional to ΔT, so that ΔT increases exponentially in time, with a time constant $\tau_r \sim 0.5\ \tau_E$. The condition to halt thermal runaway is [42]

$$\frac{\Delta F_\alpha}{F_\alpha} \leq \frac{\Delta T}{T_o} \left(1 - \frac{20}{3} T^{-1/3}\right) = -y \frac{\Delta T}{T_o} \tag{2.63}$$

Thus to halt the thermal excursion at a 5% increase in T, for example, the fractional alpha power deposition must be reduced by about 10%.

Because the required $|\Delta F_\alpha|$ is proportional to ΔT, $|\Delta T_\alpha|$ also becomes exponentially large with time:

$$\frac{|F_\alpha|}{F_\alpha} \geq \frac{\delta T}{T_o} y \left[\exp \frac{y \Delta t}{\tau_E}\right] \tag{2.64}$$

where Δt is measured from the time when the perturbation is δT. If the smallest temperature perturbation that can be identified at the onset of an excursion is 3%, then a typical value for the rate of change of $|\Delta F_\alpha|$ is $0.25\ \text{sec}^{-1}$.

Figure 2-29 shows "vacuum" ripple contours appropriate for the HFCTR plasma. (In the presence of the plasma current, the ripple well depth is reduced significantly except at the midplane.) A statistical estimate of F_α has been determined by following the guiding-center trajectories of fusion alphas with a Monte Carlo code [38]. Figure 2-30 shows the maximum possible loss fraction as a function of ripple amplitude, and of the number N of locations around the torus where ripple is applied (see Section 3.5). The loss fraction can be made as large as 25% with just one ripple location, but it seems preferable to use several locations in order to limit the required

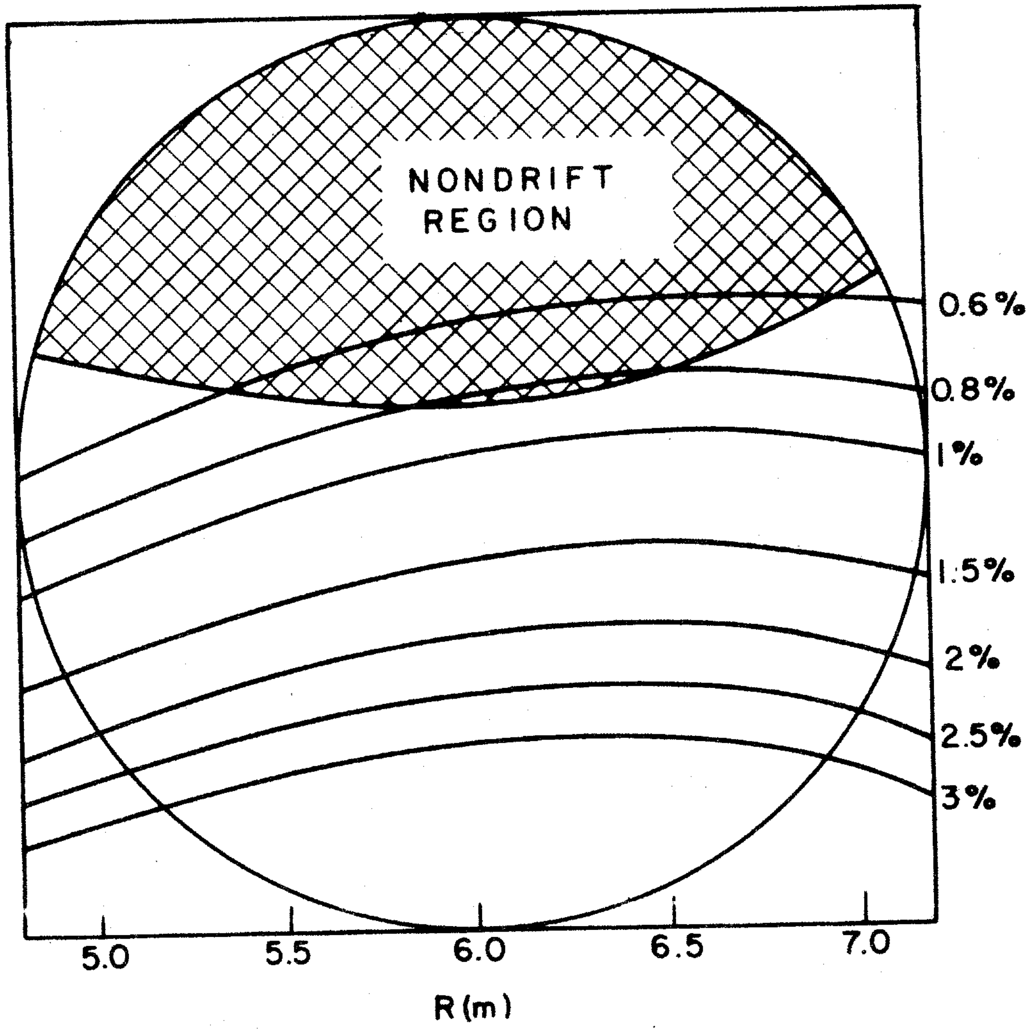

Figure 2-29 HFCTR ripple contours at the ripple centers.

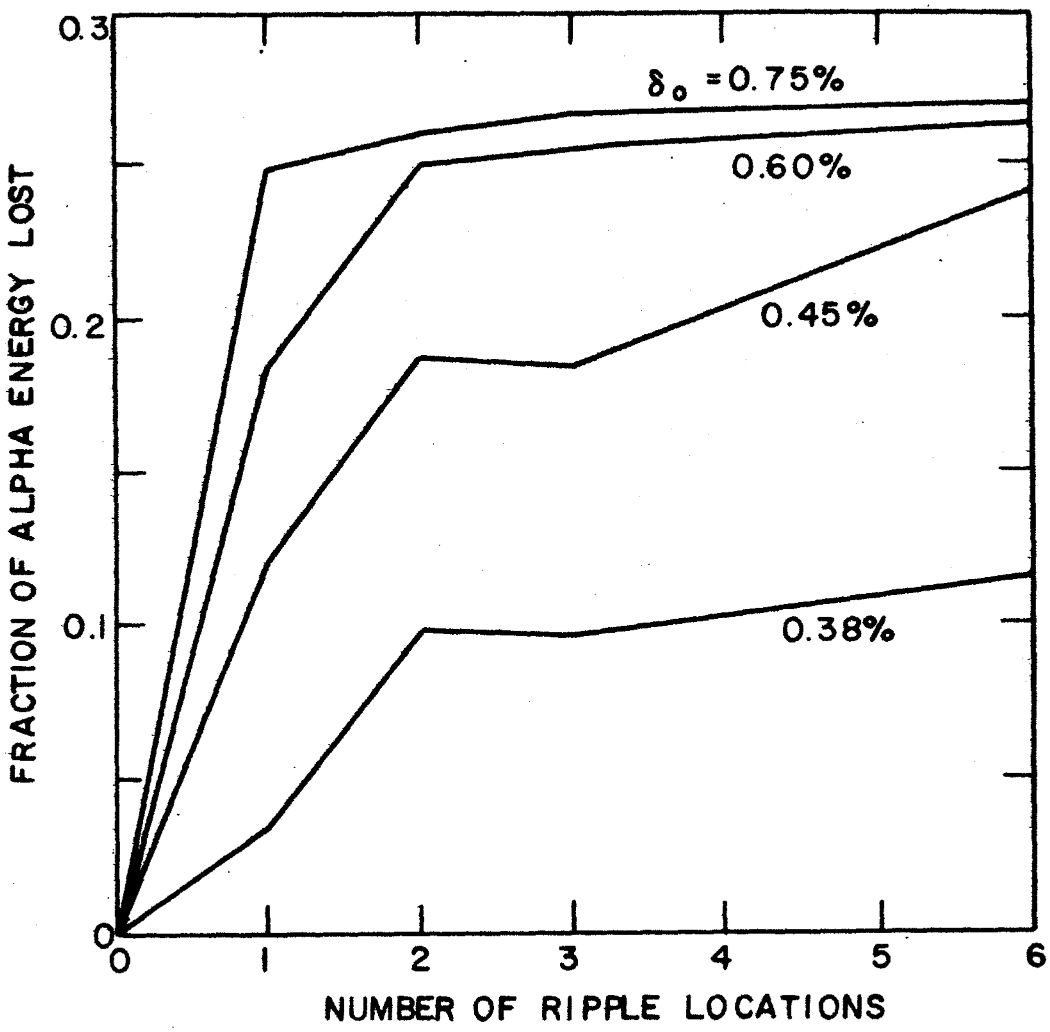

Figure 2-30 Fraction of the alpha energy lost in presence of vertically asymmetric TF ripple. δ_o is the peak-to-peak ripple on the magnetic axis.

ripple magnitude. The average resistive dissipated power in the ripple coils is estimated to be 5 to 10 MW.

It may happen that the $n\tau_E$ of the HFCTR is several times larger than the minumum value required for ignition at the desired operating temperature. In that case it will not be possible to determine an equilibrium point if $Z_{eff} \sim 1$, inasmuch as F_α cannot be reduced below about 0.70. Although the plasma density could always be lowered until the confinement time is the minimum required for ignition, the penalty to be paid is a corresponding drop in fusion power density and total power output. By enhancing the plasma radiation loss, however, it is possible to find an equilibrium operating point even with exceedingly large $n\tau_E$ values. (Here τ_E refers only to non-radiative losses). The most appropriate means of enhancing radiation is by the addition of a gas which is readily removable from the torus. This gas should also have a large atomic number in order to minimize depletion of reacting ions, and thus have a minimum effect on the fusion power density. The most suitable candidate appears to be xenon ($Z = 54$), for which a concentration of approximately 0.001 prevents ignition even when $\tau_E = \infty$ [42]. At this concentration, the fusion power density is still 90% of its magnitude at $Z_{eff} = 1$. A typical concentration of xenon may be 3×10^{-4}, which would give $\Delta Z_{eff} = 0.75$. The flux-swing for maintaining the current during the burn would have to be increased accordingly.

A possible control procedure then is to add sufficient xenon so that an equilibrium operating point is attained, with $F_\alpha \approx 0.90$ to 0.95. Temperature control near this operating point is effected by regulating F_α with the variable ripple system.

Several issues must be investigated further before ripple control can be judged feasible. For example:

(a) It must still be demonstrated experimentally that a toroidal ripple-field preferentially extracts energetic alpha particles.

(b) The enhanced first wall damage caused by escaping alpha particle bombardment must be investigated.

(c) The ripple-field diffusion time through the blanket and hot plasma must be known. If the diffusion time, τ_B, is larger than τ_r, then this control scheme is not viable.

2.5.2 Refueling Control

The plasma temperature might be regulated by adjusting the rate at which cold fuel is injected into the plasma. Cold fuel injection provides an additional power sink, P_F, with

$$P_F = 3\ T\ S_F \tag{2.65}$$

and S_F the refueling rate.

Like ripple control, several issues require further investigation before refueling control can be deemed acceptable. For example:

(a) The particle diffusion time and recycling rate must be known. These values determine whether cold fueling can be used without increasing the plasma density to undesirable levels.

(b) The time it takes cold fuel particles to reach the center of the plasma, τ_F, must be known. If this time is very long compared to the thermalization time, then only plasma surface cooling can be expected.

2.5.3 Active Feedback

Whatever thermal control or combination of controls is finally decided upon, it is almost certain to be integrated into an active feedback loop. An example of a simple feedback that uses both ripple and refueling control has been designed at the Charles Stark Draper Laboratory for the HFCTR and is described in Appendix J. Based on this feedback system a number of observations are apparent.

(a) If $\tau_B \gtrsim \tau_r$, then ripple control is largely ineffective.

(b) If $\tau_B \sim \tau_F$, then ripple control has an inherently faster response time than refueling control. This is because ripple control acts directly on the suprathermal alpha population, whereas refueling control does not.

(c) If ripple control is used as the dominant control mechanism and $\tau_B < \tau_r$, then the power supply requirements for the ripple coils should not be unreasonable. This is based on Figures 2-31 and 2-32, where the maximum current and voltage required for the ripple power supplies is plotted as a function of τ_B. These curves are parameterized in temperature perturbation (i.e. $\frac{\Delta T}{T_o}$) and are generated by assuming only 2 ripple sites need be activated. It should be noted that maximum ripple coil current has been clamped at 1.8 MA in the simulator.

2.5.4 The Onset of MHD Modes

Even without active thermal stabilization, an upper limit to a temperature runaway could possibly be established by the onset of MHD ballooning modes [20] when the plasma beta exceeds 5%. These modes are expected to re-

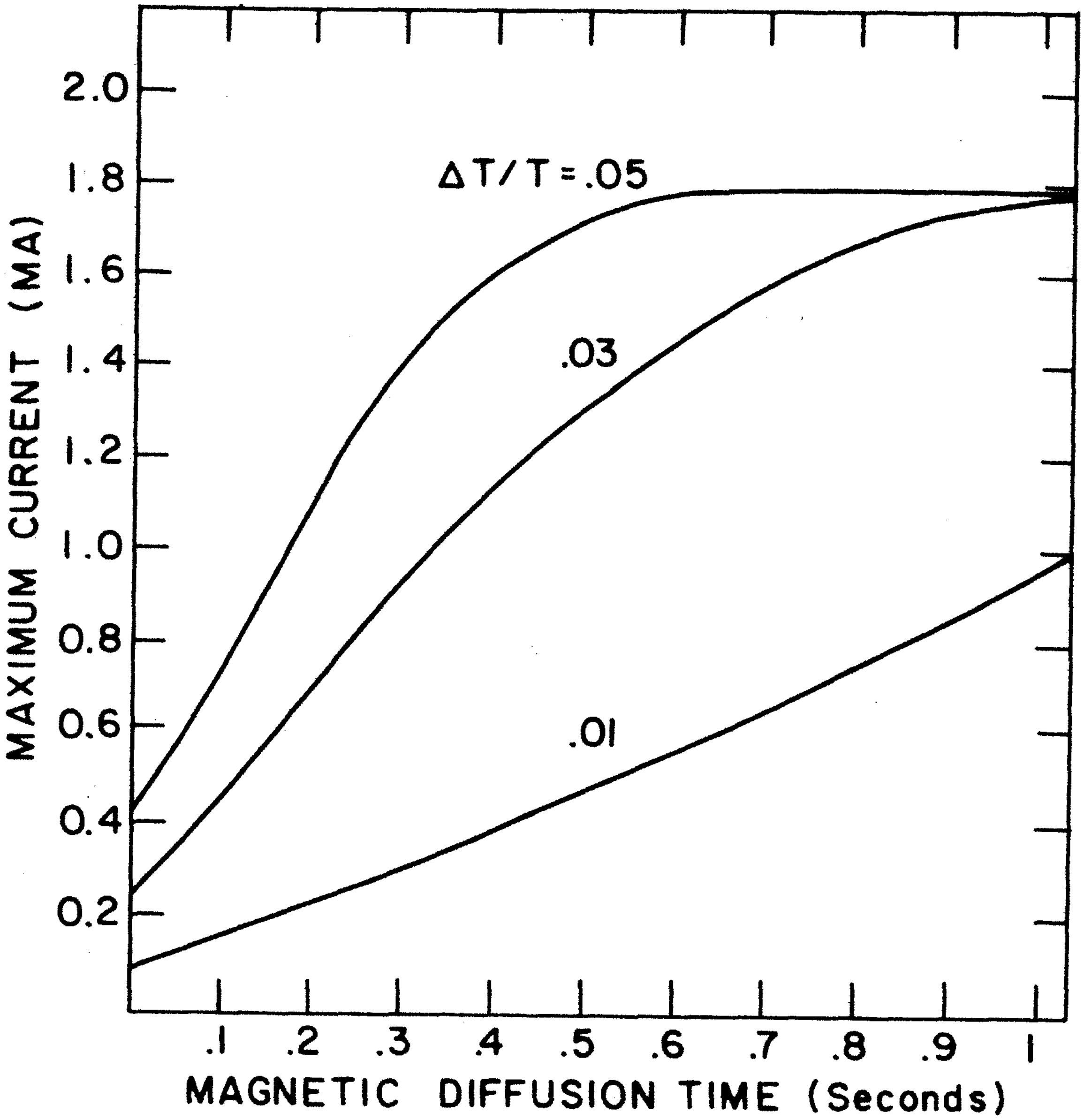

Figure 2-31 Maximum Ripple Control Coil Currents vs. Plasma Magnetic Diffusion Times and Initial Temperature Excursions

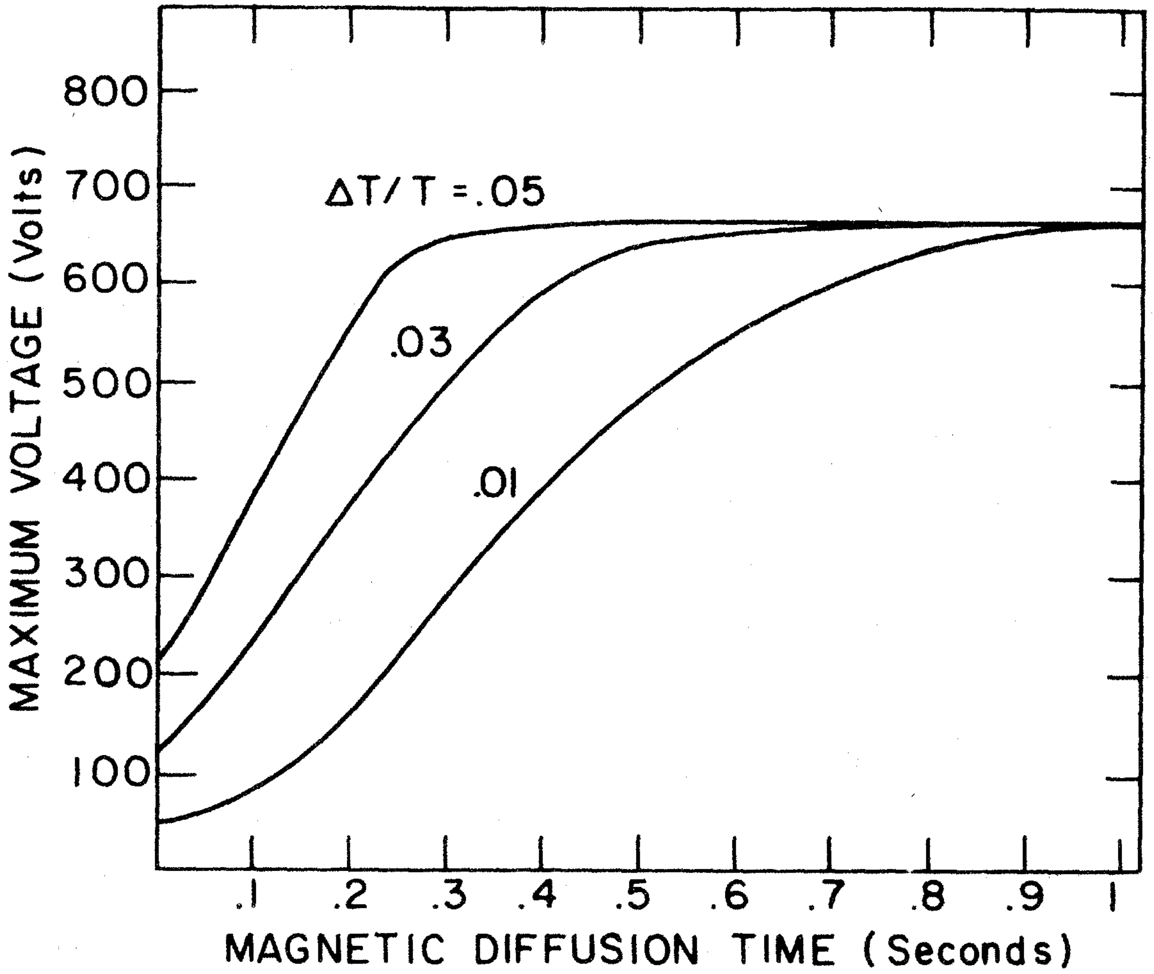

Figure 2-32 Maximum Ripple Control Coil Voltage vs. Plasma Magnetic Diffusion Times and Initial Temperature Excursions

sult in enhanced heat diffusion, and thus effectively introduce an unfavorable temperature dependence on confinement time.

2.6 PLASMA FUELING

There are two possible ways of fueling an HFCTR: gas puffing and/or pellet injection.

2.6.1 Gas Puffing

Several tokamak experiments have demonstrated the efficacy of using gas puffing to build up the plasma density. At present the physical processes involved in this fueling approach are not understood. However, simulations show that the Ware pinch coupled with anomalous particle transport near the edge could be responsible for the density buildup. Whether gas puffing will be feasible for the HFCTR is still very much an open question. A more detailed discussion of this fueling approach is presented in Appendix D.

2.6.2 Pellet Injection

Injecting small spherical pellets (diameter ~ 0.1 cm) at high velocity is an alternative fueling approach. The ORMAK experiment has used this fueling technique with considerable success [43]. The fueling experiments were done for low density plasmas. However recent theoretical work suggests that the ablation rate will not change significantly for high density plasmas [44].

One of the major questions about pellet injection is whether a reliable rapid-fire injector can be developed. For the HFCTR as many as 500 pellets/second must be injected into the plasma during start-up.

REFERENCES - SECTION 2

[1] STACEY, W. M., et al., Tokamak Experimental Power Reactor Conceptual Design, ANL/CTR-76-3, August 1976.

[2] STEINER, D., et al., ORNL Fusion Power Demonstration Study: Interim Report ORNL-TM-5813, March 1977.

[3] COHN, D. R., PARKER, R. R., and JASSBY, D. L., Nuclear Fusion 16 (1976) 31.

[4] JASSBY, D. L., COHN, D. R., and PARKER, R. R., Nuclear Fusion 16 (1976) 1045.

[5] FREEMAN, R. L., et al., 6th International Conference on Plasma Physics and Controlled Nuclear Fusion Research (Proc., Berchtesgaden, FRG, 1976) Paper IAEA, CN-35/A1, A2, A3, A4, A5, A6, A10-3, A15.

[6] BOL, K., et al., in Plasma Phusics and Controlled Nuclear Fusion Research (Proc. 5th Int. Conf., Tokyo, 1974) 1, IAEA, Vienna (1975) 83.

[7] ARTSIMOVICH, L. A., et al., Nucl. Fusion Supplement (1972) 41.

[8] VINOGRADOVA, N. D., et al., Nucl. Fusion Supplement (1972) 203.

[9] Alcator Group, Francis Bitter National Magnet Laboratory Quarterly Progress Report, QPR-FY-77-3, 1977.

[10] STACEY, W. M., Nuclear Fusion 15 (1975).

[11] POST, R. F., Plasma Physics 3 (1961).

[12] HOPKINS, G. E., USAEC Conf.-721111 (1972).

[13] KESNER, J. and CONN, R. W., Nuclear Fusion 16 (1976).

[14] GLASSTONE, S. and LOVBERG, R., "Controlled Thermonuclear Reactions", Van Nostrand Co., Princeton, New Jersey, 1960.

[15] JENSEN, R. V., POST, D. E., JASSBY, D. L., Princeton Plasma Physics Labortory Report, PPPL-1350 (1977).

[16] MANHEIMER, W. M., "An Introduction to Trapped-Particle Instability in Tokamaks", ERDA Critical Review Series, TID-27157, Washington (1977).

[17] STACEY, W. M., et al., Tokamak Experimental Power Reactor Conceptual Design, ANL/CTR-76-3, p. C-6, August 1976.

[18] MUKHOVATOV, V. S., SHAFRANOV, V. D., Nuclear Fusion 11 (1971) 605.

[19] CALLEN, F. D., DORY, R. A., Phys. Fluids 15 (1972) 1523.

[20] TODD, M. M., et al., Phys. Rev. Lett. 38 (1977) 826.

[21] METZ, M. D., Science Vol. 192 (1976) 1320.

[22] MCALEES, D., ORNL-TM-466 (1974).

[23] KREISCHER, D. E., M.I.T. Master Thesis, unpublished (1977).

[24] M.I.T. Alcator Group, 7th European Conference on Plasma Physics, Lausanne, Sept. 1975.

[25] POST, D. E., et al., Princeton Plasma Physics Laboratory Report PPP-1352 (1977).

[26] MURAKAMI, M., et al., Nucl. Fusion 16 (1976) 347.

[27] GIBSON, A., Nucl. Fusion 16 (1976) 546.

[28] BERRY, L. A., et al., in 6th International Conference on Plasma Physics and Controlled Nuclear Fusion Research, Berchtesgaden (1976), paper IAEA-CN-35/A4-1.

[29] GREEN, J. M., et al., Phys. Fluids 14 (1971) 671.

[30] KULSRUD, R. M., et al., Phys. Rev. Lett. 31 (1973) 690.

[31] VLASENKOV, V. G., et al., Nucl. Fusion 13 (1973) 509.

[32] SWEETMAN, D., Nucl. Fusion 13 (1973) 157.

[33] COHEN, S. A., Princeton Plasma Physics Laboratory Report, MATT-1171 (1975).

[34] PARKER, R., et al., paper presented at the Workshop on Plasma Fueling, Princeton, New Jersey (Nov. 1977).

[35] HUGHES, M. H., et al., Vull. Am. Phys. Soc. 22 (1977) 1092.

[36] SCHIVEL, J. F., Princeton Plasma Physics Laboratory Report, PPPL-1342 (1977).

[37] JASSBY, D. L., TOWNER, H. H., Trans. Am. Nucl. Soc. 24 (1976) 56.

[38] GOLDSTON, R. J., JASSBY, D. L., in Proceeding of the 3rd International Meeting on the Theoretical and Experimental Aspects of Heating of Toroidal Plasmas (Grenoble, 1976), vol. 1, I-8.

[39] JASSBY, D. L., *et al*., Princeton Plasma Physics Lab. Rep. PPPL-1300 (1977).

[40] JASSBY, D. L., Princeton Plasma Physics Lab. Report (1978).

[41] GLASSTONE, S., and LOVBERG, R. H., "Controlled Thermonuclear Reactions", (Van Nostrand, Princeton, N.J. 1960) p. 20.

[42] JENSEN, R., POST, D. E., JASSBY, D. L., Nucl Sci. and Engin. 65 (1978) 282.

[43] MILORA, S., FOSTER, C. A., ORNL-TM-5776 (1977).

[44] POLITZER, P. A., THOMAS, C. E., "Magnetic Shielding Effects in Pellet-Plasma Interactions", 1978 Fusion Fueling Workshop, Princeton, N.J. (Nov. 1977).

3. MAGNET SYSTEM

3.1 DESIGN FEATURES

The basic magnet system design is guided by the need to deal with the large forces created by the high field operation and the requirement that the magnet system be modularized in order to facilitate disassembly and maintenance. Additional constraints are that the pulse power requirements, the power dissipation resulting from copper coil operation, and the refrigeration losses in the superconducting magnet portion be kept within reasonable bounds.

The magnet system design which has been developed to meet these guidelines is shown in Figure 3-1. It differs from conventional designs in a number of ways:

(1) Forces between diametrically opposed toroidal field (TF) D coils are supported at the top and bottom of the trunk by means of circular end caps. As a result, the tensile force transmitted to the center straight sections of the toroidal field coils is greatly reduced. This makes possible a compact design while keeping the maximum strain in the superconductor to less than 0.1%. This is a conservative value, since experiments [1,2] show that strains of 0.2% are possible. The toroidal field coil conductor is shown in Figure 3.2 [3].

(2) The primary equilibrium field (EF) coils, i.e. the dipole coils, are DC, superconducting, and continuously operating. During start-up and shut-down, the changing EF is provided by driving a copper coil system to oppose the DC dipole coils. In addition,

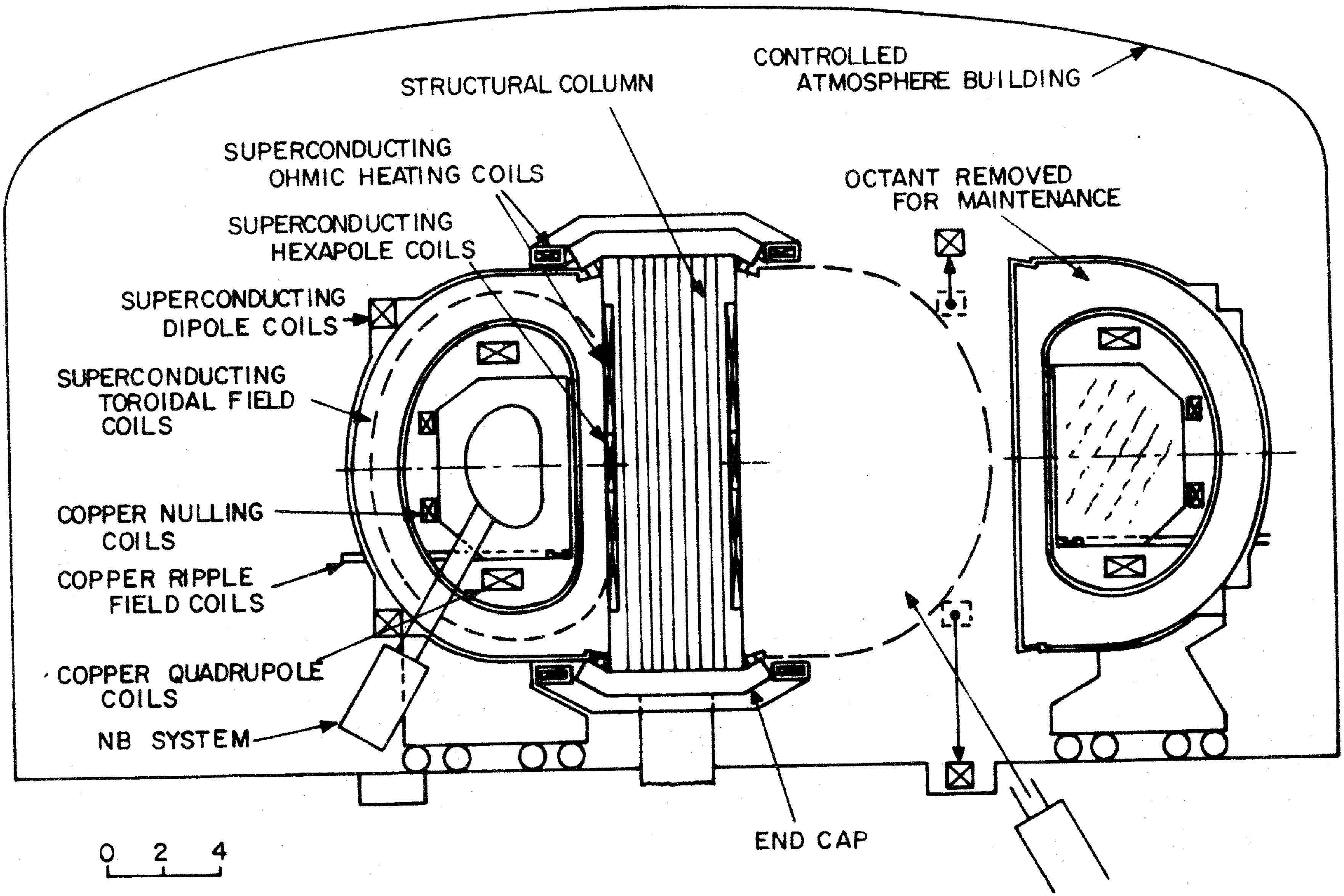

Figure 3-1 Elevation view of HFCTR showing all magnet systems.

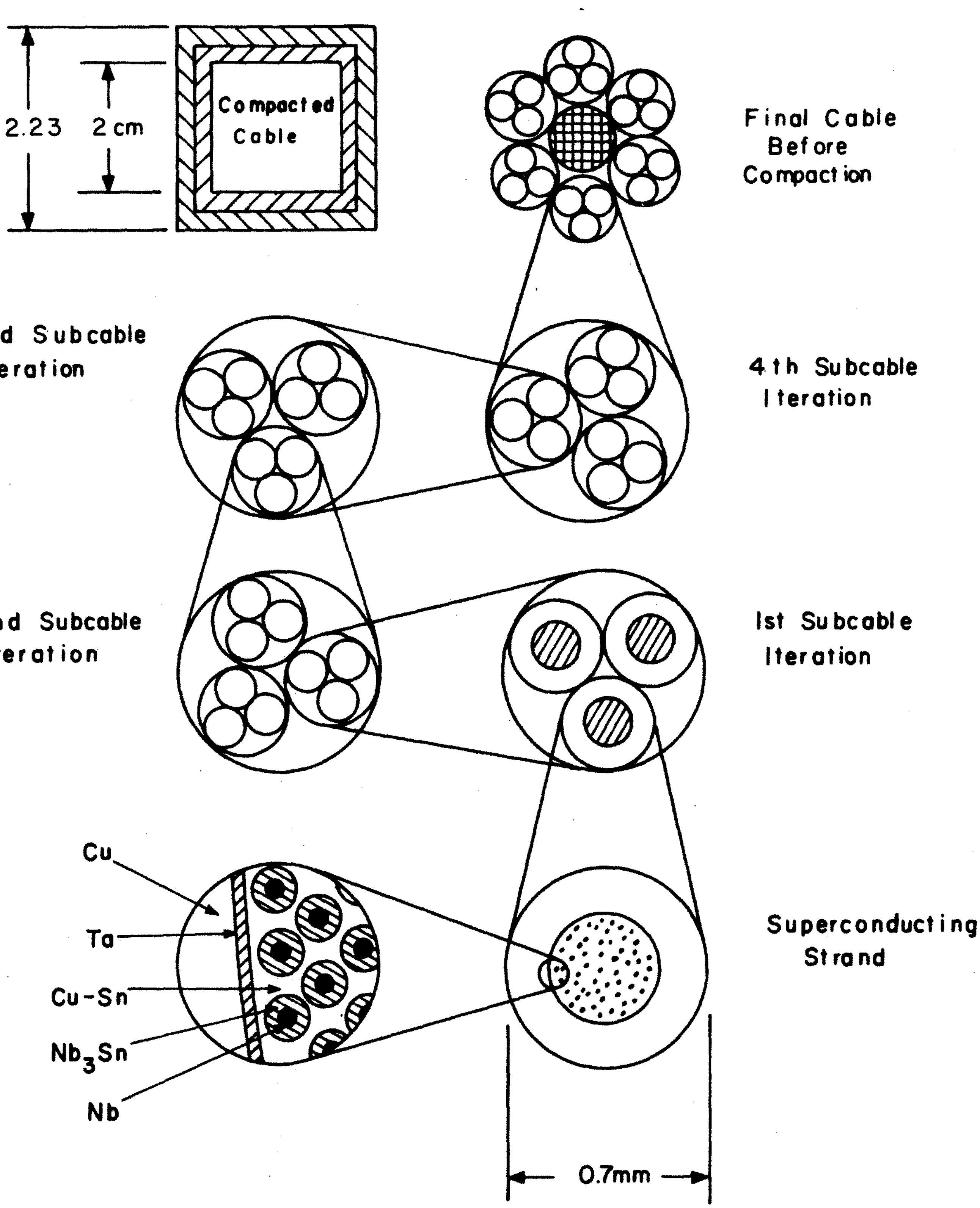

Figure 3.2 Conductor configuration

the nulling field (NF) is limited to the volume immediately surrounding the plasma. This EF arrangement greatly minimizes the pulsed power and stored energy requirements.

(3) The NF coils and an additional pair of EF coils (i.e. the quadrupole coils) are copper and located inside the toroidal field coils. They are segmented with a short section in each octant and have overlapping pressure contacts joining each segment. All other coils are superconducting and separately contained and can be moved away for module disassembly.

(4) Another vertical field coil (VF) system, is used for plasma shaping. It is superconducting and located in the core. This coil is separately energized allowing independent control of the plasma shape. The main ohmic heating (OH) coil is also located in the core. Supplementary coils adjacent to the circular reaction rings provide field compensation to decouple the OH field from the plasma.

In general all structural assemblies will need to be laminated to reduce eddy current heating and allow flux penetration during the initial pulsing. This is particularly true of the reaction rings, where it may be necessary to use nonconducting material to prevent a repulsive reaction to the ohmic heating field pulse.

3.2 TOROIDAL FIELD COIL DESIGN

3.2.1 Basic Design Features

The proposed toroidal field coil shape and design ensure that each component performs a necessary function under the combined operating conditions of toroidal field and poloidal field loading. The basic coil shape is that of a D-shaped winding path within the specified dimensions, as shown in Figure 3-3. The inner straight leg of the coil has a trapezoidal cross section, consisting of segmented plates with grooves for locating the conductor, bolted together to form an integral structure. The outer leg of the coil has a retangular cross section of plate segments bolted together. This rectangular cross section, however, has a trapezoidal winding cross section as shown in Figure 3-3 for ease in manufacturing and winding of the coil.

The D-shaped winding was chosen to obtain the advantage of constant tension over the entire coil circumference. Another major advantage of the D-shape is that the straight leg is available to support the high centering force which dominates the forces in toroidal field coils and for ease in manufacture and assembly.

The selected coil design is a pancake configuration consisting of overlapping segmented plates as shown in Figure 3-4. Overlapping of the pancake segments is arranged so that the splits at any particular location occur in only every third pancake as shown in Figure 3-4. This arrangement reduces the amount of load which must be transfered through the bolts without exceeding the available plate sizes. Overlapping of the plates enables the entire coil to be held together by bolts passing through the plates.

TABLE 3.2-I

HFCTR TOROIDAL FIELD COIL MAJOR PARAMETERS

Number of Coils	16
Current in Each Coil	13.9 MA
Peak Field on Winding	13.1 T
Coil Vertical Bore	10.5 m
Coil Horizontal Bore	6.5 m
Number of Turns	1200
Current per Conductor	11.75 kA
Conductor Width (outside of insulation & jacket)	2.088 cm
Conductor Height (outside of insulation & jacket)	2.088 cm
Conductor Jacket Thickness	0.089 cm
Conductor Insulation Thickness	0.055 cm
Coil Build (inner leg)	1.0 m
Coil Build (outer leg)	1.27 m
Number of Pancakes	27
Pancake Structural Material	310 S
Number of Splits per Pancake	9
Number of Slots per Full Plate	6
Plate Thickness	5.179 cm
Number of Bolts Between Overlapping Splits	8
Number of Bolts Across Plate Width	
inner leg	6
outer leg	10
Bolt Diameter	2.54 cm
Bolt Material	A-286 40% Cold Worked

TABLE 3.2-II

HFCTR TOROIDAL FIELD COIL STRESSES

	Analysis Type	
	Structure Only (MPa)	Homogeneous (MPa)
Plate Tensile Stress		
inner leg	148	112
outer leg	147	126
Conductor Strain (strands)		
inner leg	0.072%	0.054%
outer leg	0.071%	0.063%
Conductor Jacket		
inner leg	148	109
outer leg	147	129
Bolt Bearing Stress		
inner leg	134	91.3
outer leg	289	120
Bolt Shear Stress		
inner leg	349	237
outer leg	750	311
Maximum Plate Stress Due to Centering Force		311
Maximum Slot Tooth Bending Stress		66.6

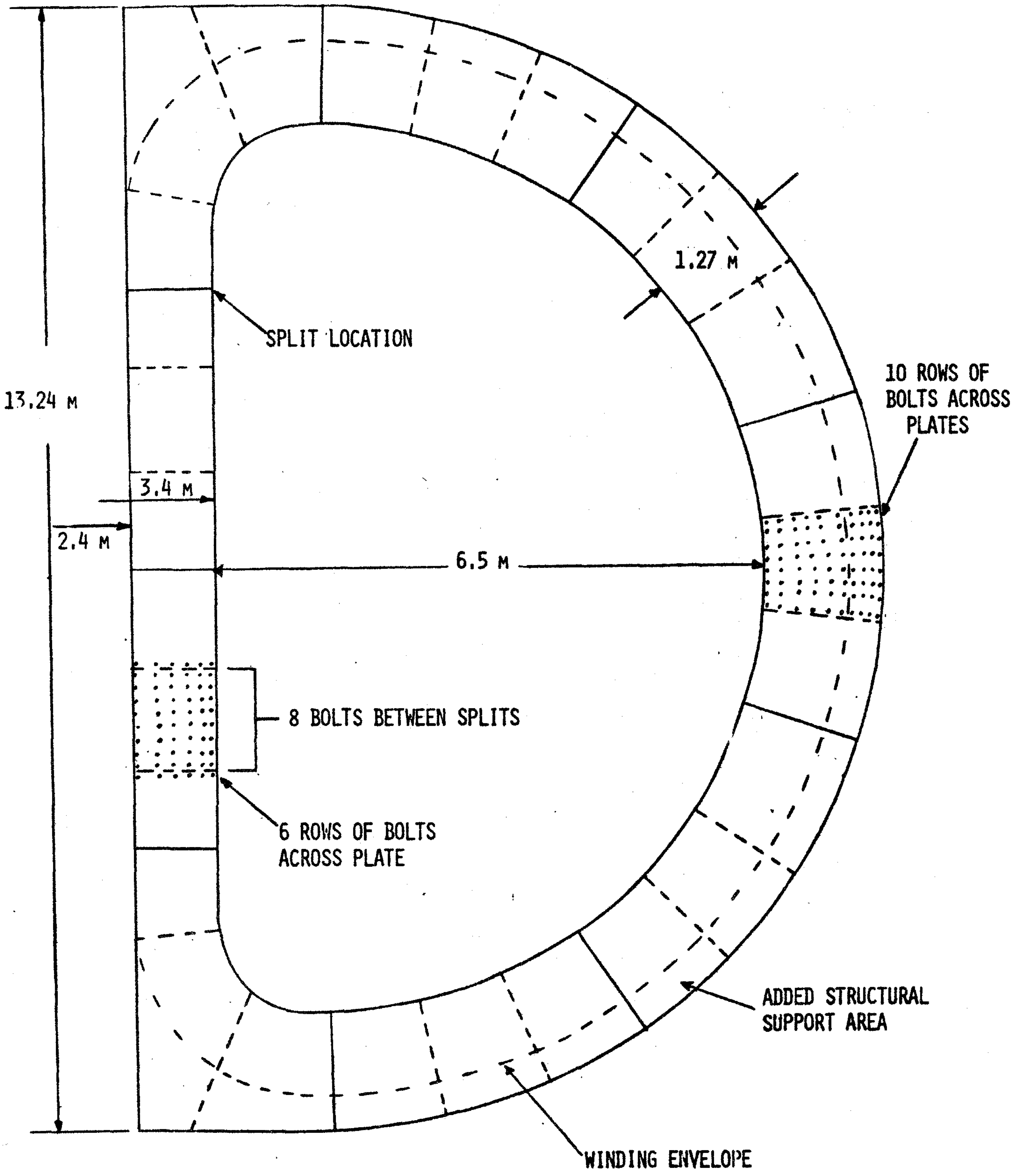

Figure 3-3 Proposed Toroidal Field Coil Design

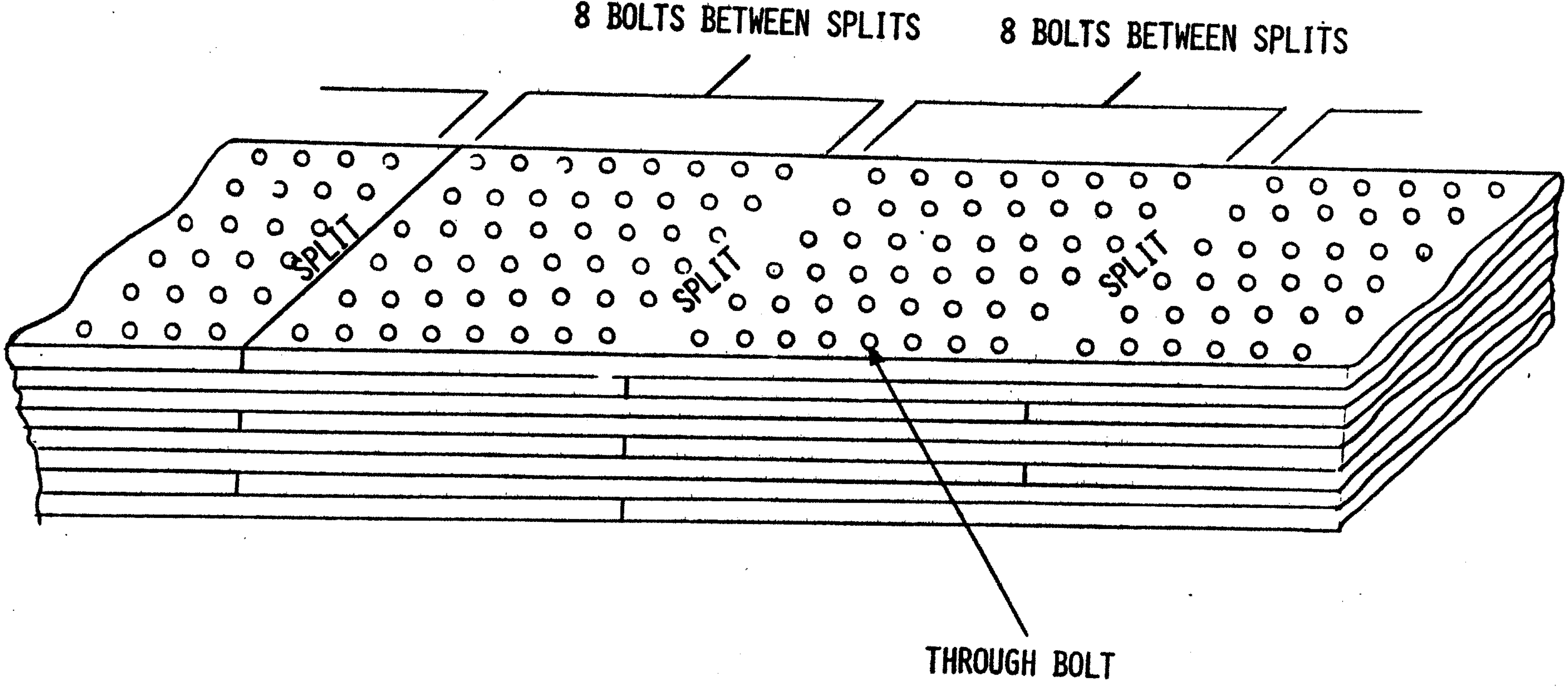

Figure 3-4 Bolt and Split Plate Arrangement

For a TF coil with a 10.5 m x 6.5 m bore, each of the coil pancakes will consist of 9 separate plate segments, as shown in Figure 3-3. The next two pancakes of the coil also consist of 9 segments but they are staggered so that the splits do not fall in line for a group of 3 pancakes.

The use of through bolts creates a homogeneous structure of plate segments. The inner leg of the coil has 6 rows of through bolts passing through the winding section of the coil at the inner and outer edges and across the center of the conductor winding region as shown in Figure 3-3. The outer leg of the coil consists of 10 rows of through bolts since the coil must carry the entire in-plane loading in contrast with the inner leg which shares its load with the center support cylinder. Bolt spacing for the outer leg is shown in Figure 3-3 with 6 bolts located through the winding as in the inner leg and 4 bolts located in the added structural area. These bolts help compact the layers of plates and maintain the plate segment as a continuous structure under load.

The conductor is wound onto each layer within slots machined into the faces of each plate. A specified number of conductors are aligned in each slot as shown in Figure 3-5, with each of the slots separated by a tooth. The tooth separating the slots and the number of conductors in each slot are based on the number of conductors required within the coil to provide a maximum field of 13 tesla. The design consists of slots machined in both sides of a plate. Four slots on the inner bore of the coil have four conductors per slot while the two slots on the outer edge of the the pancake have eight conductors per slot. This arrangement reduces and equalizes the loading on both the individual conductors and slot teeth

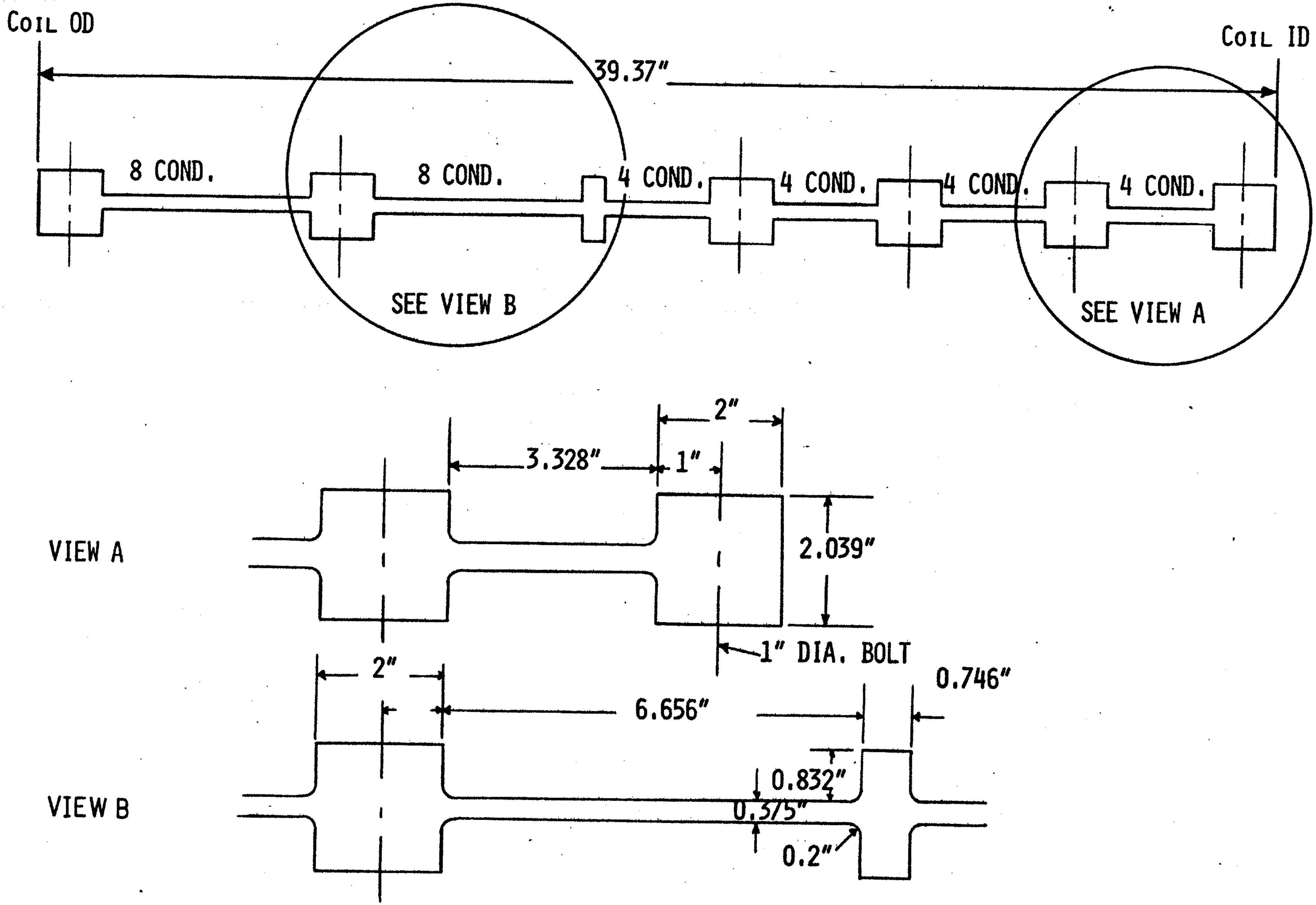

Figure 3-5 Slot, Bolts and Conductor Distribution

through the coil radial thickness. The slot teeth are wide enough to accommodate the through bolt passage to adjoining layers. Where there is no bolt passage, the tooth is wide enough to maintain a safe design stress margin when loaded by the conductors. The slot teeth therefore, serve as a method of restraining excessive motion of any conductor within the coil and to minimize the load on the conductors.

3.2.2 Mechanical Stress Analysis

3.2.2.1 Coil Forces

The principal forces that a toroidal field coil will experience are:

- Thermal Forces
- Toroidal Field Forces (in-plane forces)
- Poloidal Field Forces (out-of-plane forces)

Thermal loading of the coil and structure is due to differential contraction of different materials from room temperature to the operating temperature of 4 K. Materials with similar thermal coefficients should be used to avoid excessive strain in coil components. Coil structural material should not cause an initial tensile strain in the superconductor. A compressive strain on the conductor caused by cooldown is advantageous since it will act to decrease the net strain in the conductor during normal operation of the coil. Table 3.2–III compares various materials considered for use in a coil design.

Table 3.2-III indicates that if a conductor of Cu + Nb_3Sn with a 4:1 ratio were used, the strain on the conductor due to differential thermal contraction would be -0.05% and -0.14% for stainless steel 310 S and 2219-T87 aluminum respectively. This comparison indicates the

TABLE 3.2-III

COMPARISON OF MATERIAL THERMAL STRAIN

Material	$\% \frac{\Delta L}{L_o}$ (4 K)	Δ% 310 S	Δ% 2219-T87
Cu	-0.29	+0.10	-0.08
Cu + Nb_3Sn (4:1)	-0.23	-0.05	-0.14
310 S	-0.28	——	-0.09
2219-T87	-0.37	+0.09	——

possible advantage of using aluminum as a structural material. However in a high field compact coil, the stresses in an aluminum material would not be acceptable. Therefore, stainless steel 310 S has been selected as the structural material since high thermal stresses will not occur and its allowable stress is high.

The toroidal and poloidal forces applied to the coil are calculated by a computer code which approximates a conductor of general configuration by circular arcs and straight segments, and calculates magnetic field by a three-dimensional integration of the Biot-Savart Law.

As shown in Figure 3-6, the forces developed in the coil act outward from the coil and in the same plane. The greatest force on the coil will be exerted on the inner straight leg of the D and will gradually decrease to a minimum force at the center of the outer leg. Therefore, an unbalanced centering force is present in the horizontal direction and must be supported. To maintain a symmetric coil arrangement a bucking cylinder and/or arch binding will be required to position the coils. The net centering force for the D-shaped coil is 4.65×10^5 lb/in (81.4 MN/m) along the coil straight leg length.

Summing the moments about the coil caused by the loading shown in Figure 3-7, the coil tensile loads on the inner and outer leg are 1.875×10^2 MN (42.15×10^6 lb) and 2.214×10^2 MN (49.78×10^6 lb) respectively.

The out-of-plane force tends to create a twist about the coil array centerline, creating a moment on each toroidal field coil about its horizontal midplane. This overturning moment in the coil must be braced so that tilting of the coil will not cause mechanical failure or a detrimental effect on the

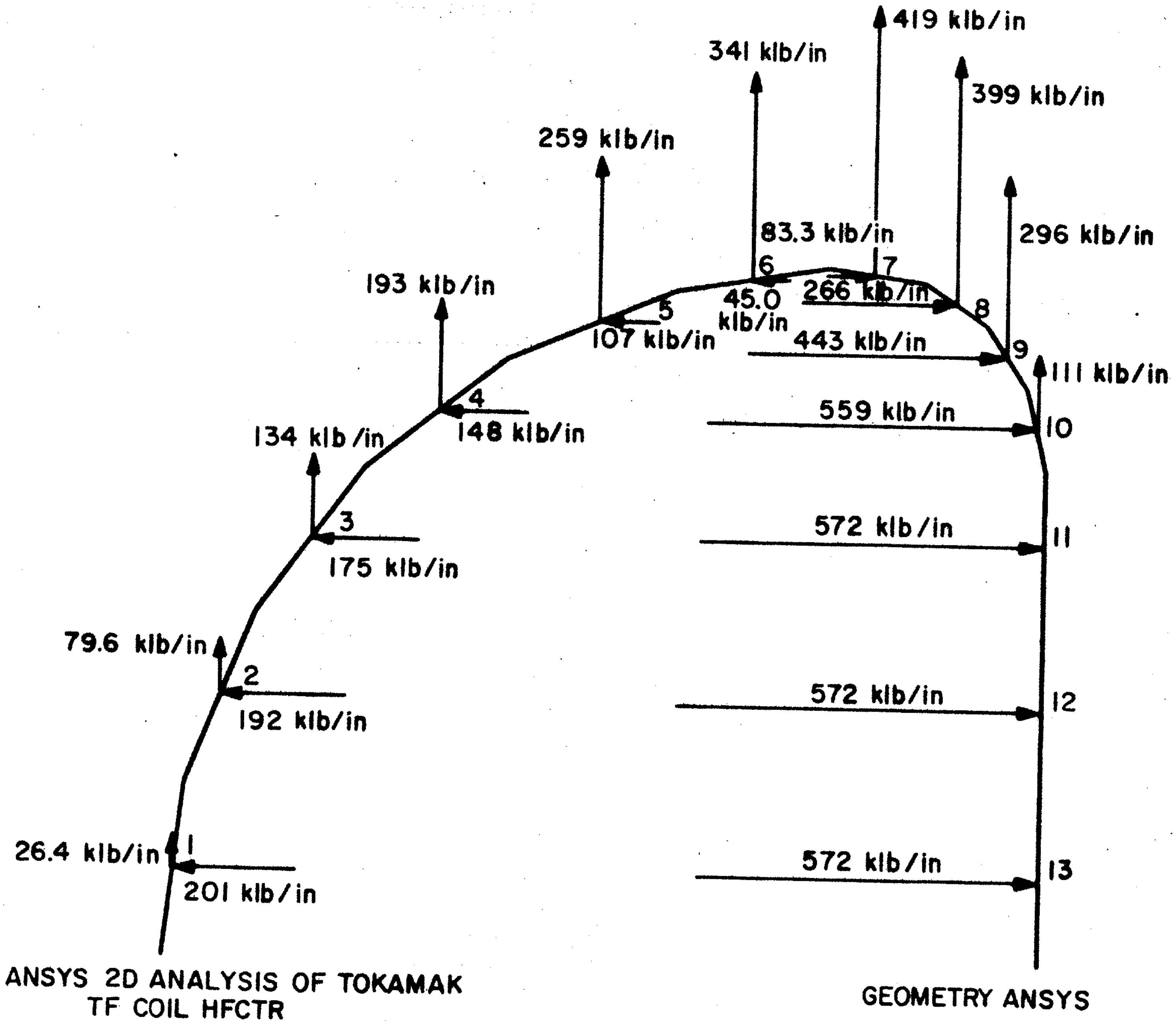

Figure 3-6 Inplane bending forces acting on TF coil.

magnetic field at the plasma. The out-of-plane forces are shown in Figure 3-7 with antisymmetric forces on the bottom half of the coil. The method of supporting out-of-plane forces is described in Chapter 5.

3.2.2.2 Coil Integrity

The overlapping segmented distributed pancake arrangement of the toroidal field coils was selected after initial calculations which predicted the ability of the bolts and plates to withstand the calculated stresses. The direct tensile stress in the plates and conductors is

$$\text{stress} = \frac{\text{Tensile force}}{\text{Effective structural area}} \tag{3.2.1}$$

The tensile force on the coil due to toroidal field loading was calculated for the inner and outer legs to be 1.875×10^8 N (42.15×10^6 lb) and 2.214×10^8 N (49.78×10^6 lb) respectively.

Since the coil is a composite structure, consisting primarily of the conductor strands, conductor jacket and structural plates an effective elastic modulus may be found for determining the stress on the individual components. This analysis assumed that no slippage or compaction of the conductor strands occurs during TF coil charging that would cause a change in the effective elastic modulus of the composite structure.

Although this is a reasonable assumption, to be conservative, all calculations were performed with two models: one is an equivalent homogeneous structure and the other assumes that only structural steel carries the load.

(1) Structure Only Carrying Load:

From Figure 3-3, the structural areas of the inner and outer legs are 6,355 cm^2 and 15,100 cm^2 respectively. The direct tensile stresses on the inner and outer legs are 295 MPa (42,800 psi) and 147 MPa (21,270 psi) respectively. These values are well within the acceptable range for stainless

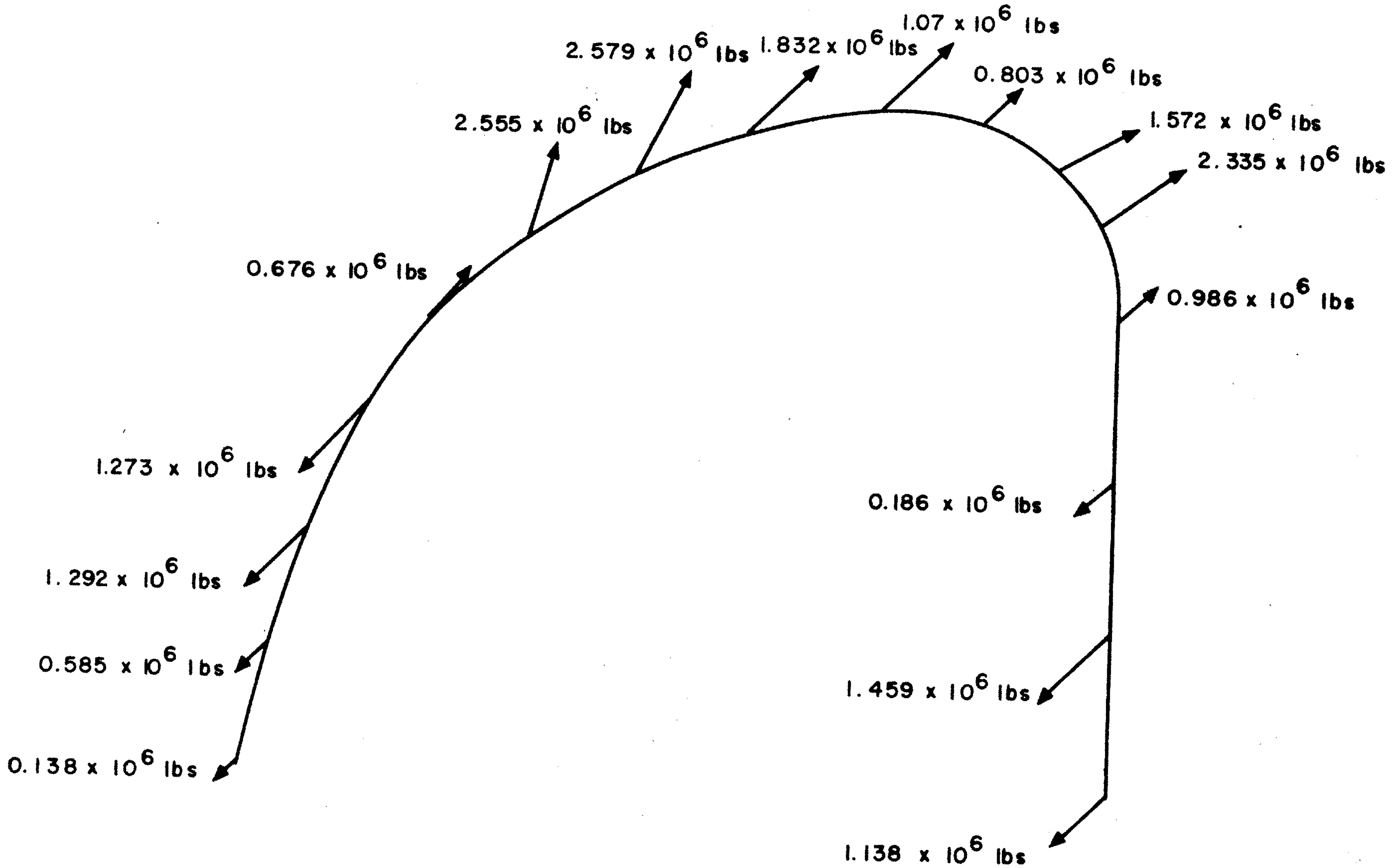

Figure 3-7 Out-of Plane Turning Forces Acting on TF Coil

steel 310 S with a yield stress of 814 MPa (118,000 psi). These calculations assumed that the entire toroidal field load is carried in the coil, when in fact 50% of the load on the inner leg of each coil is expected to be carried in the center support column. This will reduce the direct tensile stress on the inner leg to 148 MPa (21,400 psi). The direct stresses on the inner and outer leg are close to the same level, because of the increased size of the outer leg. (See Section 5.7.1.)

For the stainless steel structural material (E = 2.06×10^5 MPa or 29.9×10^6 psi) the structure strain is

$$\text{strain } (\varepsilon) = \frac{\text{stress } (\sigma)}{\text{elastic modulus } (E)} \qquad (3.2\text{-}2)$$

Substitution into equation 3.2-2 of the inner (50% load carrying) and outer leg stresses gives 0.072% and 0.071% strain respectively. The conductor strain on the inner and outer leg is assumed equal to that in the structure.

(2) Homogeneous Structure:

Since the coil is a composite structure, an effective modulus can be found for determining the individual stresses on the conductor strands, jacket and structure. The effective modulus is calculated by using the area ratios in equation 3.2-3 where a' is the ratio of an area to the total cross sectional area of the coil.

$$\begin{aligned} E_{\text{composite}} &= a'_{\text{structure}} E_{\text{structure}} \\ &\quad + a'_{\text{cond.}} E_{\text{cond.}} + a'_{\text{jacket}} E_{\text{jacket}} \end{aligned} \qquad (3.2\text{-}3)$$

Based on 1200 turns of conductor with 40% void and 0.089 cm (0.035 in) stainless steel (304 L) jacket, the composite modulus would be 1.84×10^5 MPa (26.75 × 10^6 psi). The composite coil stress on the inner leg (50% load carrying) is found from equation 3.2-1. For a total area of 9,353 cm^2 (1,449 in^2) the stress would be 100 MPa (14,540 psi). The stresses on the conductor strands, jacket and structure can be calculated by equation 3.2-4.

$$\text{Conductor Stress} = \frac{E_{\text{cond}}}{E_{\text{comp}}} \times (\text{Coil composite stress})$$

$$\text{Jacket Stress} = \frac{E_{\text{jacket}}}{E_{\text{comp}}} \times (\text{Coil composite stress}) \qquad (3.2\text{-}4)$$

$$\text{Structure Stress} = \frac{E_{\text{structure}}}{E_{\text{comp}}} \times (\text{Coil composite stress})$$

The conductor strand, jacket and structure stress in the inner leg are 63.7 MPa (9,235 psi), 109 MPa (15,870 psi) and 112 MPa (16,250 psi) respectively. The corresponding conductor strain is 0.054% in the inner leg.

The outer leg stresses for a composite structure are calculated in the same manner as was done for the inner leg. For a total area of 18,100 cm^2 (2,805 in^2) the coil stress is 122 MPa (17,740 psi). The composite modulus for the outer leg is calculated to be 1.95×10^5 MPa (2.83×10^7 psi) for a structural area of 1.51 m^2 (2,341 in^2). Substitution of the composite modulus and coil stress into equation 3.2-5 gives the conductor strand, jacket and structure stresses as 73.5 MPa (10,670 psi), 126 MPa (18,320 psi) and 129 MPa (18,760 psi) respectively. The corresponding conductor strain is then 0.063% in the outer leg.

(3) Coil Stresses Due to Centering Force:

From Figure 3-8, note that along the inner leg of the coil the outermost conductor slots (closest to the bucking cylinder) are loaded on the outermost tooth and not through the plate wall thickness. The other conductor slots will transmit the centering load through the plate walls and the bolts of the coil. The average slot loading for the outermost slot (slot #1 in Figure 3-8) is calculated by assuming that the magnetic field decreases linearly with radial distance from the maximum field point of the coil, as one moves toward the vertical center line. The maximum single conductor force occurs in slot #6 and is found by equation 3.2-5

$$\text{Maximum Conductor Force per Unit Length} = 5.68 \times 10^{-3} B_{max} \times I \qquad (3.2\text{-}5)$$

where

B_{max} = coil maximum field = 13.1 Tesla

and

I = conductor current = 11,583 Amp

The maximum conductor force is 1.51×10^5 N/m (862 lb/in). The total force for any slot is then found from the assumption of linearly decreasing force with distance in the coil straight section. In the outermost slot (slot #1 in Figure 3-8) the average conductor load equals 3.78×10^4 N/m (216 lb/in) and the total force per unit length on the eight conductors is 3.03×10^5 N/m (1,730 lb/in). The slot force for the next slot, #2, (8 conductors/slot) is 9.06×10^5 N/m (5,170 lb/in).

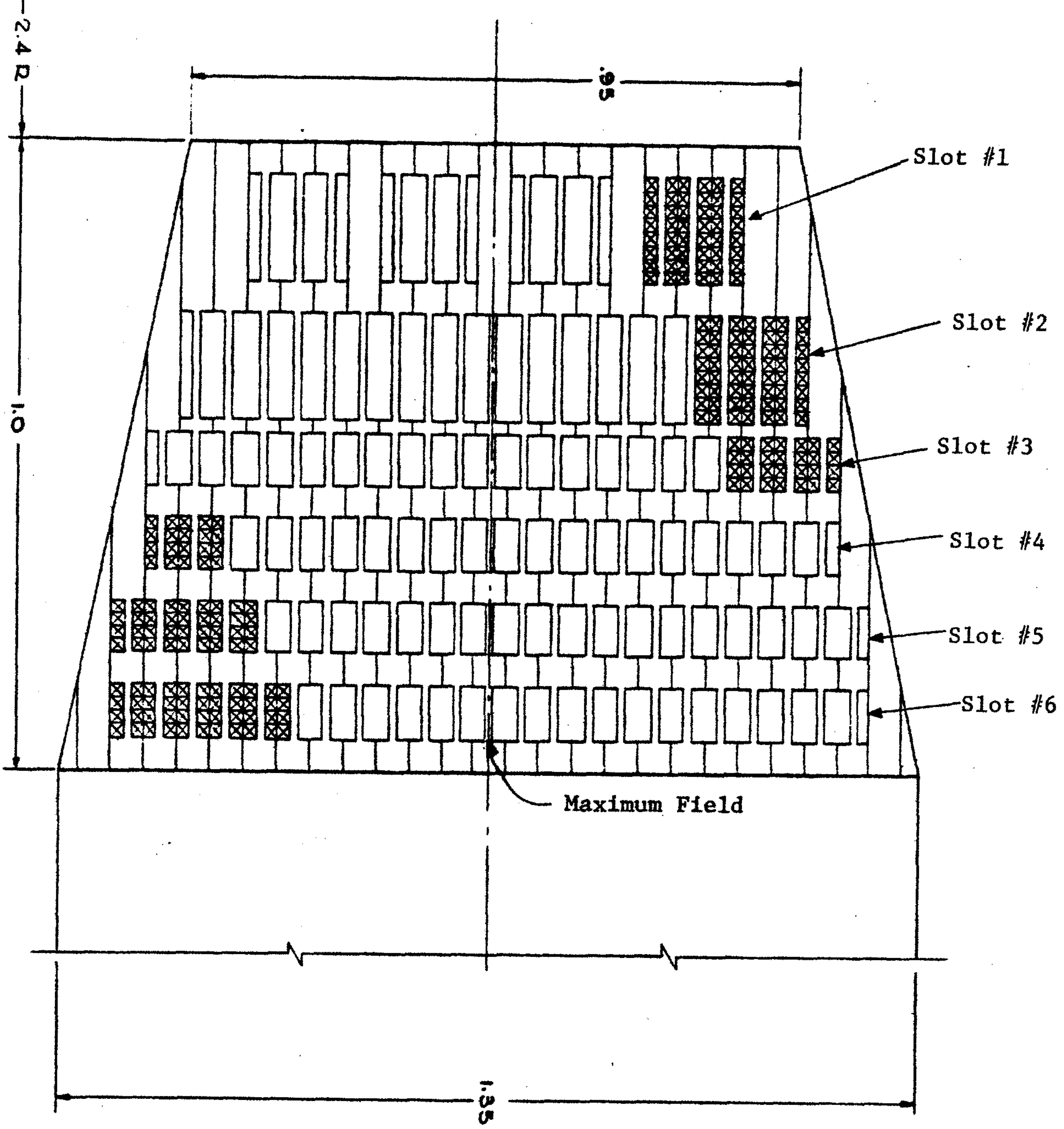

Figure 3-8 Coil Cross Section

The load carried in the plates (i.e. the plate thickness at the bottom of the slots where the plate is thinnest = 0.953 cm (0.375 in)) is the total centering load minus the load from the outermost slot. The total centering force per unit length is 76.9 MN/m (4.39×10^5 lb/in) and the load on the coil plates just before the outer tooth is 69.6 MN/m (3.975×10^5 lb/in). The maximum stresses in the plates due to the centering load occur in the plate thickness at the bottom of slot #1. The area per unit length is 4.48×10^{-1} m^2/m. Since vertical gaps have to be provided in the bucking cylinder for the OH coils, approximately only half of the straight leg length is supported. This is a conservative assumption, since some stress would be taken in bending by the outermost bolt tooth, and gives an approximate stress on a plate of

$$\text{Centering stress} = \frac{2\ (\text{centering load})}{(\text{structural area})\ (\text{unit length})} \tag{3.2-6}$$

Substitution gives a stress of 311 MPa (45,100 psi) which is within the acceptable range for 310 S stainless steel.

Repeating this procedure for a section through the next row of slots (slot #2 in Figure 3-6), the load is 35.2 MN/m (2.01×10^5 lb/in). The load carrying area per unit length is 0.181 m (280.5 in^2/m length). Using equation 3.2-6 and eliminating the factor of two correction, the stress is 194.5 MPa (28,200 psi). This value is well below that in the outermost slot. The plate stress for all other slots will be progressively smaller.

(4) Slot Tooth Stresses:

Each slot tooth must be capable of sustaining the sum of the loads of the conductors in the slot without excessive stresses. There are only two different size slot teeth in this design as shown in Figure 3-6. The conductor load is again assumed to be linear with distance from the outermost conductor to the innermost, with the maximum load being 1.51×10^5 N/m (862 lb/in).

The tooth bending stress is

$$\text{Bending stress } \sigma = \frac{6Fx}{bt^2} \qquad (3.2\text{-}7)$$

where: F is the conductor slot load on the tooth,

x is the moment arm (position of load application point),

b is the tooth length

and t is the tooth thickness.

The two slot tooth thicknesses are 5.08 cm (2 in) and 1.895 cm (0.746 in) and the slot teeth with maximum loading are those loaded by the conductors in slots #6 and #3 respectively, as shown in Figure 3-6. The bending stresses on these teeth are 14.2 MPa (2,060 psi) for slot #6 and 66.6 MPa (9,665 psi) for slot #3. Both of these stress levels are well below the acceptable limit for 310 S stainless steel. Shear stress on the teeth is even smaller and was ignored.

(5) Bolt Load Distribution (Inner Leg):

The bolt load distribution is calculated as a function of the arrangement of splits in the coil structure. Each coil has a split occuring in every third plate, as shown in Figure 3-4. This calculation is performed to determine the amount of load being transferred from the solid plate, adjacent to a split plate, through the bolt and into the split plate. The model used for this analysis is shown in Figure 3-9. For this analysis the bolt loads are shown in equation 3.2-8.

$$\begin{aligned} P_1 &= P \\ P_2 &= P_1 + \frac{1.5}{c}(P_1) \\ P_3 &= P_2 + \frac{1.5}{c}(P_2 + P_1) \\ P_4 &= P_3 + \frac{1.5}{c}(P_3 + P_2 + P_1) \end{aligned} \qquad (3.2\text{-}8)$$

The P subscript indicates the relative nearness of a bolt plane to a split plane, with P_1 being the total force on the plane of bolts nearest to a split. With the split arrangement shown in Figure 3-3, there are 8 bolts per row between split planes which indicates that the term P_4 from equation 3.2-8 would be the loading on the first bolt in this design. The term c used in equation 3.2-8 is the stiffness ratio of the bolts and plates.

$$c = \frac{k_{plate}}{k_{bolt}} \qquad (3.2\text{-}9)$$

The plate stiffness is

$$k_{plate} = \frac{A\ E}{L} \qquad (3.2\text{-}10)$$

where: L = spacing between bolts

E = elastic modules of plate

A = structural area cross section

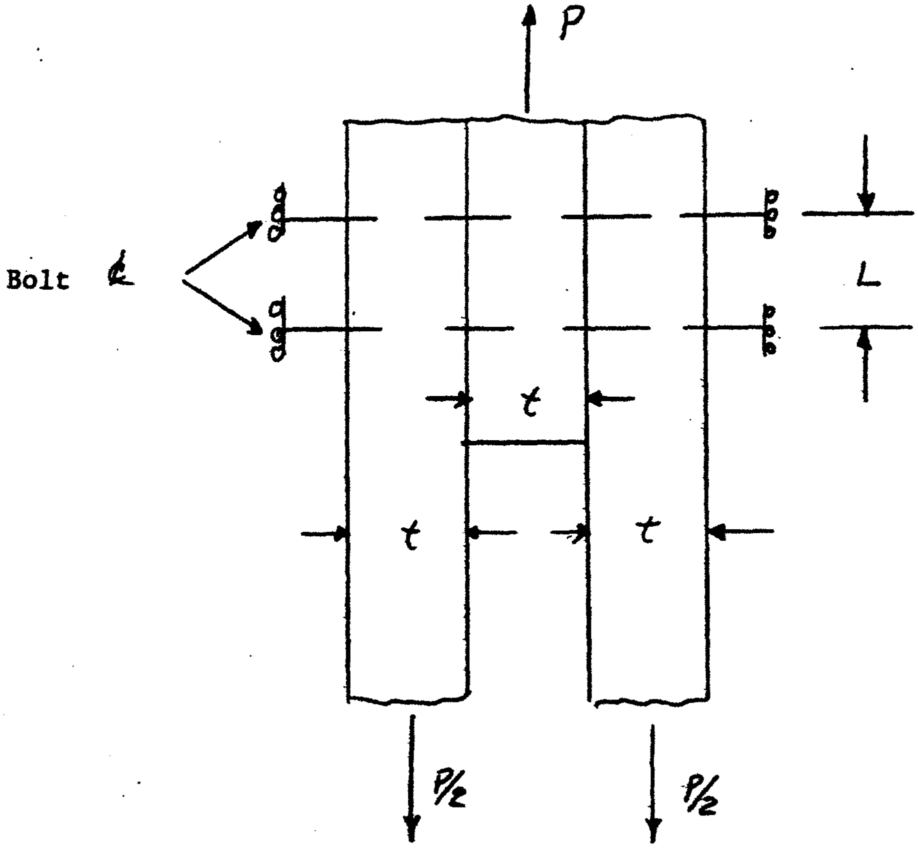

Figure 3-9 Bolt Load Distribution Calculation Model

Substitution of the proper values for the inner leg with a 12.7 cm (5 in) bolt spacing gives the plate stiffness as 3.79×10^4 MN/m (2.16×10^8 lb/in).

The bolt stiffness is calculated from the model shown in Figure 3-13 where t is the plate thickness and P is the load per plate. The total deflection of the bolt consists of the deflection due to bending and shear as shown in equations 3.2-11:

$$\text{bolt deflection due to bending } (\delta_{BB}) = \frac{1}{11.6}\frac{P_i t^3}{E\ I}$$

$$\text{bolt deflection due to shear } (\delta_{BS}) = \frac{P_i t}{2GA} \qquad (3.2\text{-}11)$$

where: I = moment of inertia for the bolts across the coil radial thickness = $N\,\frac{\pi d^4}{64}$

d = bolt diameter = 2.54 cm (1 in)

N = number of bolts across the radial thickness of the coil = 6 in the inner leg

A = area of the bolts = $N\,\frac{\pi d^2}{4}$

E = elastic modulus of bolt = 2.24×10^5 MPa (32.5×10^6 psi)

G = shear modulus of bolt = 8.07×10^4 MPa (11.7×10^6 psi)

The equivalent bolt stiffness is obtained from equation 3.2-12:

$$\frac{1}{k_{eq}} = \frac{1}{k_{BB}} + \frac{1}{k_{BS}}$$

where

$$k_{BB} = \frac{F}{\delta_{BB}} \qquad (3.2\text{-}12)$$

and

$$k_{BS} = \frac{F}{\delta_{BS}}$$

In the inner leg of the coil, the bolt stiffness is 1.85×10^3 MN/m (1.06×10^7 lb/in) and the stiffness ratio c is 20.4 from equation 3.2-9. The load in the first bolt for P_4 is found from the relationship $D = \frac{P_N}{\Sigma P_N}$, which is equal to 0.308. Therefore, the load transferred by the first bolt into the split plate is 0.308 P.

Repeating this procedure for the outer leg of the coil with the same bolt spacing between splits, but with increased plate area and 10 rows of bolts, the load transferred by the first bolt is 0.303 P.

(6) Bolt Stresses:

The bolt shear and bearing stresses were determined from the force distribution on the inner and outer legs of the coil. Since the coil stress was calculated for the two cases of structure only carrying load and a homogeneous composite coil, the bolt stresses were calculated for both cases.

With structure only carrying load, the stresses on the inner and outer legs are 148 MPa (21,400 psi) and 295 MPa (42,800 psi) respectively. The average loads per plate are 3.44 MN (7.74×10^5 lb) and 12.5 MN (2.82×10^6 lb), respectively. The load per bolt is calculated from equation 3.2-13:

$$F_{Bolt} = \frac{PD}{N} \qquad (3.2\text{-}13)$$

where: P = average plate load

N = number of bolt rows across coil thickness

D = bolt distribution

(% of total load carried in a row of bolts)

The bolt loads for the inner and outer coil legs are 1.77×10^5 N (3.97×10^4 lb) and 3.80×10^5 N (8.55×10^4 lb) respectively.

Bolt to plate bearing stress is then found from equation 3.2-14:

$$\sigma_{\text{Bearing}} = \frac{F_{\text{Bolt}}}{A_{\text{Bearing}}} = \frac{F_{\text{Bolt}}}{(\text{bolt dia})(\text{plate thickness})} \qquad (3.2\text{-}19)$$

The bearing stresses for the coil are then 134 MPa (19,490 psi) and 289 MPa (41,910 psi) in the inner and outer leg respectively. The bolt shear stress is

$$\sigma_{\text{Shear}} = \frac{F_{\text{Bolt}}}{A_{\text{Bolt}}} \qquad (3.2\text{-}15)$$

The shear stress on the inner leg is 349 MPa (50,600 psi) and 750 MPa (108,800 psi) on the outer leg bolts. For the bolt material of A-286 stainless steel with a tensile yield of 1,681 MPa (243,800 psi), and a shear yield stress of 970 MPa (93,780 psi), these loads should be acceptable.

Repeating this procedure for the composite coil calculation gives the bolt loads as 1.20×10^5 N (2.70×10^4 lb) and 1.58×10^5 N (3.54×10^4 lb) for the inner and outer legs of the coil. The bearing stress on the plate and bolts can be determined from equation 3.2-14. Substitution of the plate dimensions gives the bearing stress on the inner and outer leg as 91.3 MPa (13,240 psi) and 120 MPa (17,370 psi) respectively. Substitution of the proper dimensions into equation 3.2-14 gives a bolt shear stress of 237 MPa (34,380 psi) for the inner leg and 311 MPa (45,100 psi) for the outer leg. These values are well within the acceptable range for the bolt material.

The individual stress components on the toroidal field coil are summarized in Table 3.2-II.

3.2.3 Thermal Analysis

3.2.3.1 TF Coil Conductor Selection

The conductor selection for the toroidal field coil of the High Field Compact Tokamak Reactor (HFCTR) is an interdisciplinary design effort incorporating recommendations based upon thermal and hydraulic requirements, electrical performance, coil configuration, structural limitations, and conductor performance. To evaluate the conductor performance the following guidelines were used.

The peak magnetic field at the conductor is 13.1 tesla (at a radius of 3.4 m from the center of the device). To achieve this field, 13.9 MA per coil in a 16 toroidal-field coil array are required. Forced-flow cooling was selected as the most practical mode of cooling.

The conceptual design of the conductor for the HFCTR recognizes the advances in conductor design and fabrication which will probably be made in the years preceding the construction of the HFCTR. Two areas where improvements are likely are:

- the possible development of fabrication techniques for a higher current density superconductor than Nb_3Sn and
- the development of a "lattice" braiding technique which allows maximum use of the strands in a conductor because of the full transposition.

3.2.3.1.1 Preliminary Parametric Analysis

In developing a conductor design, a preliminary examination of the conductor stability was made. In this analysis, the conductor current, I, is calculated from:

$$I = \frac{j}{1 + \psi} \frac{n \pi d^2}{4} \tag{3.2-16}$$

where j = average current in noncopper region of the conductor

ψ = ratio of copper to noncopper

n = number of active strands, and

d = strand diameter.

In order for the conductor to carry this current, the joule heating must be less than the maximum surface heat removal capability, i.e.,

$$h \, \Delta T \geq \frac{\rho \, j^2}{\psi \, (1 + \psi)} \frac{d}{4} \left(\frac{S_a}{S_t} \right)^{-1} \tag{3.2-17}$$

where h = heat transfer coefficient

ΔT = temperature difference between the stream and the conductor, assumed here to equal 1.5° K, when the conductor has been cooled to the current-sharing temperature

ρ = resistivity of the copper stabilizer

S_a = available surface area for heat removal, and

S_t = total surface area of conductor.

To size the conductor, the surface heat removal was initially assumed to be given by the Giarratano modification to the classical Dittus-Boelter relationship for turbulent flow heat transfer (Re > 2000), i.e.,

$$h = C_1 \frac{k}{D_h} Re^{0.8} Pr^{0.4} \frac{T_b}{T_w}^{0.716} \tag{3.2-18}$$

where C_1 = 0.259, based upon small diameter smooth tube data

k = thermal conductivity

$D_h = 4A_f/P_w$ = hydraulic diameter

A_f = area for helium flow

P_w = wetted perimeter

$Re = G\ D_h/\mu$ = Reynold's number

G = mass flux per unit area

μ = viscosity of helium

$Pr = \mu\ C_p/k$ = Prandtl number

C_p = specific heat of helium

T_b = bulk temperature of the helium, and

T_w = wall temperature of the conductor.

The major energy drain associated with a forced-cooled conductor is the pumping power required to circulate the helium. The pumping power requirement (for an ideal pump) per unit length of conductor, W_p/L, is given by

$$\begin{aligned} \frac{W_p}{L} &= \frac{G\ A_f\ \Delta P/L}{\rho_m} \\ &= \frac{2G^3 A_f f}{\rho_m{}^2 g_c D_h} \end{aligned} \tag{3.2-19}$$

where ρ_m = the mass density of the helium and $\Delta P/L$ = the pressure drop per unit length. The pressure drop per unit length is given by

$$\frac{\Delta P}{L} = \frac{2\ G^2\ f}{\rho_m\ g_c\ D_h} \tag{3.2-20}$$

where g_c = the acceleration of gravity and f = the friction factor. The Koo friction factor for Re > 2000 can be calculated from

$$f = \ .0014 + \frac{.125}{(Re)^{.32}} *(K) \tag{3.2-21}$$

where C_2 = 0.046 for smooth tubes

K = friction factor multiplier for twisted cable/smooth tube, here taken to equal 2.5.

Equations (1) through (6) are used to specify the conductor configuration. Since a cabled conductor differs significantly from a smooth tube, the constants in Equations (3) and (6) have to be suitably adjusted to describe the characteristics of the cable.

3.2.3.1.2 Final Conductor Selection

The conductor cross section is reduced to 1.8 cm × 1.8 cm by compacting the lattice braided conductor to approximately 40% void. The final strand diameter selected was 0.705 mm. Several operating current densities were examined to determine which gives the lowest pumping power. Table 3.2-IV summarizes these results. A pumping power of 0.28 W/m was estimated to be acceptable. The final reference design for the HFCTR conductor was selected to operate at j_o/j_c = 0.4, where j_o is the current density in the superconductor and j_c is the critical current density of the superconductor. Below 0.4 the pumping power increased due to the increased joule heating. Table 3.2-V summarizes the reference conductor design. ψ is the ratio of copper to noncopper in a conductor.

TABLE 3.2-IV

FINAL CONDUCTOR SELECTION

j_o/j_c	J (A/cm^2)	ψ	Wp/L (W/m)
0.4	6.67×10^4	10.1	0.28
0.5	8.33×10^4	12.9	0.40
0.6	10^5	15.7	1.58

TABLE 3.2-V

FINAL REFERENCE DESIGN

Configuration	lattice braid
Number of Strands	503
Strand Diameter	0.705 mm
Percentage Void	40%
Conductor Width (inside of jacket)	1.8 cm
Conductor Height (inside of jacket)	1.8 cm
Conductor Current	11.75 kA
Copper-to-Noncopper Ratio	10.1
Strand Current Density	66.7 kA/cm^2
Ratio of Operating Current to Critical Current	0.4
Ideal Pumping Power Per Unit Length	0.28 W/m

3.2.3.2 Cryostability

After the selection of conductor dimensions, based on the design rules of thumb described above, a numerical transient analysis was used to determine the conditions under which the conductor would recover from a sudden increase in temperature. The incorporation of recent experimental data [1,2] into the transient analysis had a profound effect on the perceived feasibility of this design and has encouraging implications for the use of conductors cooled by forced-flow supercritical helium.

The initial conductor selection was based on the use of the Giarratano heat-transfer correlation for fully-developed turbulent flow in a smooth tube [3]. A number of complete transient responses to a sudden deposition of energy in one-half of a coil turn at 13.1 T were calculated. In each case, the superconductor was driven normal from 4.2°K to some higher initial temperature. For each mass flow rate, there was a maximum initial temperature from which the coil turn would recover, which is plotted in Figure 3-10. Because of the high maximum field at the coil, conventional Nb_3Sn appeared to be inadequate for the conductor selected. (Conductor parameters used in the transient analysis are shown in Table 3.2.3-I.) The highest initial temperature from which the Nb_3Sn could recover was only 8.6°K. In order to recover from a rise to 8°K, 150 kg s^{-1} m^{-2} were required. This corresponds to a pumping power per unit length of 3.38 W/m at 4.2°K. Since the total length of conductor in the sixteen toroidal field coils is 627 km, the total refrigeration requirement at 4.2°K would be 2.1 MW, which would require the entire reactor electrical output to drive the refrigerator compressors.

Because of the strong motivation to keep the toroidal field coils compact, a more advanced superconductor with the properties of the gallium-doped Nb_3Sn

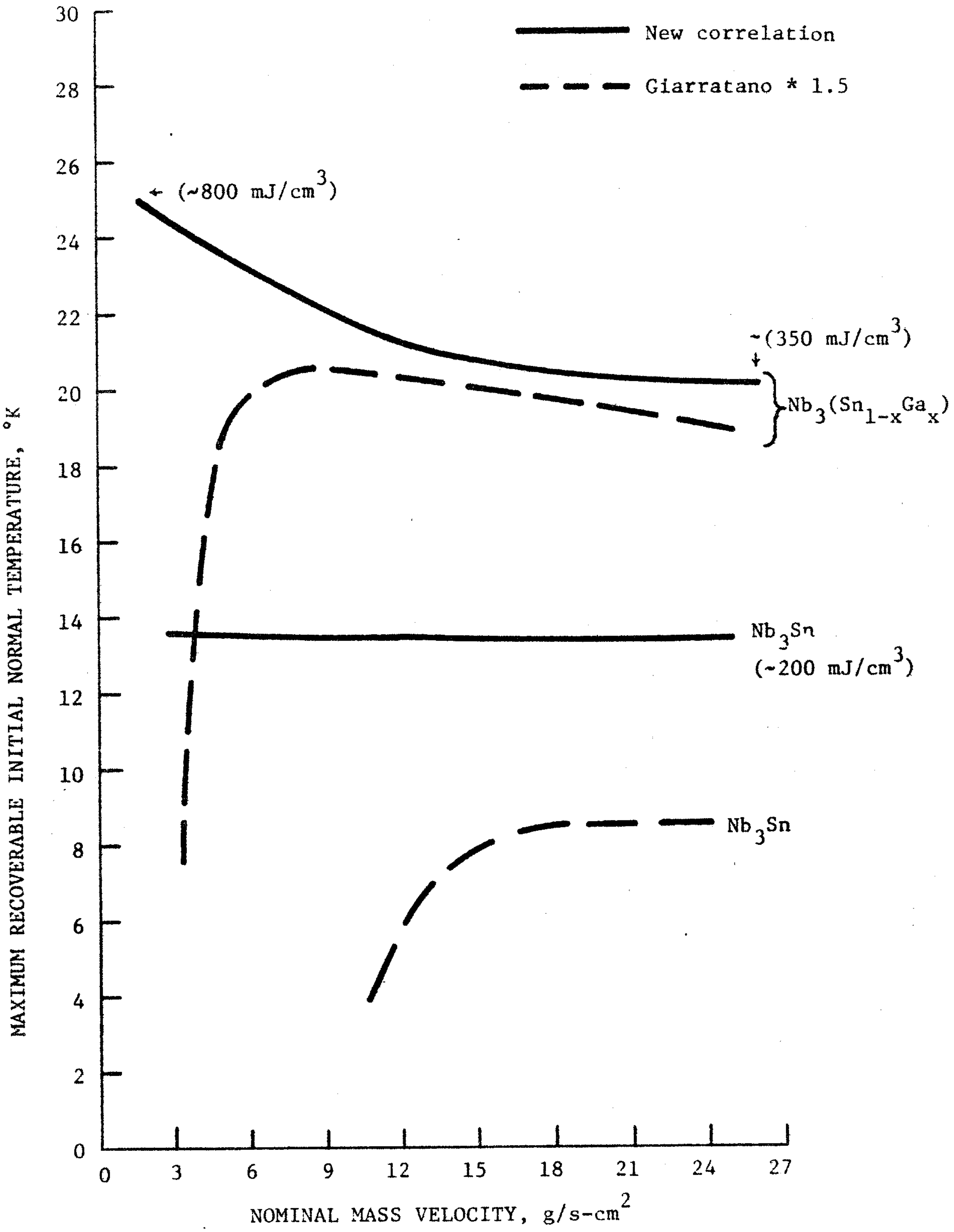

Figure 3-10 Maximum Recoverable Temperature vs. Mass Velocity for Reference Conductor with Different Superconducting Materials and Heat Transfer Correlations

TABLE 3.2.3-I

CANDIDATE SUPERCONDUCTORS FOR CRYOSTABILITY ANALYSIS OF THE TOROIDAL FIELD COILS OF HFCTR

	$Nb_3(Sn_{1-x}Ga_x)$	Nb_3Sn
Peak Field, Tesla	13.1	13.1
Non-Cu Current Density, A/cm^2	6.67×10^4	8.33×10^3
J_o/J_c	0.4	0.5
Area of conductor + He, cm^2	3.12	3.12
Void Fraction	.37	.35
Cu-to-Non Cu Ratio	10.1	0.46
Current per conductor, Amp	11583	11583
Superconductor critical Temp., K	6.3	5.7
Current Sharing Temp. K	5.9	4.9
Initial Helium Temp., K	4.2	4.2
Average Channel Length, m	250	250
Total No. of Channels	2400	2400

conductors characterized by Suenaga and Dew-Hughes (4) was investigated. Although no stranded, high-current superconductors other than NbTi or Nb_3Sn have been demonstrated, a superconductor which appeared to have mechanical and chemical properties similar to those of Nb_3Sn was selected, in order to minimize potential fabricability problems in a future demonstration reactor. Recent work by Tsuei at IBM has improved the possibility of using even more powerful superconducting materials, such as Nb_3Ge. With the use of $Nb_3(Sn_{1-x}Ga_x)$ or a superconductor with similar properties, a coil turn could recover from a sudden energy deposition of 200 mJ/cc with a mass flow rate of only 39 kg s^{-1} m^{-2}. This corresponds to a pumping power per unit length of .059 W/m or 37 kW over the length of 16 coils. Fortunately, experimental work on the heat transfer coefficients of hollow cabled superconductors by Hoenig at MIT and by Westinghouse as part of the Large Coil Program has indicated that the Giarratano correlation is grossly pessimistic at low mass flow rates [7]. In fact, superconducting cables have a relatively high heat transfer coefficient, even in stagnant helium. A new, unpublished correlation for the Nusselt number in hollow cabled superconductors was used for transient recovery analysis of the same two conductors studied previously. As shown in Figure 3-10, there is now no mass velocity limit on transient recoverability, since the maximum recoverable initial temperature does not deteriorate, down to the lowest flow rates. Cryostability now becomes a function of the helium inventory alone. The flow rate is now set by the need to remove the average coil heat losses during reactor operation, including neutron absorption, a.c. pulsed field losses, conduction through leads and coil structure, radiation to coil heat shields, and the internal energy rise associated with helium flow. The average losses have previously been calculated to equal 20 mW at 4.2 K. If a 1 K rise is permitted from the inlet to the outlet, at four atmospheres the heat that can be removed from the toroidal field coil system equals

$$Q = n_c \, n \, N \, G \, \Delta H \tag{3.2-22}$$

where $n_c = 8$ is the number of seriesed electrical channels, paralleled in a coolant channel,

$n = 20$ is the number of parallel coolant channels per coil,

$N = 16$ is the number of coils,

G is the mass flow rate per conductor and

$\Delta H = 4.18$ kJ/kg is the specific enthalpy change in the helium between the outlet and the inlet.

For $G = 10$ kg s^{-1} m^{-2}, the amount of steady-state heat which could be removed through the outlet channels is 11.8 kW, which is higher than the 10.0 kW of steady-state cryogenic losses in the conductor volume. The pumping power adds 0.62 kW to these losses. With a mass flow rate of 10 kg s^{-1} m^{-2}, it is now predicted that a conventional Nb_3Sn coil could recover from a sudden energy deposition of 200 mW/cc, which is comparable to the design criteria in the LCP program. A much higher margin of safety (~800 mW/cc) could be achieved with the advanced superconductor or, conversely, a higher-current toroidal field coil could be built within the same envelope. Conventional Nb_3Sn was selected as a reference design, because of its greater demonstrated feasibility. However, the overall feasibility of a high energy-density toroidal field coil and of the tokamak system will be improved by the development of more advanced superconducting cables.

3.3 EQUILIBRIUM FIELD REQUIREMENTS

The elongation of the plasma in the form of a D-shape is utilized to obtain values of β_T in the neighborhood of 4%. For this β_T computer codes indicate that an equilibrium external field can be produced with only a few magnetic moments. The coil system produces dipole, quadrupole, and hexapole moments, requiring one set of coils for each moment. These are shown in Figure 3-11.

This arrangement is attractive for designing D-shaped plasma configurations and for using a possible feedback system. In addition, the coil system offers: (1) considerable flexibility in actual coil location, and (2) the allowance of a large amount of space for neutral beam lines and the location of ripple injection coils, features which cannot be provided by the "conducting wall" approach [4].

Figure 3-1 and Table 3-I show the location of the equilibrium field coils in the present design. The dipole field coil is superconducting and is located outside the toroidal field coil ($R = 10.25$ m, $z = \pm 5.5$ m; where $z = 0$ is the toroidal mid-plane). The copper quadrupole field coil is placed inside the toroidal coil ($R = 6.0$ m, $z = \pm 3.7$ m). The hexapole field coil is located just inside the TF coil trunk ($R = 2.3$ m, $z = \pm 0.5$ m). The coil currents are determined with the emphasis on minimizing the copper coil current (and power) as well as limiting the current in the superconducting coils. The dipole field coils are superconducting because of the large currents required for the dipole moment. The average power dissipation of the copper quadrupole coils is about 25 MW during the 500 second plasma burn.

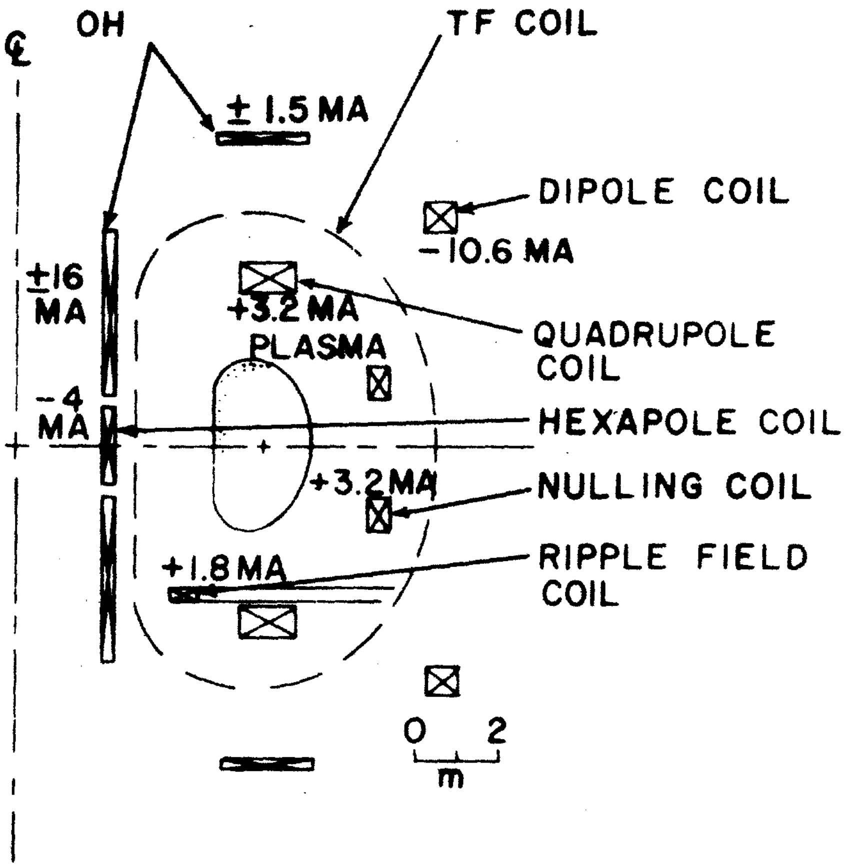

Figure 3-11 Vertical Field Coils

Table 3 - I

HFCTR VERTICAL FIELD COILS

Coil	I(MA)	R_1(m)	R_2(m)	Z_1(m)	Z_2(m)
Dipole	-10.6	9.90	10.60	5.15	5.85
Quadrupole	3.2	5.55	6.60	3.30	4.10
Hexapole	-4.0	2.20	2.40	0	1.00
Null	3.2	8.25	8.85	1.15	1.85
OH (Core)	±13.0	2.10	2.40	1.00	5.20
OH (Compensating)	±1.5	4.70	7.20	7.40	7.60

The copper nulling field coils located at ($R = 8.55$ m, $z = \pm 1.50$ m) are used to provide the equilibrium field correction at plasma initiation. Figure 3-12 shows the nulling field and the DC equilibrium fields. The nulling field is decreased as the plasma current increases and simultaneously provides part of the magnetic flux swing for ohmic heating. These field coils along with the quadrupole and hexapole field coils will be continuously adjusted during the start-up phase. The total energy transfer for the nulling field is about 500 MJ, or about 20% of the stored energy in the equilibrium field. This represents a substantial reduction in pulsed energy requirements compared to other tokamak designs. The peak NF power is 66 MW and the average over the 500 second burn is about 0.4 MW.

Figure 3-13 shows the total equilibrium field profile at plasma initiation and ignition. The pressure gradient toward the TF column can be varied by adjusting the hexapole current. A flux swing through the core of about + 15 volt-seconds arises from energizing the hexapole coil.

A view of the equilibrium flux surface configuration is shown in Figure 3-14. The pressure profile is chosen to be $p(\Psi) \simeq \Psi^{\alpha}$ ($\alpha = 1.3$). The plasma column has a typical D-shape with the option that the hexapole field coil current can be made strong enough to shape the plasma edge vertically straight at $R = 4.8$ m. It gradually decreases to -0.02 at the outer edge where $R = 7.3$ m. These values are calculated on the horizontal plane. The external field pattern and the variation of the index on the horizontal plane are shown in Figures 3-15 and 3-16, respectively. Since most of the plasma current flows in the outer portion of the plasma, the effective index at 6.5 m is about -0.5.

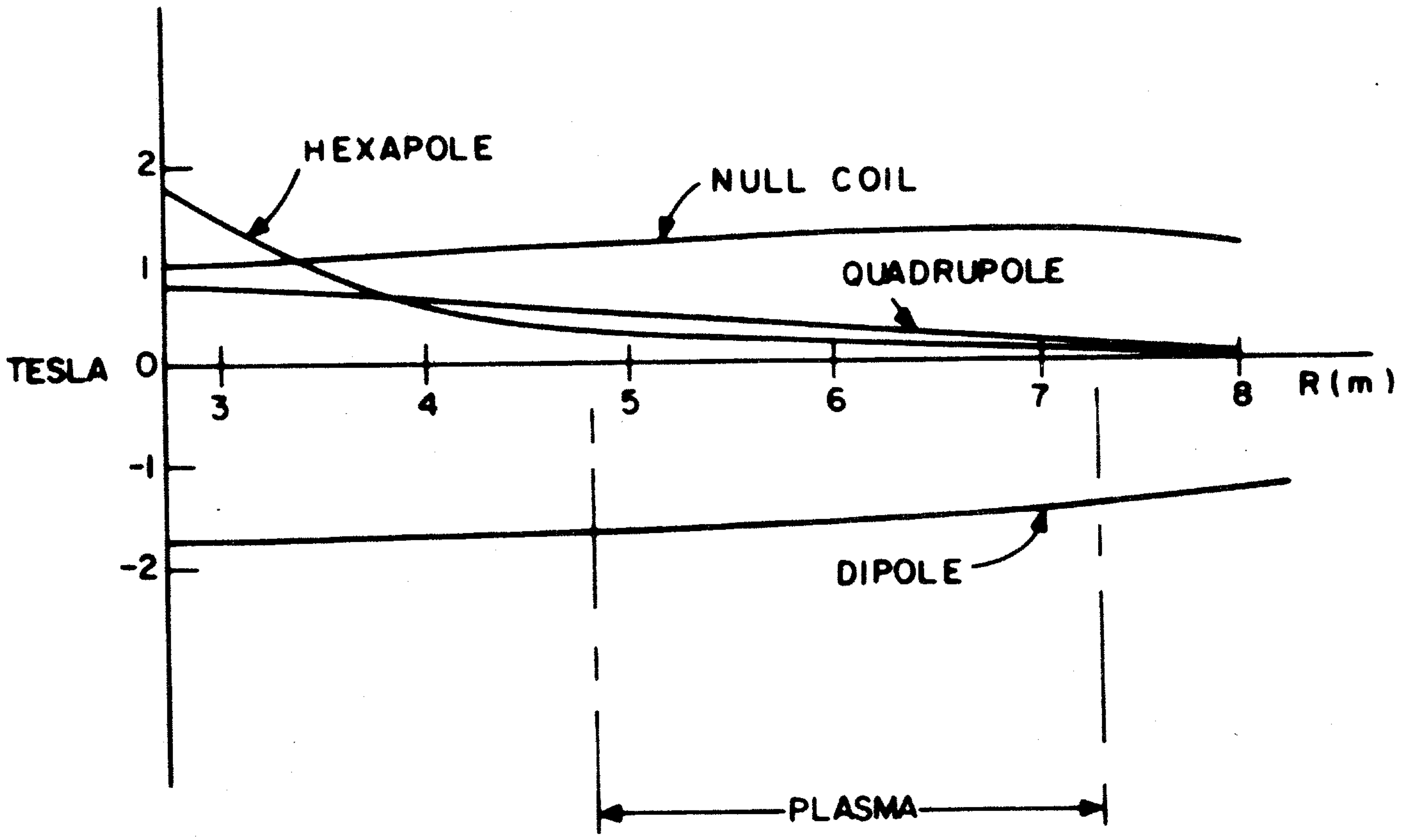

Figure 3-12 Profiles of the component equilibrium fields (at $z = 0$) during plasma initiation.

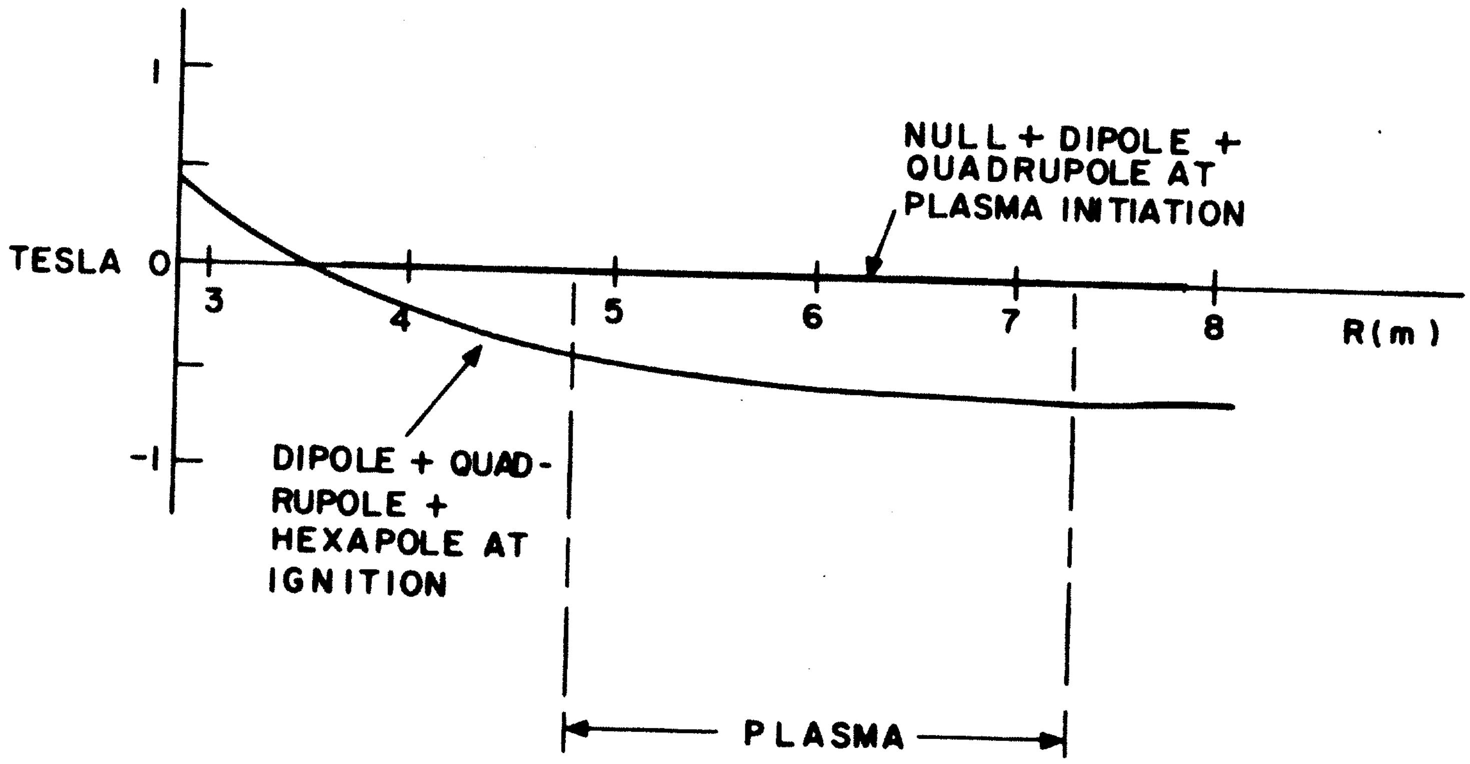

Figure 3-13 Profiles of the total equilibrium field (at z = 0) during plasma initiation and ignition.

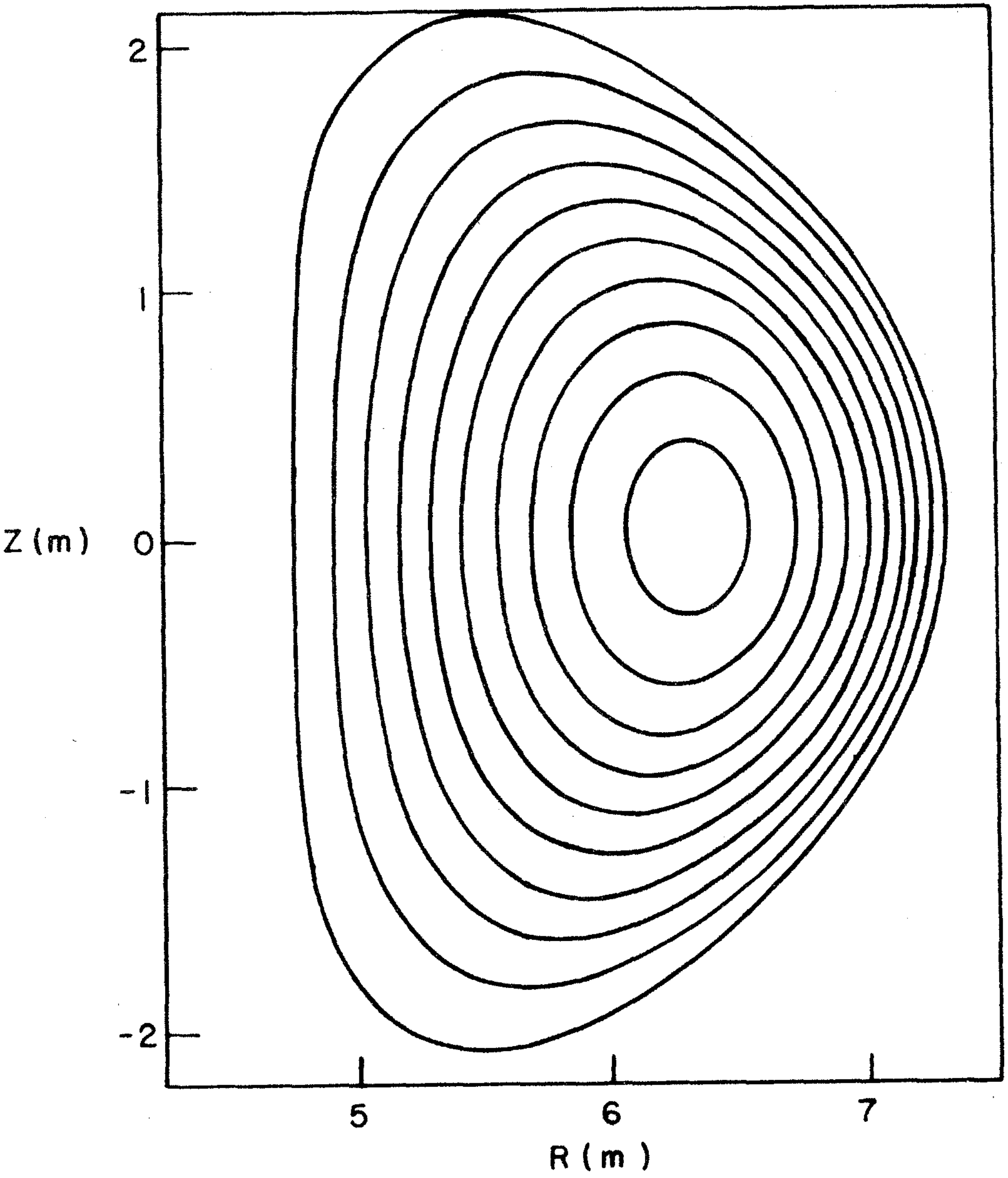

Figure 3-14 Plasma equilibrium flux surface configuration at ignition.

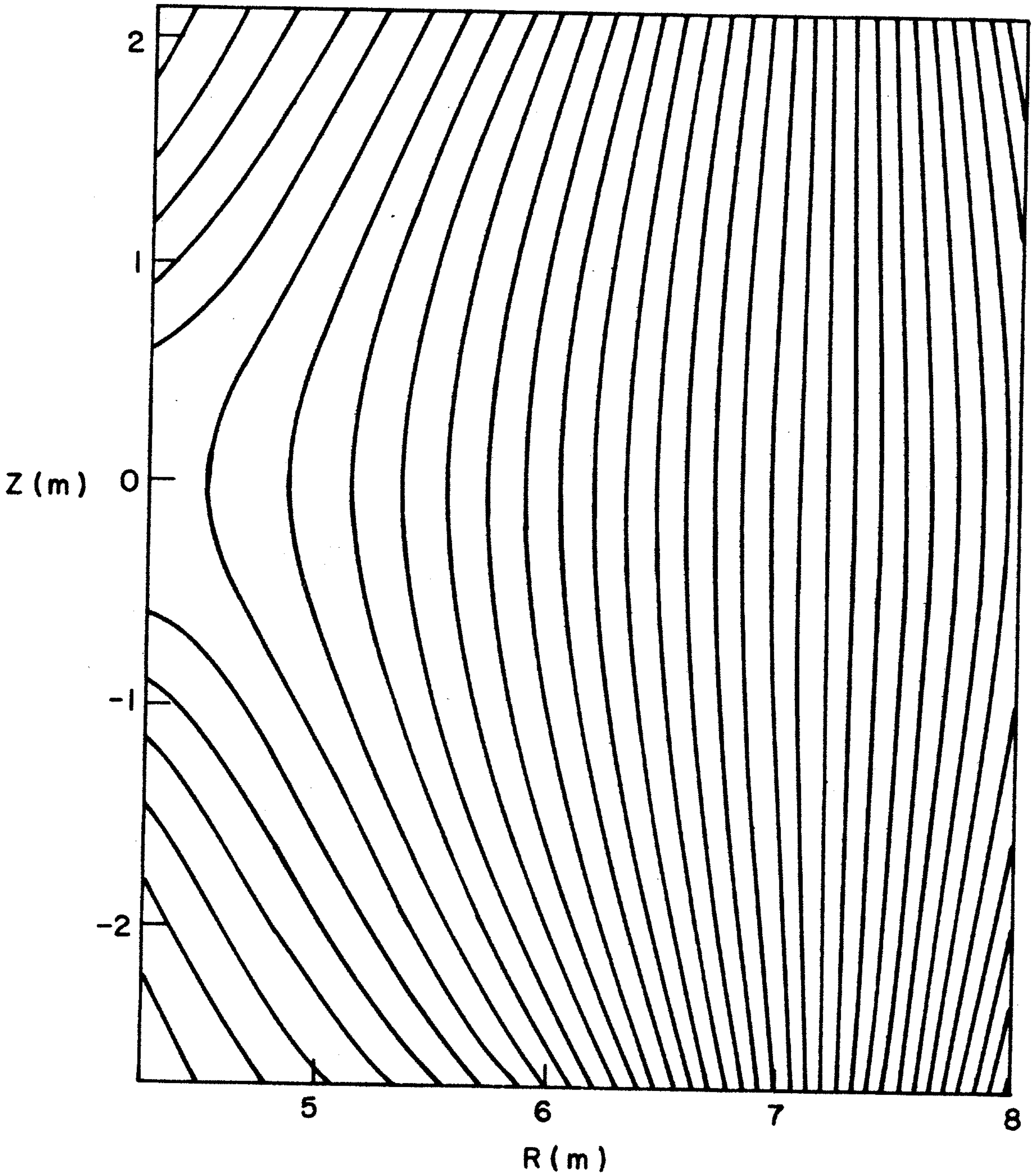

Figure 3-15 Equilibrium vertical field pattern at ignition.

This undesirable curvature can destabilize the plasma in the vertical direction on a very short time scale ($\tau_A \sim \frac{a}{v_{Alfen}}$), making a feedback stabilization system infeasible. However, this time scale can be lengthened by using the quadrupole coils as passive stabilization coils. Although the magnetic pressure decays away due to the resistivity of the passive coils, this decay time (~0.1 to 0.5 seconds) is long compared to τ_A. With these longer time scales an active feedback stabilization circuit can respond to maintain the vertical plasma location.

Figure 3-16 shows an example of the stabilizing effect of a pair of passive stabilizing coils at various vertical positions. In this calculation the plasma has a uniform current profile, and is elongated to an elliptical shape of b/a = 1.5. As Figure 3-17 demonstrates, the marginal stability condition is satisfied if $z \simeq 1.8 \times b$. This indicates that the quadrupole coils can provide passive stabilization while simultaneously allowing ample space for a blanket and shield.

3.4 THE OHMIC HEATING SYSTEM AND FLUX REQUIREMENTS

For I_p = 6.7 MA at B_T = 7.4 T the flux swing requirement (in volt-seconds) consists of

Start-up	110	inductive
	10	resistive
	120	
Burn	60	
	180	Total

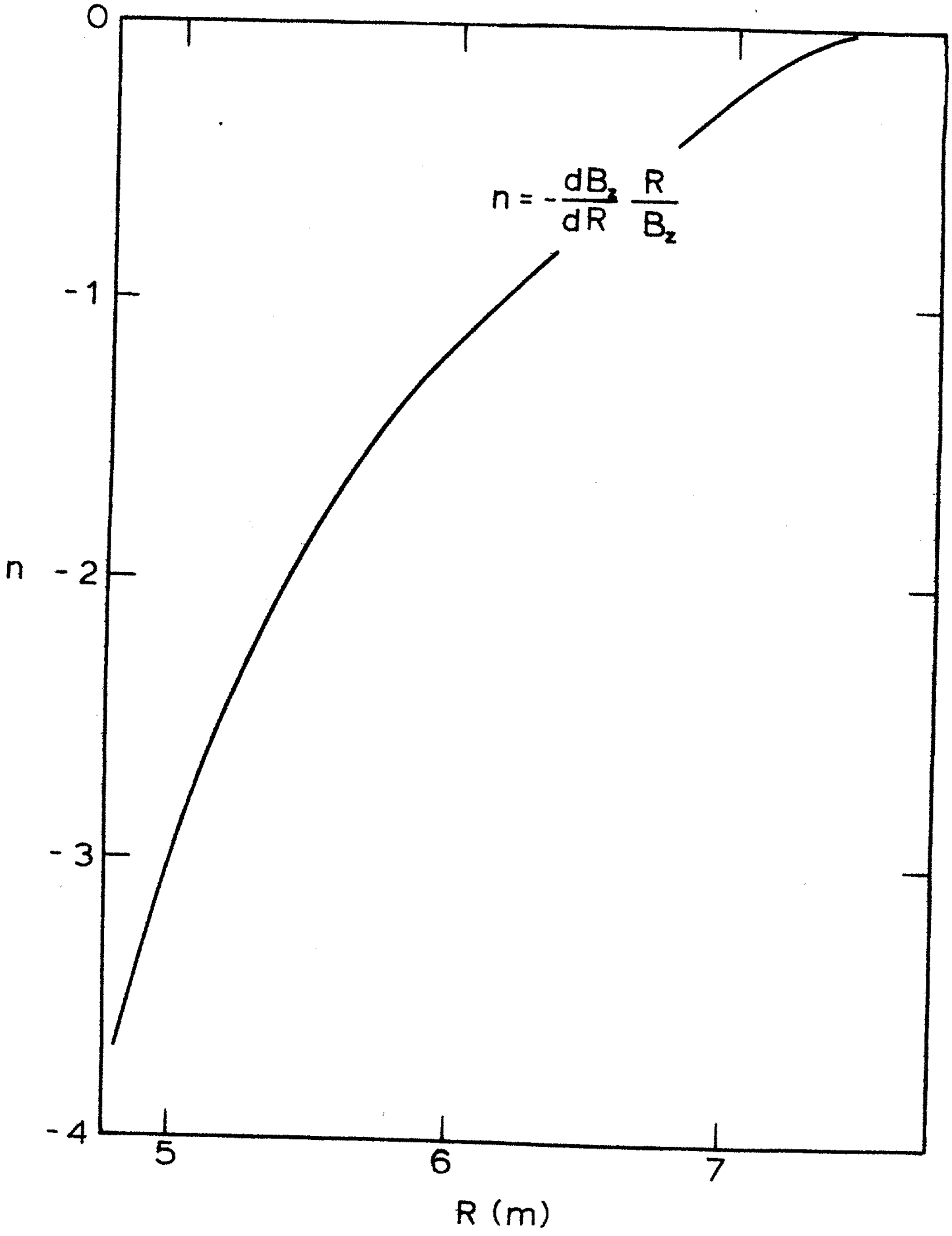

Figure 3-16 n vs. R, where $n = -\frac{dB_z}{dR}\frac{R}{B_z}$.

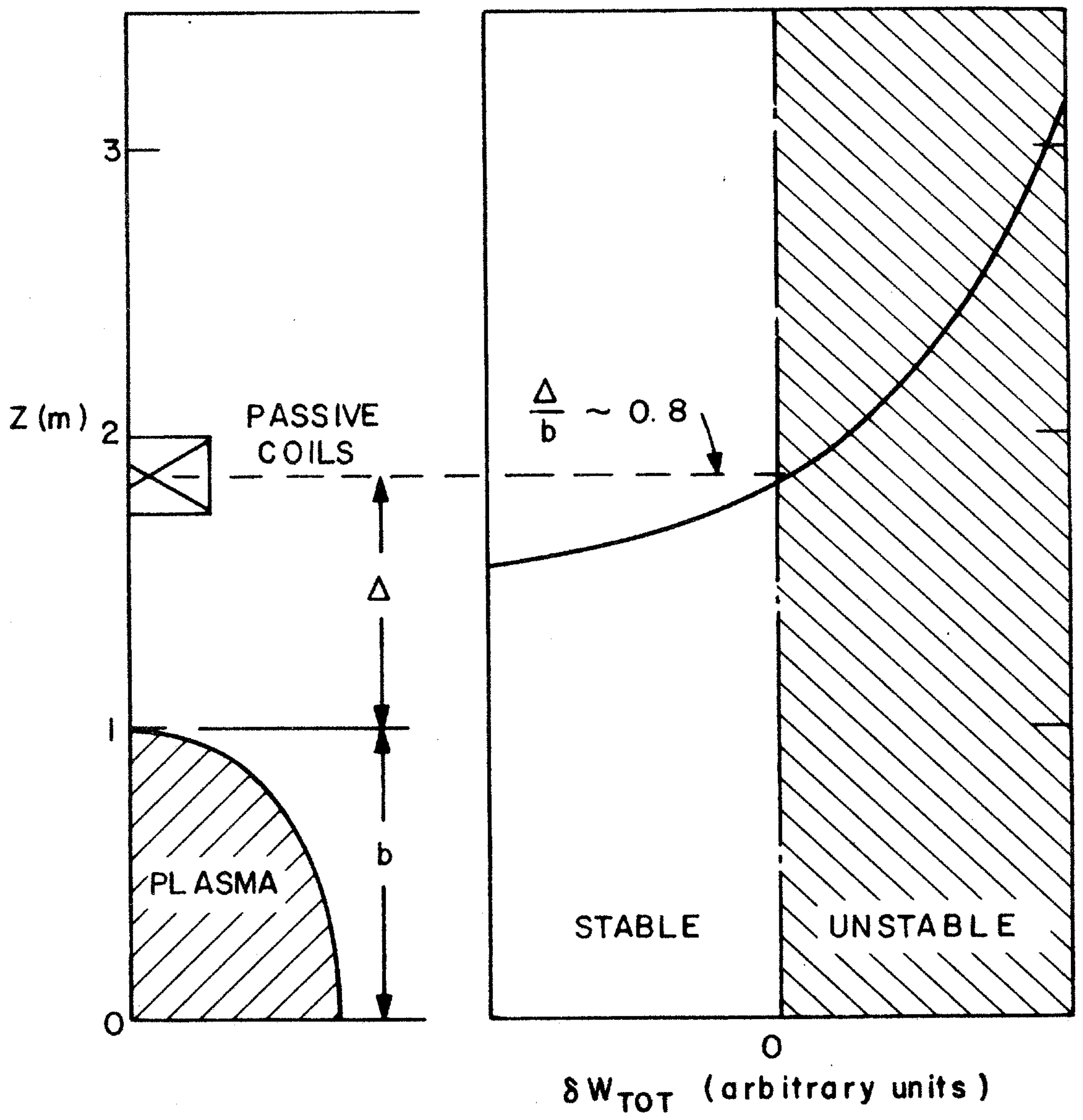

Figure 3-17 Quadrupole coil location required to provide effective vertical stabilization.

The flux waveforms of the ohmic heating, nulling, and hexapole fields and of the plasma current are shown in Figure 3-18.

Part of the start-up flux swing is provided by the nulling field coil which is energized prior to plasma initiation to provide the correct initial vertical field. During initiation, i.e. during the first several milliseconds of start-up, the NF and OH flux change generates the 270 volts across the plasma needed for plasma breakdown. The equilibrium field coils provide about 60 volt-seconds of fast flux required for start-up, while the OH coil system supplies the remaining flux. During start-up the OH changes from a peak field of 5.5 T to about zero.

The OH system consists of the primary coil located in the core, diagrammed in Figure 3-11, and an auxiliary coil located above (and below) the TF coil adjacent to the reaction ring. Table 3-I lists the primary and auxiliary current and coil positions. This auxiliary coil provides field compensation so that the OH swings from zero to about -5.5 T. Between burn cycles it is returned to 5.5 T. The pulse energy loss in the superconducting OH coils is estimated to be 1.5 MJ per fast pulse and is one-tenth of this for the burn cycle. The maximum stored energy in the OH field is 1 GJ.

The field change on the TF coil from the increasing equilibrium and poloidal plasma fields amounts to about 0.8 T and will occur during start-up. A preliminary calculation shows that the eddy losses in each TF coil are 1.5 MJ. Since the peak OH field in the TF coil is only a few hundred gauss, the fast flux swing generated by the OH will have a minimal impact on the TF coils.

The close coupling between the OH and hexapole EF coils will require programmed voltage control on both windings to obtain appropriate timing of the currents. Table 3-I lists the positions and currents of the coil system.

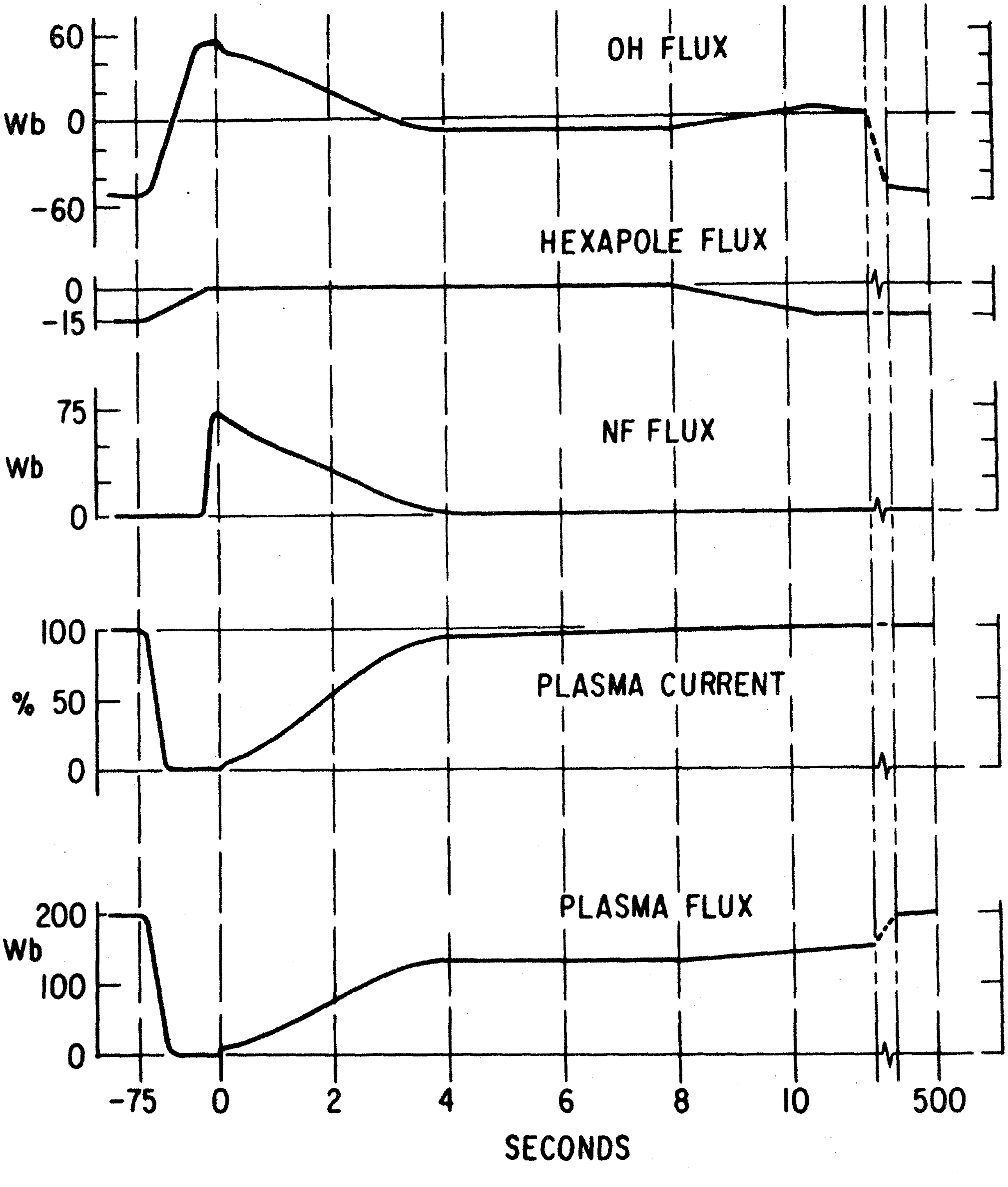

Figure 3-18 Waveforms of magnetic flux and plasma current.

3.5 RIPPLE COIL SYSTEM

In the HFCTR the ripple coil system serves two functions: It permits the central plasma region to be heated by neutral beams of only 120-keV energy (see Section 5), and it enables control of the equilibrium operating point (see Section 2.5). It is essential for at least the first application that the toroidal field ripple have a large top-bottom asymmetry [5], as indicated in Figure 3-19. When neutral beams are injected vertically from the side of stronger ripple, energetic ions formed from the beams are trapped in the ripple magnetic well and drift upward with the ∇B-drift velocity to central plasma region, where the ripple becomes small (< 1%), the upward drift ceases, and the fast ions take up banana orbits.

The design considerations for establishing the required vertically asymmetric ripple have been discussed previously [4], with examples given of various TF coil configurations, as well as the use of auxiliary ripple coils, to create the prescribed ripple contours. More recently, an optimal ripple-coil configuration consisting of a pair of trapezoidal current loops bracketing the vertically injected beam has been developed [5]. This configuration has been adopted for the HFCTR. A similar ripple-coil design is being implemented on the ISX-B tokamak at ORNL, where the first test of ripple injection will be carried out in 1978-79.

3.5.1 Ripple Coil Configuration

The ripple-coil geometry must satisfy a number of critical requirements:

(1) Placement of the ripple coils must not restrict neutral beam access.

(2) The ripple must be high (∿ 5%) in the region of the plasma where

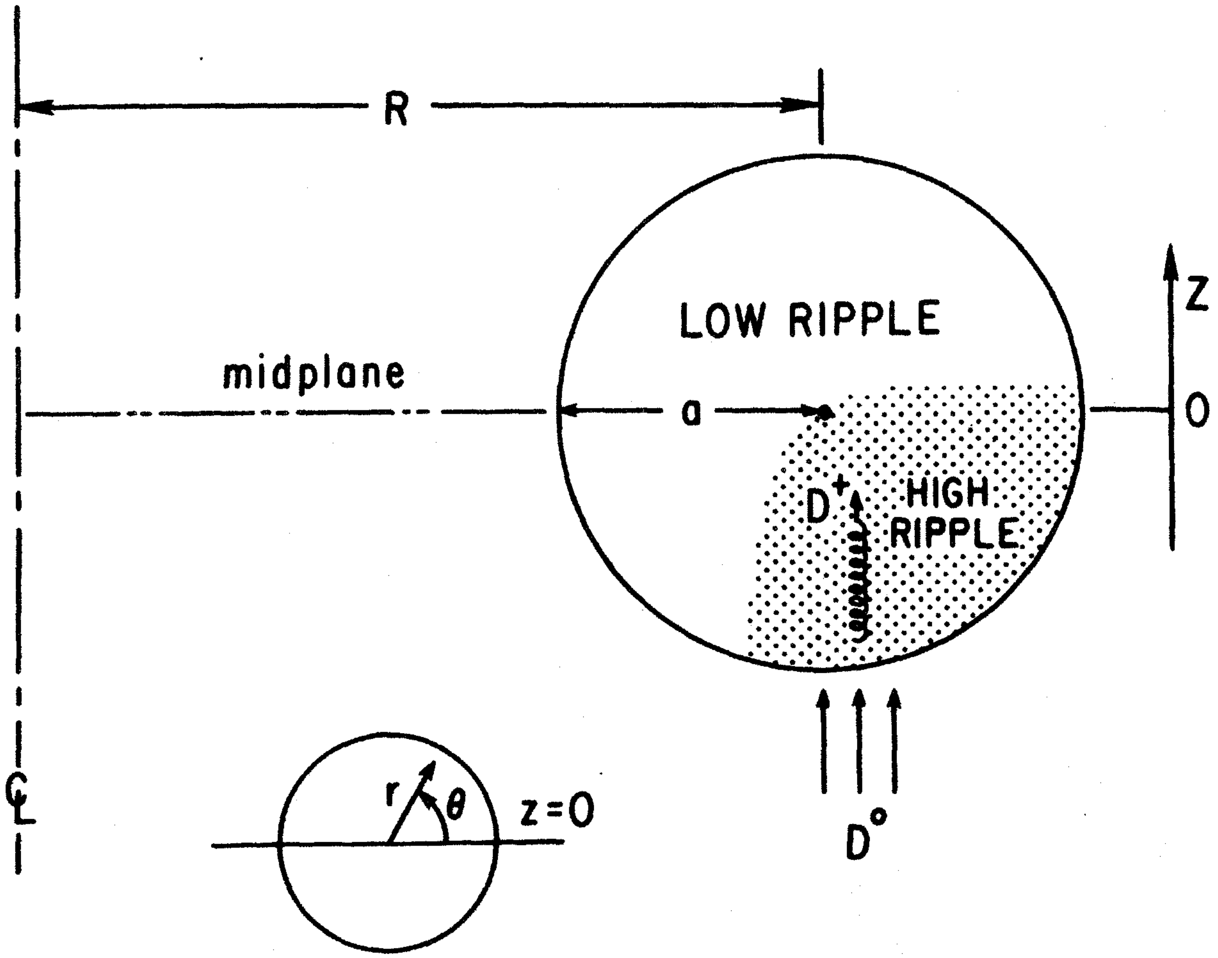

Figure 3-19 Vertical injection of energetic deuterium atoms into a tokamak plasma with vertically assymetric ripple.

the fast neutrals are ionized, but must decrease to $\lesssim 1\%$ near the midplane so that the vertically drifting fast ions pitch angle scatter out of their local magnetic well (Figure 3-19). Minimizing the ripple strength throughout most of the plasma is also important for reducing the perturbation of magnetic flux surfaces.

(3) The toroidal variation of the ripple must be sufficiently rapid to overcome the 1/R variation of $|B|$ along a field line in the injection region.

(4) The coils must be positioned so that the fast ions are first trapped near the bottom of the ripple magnetic well, in order to minimize the probability of detrapping from the ripple well before reaching the central plasma region.

The ripple field produced by the two horizontal "eyeglass coils" shown in Figure 3-20 is optimal because the injector is located at the center of the magnetic well, the sides of the well are very steep, and the coil size can be chosen so that the variation of the ripple strength is optimized [6]. Note that the oppositely circulating currents in adjacent coils produce a field minimum for the injected beam. In order to provide the most satisfactory ratio of ripple strengths at the magnetic axis and plasma edge, the ripple coils should be located between the vacuum vessel and the TF coils. If the ripple coils are located outside the TF coils, the required coil current is prohibitively large. If the ripple coils are placed too close to the plasma, the near fields of the coil currents can cause severe perturbation of the magnetic structure in the plasma. In the HFCTR, the ripple coils are placed just outside the tritium breeding and neutron reflector region, as shown in Figure 3-1.

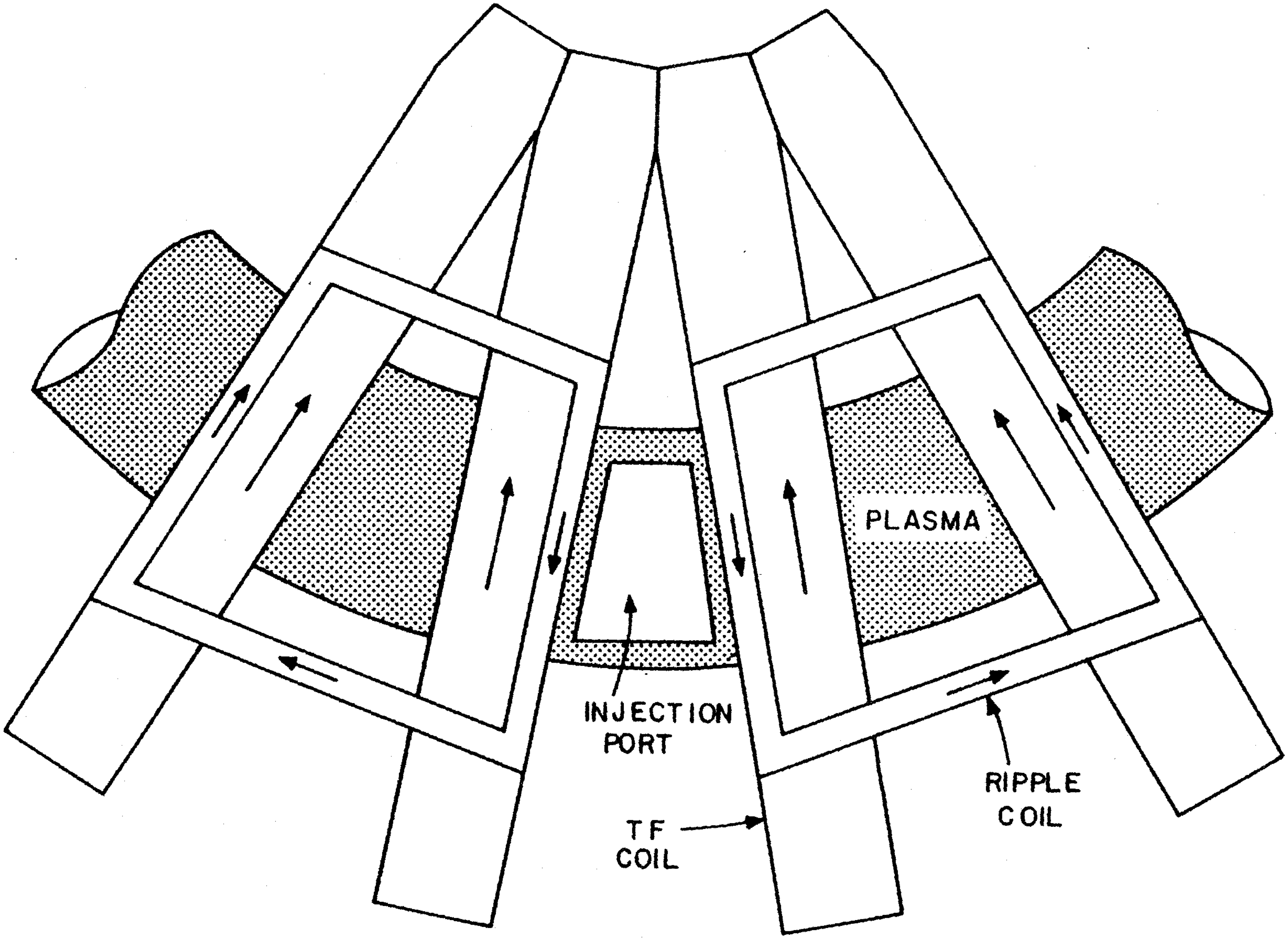

Figure 3-20 Schematic of "eyeglass" ripple coils bracketing vertically injected beam.

In order that the perturbed field have an optimal fall-off distance, the toroidal periodicity of the ripple-coil pairs should be approximately $\pi a/R$ radians [6]. For the HFCTR, this condition corresponds to installing 10 coil pairs in a uniform distribution around the torus. Because there are 16 TF coils, it is most convenient to have 8 injector locations with 8 ripple-coil pairs in the horizontal plane, as shown in Figure 3-21. The oppositely circulating currents in successive coils produce alternate maxima and minima in the toroidal field, with the injectors located at the 8 field minima. The optimal radial extent of the coils should be just sufficient to shadow the plasma region.

3.5.2 Ripple Coil Parameters

A number of parameters were varied in order to determine the specific design of the ripple coils. These parameters included the number of turns per coil, the distance from the midplane, the axial (i.e., toroidal) extent of the coils, the radial extent of the coils, the coil current, and the total power dissipation. In the HFCTR, the beam injectors are located below the tokamak. In order to minimize the coil current it is assumed that the plasma can be shifted 50 cm below the midplane during the beam heating stage, with a vertical elongation no greater than 1.25 during this period. (The final elongation of 1.6 is attained during alpha-particle heating.) Taking into account the desired ripple configuration in the plasma, the need for adequate shielding of the coil insulation (if required), geometric parameters that must allow space for up to 125 MW of neutral-beam injection, and manageable resistive dissipation, the most suitable parameters were found to be the

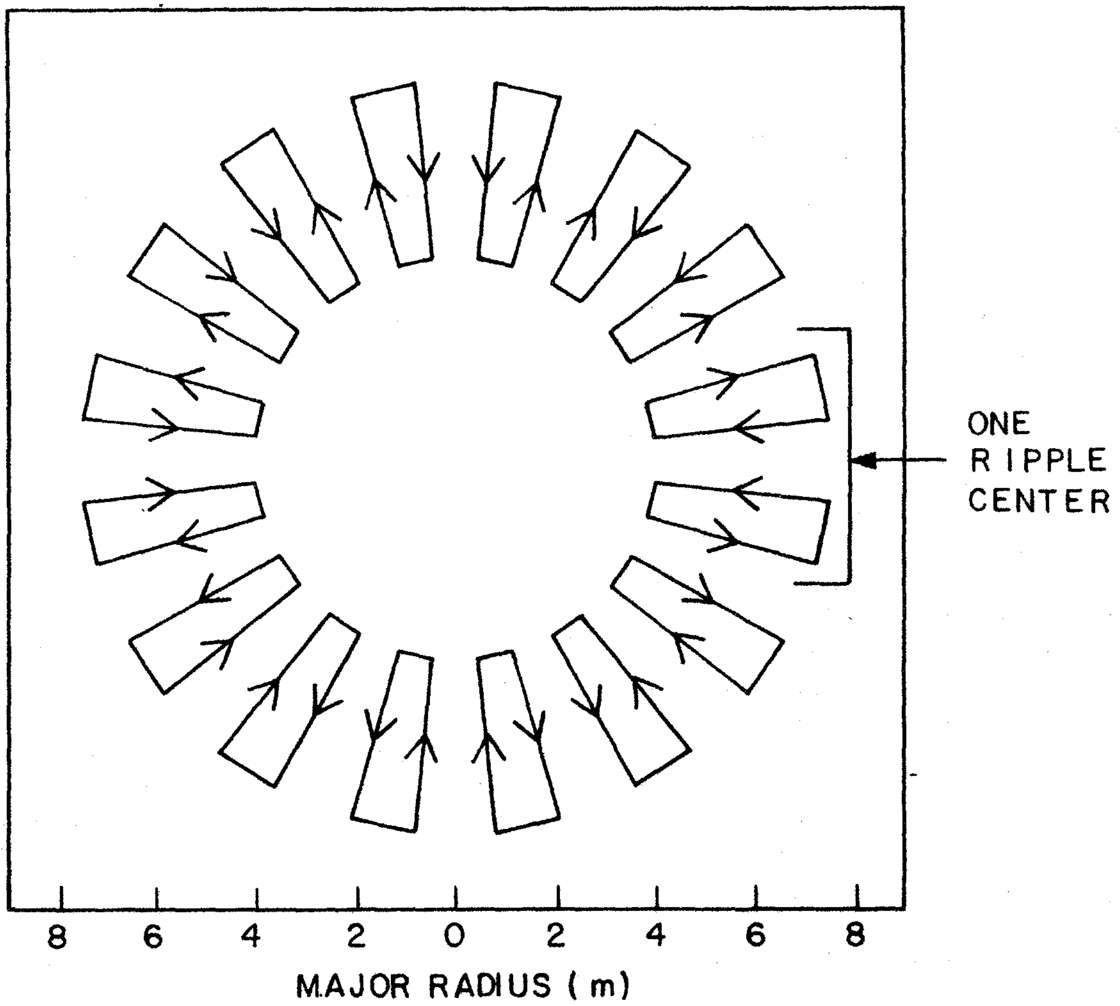

Figure 3-21 Plan view of HFCTR ripple coil layout, for 8 injection ports. Arrows show direction of coil current.

following:

- Distance from device midplane to ripple-coil plane = 3.0 m.
- Horizontal distance for injection between adjacent coils:
  1.5 m at R = 6.6 m.
- Radial extent of coil: from 4.0 m to 7.5 m.
- Coil Current = 1.8 MA.
- Resistive power per coil set = 16 MW (128 MW total).

With a current density of 30 MA/m^2, the cross-sectional area of each ripple coil conductor is 0.060 m^2. The out-of-plane force per unit length of the coils, due to interaction of the coil current with the toroidal field, is 16 MN/m, while the stress in the conductor is 142.9 MPa. The torque on each coil is 60 MN-m. One advantage of the horizontal coil set is that it is not subject to any centering force.

Figure 2-36 shows the ripple contours in the plasma produced by the coil configuration of Figure 3-21. Effective heating of the central plasma is obtained with 120 keV D^o beams, as discussed in Section 5. The eight coil sets are activated only during the 4-sec higher-density period of the startup stage, so that the average power consumed for this purpose is only 1 MW when averaged over the burn time of 500 sec. Because some of the ripple coils can also be used for plasma temperature control throughout the burn (see Section 2.5), the average power dissipation over the burn could be as large as 5 to 10 MW.

REFERENCES - SECTION 3

[1] Deis, D. W., et al., "Mechanical Strain of Large Multifilament Nb_3Sn Conductors for Fusion Magnets", Lawrence Livermore Laboratory, Report UCRL-78890 (1977).

[2] Deis, D. W., et al., "Evaluation of Large, Multifilament Nb_3Sn Conductors with a New 12-T Tensile Stress Apparatus", Lawrence Livermore Laboratory, Report UCRL-79192 (1977).

[3] LPX Status Report, "Preliminary Design Consideration for LPX Superconducting Long-Pulse Experiment", PPPL, M.I.T. and Westinghouse Large Rotating Apparatus Div., LPX-TM-1, Jan. 1978.

[4] TNS Scoping Studies, "Interim Status Report for the First Half of FY-77", GA and ANL, ANL Report ANL/FPP/77-2.

[5] Jassby, D. L., Goldston, R. J., Nucl. Fusion 16 (1976) 613.

[6] Goldston, R. J., et al., Princeton Plasma Physics Lab. Rep. PPPL-1398 (1977), Proc. 7th Symp. on Engin. Aspects of Controlled Fusion.

[7] Hoenig, M.O. and Montgomery, A.G., "Cryostability Experiments of Force Cooled Superconductors", Proc. 7th Symp on Engin. Aspects of Controlled Fusion (1977)

4. BLANKET AND SHIELD

The objective of the blanket and shield design study is to identify materials and geometries which are compatible with the goals of efficient power conversion, net tritium breeding, structural integrity of the first wall and adequate neutron shielding for the toroidal field coils. This is a challenging design problem, because of the high neutron flux density and the compactness of the reactor design. Rationales are presented in this section for the selection of TZM as the blanket and first wall structural material, lithium as the breeding material, and FLIBE as the blanket and first wall coolant. The method of selecting a geometry for the blanket and shield, including the placement of breeding, moderating, reflecting and shielding regions, is described. Coolant pumping power was calculated, including MHD pressure drops. Thermal stresses in the first wall were calculated, with and without TZM protective armor. The armor protects the coolant tubes and provides thermal inertia to reduce tube thermal stresses.

4.1 FLIBE-LITHIUM BLANKET CONCEPT

The power conversion and breeding blanket is designed for use at high neutron wall loadings in intense magnetic fields. Since highly conducting lithium is the tritium breeding material, the functions of breeding and cooling are separate for efficient operation of the blanket in the 7.4 T field.

The basic concept behind the blanket design is to use lithium as the breeding material while cooling the blanket with FLIBE (2 LiF • BeF_2). A section diagram of the outboard blanket and shield is shown in Figure 4-1. The first surface seen by the plasma consists of a set of tubes cooled by FLIBE. These tubes intercept all the alpha power ($\sim$ 1 MW/m^2) as a surface heat load. As shown in Figure 4-1 the first wall tubes are physically separated from the backing wall. This facilitates removal of the first wall tubes and reduces the thermal stress on the backing wall.

Beyond the backing wall there are four molten lithium breeding regions (95% Li - 5% Mo) separated by coolant tubes spaced to give the same peak lithium temperature in all regions. A limit of 1000 C is set for this peak. The tube wall temperature at the outlet is 650 C. Higher coolant and tube wall temperature would increase the thermal efficiency but require either a thinner lithium region or more tubes (resulting in smaller breeding ratios). The lithium is essentially stagnant, and flows only fast enough to maintain a low tritium inventory (cycle time $\sim$ 1 day). Beyond the breeding regions is the two-part graphite and stainless steel moderator/reflector and the composite stainless steel and boron carbide shield. The methodology used in designing the blanket/configuration is shown below (here q''' is the volumetric heat generation rate, $T_{b\ max}$ is the peak lithium temperature and T_{exit} is the exit tube wall temperature). The design has not been optimized.

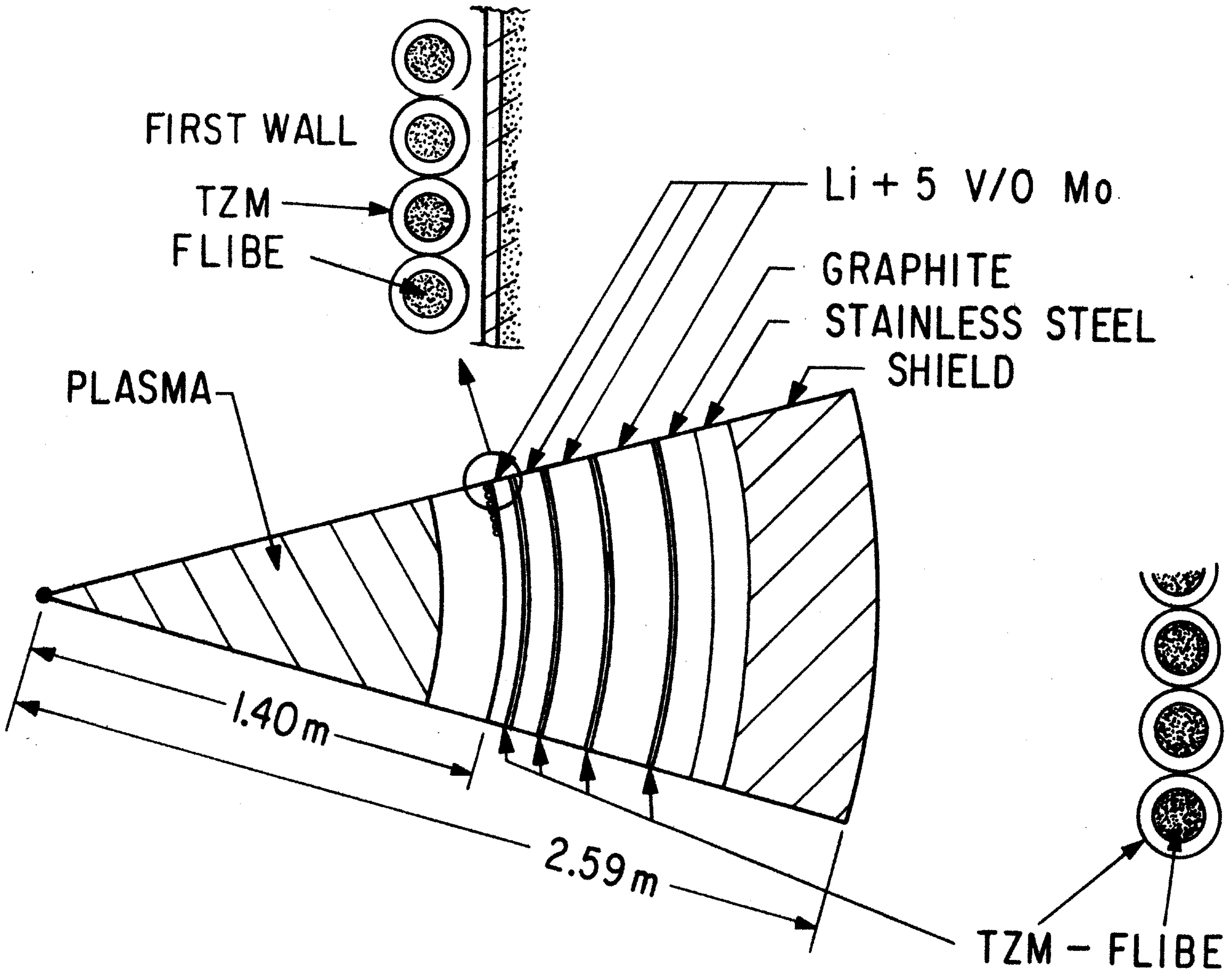

Figure 4-1 Section diagram of the outboard blanket and shield.

Blanket/Shield Formulation

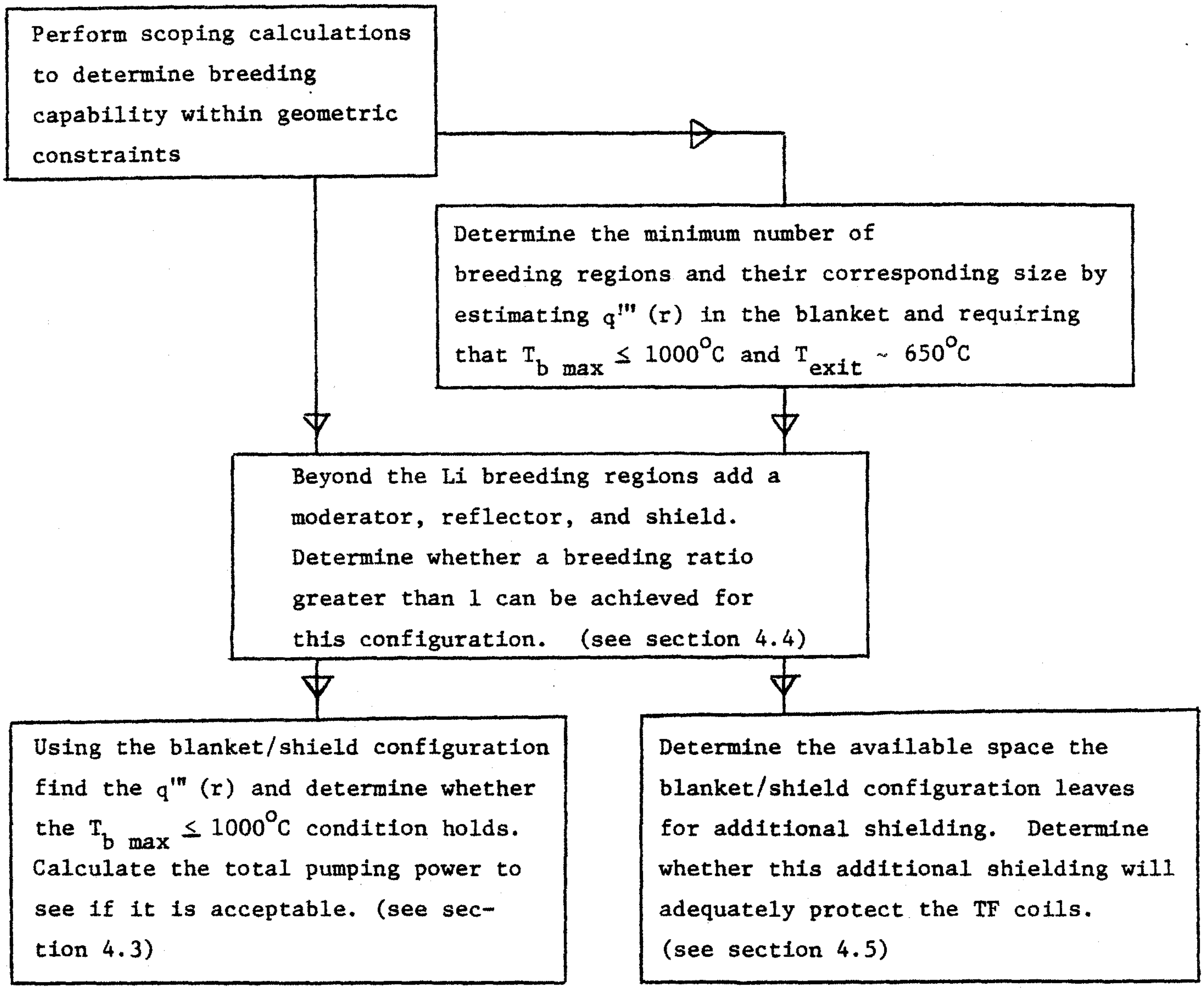

Perform scoping calculations to determine breeding capability within geometric constraints

Determine the minimum number of breeding regions and their corresponding size by estimating $q'''(r)$ in the blanket and requiring that $T_{b\ max} \leq 1000^{\circ}C$ and $T_{exit} \sim 650^{\circ}C$

Beyond the Li breeding regions add a moderator, reflector, and shield. Determine whether a breeding ratio greater than 1 can be achieved for this configuration. (see section 4.4)

Using the blanket/shield configuration find the $q'''(r)$ and determine whether the $T_{b\ max} \leq 1000^{\circ}C$ condition holds. Calculate the total pumping power to see if it is acceptable. (see section 4.3)

Determine the available space the blanket/shield configuration leaves for additional shielding. Determine whether this additional shielding will adequately protect the TF coils. (see section 4.5)

4.2 CHOICE OF STRUCTURAL MATERIAL

With only a limited data base for irradiation effects on fusion reactor candidate structural materials, the choice of a particular material is very difficult to make. For example, while the damage caused by neutron irradiation at high temperature is much greater in stainless steel than in the refractory metals (Nb, V-Ti, Mo), recent results indicate that long wall lifetimes are possible with type 316 stainless steel if low temperature operation (∿ 300-400 C) is employed [1]. At this temperature, damage caused by the material lifetime is determined principally by damage due to the displacement of atoms in the lattice structure. There may well be an optimum operating temperature for molybdenum and other refractory metals as is the case for stainless steel.

Other considerations must be taken into account in the structural material choice. The material should have high strength; it should be compatible with a coolant which does not interfere greatly with the breeding of tritium; it should be fabricable; it should have little residual activity; and it should present no significant resource problems.

Type 316 stainless steel and molybdenum alloy TZM (99.39% Mo, 0.5% Ti, 0.08% Zr, 0.03% C) are two material choices for fusion reactors. In the near term, experiments and some prototypes will almost certainly be built with stainless steel. At the demonstration power reactor stage - and beyond - a refractory metal could conceivably be employed. For a given thermal loading, the thermal stresses in stainless steel are between 5 and 8 times those in TZM. At the same temperature, the damage caused by neutron irradiation in stainless steel is between 3 and 10 times that in TZM [2]. The biological hazard potential of stainless steel is one half that of TZM up to one day following shutdown. Beyond one day, the biological hazard potential of stainless steel is greater than that of TZM and, after two weeks, is at least ten times that of TZM for the next one hundred years [2]. TZM is compatible with lithium bearing molten salts such as FLIBE ($2\ LiF \cdot BeF_2$), and a TZM structure can allow for adequate breeding of tritium. In the long term, chromium-base stainless steels do present a resource problem, and a large nickel-base stainless steel technology will have to be developed if stainless steel is the commercial choice, just as a molybdenum technology will have to be developed if TZM is the commercial choice. The principal problem associated with the use of TZM is that welds in TZM, while possible with adequate purity control, have not been demonstrated to be feasible for large structures.

As a result of the above considerations, TZM has been chosen for the primary structural material to be used in the HFCTR. The problem of fabrication has, to some extent, been alleviated by a modular blanket design which allows sections of the blanket to be completely fabricated at the point of manufacture, where good quality control is feasible. The design also allows for the primary vacuum welds to be made with stainless steel in the moderator/reflector region (see Section 4.7).

TZM is compatible with FLIBE, which can provide good heat transfer while allowing net breeding ratios in excess of unity to be obtained even when penetrations of the blanket are taken into account (see Section 4.4).

The structural material choice has not been optimally integrated with other aspects of the blanket/shield design. For example, structure nearest the plasma might consist of TZM with stainless steel used at points where the neutron fluence is smaller. This arrangement improves the breeding ratio, since the parasitic low energy neutron absorption is worse for TZM than for type 316 stainless steel.

4.3 THERMAL HYDRAULICS

4.3.1 Choosing a Coolant

The coolant material for a compact, high-field tokamak reactor must be compatible with a number of stringent requirements set by the structural material choice, the limited space available for adequate breeding and shielding, and the allowable auxiliary power.

The compactness of the HFCTR design suggests the need for a dense, neutronically favorable coolant that is chemically compatible with the structural material. The available auxiliary power for coolant pumping is predominantly a question of economics. For this study a pumping power that does not exceed 2% of the gross thermal power is felt to be reasonable. This power limit favors a coolant with a moderate friction factor and a low electrical conductivity.

There are three classes of coolant materials which have acceptable thermodynamic properties: liquid metals, pressurized gases, and molten salts. Liquid metals have large electrical conductivities, and therefore result in unacceptable pressure drops due to MHD reaction to the magnetic fields. In addition, handling large mass flows of liquid metal might be difficult and hazardous.

Pressurized gases ($\sim$ 440 to 730 psi) would require a significant void fraction within the blanket and do not yield the most compact design.

Of the molten salts, an eutectic mixture of lithium fluoride and beryllium fluoride, FLIBE, seems most favorable. Its relatively low electrical conductivity greatly reduces MHD derived flow impedances and it offers good breeding within the coolant.

4.3.2 Thermal-Hydraulic Results Using FLIBE as the Coolant

The objective of the thermal hydraulic design is to show that breeding ratios larger than one can be achieved in a compact design. It is found that approximately 50 cm of lithium are required for adequate breeding. Cylindrical symmetry is used for simplicity in the calculations.

The coolant tubes make up the first wall and the four coolant channels (i.e. the channels that surround the breeding regions). Each coolant tube runs toroidally around one reactor octant and has radial inlet and outlet legs, facilitating reactor modularization. The locations, dimensions, and number of tubes per octant are given in Table 4-I. The pumping power, pressure drop, coolant velocity, and heat extraction is given in Table 4-II. It is assumed that there is a uniform neutron wall loading of 4 MW/m^2.

The inlet and outlet leg of each tube are each 4 m long and perpendicular to a 7 T toroidal field. The MHD pressure drop is estimated by extending the results of Reference [3] into the turbulent regime to get

$$\Delta P_{MHD} = 1.3 \frac{\mu v L}{(D/2)^2} \left(\frac{Ha^2}{Ha - 1} - 3 + Ha^2 \right) \tag{11}$$

where

$$Ha = \frac{B_T D}{2(\mu/\sigma)^{1/2}}$$

Table 4 - I

	Tube Inner Diameter (cm)	Tube Thickness (cm)	Tube* Location (m)	Number of Tubes per Octant
1st Wall Tubes	1.2	.15	1.40	880
1st Channel (closest to plasma)	1.33	.125	1.47	868
2nd Channel	1.33	.125	1.59	942
3rd Channel	1.33	.125	1.75	1037
4th Channel	1.33	.125	1.97	1167

*Distance is from plasma axis to tubes on the half-plane.

Table 4 - II

	Coolant Velocity (m/sec)	Pressure Drop (psi)	Heat Extracted per Octant (MW)	Pumping Power per Octant (MW)
1st Wall Tubes	3.81	127	64.2	.332
1st Channel	3.10	89.3	61.5	.230
2nd Channel	2.32	60.6	51.3	.127
3rd Channel	1.81	44.0	44.1	.029
4th Channel	1.36	30.7	37.3	.047

L is the inlet or outlet length, μ the viscosity, σ the coolant electrical conductivity, D the tube diameter and v the coolant speed. The MHD pumping power is approximately

$$P.P._{MHD} = AL\sigma v^2 B^2$$

where A is the flow area.

The first wall removes all of the alpha power, 488 MW, by way of 880 tubes which run toroidally around the inside of the torus. The induced EMF caused by the coolant flowing transverse to the ∿ 7 T field at the inlet and outlet is 0.34 volts, less than the approximate 1 volt limit set by corrosion requirements [4]. The maximum temperature of the first wall tubes is about 760 C. The bulk coolant temperature rise for all tubes is 36 C with an inlet temperature of 544 C and an exit temperature approximately 650 C.

The total pumping power of the blanket coolant is about 6.5 MW, or a ratio of pumping power to gross thermal power of about 0.3%. The worst-case radial temperature profile in the blanket assuming a uniform tube wall temperature of 650 C is shown in Figure 4-2. The radial temperature profiles vary in poloidal angle due to the nonuniform neutron wall loading. The worst-case profile (i.e. wall loading ≃ 5.6 MW/m^2) is of greatest interest, since the structural material cannot exceed the 1000 C temperature limit at any point in the blanket.

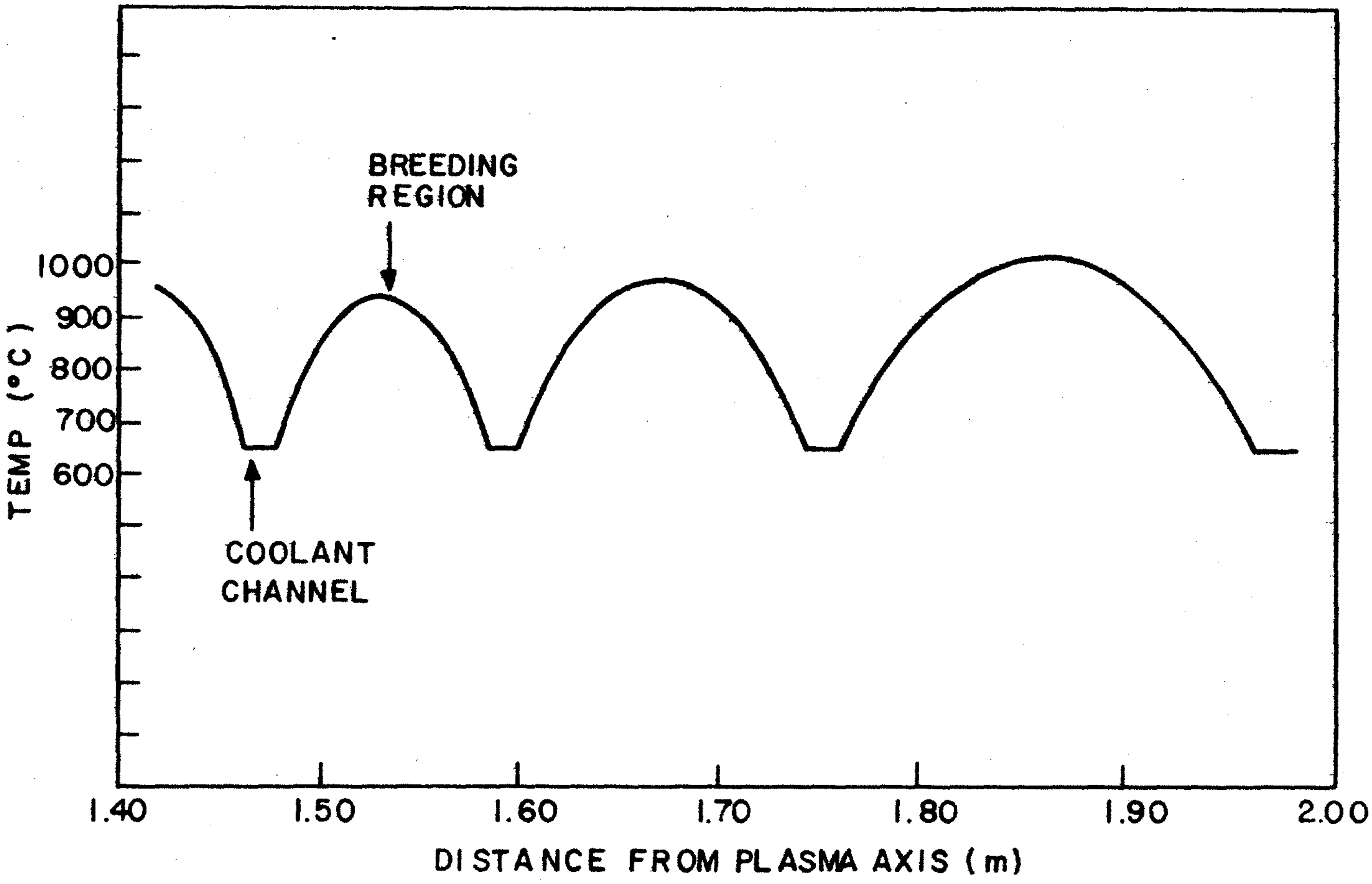

Figure 4-2 Blanket's radial temperature profile for the case of $P_w = 5.6$ MW/m^{-2}.

4.3.3 First Wall Analysis

The first wall is the first structure seen by the plasma. The tubes which comprise the first wall enter and exit radially at the ends of a module and run through a 45° section once in the toroidal direction. There are several advantages to such a scheme.

(1) The first wall does not have to withstand vacuum induced pressure loads, instead a thicker backing wall can be used to contain the lithium without the penalty of high thermal stresses from the surface heat flux.

(2) The first wall tubing has inherently low thermal stresses from the surface heat flux.

(3) If desired, the first wall can be constructed of materials other than TZM and FLIBE.

(4) If damaged, it may be possible to replace the first wall without replacing the breeding blanket.

Current Configuration

The first wall uses TZM as the structural material and FLIBE as the coolant. As shown in Appendix I, a linear elastic analysis has been performed for a cylindrical tube under the following conditions:

$$q''' = \text{constant},$$

$$\varepsilon_z = \text{constant}$$

$$\left.\frac{\partial T}{\partial r}\right|_{a_1} = \begin{cases} \dfrac{q''(a_1)}{K} \cos\theta , & \text{for } 0 \leq \theta \leq \dfrac{\pi}{2} \\ 0 , & \text{for } \dfrac{\pi}{2} < \theta < \pi \end{cases}$$

$$k \left.\frac{\partial T}{\partial r}\right|_{a_2} = h(T(a_2) - T_F)$$

where q''' is the volumetric heat generation in the tube, ε_z the strain in the z-direction, $T(r)$ the radial temperature, T_F the bulk coolant temperature, a_1 the outside tube radius, and a_2 the inside tube radius. Keeping ε_z constant assumes the tube is allowed to expand in the axial direction, but is constrained against any bending.

Using the above model along with the reference design values of $a_1 = 7.5$ mm, $a_2 = 6.0$ mm, $v_{FLIBE} = 3.81$ m/sec, and $h = 1.0 \times 10^{14}$ w/m^2 - K; Figures 4-3 and 4-4 were generated. From figure 4-4 it is apparent that the maximum film drop is 100 C and the maximum first wall temperature drop is 16 C. Figure 4-3 reveals that the maximum thermal stress is 101 MPa (14.6 ksi). Based on this latter value, it is found that $|\sigma_{max}/E| = 0.04\%$. Unirradiated data indicates a life of 10^7 cycles to failure for TZM at 1000 C with a strain range of $\sim 0.06\%$ [5]. Unfortunately the irradiated fatigue properties of TZM are not available.

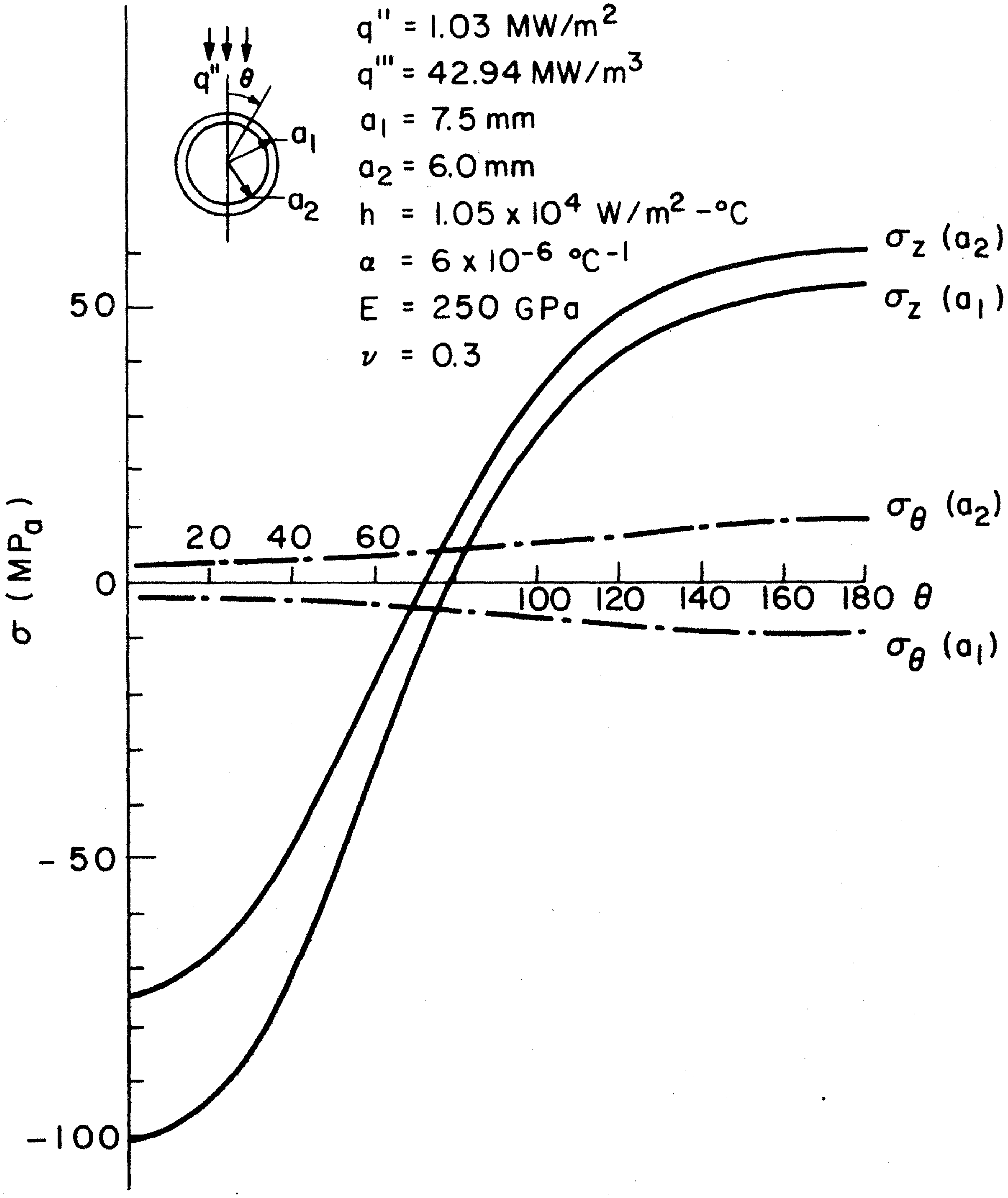

Figure 4-3 Thermally-Induced Stresses in the First Wall Cooling Tubes

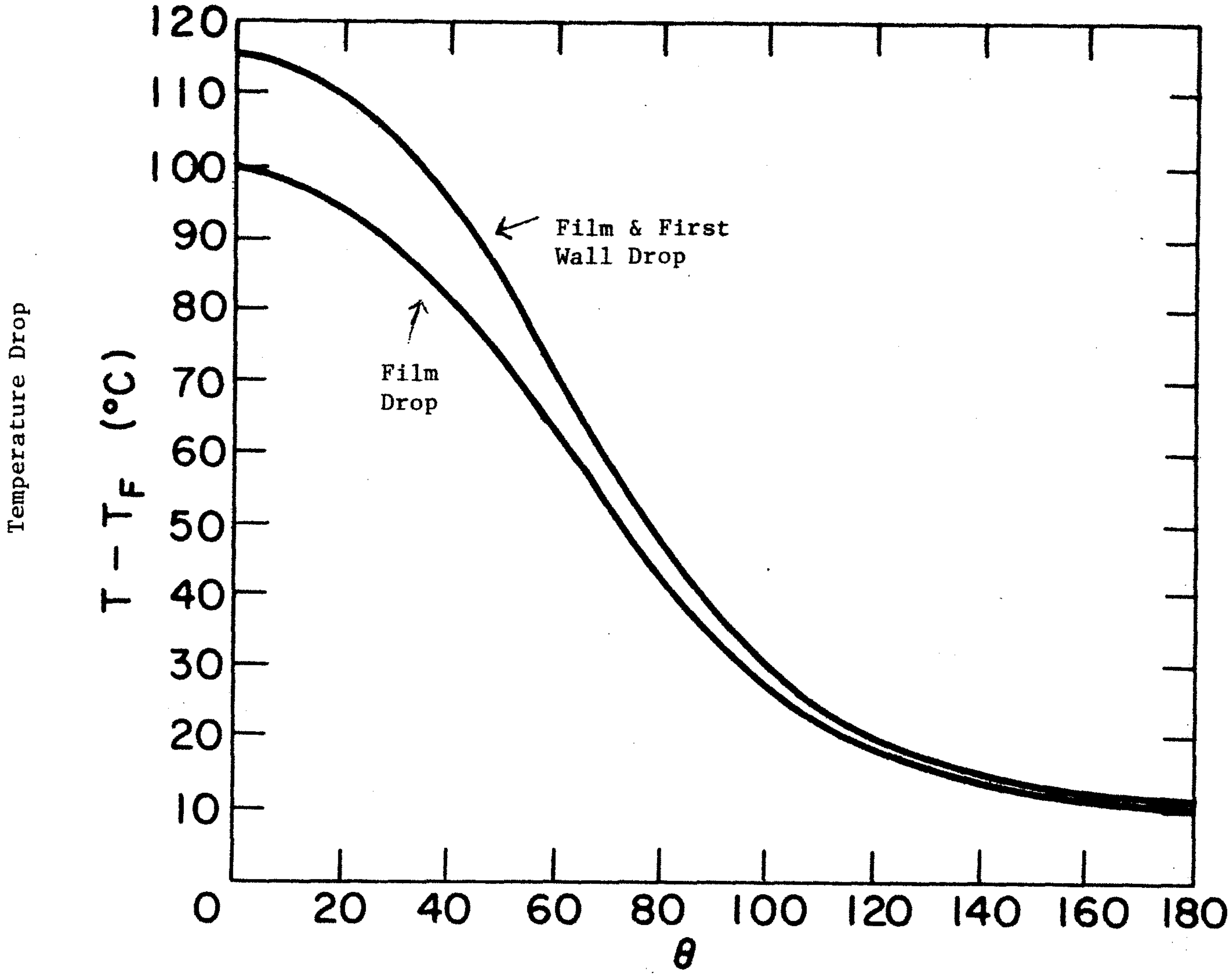

Figure 4-4 Temperature Drops vs. Cylindrical Angle in the First Wall Cooling Tubes

4.3.4 First Wall Armor

A scheme to protect the first wall tubes from plasma disruptions and also reduce the alternating component of thermal stress is currently under consideration. The basic idea is to provide thermal inertia in a first wall "armor" which would be several centimeters thick with coolant tubes welded or brazed to the back. The armor is likely to be composed of a material such as TZM. A schematic diagram of the armor is shown in Figure 4-5.

To reduce the large stresses and strains in this armor block it is proposed to cut or forge a checkboard pattern of grooves most of the way through the block. Though the stress analysis is still in a preliminary stage, a rough 2-D plain stress model indicates that the grooves reduce the axial stress in the coolant tubes by an order of magnitude. This analysis was done for the case of the groove depth equal to the separation distance between adjacent grooves.

Before the first wall armor can be incorporated into the HFCTR design, the stress levels must be more accurately estimated and the effect on the breeding ratio analyzed.

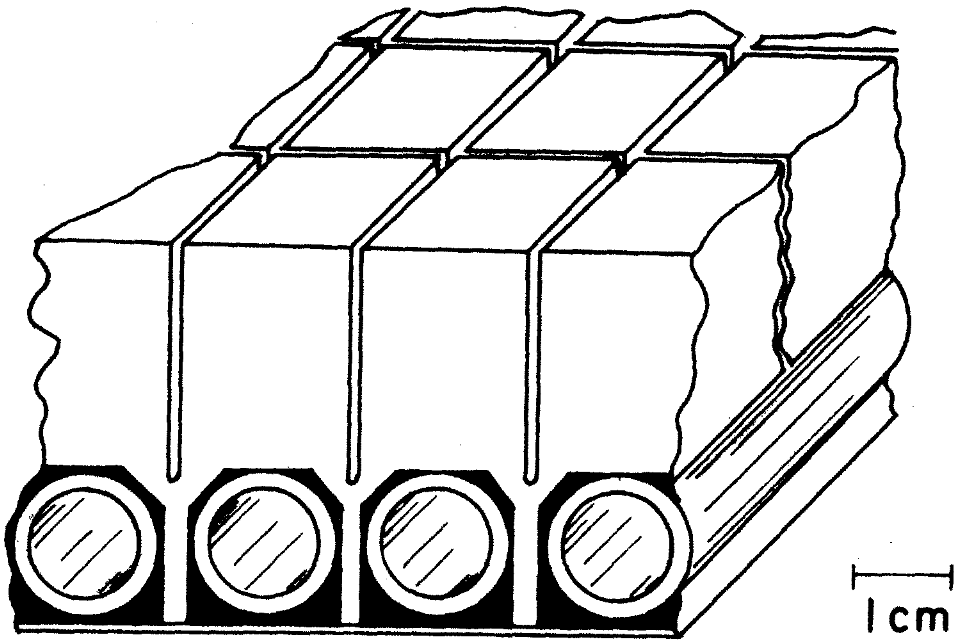

Figure 4-5 First Wall Cooling Tubes with Armor

4.4 NEUTRONICS

The primary focus of the neutronic calculations has been to determine a blanket/shield configuration which gives a satisfactory breeding ratio.

The one dimensional transport code ANISN, [5, 6, 7], has been used for the analysis. ANISN gives a discrete ordinate solution to the Boltzmann transport equation and incorporates anisotropic scattering. An S_8, P_3 approximation in cylindrical geometry was used throughout the analysis. The neutronics results described below were obtained using 20 group neutron cross section data generated for an earlier fusion reactor scoping study [8]. The accuracy of these results was verified with 121 group coupled neutron-gamma cross section data set from ORNL [9].

The criteria for the breeding ratio are discussed in Appendix F. The present design gives an estimated net breeding ratio of 1.05. The neutron attenuation criteria for adequate coil shielding are discussed in Section 4.5. Finalization of the design will require modification of the outboard and inboard configurations to provide adequate neutron attenuation while maintaining a breeding ratio greater than unity.

4.4.1 Comparison of Inboard and Outboard Configurations

The geometry of a compact tokamak reactor imposes rigid constraints on the size of the blanket and shield, especially toward the center of the torus. This "inboard" blanket/shield thickness is limited to approximately 1.0 meter while the "outboard" blanket/shield thickness limit is approximately 1.3 meters. The respective breeding ratios in the inboard and outboard blanket/shield configurations necessary to give a net breeding ratio greater than unity are discussed in Appendix F.

Based on equilibrium and toroidal coil shielding requirements coupled with space limitations (as discussed in Section 4.5) the present outboard blanket/shield will provide adequate shielding of the equilibrium coils. However, additional shielding is necessary for the toroidal coils. It is expected that this can be achieved while meeting breeding ratio requirements in the following manner:

(1) Optimize breeding in the outboard blanket/shield with the constraint of maintaining adequate equilibrium coil shielding;

(2) Optimize shielding of the inboard blanket/shield so that the toroidal coil shielding requirements are met; and

(3) Add an additional shield between the equilibrium and toroidal coils on the outboard side of the reactor to meet toroidal coil shielding requirements.

This scheme appears realizable in terms of present overall design limitations, but will have to be demonstrated by neutronic calculations.

The neutronic calculations thus far performed focused on the outboard blanket/shield breeding ratio. However, comparative calculations were made for realistic-size inboard configurations and showed these inboard configurations to breed at approximately 75% of the outboard configurations. As stated previously, it is anticipated that inboard shielding requirements will necessitate reducing the breeding capability of the inboard configuration.

4.4.2 Outboard Blanket/Shield Analysis

Design Considerations

The design of the outboard blanket/shield configuration evolved through a series of neutronic calculations, taking into account thermal hydraulic considerations as described in Section 4.3, to that shown in Figure 4-6.

Results of Calculations

The results of the neutronic calculations for the outboard blanket/shield configuration are shown below.

Problem ID	Breeding Ratio	Neutron Current Attenuation Factor	Blanket/Shield Thickness cm	Comment
700	1.18	3.6×10^3	119	Reference case (Figure 4-6)
701	1.23	5.9×10^3	124	Increase thickness of last cooling channel to 7 cm
700 A	1.23	2.5×10^3	119	121 group calculations - compare with 700

The reference calculation, modelling the configuration shown in Figure 4-6, gave a breeding ratio of 1.18 using the preliminary 20 group neutron cross section data set. A 5% increase in the breeding ratio was obtained by increasing the thickness of the outer coolant by 5 cm.

4.5 NEUTRONIC SHIELDING OF COILS

4.5.1 Normal Coil Radiation Damage Estimates

The normal coil systems that are inside the TF coils must be adequately shielded from neutrons to prevent excessive damage. The most vulnerable part of these coils is the insulation. Studies of neutron damage (fission spectrum) have indicated the types of insulation that are usable at increasingly higher integrated neutron fluences: (1) mylar, (2) epoxy-impregnated fiberglass, (3) mica, and (4) alumina. The mode of "failure" is a major resistivity

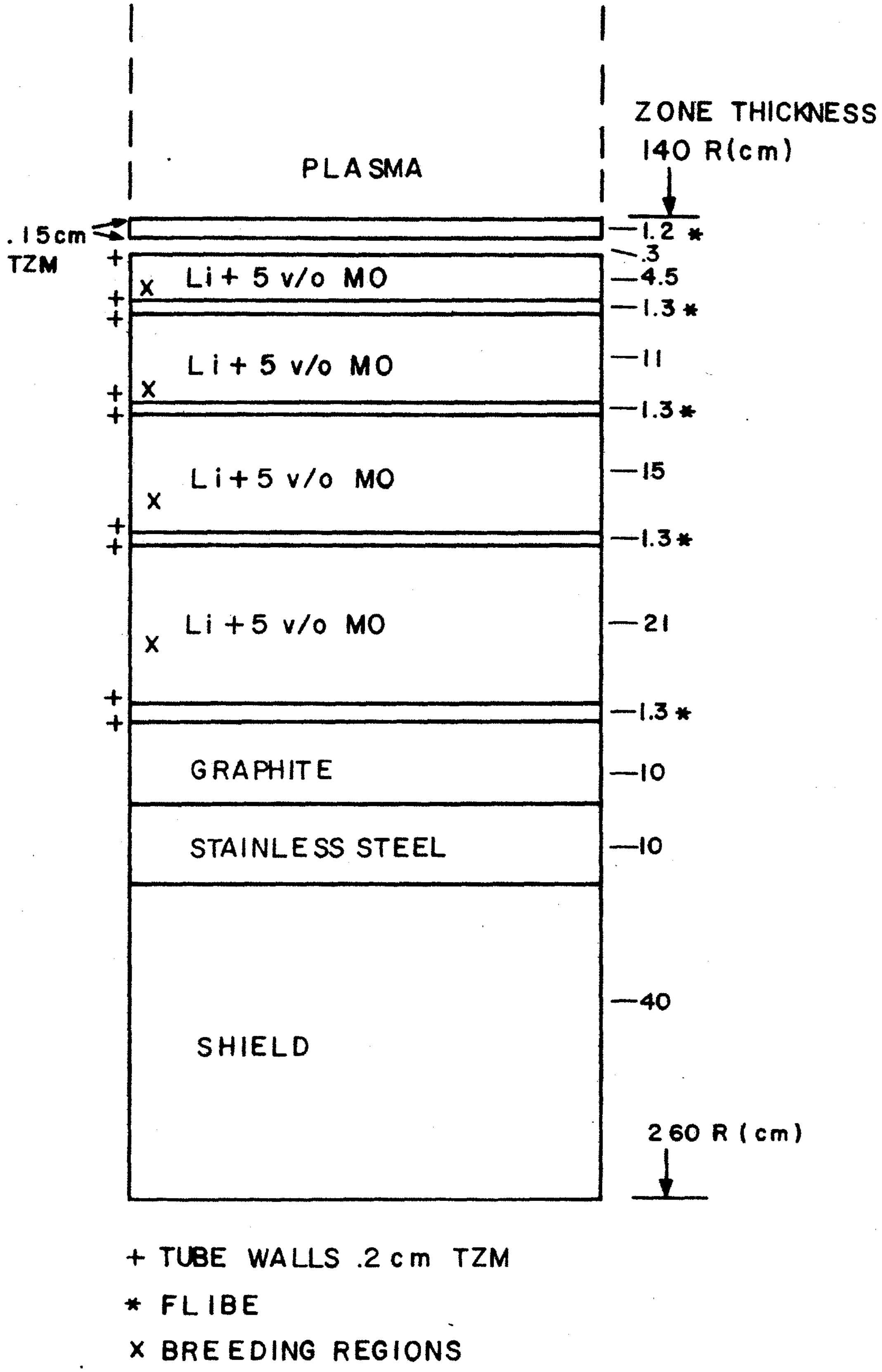

Figure 4-6 Outboard blanket/shield configuration.

decrease which occurs at the onset of severe structural damage (i.e., usually not before structural damage).

Mylar is easy to use, but is subject to rapid damage for the anticipated neutron flux. Glass-epoxy is also easy to use and can withstand a neutron fluence which is an order of magnitude larger than mylar (i.e. considerable glass-epoxy damage occurs at 10^{22} neutrons/m^2). Phylogopite mica with an inorganic binder can be used up to 980 C and can tolerate a large neutron fluence ($\sim 10^{25}$ neutrons/m^2). Alumina can tolerate the greatest neutron fluence, but may be too difficult to use on a large scale in complex geometry [10].

The integrated first wall neutron fluence, corresponding to a first wall neutron loading of 4 MW/m^2, is 1.8×10^{18} neutrons/m^2 - sec, or 5.6×10^{25} neutrons/m^2 - year. This is based on an average first wall neutron loading of 3.4 MW/m^2 - year for an 85% duty cycle. The normal coils will be exposed to this higher than average neutron flux due to the asymmetry of the plasma. As shown in Figure 1-3, the normal coil shielding requirement is dependent on the attenuation characteristics of the outboard blanket/shield. The outboard blanket/shield then must reduce the neutron current incident on the normal coils such that their insulation lifetime is greater than the lifetime of the plant (about 20 years).

The neutron current attenuation of the outboard blanket/shield as now designed is 2.5×10^3. (See Figure 4-3 and Section 4.4) This gives a maximum neutron current at the normal coils of 2.0×10^{22} neutrons/m^2 - year. The estimated normal coil insulation lifetime is then approximately 0.5 years for glass epoxy and 500 years for mica. Hence, if mica is used as the insulator the neutron attenuation of the current outboard blanket/shield design is adequate to ensure a 20 year insulation lifetime.

4.5.2 TF Coil Radiation Damage Estimates

Neutron damage to the TF coil occurs in many ways, including:

(1) damage to the superconductor itself, resulting in a lower critical temperature and a lower critical current density at a given value of magnetic field strength, and

(2) increase in the resistivity of the stabilizer material contained within the superconducting coils.

Both of these effects have been considered and adequate shielding provided to assure operationally acceptable TF coils system characteristics. Damage to ground wall insulation has not yet been considered.

Superconductor Damage

For Nb_3Sn, the critical temperature is lowered about 0.8 C for a neutron fluence of 4×10^{22} neutrons/m^2 [11] ($E > 0.1$ MeV). The critical current density is not appreciably degraded for integrated fluxes up to 5×10^{22} neutrons/m^2 [11]. This damage may be fully reversed by a 300 K anneal. Using the criterion that the neutron fluence to the superconductor must not exceed 4×10^{22} neutrons/m^2 for the 20 year design plant life, the required maximum neutron attenuation factor is 2.5×10^4, based on a first wall neutron loading of 4 MW/m^2 at an 85% duty cycle.

Stabilizer Damage

The stabilizer material incorporated in a superconducting composite is required to carry the current in the coil at times when the superconductor goes normal. The electrical resistivity of this material is of primary concern; thus factors that increase the resistivity must be taken into account. The neutron fluence is one such factor.

There are two possible choices for stabilizer material, copper or very pure aluminum. The rate of resistivity increase with neutron fluence (E > 0.1 MeV) for these two materials is given by [11]

$$\text{Copper:} \quad \frac{\Delta \eta}{\phi_n} = (8 \pm 1) \times 10^{-26} \frac{\Omega - \text{cm}}{\text{n} - \text{cm}^{-2}}$$

$$\text{Aluminum:} \quad \frac{\Delta \eta}{\phi_n} = (3 \pm 1) \times 10^{-25} \frac{\Omega - \text{cm}}{\text{n} - \text{cm}^{-2}}$$

The initial resistivities of copper and pure aluminum at 13 T (at 4 K) are approximately 6×10^{-8} Ω - cm and 8×10^{-9} Ω - cm, respectively. The incremental change and final resistivity for a neutron fluence of 4×10^{22} neutrons/m^2 is given in the table below:

	$\Delta\eta$	η_{final}
Copper	320×10^{-9} Ω - cm	380×10^{-9} Ω - cm
Aluminum	1200×10^{-9} Ω - cm	1208×10^{-9} Ω - cm

These large changes are unacceptable, implying that much better shielding is needed than is required to protect the superconductor alone.

Designing the TF coils for a 20 year lifetime, and assuming a maximum first wall neutron loading of 4.9×10^{25} neutrons/m^2 - year, a neutron attenuation factor of 1×10^6 would produce the following:

	$\Delta\eta$	η_{final}
Copper	8×10^{-9} Ω - cm	68×10^{-9} Ω - cm
Aluminum	30×10^{-9} Ω- cm	38×10^{-9} Ω - cm

These final resistivity values are probably within acceptable limits. Because of the unique capability of the HFCTR to remove a TF coil module during each routine blanket and first wall replacement, defects could be annealed out regularly, during the life of the reactor.

The outboard blanket/shield as now designed gives a neutron attenuation factor of 2.5×10^3 (see Section 4.4). The outboard blanket/shield will not by itself be able to attenuate the fast neutron flux by the additional factor of 400 required to meet the attenuation criterion of 1×10^6. However, there is at least 0.2 m of usable space between the blanket/shield and the TF coils in which a secondary shield can be located. The outboard blanket/shield itself, (required to provide most or even all the breeding capability of the system) can be extended an additional 0.2 m in thickness, and has still to be optimized for breeding and shielding characteristics.

The limited usable space between the first wall and the TF coils on the inboard side of the torus (1.0 m), coupled with the goal of obtaining a fast neutron attenuation factor of 1×10^6, may necessitate that the inboard blanket/shield simply provide shielding, and no breeding. It has been calculated that 97 cm of a 30% B_4C, 70% S.S. shield provides the required attenuation. A pure shield on the inboard side is also desirable from the viewpoint of engineering design simplification.

4.6 BEAMLINE SHIELDING

The injector ports must be shielded during the burn phase of the operation cycle such that the neutron flux on the closest TF coils remains within the limits defined in Section 4.5. This additional shielding is expected to be minimal, since shielding plugs will be placed in the injector ports during the burn phase to protect the cryopanels in the beamlines. However, there is enough space near the beamlines where additional local shielding can be provided.

REFERENCES - SECTION 4

[1] Conn, R. W., in "Proc. ANS Conf. on the Technology of Controlled Nuclear Fusion", Richland, Washington, Sept. 1976.

[2] UWMAK III, Fusion Feasability Study Group, University of Wisconsin, Madison, Wisconsin (1976).

[3] Hoffman, M. A. and G. A. Carlson, "Calculation Techniques for Estimating the Pressure Loss for Conducting Fluid Flow in Magnetic Fields". Lawrence Rad. Lab UCRL - 51010 (1973).

[4] W. R. Grimes and S. Cantor, "Molten Salts as Blanket Fluids in Controlled Fusion Reactors", ORNL Report ORNL-TM-4047 (1972).

[5] Engle, W. W., "ANISN, A One-Dimensional Transport Code, General Anisotropic Sn", ORNL (1965).

[6] Bell, G. I., Hansen, G. E., and Sandmeier, H. A., "Multiple Treatment of Anisotropic Scattering in Sn Multigroup Transport Calculations", Nuc. Sci. Engr., 28, 376 (1967).

[7] Abdou, M. A. and Maywood, C. W., "Neutronics and Photonics Design for CTR Blankets and Shields", Nuclear Engineering Department, Univ. of Wisconsin, 206-234 (July, 1973).

[8] Cook, A. G., Department of Nuclear Engineering, M. S. Thesis, MIT (1976), unpublished.

[9] DLC-37, Coupled 100 Neutron, 21 Gammam Ray Group Cross Sections for EPR Neutronics, RSIC, ORNL, March 1977.

[10] Hay, R. D. and E. J. Rapperport, "A Review of Electrical Insulation in Superconducting Magnets for Fusion Reactors," MEA, Cambridge, MA (1976).

11 Guess, J. F. et al., "A Survey of Radiation Damage Effects in Superconductivity Magnet Components and Systems", ORNL-TM-5187 (1975).

5. COIL SYSTEM MECHANICAL DESIGN

The coil system mechanical design includes many original features in order to achieve both total modularization and the nearly monolithic structure necessary to support high magnetic forces. Total modularization requires a cryostat with moveable walls, flat electrical joints in the inner equilibrium field coils, mechanical vacuum seals, module transporters, and a system of automated actuators. The high strength structure requires a good press fit between coils in adjacent modules, support of overturning loads by a staggered set of shear panels and friction between coil modules, and supplementary support of vertical coil forces through the end caps and central column. These design concepts are described in this section and the overall mechanical layout is illustrated.

5.1 BASIC CONCEPT

The basic concept of the HFCTR is eight wheeled modules which can be rolled together into a toroidal configuration around a central core. Each module as illustrated in Figure 5-1 consists of two superconducting toroidal field coils, a sector of the blanket and shield, and segments of the copper vertical field coils all permanently mounted on a wheeled base, so that one of the modules can be pulled out of the toroid and be replaced with a precooled spare module.

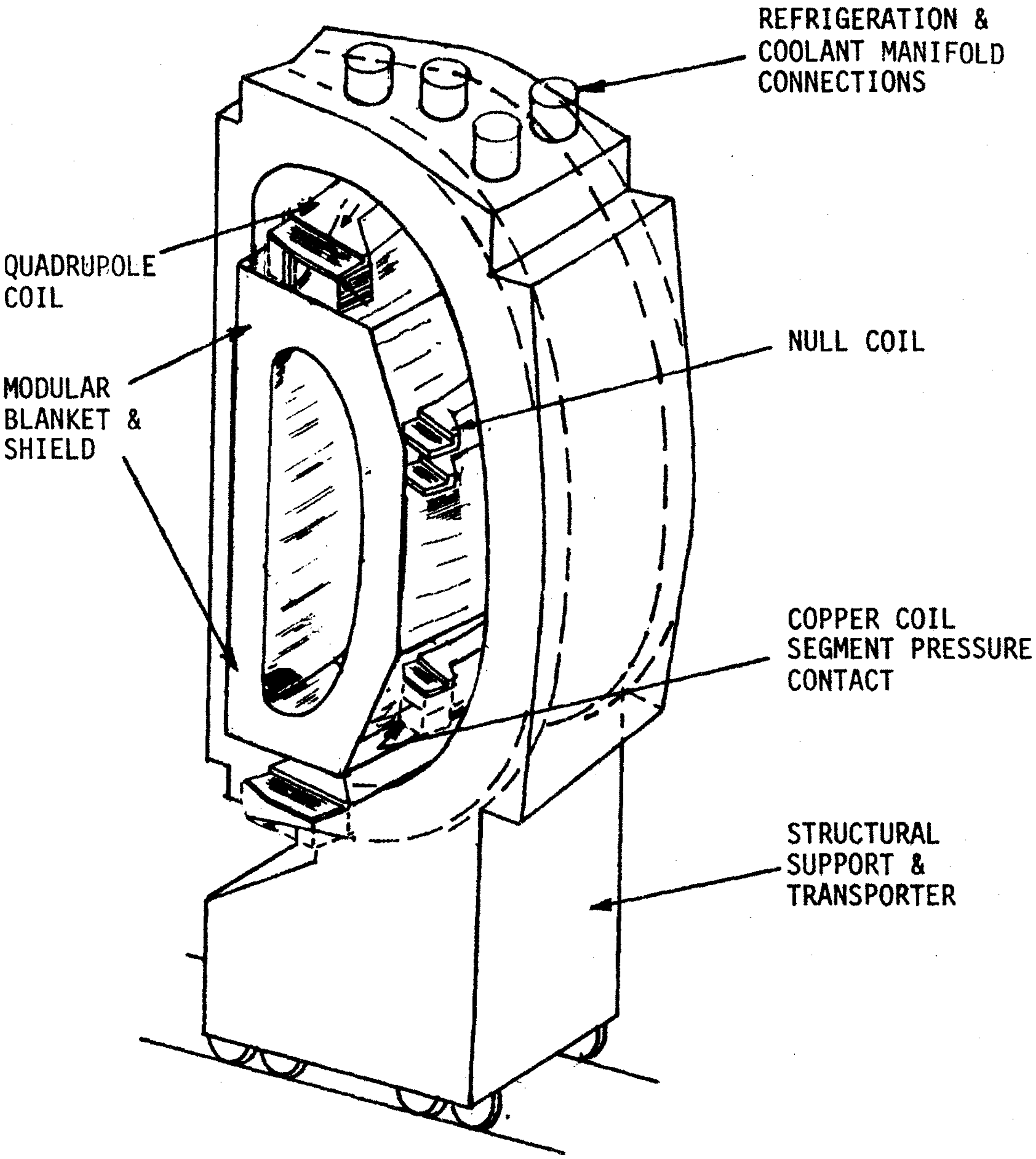

Figure 5-1 TF Sector Module

The goal of modularization is to provide a reactor in which a sector of the blanket or a damaged TF coil can be replaced within a few days. High availability is essential to the economic performance of any power plant.

The wheeled base is equipped with two sets of wheels so that the module can be moved on a radial track out of the toroidal configuration and then transported circumferentially around the reactor to a radial track which will guide the module to a hot cell where detailed disassembly and repair can be performed. Such a set of tracks is illustrated in Figure 5-2. The reactor and the tracks are located in a helium filled building at atmospheric pressure.

The reactor cell has walls of concrete approximately two meters thick to provide shielding for personnel during the operation of the reactor. The space inside the building cannot be entered by unskilled personnel during brief shutdown periods and all maintenance operations will be performed remotely. The building also provides support for a framework which carries the upper OH and dipole coils when disassembled and carries all of the lines and quick disconnects which bring power and coolants to the reactor. The neutral beam injectors can be retracted into pits between the radial tracks so that they can be moved out of the way to permit the withdrawal of a module (Figure 5-3).

By moving large modules to a hot cell for detailed repair the repairs can be made after the reactor is back in operation. Modularization greatly simplifies the remote handling equipment which must be in the vicinity of

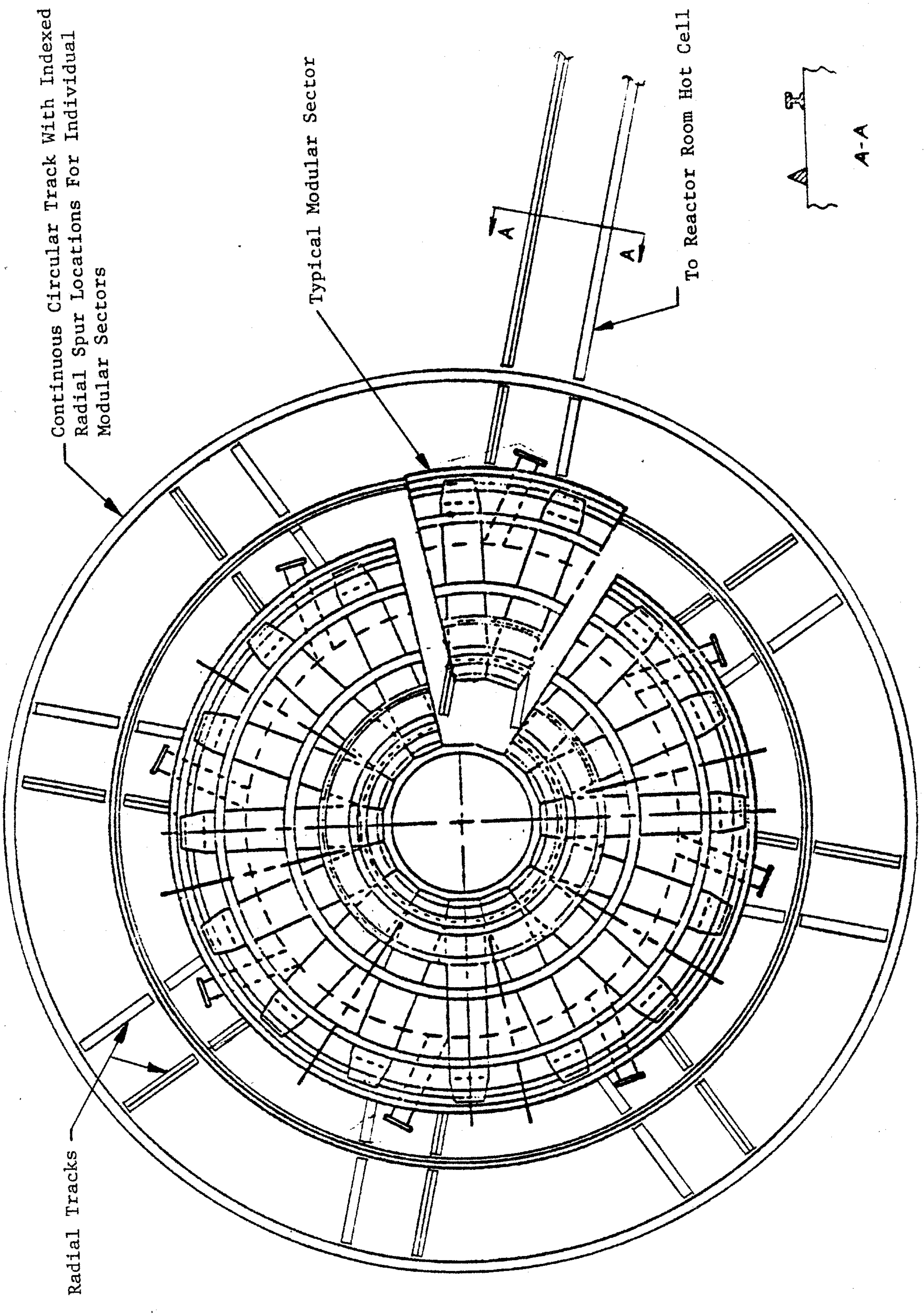

Figure 5-2 Plan View Showing Track System

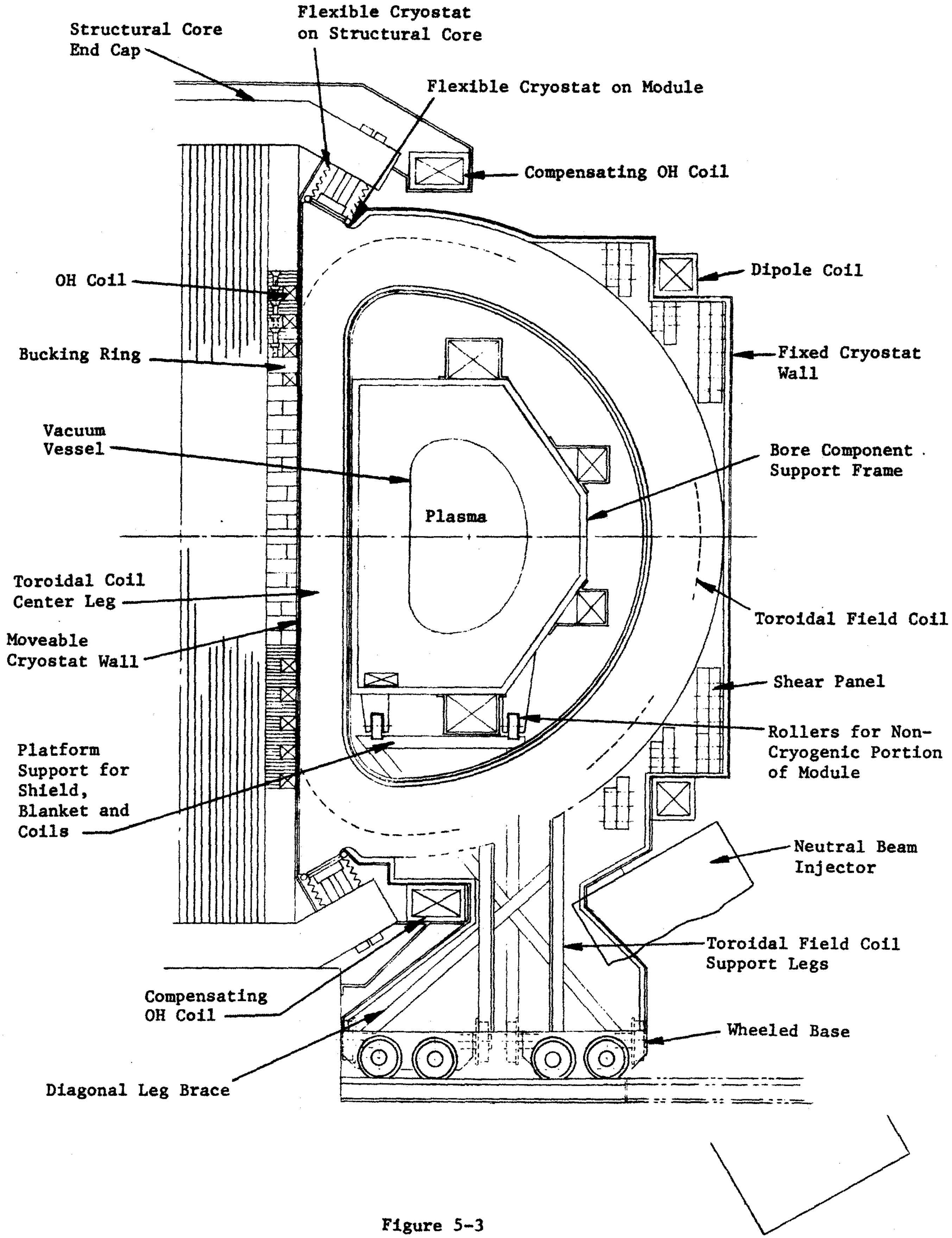
Structural Core
End Cap
Flexible Cryostat
on Structural Core
Flexible Cryostat on Module
Compensating OH Coil
Dipole Coil
OH Coil
Bucking Ring
Fixed Cryostat
Wall
Vacuum
Vessel
Bore Component
Support Frame
Plasma
Toroidal Coil
Center Leg
Toroidal Field Coil
Moveable
Cryostat Wall
Shear Panel
Rollers for Non-
Cryogenic Portion
of Module
Platform
Support for
Shield,
Blanket and
Coils
Neutral Beam
Injector
Toroidal Field Coil
Support Legs
Compensating
OH Coil
Wheeled Base
Diagonal Leg Brace

Figure 5-3

the reactor. This equipment will be in the nature of automatic devices which are built to perform a specific function with minimal human monitoring, instead of manipulators which require a human operator. No manipulators are required for the exchange of a module. However, manipulators in a shielded mobile floor unit are available as a backup in case of a failure of the automatic devices.

5.2 MODULE STRUCTURAL SUPPORT

The details of the construction of a module are shown in Figures 5-3, 5-4, and 5-5. The basic mechanical structure is a wedge shaped box formed by two TF coils and the shear panels which fasten them rigidly together. This box structure is supported on four legs which rest on the wheeled base.

This box construction makes the concept of modularization possible because it provides a way to support the individual TF coils against the out-of-plane forces without having shear panels between the modules. The modules can be removed without having to dismantle shear panels. This greatly simplifies the automation of the module replacement process and greatly simplifies the provision of a cryostat around each individual module. The manner in which the out-of-plane forces on a module are supported is shown in Figure 5-5. The force couple applied to the box by the out-of-plane forces is balanced by clamping the wheeled base solidly to the track which is part of the floor of the building. Sixteen bolts of .2 m diameter located 2 m from the module center line on either side of the module will be required to carry the 13.6 MN anchoring force if operated at 75% of a 517 MN/m^2 yield stress. The residual out-of-plane force along with the weight of the TF coils is taken from the 4 K TF coil to the 300 K wheeled base through the long thermal path of the legs.

The bolt size calculation assumes that none of the out-of-plane force couple is supported by the structural core. Actually the friction of the centering force on the bucking cylinder, assuming a coefficient of friction of 0.2, is adequate to completely support all the out-of-plane forces developed in the module. However, the transfer of the out-of-the plane forces in the outer leg to the portion of the center leg which is in contact with the bucking cylinder places additional bending stress on the TF coil plates. (See Section 5-7 and Figure 5-10.) The size of this additional loading is not easy to calculate and remains to be investigated. Also the torsional rigidity of the built up structural column should be calculated to determine if the torsion produced by the out-of-plane forces would cause an unacceptable deflection, before using the center column to support out-of-plane forces.

5.3 THE MODULE CRYOSTAT

Each module is enclosed in its own individual form fitting cryostat wall which is shown by the double line in Figures 5-3, 5-4, and 5-6. The cryostat wall is supported about 0.635 cm away from the coil surface on thermally

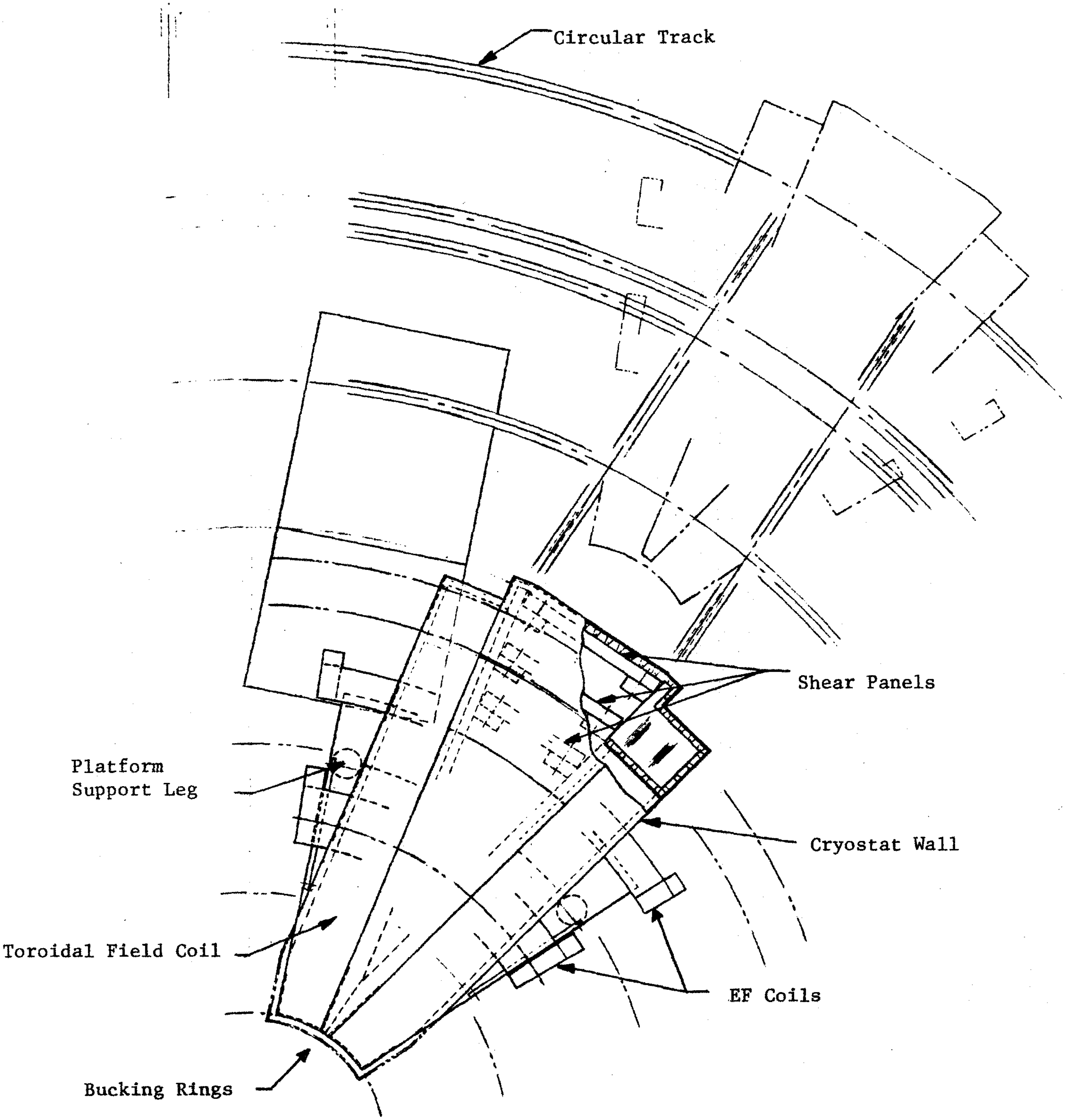

Figure 5-4 Top View of a Module

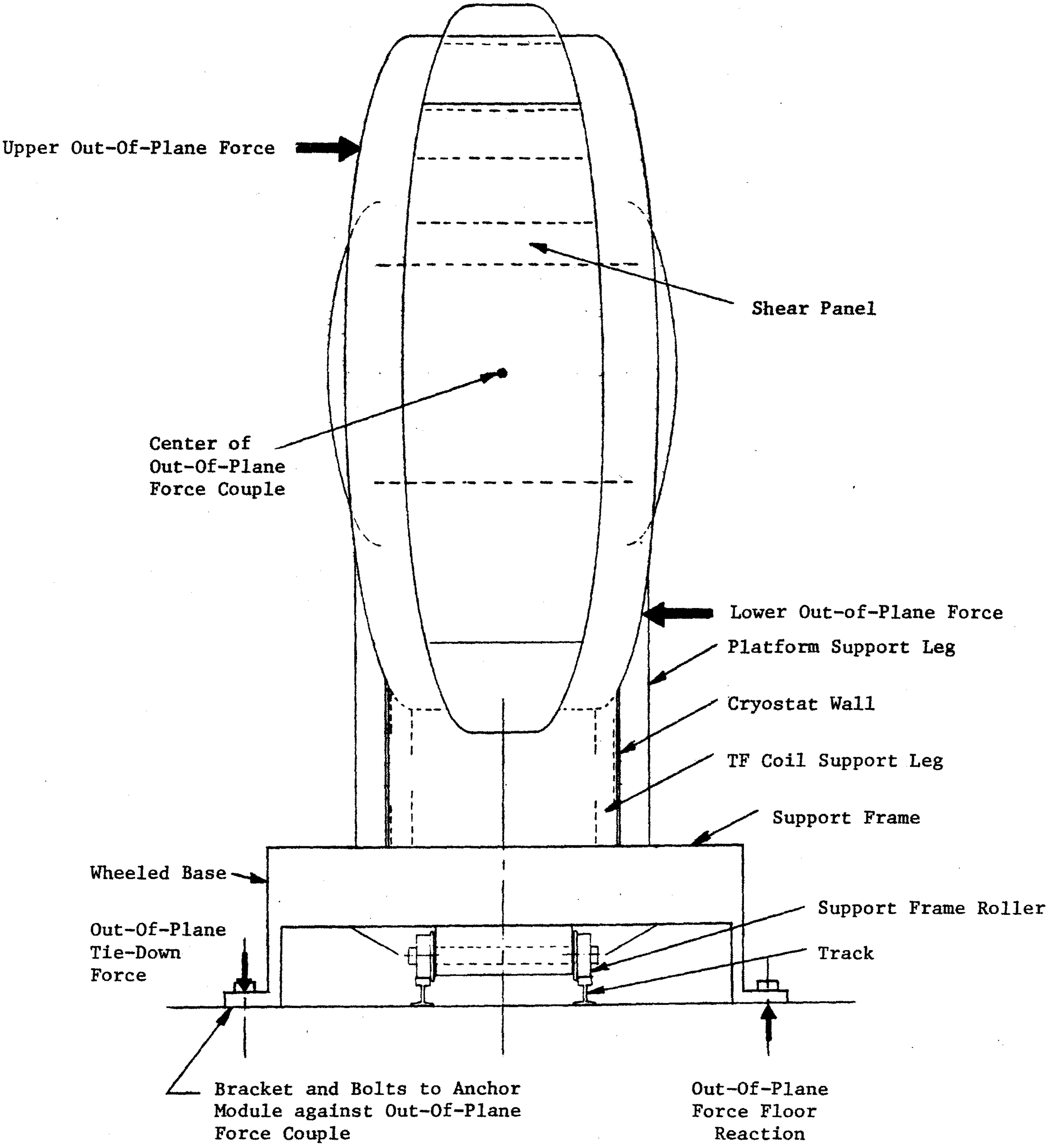

Figure 5-5 View of Module Looking Toward Center of the Toroid

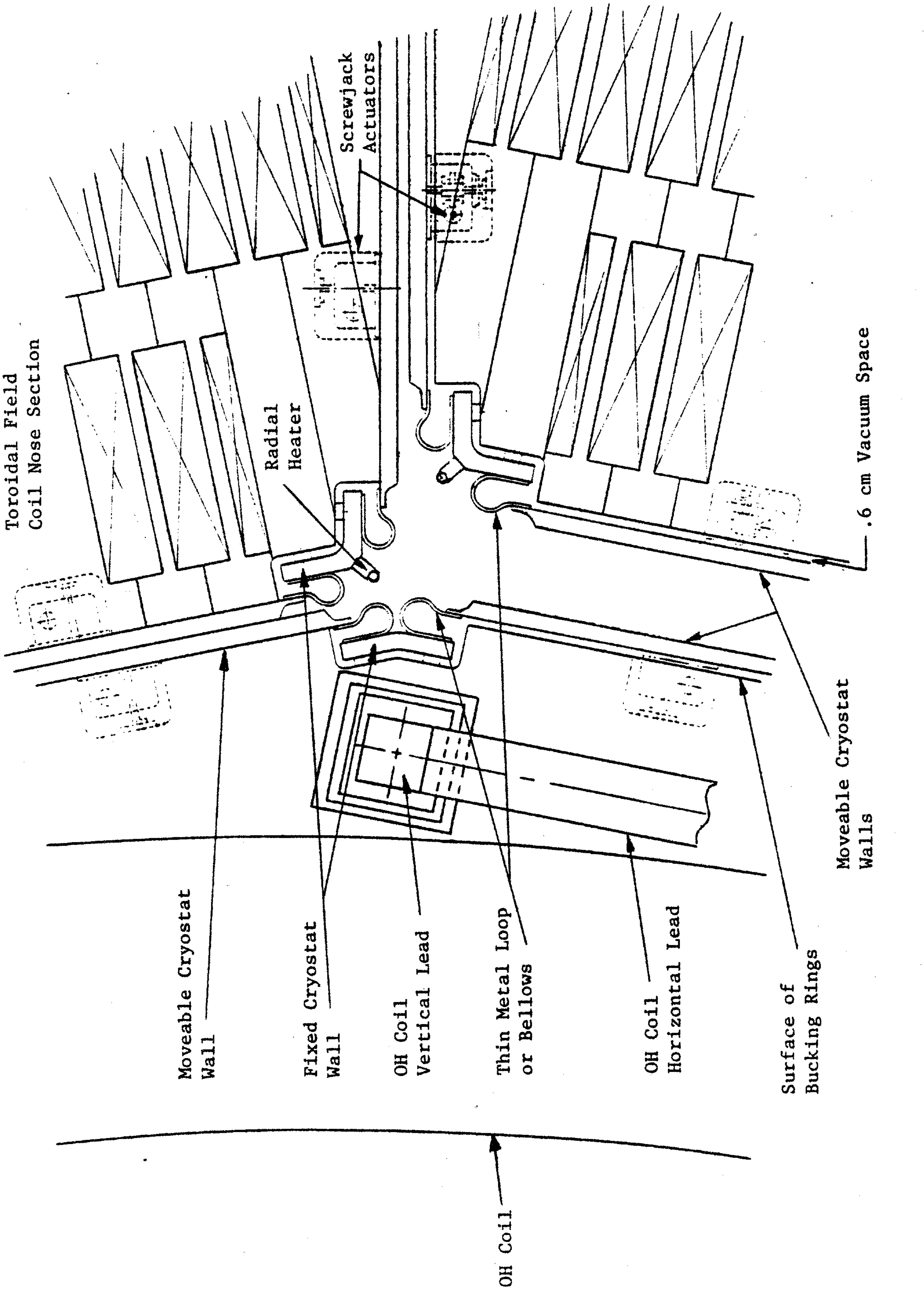

Figure 5-6 Details of Moveable Cryostat Walls and OH Coil Leads at TF Coil Nose

insulating standoffs fastened to the coil plates. The cryostat wall encloses the two TF coils and the shear panels between them. It also encloses the support legs and the diagonal braces for the legs. The cryostat wall must be thick enough to carry the one atmosphere loading without excessive deflection, but this is not difficult to achieve because the coil and the shear panels are provided with enough standoffs so that the external load is effectively transferred to the coil plate structure. At no place are magnetic forces carried across the insulating vacuum space except at the legs.

At the center leg where the TF coils at 4 K come in contact with the structural core bucking cylinder which is also at 4 K and the neighboring TF coils which are at 4 K, the cryostat wall is permitted to collapse so that no vacuum space remains. This moveable cryostat wall is a flat plate which is either supported by Bellville springs or by small screwjack actuators so that the wall can be driven against the atmospheric pressure away from the surface of the 4 K coil to develop an insulating vacuum whenever the module is removed. Figure 5-6 shows how the moveable cryostat walls will be arranged on the TF coil and bucking cylinder at the TF coil nose. A thin metal loop or a bellows permits the moveable cryostat wall to move with respect to the fixed cryostat wall. Such moveable cryostat walls are required at every point where a force is applied to the 4 K coil from an adjacent 4 K structure. This situation also occurs where the structural core end caps contact the ends of the straight central leg of the TF coils, as can be seen in Figure 5-3.

The moveable cryostat vacuum wall which makes possible the form-fitting cryostat introduces one major problem. When the TF coils are in place against the bucking cylinder and the cryostat walls are collapsed against the TF coil, the walls then acquire the 4 K temperature of the coil. The air outside the cryostat walls may enter the cracks between the collapsed cryostat walls and freeze, thus bonding the modules to the bucking cylinder. If the reactor cell operated in an atmospheric air environment, it is expected that the bellows areas would eventually be filled with frozen air. This causes no problem during the operation of the reactor, but the frozen joints must be unbonded prior to removing a module for replacement.

The problem of freeing frozen cryostat walls can be solved by electrically heating the collapsible cryostat walls on the module to be moved and by heating the adjacent walls on the neighboring modules and bucking cylinder. This is done by passing current through the high resistance stainless steel moveable cryostat walls for a few minutes before the module is to be moved. Tubular electric heating elements are installed at the corners of the modules to melt the ice in the vicinity of the flexible bellows. After a module has been removed, the current in the moveable cryostat walls is turned off and when the insulating vacuum space is reestablished, the room temperature atmospheric helium over the surface of the cryostat walls will keep them warm enough to prevent air from freezing. The radiant heater in the corner next to the bucking cylinder formed by the removal of a module may have to be left on to prevent a continuous buildup of ice or frozen air which would prevent the reinsertion of a module. Quite possibly such a heater might be required at the crack between the cryostats at the bore side of the inner leg of the TF coil but the presence of the hot vacuum vessel should prevent any appreciable buildup of frozen air or frozen water vapor at this joint. Rough calculations indicate that heating the collapsible cryostat walls for five minutes should be adequate to free them. During this time there will be little heating of the coil because the heat transfer across the collapsed vacuum space will be lowered when the TF coil centering force is relaxed. An alternative defrosting technique is to use a directed beam of near infrared energy to heat the frozen air and ice directly without appreciably heating the cold structure.

A vacuum enclosure around the entire reactor either at the outer periphery of the torus or beyond the circumferential track would at first glance appear to be a positive solution to the crack freeze-up problem. But both locations have disadvantages which make them unattractive.

A vacuum shell at the periphery of the torus would have to have openings through which a module could be moved. During the time that the vacuum is released and this opening is uncovered, air will freeze in all the cracks between the modules which have not been moved. The removal of a module through the side of the shell without breaking the vacuum on the shell is impractical considering the immense size of the vacuum transfer container which would be required.

A vacuum shell beyond the circumferential track would permit the modules to be removed and replaced without leaving the vacuum environment. But such a vacuum shell would in fact be a vacuum building of a size considerably greater than the NASA Test Facility at Plum Brook, Ohio [1]. A fair and systematic comparison between the three possible operating environments of vacuum, atmospheric air and atmospheric helium remains a subject for further study. However, a few major design considerations should be noted concerning the trade-off between the three candidate atmospheres. Notice that the reference design incorporates all of the same features in the flexible cryostat design that it would have in an atmospheric air environment, with provisions for rapidly defrosting frozen air. This is because of the possibility that residual air and water in an evacuated or helium environment will gradually condense and build up on the cold exposed surfaces. While the avoidance of frozen air is a possible major advantage of helium or vacuum, the principal motivations for the use of helium or vacuum are to avoid long down times due to the need for substantial detritiation before opening up the primary vacuum vessel to air and the time required to reestablish high vacuum in the plasma region after reassembly. The use of a vacuum environment is expected to be superior to helium for both of these purposes. A vacuum environment may even eliminate the need for a flexible cryostat on the inner TF coil leg. A portable nitrogen-cooled radiation screen could drop in front of the exposed surfaces, when a TF coil has to be moved.

5.4 THE MODULE BLANKET, SHIELD AND PF COILS

The module is made up of the cryostat and the parts that are contained in it and the blanket, shield and PF coil components which are outside the cryostat in the atmosphere. These two portions of the module have no contact with each other except at the surface of the wheeled base.

The support legs for the shield, blanket, and coil sector are located outside of the cryostat as can be seen in Figure 5-4. These legs support a platform at the bottom of the TF coil bore which carries a sector of circular track. The frame which carries the shield, blanket, and coils has rollers which roll on the track so that this non-cryogenic portion of the module can be rolled out of the bore of the coil and onto a transport cart which can carry it to a hot cell. Thus it is not necessary to move the entire module circumferentially to a hot cell if only the blanket is to be replaced.

Figure 5-4 also shows that the outer surface of this blanket, shield, and coil structure is exposed between the modules and is therefore readily accessible for the automatic connection of the neutral beam injectors, coil leads, and coolant leads. These latter two connections are made from the building-supported frame above the reactor where they can be readily retracted out of the way of the radial movement of the module.

5.5 POLOIDAL FIELD COIL CONNECTOR DESIGN

In previous tokamak designs, the TF coils can not be removed for repair because they are locked into place by the vacuum vessel and PF coils which pass through the bore of the coil and by the shear panels which are bolted between the TF coils. In order to modularize the HFCTR so that the TF coils can be pulled out, all three of these locks must be broken. In Section 5.2 a solution to the shear panel barrier was described. This section presents a PF coil connector design which should break the PF coil barrier.

Ideally, when a module is rolled into its position in the toroid, every turn of each of the four PF coils inside the bore should make a reliable contact with the same turn in the adjacent module. These conductor connections should have a contact drop which is low enough to assure that the temperature never rises high enough to cause damage to the conductor contact surface or the conductor insulation. In addition the hoop tension in the coil must be carried around the electrical joint in a way which will guarantee that the contact surface will not wear out in millions of plasma pulses. It is estimated that tolerance buildup could cause a given coil turn to be as much as 0.6 cm out of vertical alignment with its neighbor. Even to attain this alignment, leveling jacks will have to be provided to make adjustments in the vertical position of the TF coil bore frame which supports the PF coil segments. It is optimistic to expect that the assembly tolerance can be maintained down through the bore components support wheels, the module rollers and foundation and back up through these same components to the appropriate coil turn in the neighboring module.

Each quadrupole and null coil must develop 3,200,000 ampere turns. As a compromise between the desirability of lower current to minimize bus costs and higher current to make the connector design easier the current in each conductor will be 128,000 amperes. It is believed that the connector design which follows can meet all of these specifications.

Figure 5-7 shows a side view of the connectors. The copper conductors are firmly clamped together in the bore components frame which can be seen in Figure 5-3. These conductors will be plates 103 cm wide formed by brazing together extruded copper conductors 2.54 cm thick and 11.4 cm wide with a water hole in the center. Outboard of the conductor clamp, the conductors will be made up of thin sheets of copper for a length of about six inches, thus giving the contact plates the flexibility to adjust up or down about 1.0 cm. The contact plates are one half the thickness of the conductor in the overlapping area. The unstepped side is insulated. The stepped portion of the "socket" side of the connector is faced with numerous lengths of "Multilam" strip (2). This is a commercially available component used for the past several years for making high current connectors. Its use guarantees many hundreds of contact points spread over the entire mating area even though there is some warpage in the plates, thus permitting the use of much lower clamping pressure for a given contact resistance than would

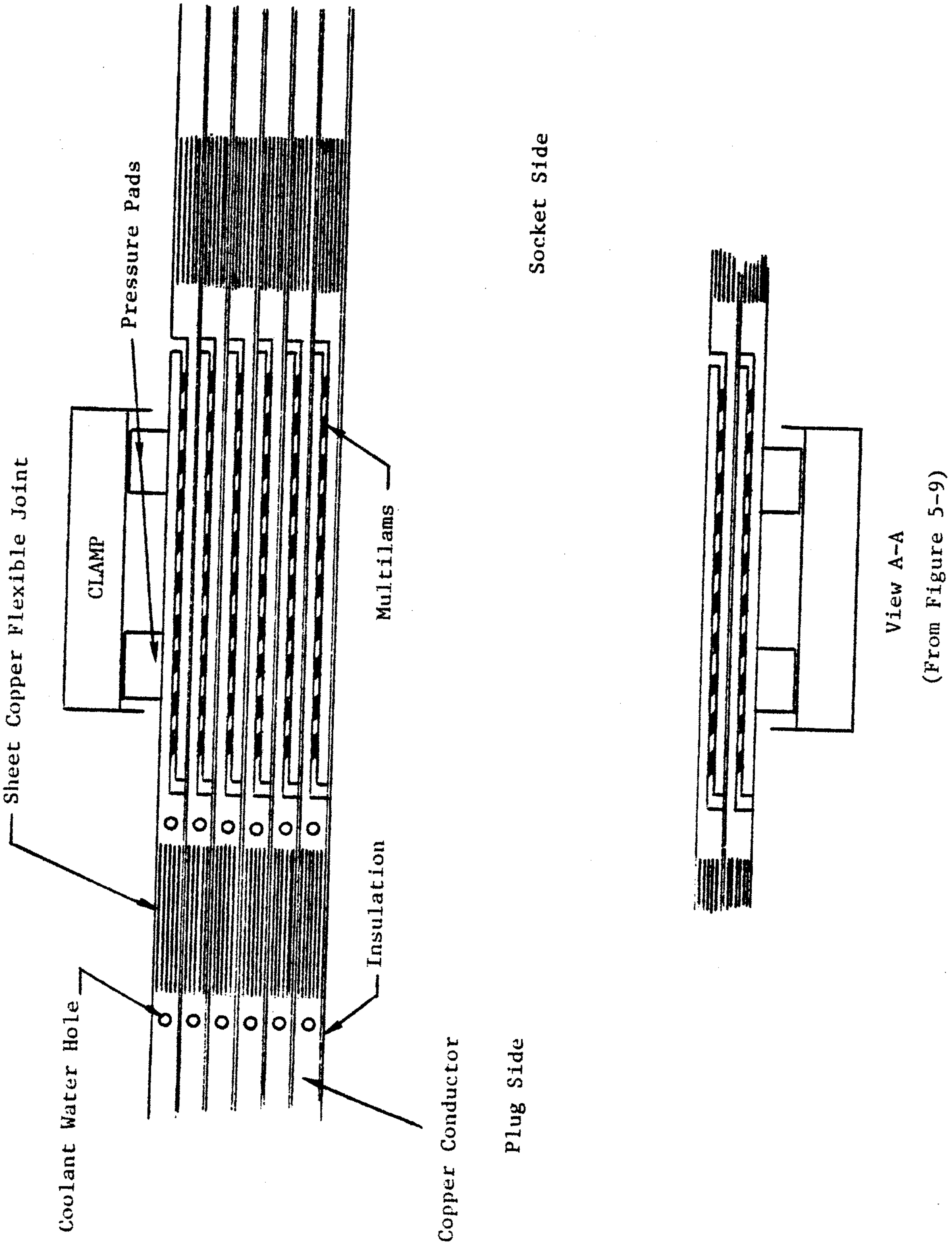

Figure 5-7 Side View of EF Coil Connector

be required with simple flat surfaces. The spacing between the conductors at the support clamp is such that the contact fingers interleave without any surface pressure between them except for that which is required to spring the flexible copper sheets to obtain vertical alignment. Beveling of the leading edges of the fingers displaces the contact fingers as necessary as the connector halves are engaged. This connector is thus of the "zero insertion force" type which is widely used by the electronic connector industry. Once the fingers are interleaved, the clamp is engaged to squeeze the stack of fingers together and thus properly deflect the many hundreds of contact springs in the Multilam strips. The sheet copper provides the flexibility required as the stack height changes with the application of the clamping pressure. Cooling water is circulated through the conductors and finger plates as shown in Figure 5-10.

This connector design has the advantage that it will tolerate wide misalignment in the horizontal direction. Furthermore it will tolerate the different insertion paths which are obtained depending on which of the two neighboring modules is moved, as illustrated in Figure 5-9. The clamping pressure is insufficient to enable the connector friction to support the hoop tension which develops when the conductors are carrying current. Furthermore, experience with the PDX tokamak at Princeton using fingers without multilams showed that the application of a clamping pressure adequate to take the hoop tension across the joint by friction caused the contact surfaces to weld together so that the connector could not be taken apart. This hoop tension must be supported by automatic clamps which firmly attach the bore component support frame of one module to that of the adjacent module. No matter how firmly these coil segments are supported, there will be some movement of

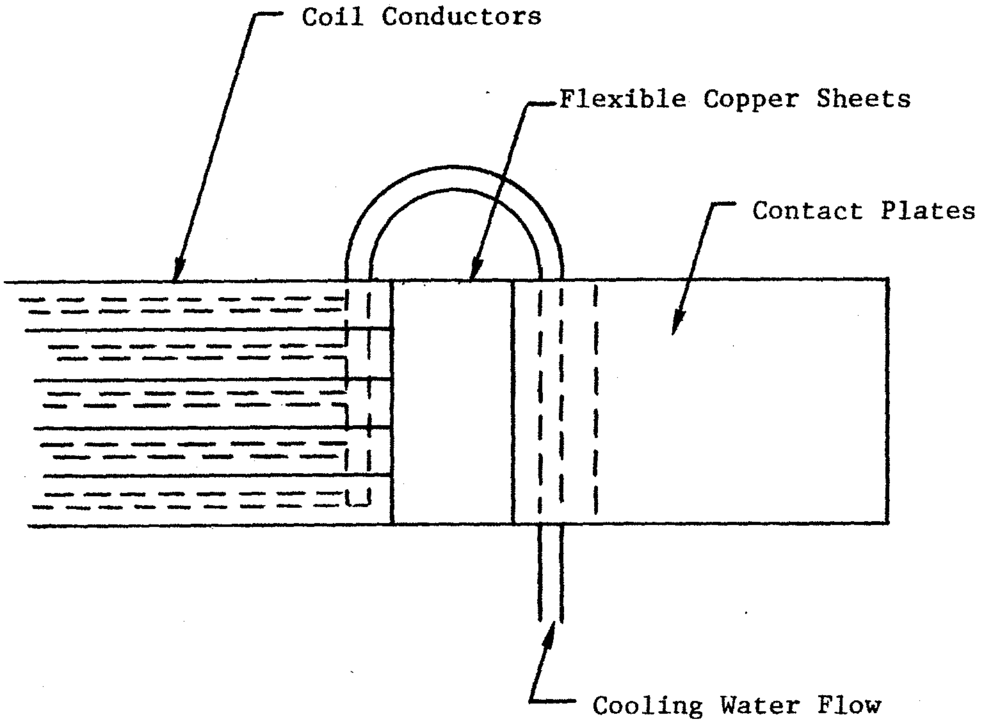

Figure 5-8 Top View of Connector Showing Cooling Water Channels

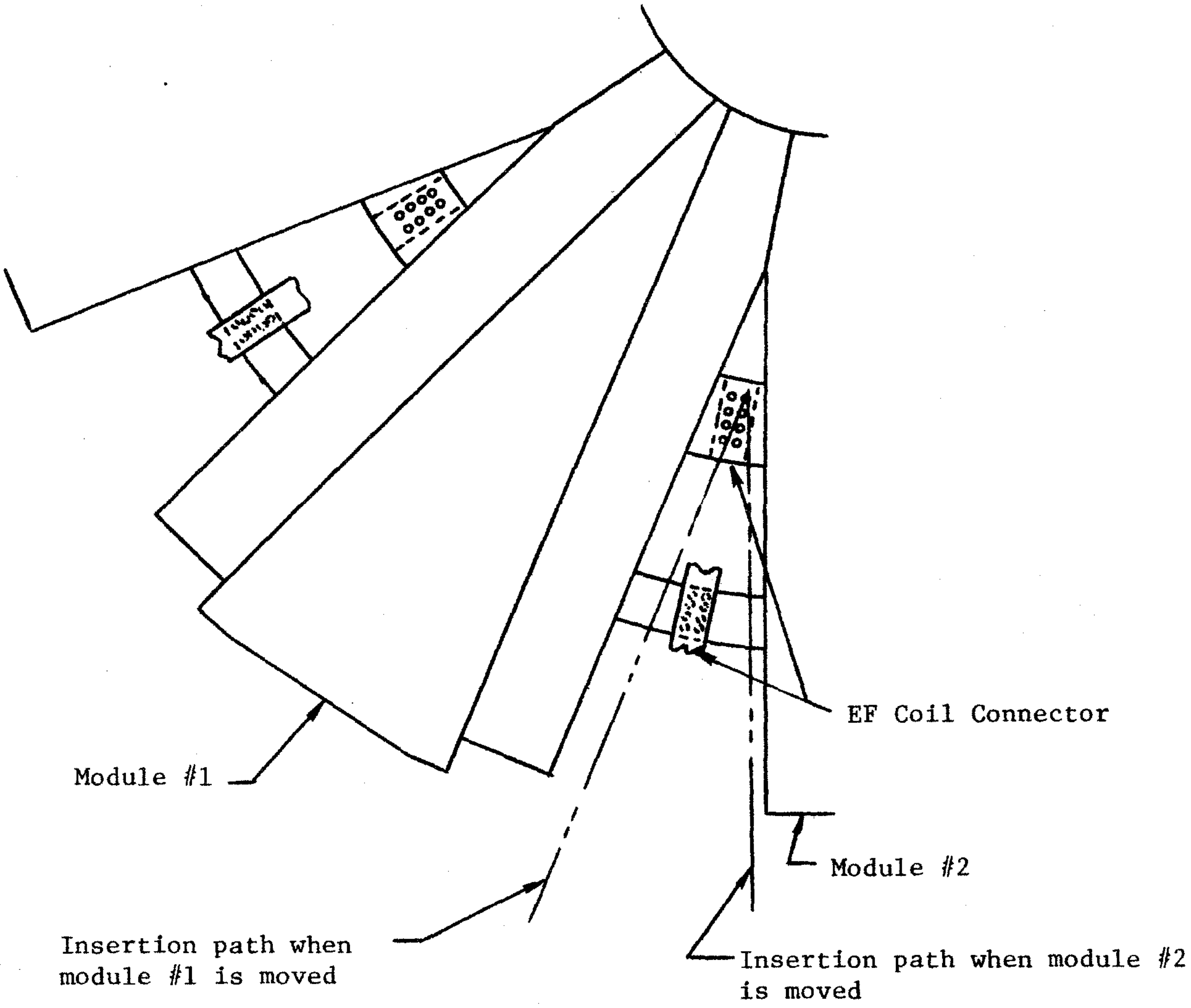

Figure 5-9 Top View of Module Showing the Position of the Connectors Between the Modules

connector fingers each time the coil is pulsed. Here again the Multilams solve a problem. Tests at the Westinghouse Research Labs simulating an early inside poloidal field coil design for TFTR, showed that Multilam connectors could withstand deflections of 1 cm while simultaneously carrying current with sufficiently low wear rates to permit a lifetime of a half million pulses.

5.6 VACUUM VESSEL DESIGN

The outline of what appears to be a vacuum vessel in Figure 5-3 has so far been called the bore components support frame because it supports the PF coils, the blanket, and the shield. But there must be at least one vacuum tight chamber inside this frame. The sector of the vacuum vessel in each module will interface with its neighbor at a flange. It has been common practice in the past to make this flange an internal flange so that a seal weld could be made from the inside of the vessel by a welder working in the plasma space. This approach appears to be incompatible with the high wall loading of the HFCTR and with the goal of quick disassembly. An internal flange would also be difficult to cool.

As is readily seen in Figure 5-3, a weld around an external flange would be difficult to make, because there is no space for the welder to pass down between the vacuum vessel throat and the TF coil center leg. It would also be very difficult to design a completely automatic welder to work around the PF coils.

What is really needed is a non-welded vacuum tight seal between external flanges. Pressure-actuated deformable metal seals are used in ultra-high vacuum valve closures. It is therefore conceivable that this type of sealing element could be placed between flanges which are clamped together by screwjack actuated clamps. Such an arrangement can be made insensitive to the horizontal and vertical positioning of the flanges and it would operate very well to seal in the blind space next to the TF coil center leg. The entire operation is completely automatic. When the replacement module has been rolled into place, the flanges between modules are adequately positioned to permit the operation of the clamps. The seals are mounted on a short length of bellows, so that the clamps will have to distort the heavy wall of the vacuum vessel in order to seal the flanges.

5.7 STRUCTURAL CORE DESIGN

The structural core performs four functions: it supports the centering force of the TF coils, supports the OH and hexapole coils, applies a compression force to the TF coil inside leg straight section, and picks up some of the torque developed on the TF coils by the out-of-plane forces. Since the OH and hexapole coils are superconducting, the entire structure is cooled to 4 K. Moreover, since the unit pressures due to the TF coil centering force are too great to be taken across a vacuum insulating space, there is little alternative to operating the bucking cylinder at 4 K.

The construction of the structural core is shown in Figure 5-3. An outer cylinder is made up of alternate layers of OH coils and bucking rings. The bucking rings are not round on the outside but are instead a sixteen sided polygon, being flat where the TF coil noses interface. Since the sixteen sided bucking rings are sixteen-sided and there are only eight coil modules, they automatically provide the keying of the TF coil noses to the bucking cylinders and therefore provide support for the TF coil out-of-plane forces at the TF coil center leg. This is illustrated in Figure 5-10. A simple calculation shows that a friction coefficient of 0.2 is more than adequate to support the overturning forces on the inner legs through static friction between the TF coils and the structural core. The shear panels provide support for the out-of-plane forces only on the outer leg. The bucking rings are of two different outside dimensions with the smaller dimension rings providing a vertical separation of the larger dimension rings to make a slot for the OH coils. Each ring is made of four plates three inches thick, and the ring is not continuous but is formed from four 90° segments. The rings will be provided with center fits so that they interlock into a precision cylinder as they are stacked. Since the segments are loaded in compression it is not necessary that they be bolted together to carry the load but they will be bolted together sufficiently to assure a solid structure during assembly.

It has not yet been resolved whether the superconducting leads must be brought up the outside of the OH coils or not. There is some concern that there will be excessive ac loss if the lead conductor is run up the high field region in the center of the solenoid. If the lead must be run up the outside of the OH coil, this can be done with very little sacrifice in OH coil diameter as can be seen in Figure 5-6. A lead can be brought to an OH or hexapole coil at each of the sixteen corners. The joint between the OH coil lead and the vertical lead will be exactly like the resistance welds

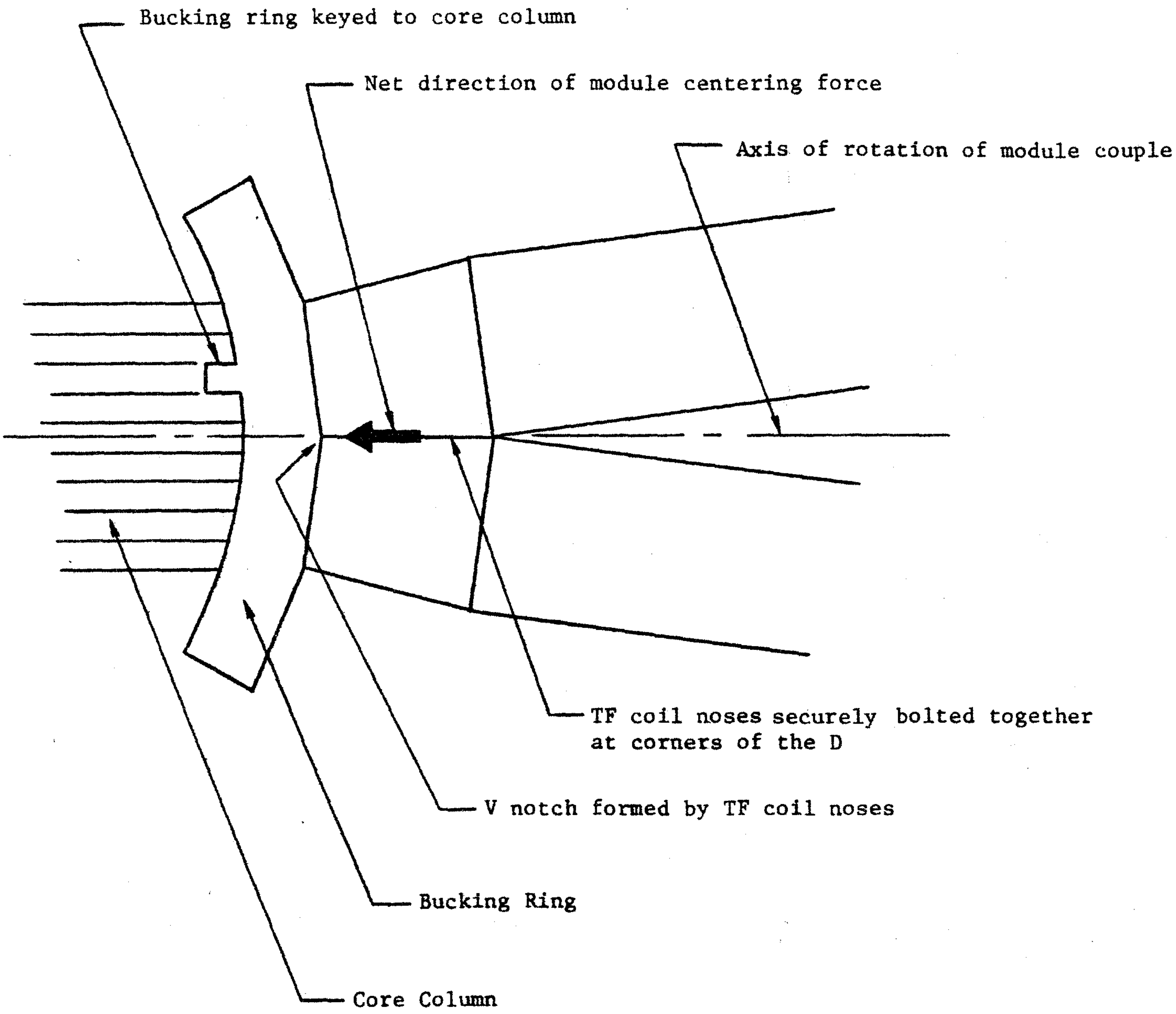

Figure 5-10 Keying of TF Coil Noses to the Core Column

developed for the superconducting cables used in the Westinghouse/Airco Large Coil Program conductor, except that the cable ends are mitered to make a 90° angle. It should be noted that both the moveable and the fixed cryostat walls must span the OH coil gap between bucking rings regardless of whether the OH coil leads are brought up the outside or the inside of the solenoid.

Each of the plates which make up the bucking rings must be individually helium cooled, either by circulating cold gas or by conduction. It would be very advantageous to have all the cooling connections on the outside of the solenoid so that a single leak can be reached for repair by removing only one module. The building construction costs are reduced, since the building does not need to have the headroom or the crane size necessary to lift the 1000 ton (10^6 kg) core column out of the cylinder of stacked bucking cylinders. This advantage is obtained because the core column is built up plate by plate in place before the bucking rings and OH coils are stacked. This is only possible if the OH coil connections and the helium coolant connections are on the outside of the solenoid. If these connections are on the inside of the solenoid, then the connections must be made before the core column is lowered into place. With external leads, remote maintenance of the OH coils and the helium coolant connections can be done without moving the core column. Also if the leads are on the outside, the core column can be made to interface with the inside of the bucking rings and thereby help to support the TF coil centering force. This also means that the ID of the bucking rings can be keyed to the core column at several places around the circumference in Figure 5-10 to support the torque developed by the out-of-plane forces on the center leg of the TF coil.

The core column is made of flat plates 15.2 cm thick bolted together to form a solid cylinder so that the core will be stiff in torsion and therefore able to support the torque developed by the out-of-plane forces. With this bolted construction, the core can be assembled in place with a crane sized to lift only a single plate.

The insulating structure to support the structural core has not yet been designed.

5.7.1 Compression of TF Coil Trunk Straight Section

The TF coil structural system is designed to have 50% of the inner leg tension carried by the central core column. This function is accomplished by the core column end cap structure shown in Figure 5-3. The core column end cap is a disc made of overlapping half discs four inches thick stacked four deep. This disc is fastened to the vertical core column plates by cap screws screwed into the ends of the plates. The diameter of the end cap extends somewhat over the TF coil center leg. At the outer periphery of the end cap are sixteen force pads which are moved by screwjack actuators. Each pad presses against a sloping surface on a TF coil at an angle such that the radial force which would be provided by a reaction ring is developed and a vertical force equal to 50% of the TF coil tension is developed. The free body diagram for the corner of the D coil is shown in Figure 5-11. The

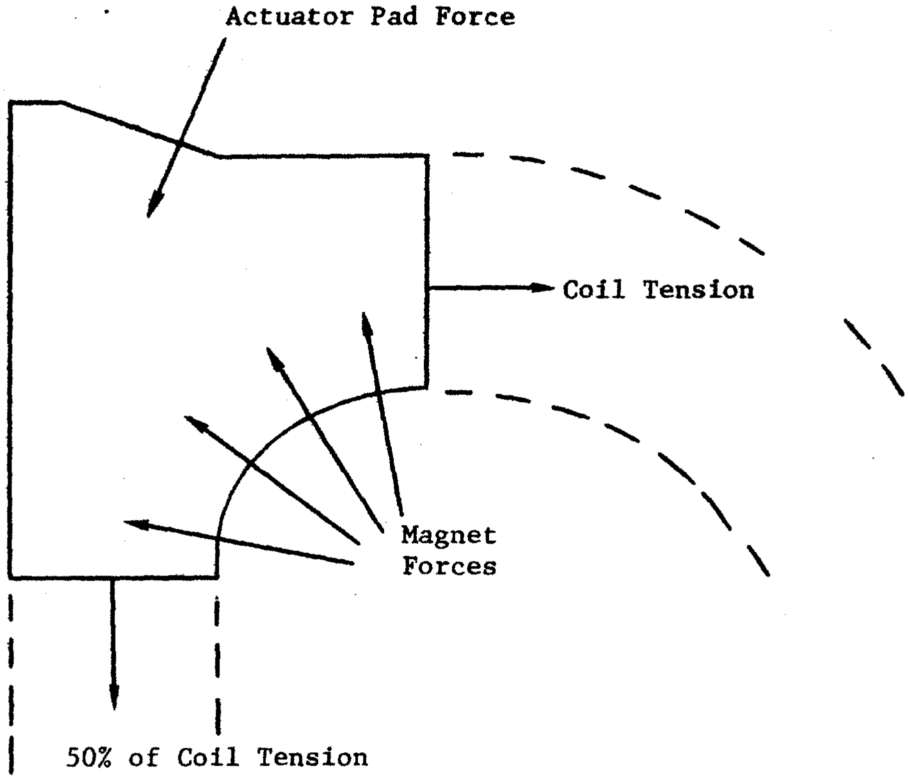

Figure 5-11 Free Body Diagram of a Corner of the TF Coil

corner is assumed to be a rigid body with only the magnetic forces, the horizontal and vertical coil tension forces, and the actuator pad force applied. In order to be in equilibrium, the actuator pad must apply a force of 201 x 10^6 N. This force can be provided by twelve eight inch (20.3 cm) diameter screws. It is not necessary that these screws be turned under load. These screws serve mainly to retract the force pad so that the TF coil module can be removed. Only the pads associated with the module to be removed need to be actuated. The other pads remain in place to firmly hold the reactor together. The vertical force developed by the screws stresses the core column in tension while the radial tension force in the coil module is reacted against the force on the TF coil 180° away just as with a reaction ring.

Since the end cap is at 4 K and the TF coil is at 4 K, moveable cryostat walls must be provided on each force pad and on the TF coil area where the force pad makes contact. The moveable cryostat wall on the pressure pad must be capable of a movement of about 15.0 cm so that the module will clear it when the module is withdrawn. A fixed cryostat wall covers the entire end cap. The details of penetrating the end cap and the fixed crysstat wall with the OH coil leads and the helium coolant leads remain to be worked out.

5.8 DIPOLE AND OH COMPENSATING COIL SUPPORT

The superconducting dipole and OH compensating coils along with all the coolant headering and electrical power distribution above the toroid will be supported on a framework which is carried by the walls of the building which lie beyond the circumferential track. The objective of this design is to permit the removal of a module with the least possible disturbance to these overhead components.

Locating the retaining ring function inside the structural core cryostat eliminates the need for raising the retaining ring when a module is to be removed. The OH compensating coil can probably be fixed in its vertical position because the module can move radially under it. The dipole coil support structure is equipped with screwjacks which can raise and lower it to permit module movement. Thus there is no disadvantage to removing this coil from all of the modules when only one module is to be moved. Flexible leads to this coil enable it to be lifted without breaking any connections.

Power and coolant flow to TF coils in the cryostat and power and coolant flow to the components in the TF coil bore are supplied through connectors whose moveable parts are actuated by screwjacks on the support frame. Only those connections to the module to be moved will be broken, thus reducing the number of total operations of the connectors and enhancing the reliability.

The compensating OH coil below the toroidal field coil system will not need to be moved to remove a module as can be seen in Figure 5-3. The upper retaining ring function will be identical with that of the lower retaining ring, i.e. it will be inside the cryostat of the structural core. The dipole is mounted on screwjacks which permit it to be lowered down below the tracks when the module is to be moved. There is no headering of any kind below the toroidal field coil module where it would interfere with the movement of the transporter.

5.9 SUMMARY OF THE COIL SYSTEM MECHANICAL DESIGN

The design features which help to lower the cost of the HFCTR are:

(1) Avoidance of a vacuum building.

(2) Use of a low building by eliminating the need to lift core column plates out of the OH coil bore.

(3) Use of a low capacity crane by assembling center core one plate at a time.

(4) Placement of EF coils inside the TF coil bore to reduce overall vertical field coil size and power.

(5) Retaining ring function obtained by use of end caps located inside the structural core cryostat.

The design features which reduce the down time for maintenance are:

(1) Individual modules can be removed without moving or disturbing the remaining modules in any way.

(2) Services are disconnected only from the module to be removed.

(3) Only the neutral beam injector for the module to be moved is moved.

(4) Large modules are replaced without the use of manipulators.

(5) No cooldown of TF coils or structural core required for a module exchange.

(6) A flexible joint design permits modularization of interior poloidal field coils.

(7) Use of mechanically actuated vacuum seal joints permits rapid access to vacuum vessel seals.

REFERENCES - SECTION 5

(1) R. W. Werner, Report ORNL/TM-5664, Oak Ridge National Laboratory, December 1976.

6. REMOTE MAINTENANCE PROCEDURE

HFCTR incorporates an entirely automated disassembly/ressembly procedure for a complete 45° modular sector of the toroidal reactor. This allows first wall or blanket replacements, annealing of defects in superconductor matrices and unscheduled repair of faults with sufficiently short downtimes to be attractive in a commercial utility application. This section describes the rationale for automation and the assumptions needed to define an automated procedure. The scenario for a module replacement is described and the technique used for timing the mechanical operations involved in a module replacement is explained. The timing method was previously developed by Sniderman [1]and is described in detail in Appendix H.

6.1 OCTANT MODULE REPLACEMENT

For a commercial tokamak reactor to be competitive, it is necessary that the plant availability compare favorably to that of existing fossil and fission plants. One of the major planned or scheduled maintenance operations is the replacement of the first wall portion of the plasma vessel and possibly the blanket/shield. The HFCTR concept has been designed so that an octant module can be readily removed and exchanged with a new or rebuilt octant.

A generally accepted approach to disassembling and then reassembling complicated equipment is for an individual technician to perform the many required functions using his hands along with the required tooling. This is the simplest possible maintenance method with the minimum necessity for the development of special exotic gadgets and tooling. This basic concept also assures that several alternative means of performing the tasks can be used as a back-up in the event of relatively simple problems such as bolt galling or leaking joints.

Numerous reactor concept designs have attempted to maximize the use of "hands-on" operations in their studies. Because of the intense activation of the structure caused by the absorption of neutrons produced by D-T reactions, it is not possible to handle certain of the reactor components without shielding the technician. Numerous reactor studies have proposed the use of master-slave or motor-controlled manipulators in conjunction with a mobile shielded vehicle for performing maintenance tasks on radioactive components. The use of manipulators to replace "hands-on" operation requires approximately 6 to 10 times as much time for the performance of simple tasks [1] and can be much higher if the operator's vision is limited. Since a quick, efficient operation is one of the major goals of this reactor, it was decided that manipulators could not fulfill the needs and would not be used except for emergency and/or backup contingency operations.

Therefore, a different means of performing the planned, repetitive type of maintenance and servicing was required. It was decided to design from the beginning a fully automatic, computer controlled, plug-in component concept. This approach affects the design of many individual components and their interfaces with the complete tokamak.

The scenario for a module removal is as follows:

(1) Shut the plant down.

(2) Reposition the dipole field coils away from the reactor.

(3) Disconnect and lower the neutral beam injector below the floor.

(4) Disconnect the utility joints to the module to be replaced.

(5) Disconnect the various vacuum closures for the module to be replaced.

(6) Move the old octant module out.

The assembly of the replacement octant module would basically be the reverse of the removal.

6.1.1 Basic Assumptions

To determine the time required to perform the complete exchange of an octant module, it is necessary to determine the main tasks which are involved in the overall operation and then to break these main tasks into small increments for which discrete time elements can be estimated. For these time estimates to be realistic, a listing was prepared of the various assumptions necessary for the specific operations to be performed.

The basic operation and equipment assumptions used in determining the performance time for an automatic octant module replacement are listed below:

- One or more complete octant modules will be replaced during a scheduled shutdown.
- The complete octant module which is to be replaced is composed of two toroidal field coils, enclosed in a form-fitting dewar, a first wall, blanket/shield and portion of the poloidal field coils located inside the toroidal field coils and the necessary enclosure to form a vacuum around the plasma.
- Storage area will be available for modules removed from the reactor and rebuilt modules available for reassembly.

- The replacement octant module will have been assembled with all possible testing completed during the actual assembly so that a minimum amount of testing will be required during the actual replacement operation.
- The rebuilding of a removed octant module will be performed in a hot cell away from the reactor room with sufficient time available that well-trained personnel will be working in a noncritical path environment.
- The reactor room will be of sufficient size to permit the movement of an octant module on a set of tracks around the circumference of the tokamak. Individual radial spur tracks will form a connection between the individual module radial movements to the circumferential movement in and out of the reactor room.
- The first wall and blanket/shield assembly can be removed from the inside of the toroidal field bore by means of a circumferential movement of the assembly. (This will probably be done in the hot cell area but it is feasible for the replacement to take place in the reactor room).
- The time estimates assume that sufficient manpower will be available to conduct the prescribed work — this will permit the parallel performance of tasks at multiple locations when required.
- There will be automatic equipment built into the support structure, the reactor room and the tokamak components to perform the various functions required such as torquing of bolts, movement of clamps, joints and fixtures, testing for proper connections, etc.

- The octant module will be designed so that all the connections, joints, seals, etc., are located in an open accessible area with sufficient clearance for the required movements of the automatic equipment. An attempt will be made to limit this movement to horizontal and vertical directions.
- Viewing of work operations will be provided by both permanent and portable remotely operated and controlled lights and TV cameras.
- All the designated joints will have built-in captured seals, bolts, couplings, etc. This feature will provide the means for quick, easy assembly and will minimize the possibility of missing and/or lost parts.
- The connections will be quick-acting types with built-in means of assuring that the joints have been properly connected and that the required seals are working.
- The electrical leads will have a "springy" or flexible section included in the design.
- Octant module toroidal field coils will be cooled prior to maintenance operations and maintained cold while being transported into position as a replacement octant.

6.1.2 Module Motion During Maintenance Operations

Each octant module is supported on a wheeled or roller transporter, so that once the braking or restraining force is removed, the module can be moved by the application of the proper force against a solid member. There are several operations prior to the movement of an octant module out of its operating location, which are outlined in the section on the removal procedures and are not repeated here.

The first movement associated with the octant module will be a 0.635 cm movement activated by screw jacks which will permit a separation of 0.635 cm between the toroidal field coil and its dewar wall. This separation is possible due to the incorporation of bellows joints in the dewar structure surrounding the module. This movement will be made by the use of screw actuators attached to the inside surface of the dewar walls. These actuators will be arranged in two vertical rows for each dewar wall which is to be moved. Within a row, the actuators are positioned one above the other with approximately 38.1 cm between their center lines. The control can be supplied by flexible cabling so that all the actuators on one dewar wall face move simultaneously and provide the required force to move the module dewar wall approximately 0.6 cm in relation to the TF coil.

The next octant module movement is the disassembly of the internal equilibrium field coil connections which will be approximately a 30.5 cm radially outward movement. The actuation will be by the same screw jacks used for the initial 0.6 cm movement, with the moving force being supplied at both the top and bottom of the center support column.

The complete octant module must then be moved approximately 9.14 m radially outward until it reaches the track running circumferentially around the perimeter of the device. It is envisioned that a tractor will be positioned on the circumferential track and the transporter moved by means of pulleys until it reaches the circular track. Once the transporter is at the peripheral track, the transporter peripherial wheels will be lowered and the radial wheels raised. The transporter would then be moved around the outside of the reactor until it reached the radial track leading out of the reactor room.

The new or replacement octant module will have previously been moved into the reactor room and positioned on the peripheral track adjacent to the radial track where the old unit is to be moved. Once the old module is clear of the radial track, the new unit can be brought into position. These tracks will be precision machined surfaces combined with cam guide rollers to assure proper guidance and alignment for the movement and placement of the new module.

6.2. DISASSEMBLY/REASSEMBLY TIMING TECHNIQUES

If the total time allocated to perform a complicated operation is estimated in terms of calendar months, it may be acceptable to list the general tasks to be performed and to assign performance times in terms of eight-hour shifts, or more generally days of fractions of a day. But if the total operation is planned to be performed within a scheduled week-end shutdown, it is necessary to evaluate the complete task in extremely fine detail and then to assign performance times to the discrete steps based on achievable goals. This study has been performed in the latter manner. The various operations have been outlined and the tasks broken down into small discrete actions, and reasonable times have been assigned to each step. Where it was considered feasible, parallel performance of operations were used.

It was assumed that the equipment and procedures had been used numerous times before and the personnel involved were also well trained and fully familiar with the operations being performed. Therefore, a minimum amount of time would be required for routine maintenance.

The time frames were based on working continuously twenty-four hours per day from the start of one operation to its completion and then immediately starting the next operation. This philosophy does not provide for the normal productivity limitations associated with the performance of any mechanical operation which is controlled and monitored by human personnel, such as:

(1) Personnel rest periods

(2) Change of shift requirements

(3) Malfunction of equipment

(4) Seals or joints not mating properly and operations having to be repeated

(5) Check listed stop points (even though the operation can be computer controlled, there are stop and check points required where corrections must be instituted)

(6) Natural tendency to start each new function slowly to assure that it is performing properly

(7) Possible additional functions which have not been included in the planning.

To account for these normal conditions and contingencies, a factor should be added to the overall time. A 40% factor has been chosen which is based on personal experience and discussions with personnel closely associated with servicing functions.

It must be noted that the time estimates which have been developed are only for the actual exchange of octant modules and do not include functions such as plant shutdown, start-up, plasma wall degassing, evacuation, testing operations, etc.

As stated previously, the development of the time frame required to remove an octant module and to replace it with a new module was the result of dividing the major operations into extremely small finite steps and then assigning a reasonable amount of time for the performance of each of these steps. (These steps and times are shown in Appendix A.) The individual time elements were then totaled to determine the performance time for the major steps. The results are presented in Table 6-I.

TABLE 6 - I

SCENARIO OF PROCEDURES FOR EXCHANGE OF AN OCTANT MODULE

Major Procedure Steps		Performance Time (Minutes)
(1)	Loosen and disconnect toroidal field coils from center column	200
(2)	Disconnect and move the neutral beam injector	186
(3)	Move external dipole field coils vertically away from the toroidal field coils	16
(4)	Disconnect utility services and vacuum vessel attachments	179
(5)	Move old octant module out	200
(6)	Move new octant module into position	132
(7)	Connect and tighten toroidal field coil to center column	205
(8)	Connect utility services and vacuum vessel attachments	400
(9)	Reposition external poloidal field coils	16
(10)	Reposition neutral beam injector	401
(11)	40% Contingency	774
		2709 Min (45.2 Hr)

REFERENCE - SECTION 6

(1) "Fusion Reactor Remote Maintenance Study", WFPS-TME-087; Dated May, 1978; EPRI Contract RP-1044-1 (To be published)

7. ELECTRICAL SYSTEM DESIGN

The electrical system design study concentrated on the circuit design and the equipment ratings of the poloidal field power conversion system, because of its many unique features. The start-up scenario for the plasma (Section 2.3) is uniquely well-defined, including subtle features such as controlled change of elongation with time, controlled vertical as well as radial motion and independent control of elongation and triangularity. This required a new derivation of the plasma characteristics as an inductive electrical load, described in this section and in Appendix J. Another unique feature of the HFCTR is the use of permanently biased and transiently nulled dipole and quadrupole coils. This leads to voltage-current profiles at the coil terminals which have not been previously considered and which suggest an original circuit topology for the dipole coil power conversion system. The unique magnetic circuit design also presented opportunities for original methods of driving or connecting the several independent coil systems. A trade-study is described in this section, which compares straightforward independent drives for each ohmic heating and equilibrium coil with the use of interior coils for plasma initiation, antiseries connections of the dipole and quadrupole coil, operation without a null coil and decoupling with antitransformers. A rationale is presented in this section for the selection of the former two options and the rejection of the latter two. A complete circuit design for the poloidal field system is explained and illustrated in this section. The section also includes the analysis of a redundant system of thermal energy storage system which allows the production of electrical power between plasma pulses.

7.1 CIRCUIT EQUATIONS

The start-up scenario described in Chapter 2 is sufficiently specific to justify the use of poloidal field circuit equations which specify the changes of flux linkages as functions of plasma current, position, minor radius, elongation, poloidal beta and internal inductance. The derivation of a generalized expression of Kirchoff's voltage law for the plasma is shown in Appendix J. The special cases of the generalized voltage law are those of initiation, plasma growth, plasma current growth and auxiliary heating. The simplifying assumptions used for each case are listed below.

(1) Initiation

  (a) Resistive voltage is based on a detailed energy balance, including ionization, impurity line radiation and "empirical" losses, but neglecting the thermal capacity of the plasma.

  (b) The inductive voltage is set only by the safety margin of the predicted maximum resistive loop voltage. A safety factor of 2.0 was selected. This will automatically raise the plasma current to its specified value within the allotted time of 30 ms.

(c) During initiation, β_p is ignored in the equilibrium equation. $\dot{l}_i/2$ is assumed to equal zero.

(2) Growth off of a limiter

(a) $\dot{R} = -\dot{a}$ (7.1)

(b) The change of elongation with time is assumed to be independently controllable.

(c) $\dot{l}_i/2$ assumed to equal zero.

(d) The design criterion that $\dot{q} = 0$, which assures minimum skin current, was not used. In fact, q rises from 4.0 to 5.5 during growth off of a limiter in the reference scenario. J was held constant instead. At this time, there is no reason to believe that some current diffusion in the minor radial direction can not be tolerated.

(3) Stationary plasma

(a) $0 = \dot{R} = \dot{a} = \dot{\delta} = \dot{M}_{p-k}$ (7.2)

(4) Auxiliary Heating

(a) Flux is conserved.

$$0 = L_{p,int}\, \dot{I}_{p,int} + I_{p,int}\, \dot{L}_{p,int} \tag{7.3}$$

and
$$0 = L_{p,ext}\, \dot{I}_{p,total} + I_{p,total}\, \dot{L}_{p,ext} + \sum \frac{d}{dt} (M_{k-p} I_p) \tag{7.4}$$

where M_{k-p} is here the mutual inductance between an external coil and the external surface of the plasma.

(b) $\dot{l}_i/2 = 0$. This simplifying assumption is clearly only approximate. It is necessary to conform to the scenario described in Section 2.3, in which neither total plasma current nor internal plasma current change during auxiliary heating. This is an overspecification of plasma behavior, but a more accurate expression of the change in plasma current and internal inductance is very difficult without the aid of intermediate MHD equilibria vs. time.

Although no literature is known to exist on the subject of circuit modeling during FCT heating, a few circuit relations can be deduced from the global properties calculated by Clarke and Sigmar (1).

$$I(\psi_o) = \begin{cases} \dfrac{\psi_o}{R_c} & \text{low } \beta \\ \dfrac{\psi_o}{R_c}(1 - d^2)^{-1/2} \simeq \dfrac{\psi_o}{R_c}\left(\dfrac{\bar{\beta}_p}{A}\right)^{1/3} & \text{high } \beta \end{cases} \tag{7.5}$$

where $I(\psi_o)$ is the plasma current, ψ_o is the initial constant poloidal flux, R_c is the geometric plasma major radius and d is a relatively complicated flux function which is always less than one. Notice that the plasma current does not have to change very much to maintain pressure equilibrium until $\bar{\beta}_p > A$. Since this does not occur in the HFCTR design, the change in plasma current during auxiliary heating is neglected, until either a better analytical approach or intermediate MHD equilibria are available.

7.1.1 Coil Terminal Voltages

During all the periods of the start-up scenario, with the exception of plasma initiation, it was possible to deduce the coil terminal voltages from the plasma scenario, described in Section 2.3. This scenario describes the evolution of plasma current, temperature, density, position, minor radius, elongation, triangularity, index of curvature and resistive volts vs. time.

A set of generalized expressions of Kirchoff's voltage laws, describing flux linkages and equilibrium requirements as functions of the above parameters, was developed (see Appendix J) and applied to the specific MIT scenario. Only the coil terminal voltages at the beginning and end of each phase of the start-up scenario were calculated, since these voltages should provide adequate information for sizing power conversion systems.

A table of terminal voltages on a single turn basis is shown in Table 7.3-IV. The change of most of these parameters vs. time, including major radius, minor radius and poloidal beta, had significant effects on the sizing of the power supplies, and can not be validly ignored. The effect of the change in elongation vs. time was small, while the effect of triangularity vs. time affected only the hexapole power supply requirements. However, it should be noted that insufficient experimental evidence exists (2) to confirm the validity of the expressions for the effects of elongation and triangularity on power supply requirements. The change in flux linkages vs. time caused by the change of mutual inductance between the plasma and the equilibrium field coils was also large, and can not be ignored.

The large change in $\bar{\beta}_p$ during auxiliary heating required a rapid increase of equilibrium field and a rapid decrease of ohmic heating coil volt-seconds, in order to avoid large skin currents in the plasma. The decrease in ohmic heating current is so great that it requires another 400 s before the OH coil current has returned to the current in the coil at t = 4.0 s. The large, reversed voltages don't necessarily affect power conditioning costs adversely, because similarly large voltages are needed for shutdown. However, turning more of the neutral beam power on earlier may be desirable, both to reduce the resistive volt-seconds accumulation during start-up and to reduce the large "overshoot" of OH current before the auxiliary heating period.

7.2 ALTERNATIVE COIL CONCEPTS

7.2.1 Use of Interior Coils for Plasma Initiation

The usual method for initiating a tokamak plasma is to induce a high toroidal electric field in the plasma region by pulsing the ohmic heating coils. The equilibrium field coils are pulsed from zero net field and attempt to provide plasma equilibrium in an open loop controller, during the initiation period. The equilibrium field coils also provide some of the needed induced voltage across the plasma.

An alternative method for initiating the plasma would be to pulse the null and quadrupole coils simultaneously, while holding the ohmic heating current constant. The currents in the quadrupole and null coils are controlled independently, so that they simultaneously satisfy the equilibrium field and volt-second requirements of the plasma. This is somewhat more complex than the usual way of initiating the plasma, but it is not a dramatic break with past practice. For example, the Alcator poloidal field systems include decoupling field coils which provide equilibrium field to the plasma, but no volt-seconds, as well as ohmic heating coils which provide volt-seconds, but no equilibrium field. If the plasma were controlled by these two coils, along with decoupling antitransformers between the OH and DF coils, one could create a simple "orthogonal" poloidal field system with two sets of totally independent controls. However, the Alcators and other tokamaks use EF coils which provide significant volt-seconds to the plasma, and most tokamaks have independent sets of poloidal field coils which couple strongly with each other. The alternative HFCTR initiation circuit simply goes one step further and uses two independent, but in no way orthogonal, coils to initiate the plasma.

Using the null and quadrupole coils to provide initiation field promises cost benefits over using the OH coil, because only a fraction of the flux linking the plasma must link the OH coil. Since the OH coil has the highest number of ampere-turns of any of the poloidal field coils, because of its poor coupling to the plasma, any increases in the peak voltage seen by the OH coil has a disproportionately large effect on the cost of its power supplies and of the coil. The only alternative solution is to have ohmic heating coils inside the toroidal field coil as in PLT or to have a smaller, auxiliary, ohmic-heating-type coil, used for initiation only, as proposed by Thomassen (3). Either approach involves placing coils between the inside leg of the TF coils and the plasma, which is probably impossible to service and which add to the machine radial build. The use of only two accessible EF coils for plasma initiation introduces no new engineering problems, since the coils were already "there" for other purposes.

Having decided to use the two inner EF coils for initiation, a spectrum of scenarioes is possible. We have chosen the case where the quadrupole coil is constrained to reach its equilibrium, steady state current at the end of initiation. Since a small change in quadrupole current causes a large change in the index of curvature of the equilibrium field, plasma radial and vertical stability can be assured by "biasing" the quadrupole and null coil initial currents. Using the same model of the plasma energy balance as in the discussion of ohmic heating coil requirements in Section 7.1.1, the terminal voltages on all of the poloidal field coils were calculated. After initiation, the rates of change of all coil currents are identical with the case in which the ohmic heating coils were used for initiation. A comparison between the two methods of initiation is shown in Table 7.2-I.

TABLE 7.2-I

INDUCED VOLTAGES DURING INITIATION

USING NULL AND QUADRUPOLE COILS VS. USING OH COILS

Coil	Initiation Using OH Coil	Voltage Using Null and Quadrupole Coils		Peak Volt-Ampere Product, OH	Peak VA N + Q
OH	- 243 V/T	- 38.6 V/T		6,318 MVA	1,004 MVA
Null	- 210 V/T	- 171 V/T		1,344 MVA	1,094 MVA
Dipole	- 124 V/T	- 175 V/T		2,629 MVA	3,710 MVA
Quadrupole	- 173 V/T	- 440 V/T		1,107 MVA	2,816 MVA
			Σ MVA	11,398 MVA	8,624 MVA

Since no polarities of voltages or currents are changed, no change in the topology of any poloidal field circuit is dictated. Notice that the peak voltage induced across the ohmic heating coil has been reduced by a factor of six. The peak voltages of the dipole and null coils have been slightly reduced, while the quadrupole voltage has more than doubled. If the sum of the absolute values of peak voltage and peak current for each poloidal field coil is taken as the best simple indicator of total circuit and coil cost, the use of null and quadrupole circuits reduces the cost of the initiation circuits by 25%. The as yet unquantified problem of eddy current losses in the cryogenically-cooled central cylinder has been greatly reduced and the cryostability constraints on all of the superconducting coils have been eased, especially the OH coils. Notice, however, that the peak current of the quadrupole coil has increased from 6.4 MAT to 7.26 MAT. The reason for the large current swing in the quadrupole is its low vertical component of field at 6.95 m. Optimization of coil placement and scenario development for this approach is a subject for further study.

7.2.2 Operation Without a Null Coil

The use of a nulling coil inside the toroidal field coils along with a steady-state, superconducting dipole coil outside the toroidal field coils appears to be very attractive when compared with pulsing a single, external dipole coil, for several reasons:

(1) The amount of magnetic energy swing in the open-circuit equilibrium field coil system is four times lower, using the null coil. This leads one to expect substantially lower power supply costs.

(2) The "coaxial cable" effect of placing both the plasma and pulsed

equilibrium field coil currents inside the TF coils shields the TF coils from much of the pulsed vertical fields.

(3) Similarly, the variation in overturning forces is reduced.

However, disadvantages can also be identified with the nulling coil approach.

(1) Since steady-state dipole current remains the same, one must purchase an additional (nulling) coil, without expecting much improvement in the cost of the dipole field coil.

(2) Being a normal, copper conductor coil, the null coil will dissipate a modest amount of power.

(3) If inside poloidal field coil joints are not proven feasible, then both the null and inside quadrupole coils must be eliminated.

(4) Substantial voltages are induced in the dipole coil, even with partial cancellation of these voltages by the dipole coil. The dipole coil circuit is at a topological disadvantage, compared to the circuit for a pulsed dipole coil, because it must withstand peak voltage at peak current.

A definitive trade-off study can not be performed at this time, because of imprecise knowledge of pulsed ac losses. However, a fair comparison of power supply requirements can be made, by using the same techniques that were used to calculate terminal voltages for the specific HFCTR plasma scenario and poloidal field coil disposition in Section 7.1.2. In the case of no nulling coil, all coils are kept in the same positions as before, except that the nulling coil is eliminated. The dipole coil is now servoed to provide plasma radial equilibrium during start-up and shutdown. The quadrupole coil could now continue to operate in steady-state, which would require a bias on the dipole coil to null the quadrupole field at t = 0, or it could be pulsed from zero initial current along with the dipole coil. Any in-between mode of operation is also possible. A pre-biased quadrupole coil was selected, in order to make the two alternatives being compared as similar as possible.

The coil terminal voltages, with and without a null coil, are shown in Table 7.2-II, at different times during the plasma scenario. Taking the sum of the absolute values of peak current times peak voltage as a good indicator of the overall poloidal field power conversion system cost, we get an overall power supply "rating" of 13,250 MVA without a null coil and 11,300 with a null coil. The power requirements of the dipole coil increased by a factor of 2.3, but this is partially balanced by the elimination of the null coil supply and a slight reduction of OH peak power. Taking into account the antiseries connection of the quadrupole and the dipole coil in the case with a null coil, the poloidal field system "rating" is decreased to 9,120 MVA.

Using this overall rating as a figure of cost, the poloidal field power conditioning system should be about 45% larger for the case with no null coil.

TABLE 7.2-II

TERMINAL VOLTAGES ON A SINGLE TURN BASIS FOR HFCTR WITH NO NULL COIL

Coil	$0 < t < .03$ s Initiation	$.03$ s $< t < 2.0$ s Plasma Growth	2.0 s $< t < 4.0$ s Current Growth	4.0 s $< t < 8.0$ s Auxiliary Heating
OH	-229	-82.3	-15.0	30.8
Null	——	——	——	——
Dipole	-289	-95.6	-32.3	-61.2
Quadrupole	-183	-54.0	-4.83	9.65

All voltages in volts/turn

PEAK VOLT-PEAK AMPERE PRODUCTS

	With Null Coil			Without Null Coil		
Coil	Peak Voltage	Peak Current	$V_{pk}I_{pk}$	Peak Voltage	Peak Current	$V_{pk}I_{pk}$
OH	243	26.0	6,318	229	26.0	5,954
Null	200	6.4	1,280	——	——	——
Dipole	124	21.2	2,629	289	21.2	6,127
Quadrupole	173	6.4	1,107	183	6.4	1,171
Sum, MVA			11,300			13,250

7.3 CIRCUIT DESIGN

7.3.1 Ohmic Heating Coil Power Conditioning Systems

The ohmic heating (OH) coil power conditioning system is the largest and most expensive of the power conditioning systems driving the poloidal field coils. The ohmic heating coil flux vs. time is shown in Figure 1-5, along with the flux scenarioes of the other poloidal field coils. The peak current ratings of the ohmic heating coils are shown in Table 7.3-I, referred to a single turn, along with those of the other poloidal field coils. The resistances and self and mutual inductances of the poloidal field coils at full radius and reduced radius are shown in Tables 7.3-II and 7.3-III. The poloidal field coil terminal voltages, referred to a single turn, at significant times during the plasma scenario, are listed in Table 7.3-IV. The method for computing the terminal voltages is described in Appendix J.

The ohmic heating coil power conditioning system is characterized by the following requirements:

- The ohmic heating coil is half-biased, meaning that it is charged to a given current before the beginning of a pulse and that its current is completely reversed by the end of the burn period, during normal operation. Therefore, a power supply which can carry current in two directions is required.
- A very high power (≃ -7,000 MVA) is regenerated from the OH coil during the initiation period. The circuit must be capable of absorbing this high rate of energy regeneration.

TABLE 7.3-I

CURRENT SWINGS AND INDUCTIVE VOLT-SECONDS CONTRIBUTIONS IN HFCTR

	I(0) (MA)	I(F) (MA)	$\Delta\Phi_p$(F) (V-s)
P	0	6.7	82.4
D	-21.2	-21.2	0
Q	6.4	6.4	0
H	0	- 8.0	-14.5
N	6.4	0	-60.8
OH	26.0	-26.0	-60.8
C	3.0	- 3.0	-12.4

$\Delta\Phi$, plasma + $\Delta\Phi$, coils = - 66 V-s, left over for plasma resistive volt-seconds.

TABLE 7.3-II

INDUCTANCE-RESISTANCE MATRIX ON A SINGLE-TURN BASIS FOR HFCTR

	P	D	Q	H	N	OH	C	R
P	12.3	4.62	5.51	1.81	9.50	1.17	2.07	-
D	4.62	25.3	5.16	0.696	8.86	0.670	4.40	0
Q	5.51	5.16	11.7	1.06	6.75	1.05	3.09	0.539
H	1.81	0.696	1.06	4.84	1.19	1.08	0.403	0
N	9.50	8.86	6.75	1.19	25.0	0.954	3.14	1.52
OH	1.17	0.67	1.05	1.08	0.954	1.62	0.533	0
C	2.07	4.40	3.09	0.403	3.14	0.533	9.15	0

P = plasma, D = dipole, Q = quadrature,

H = hexapole, N = null, OH = ohmic heating (main),

C = ohmic heating (compensating)

R = resistance, based on $\rho_{cu,\ 50° C} = 1.9\ \mu\ \Omega - cm$

All numbers in $\mu H/turn^2$ or $\mu\ \Omega/turn^2$

TABLE 7.3-III

INDUCTANCE-RESISTANCE MATRIX ON A SINGLE-TURN BASIS

FOR HFCTR AT t = 0

AT R = 6.95 m AND a = 0.25 m

	P	D	Q	H	N	OH	C	R
P	3.19	6.01	6.20	1.55	13.4	1.10	2.47	-
D		25.3	5.16	0.696	8.86	0.669	4.40	0
Q			11.6	1.06	6.75	1.05	3.09	5.39
H				4.84	1.19	1.08	0.403	0
N					25.0	0.954	3.14	1.52
OH						1.62	0.533	0
C							9.15	0

p = plasma, D = dipole, Q = quadrature,

H = hexapole, N = null, OH = ohmic heating (main),

C = ohmic heating (compensating),

R = resistance, based on $\rho_{Cu,\ 50°\ C} = 1.9\ \mu\ \Omega - cm$

All numbers in $\mu H/turns^2$ or $\mu\ \Omega\ /turns^2$.

TABLE 7.3-IV

TERMINAL VOLTAGES ON A SINGLE TURN BASIS FOR THE MIT HFCTR

Dipole and Quadrupole Driven Independently

Coil	$0 < t < .03s$ Initiation	$.03s < t < 2.0s$ Plasma Growth	$2.0s < t < 4.0s$ Current Growth	$4.0s < t < 8.0s$ Auxiliary Heating
OH	- 243	- 94.3	- 19.4	13.8
Null	- 200	- 39.2	- 4.7	- 19.8
Dipole	- 124	- 34.7	- 5.7	- 3.93
Quadrupole	- 173	- 52.1	- 4.6	5.49

All voltages in volts/turn.

Dipole and Quadrupole Connected in Antiseries

Coil System	$0 < t < .03s$ Initiation	$.03s < t < 2.0s$ Plasma Growth	$2.0s < t < 4.0s$ Current Growth	$4.0s < t < 8.0s$ Auxiliary Heating
OH	- 243	- 94.3	- 19.4	13.8
Null	- 200	- 39.2	- 4.7	- 19.8
Dipole + Quadrupole	- 71.8	- 19.0	- 4.3	- 5.59

With the dipole and quadrupole coils in antiseries, the single-turn voltage on the quadrupole coil scales as 6.4 MAT/ - 21.2 MAT = - .302 × actual V/T.

TABLE 7.3-V

INSTANTANEOUS POWERS VS. TIME IN HFCTR OPERATING SCENARIO

System	Current (MAT)	Voltage (V/T)	MVA	MW, Line	MVA, Line
t = .03 s					
OH	33	-94.3	-3,112	-3,276	-4,095
Null	6.34	-39.2	- 249	- 262	- 328
Dipole	-21.2	-34.7	736	775	969
Quadrupole	6.4	-52.1	- 333	- 351	- 438
Neutral Beams	—	—	—	—	—
Total				-3,114	-3,892
t = 2.0 s					
OH	11	-19.4	- 213.4	- 225	- 281
Null	5.4	- 4.7	- 25.4	- 26.7	- 32.4
Dipole	-21.2	- 5.7	121	127	159
Quadrupole	6.4	- 4.6	- 29	- 30.5	- 38.1
Neutral Beams	450 A	120 kV	58	68.2	75.8
Total				- 87	-116.7
t = 4.0 s					
OH	- 5	13.8	- 69	- 72.6	- 90.8
Null	4.4	-19.8	- 87.1	- 91.7	-114.6
Dipole	-21.2	- 3.93	83.3	87.7	110
Quadrupole	6.4	5.49	35.1	36.9	46.1
Neutral Beams	3,600 A	120 kV	432	508	564
Total				468	515

Assumptions:
$\eta = 0.95$ for coil power conditioning systems
$\eta = 0.85$ for neutral beam power conditioning
p.f. = 0.8 for coil rectifiers at full load
p.f. = 0.9 for neutral beam power conditioning

- A moderately high (~3,000 MVA) power should be supplied controllably from the OH power conditioning system during start-up and shutdown.
- The ohmic heating coils are required for real time control of the plasma, being responsible for the avoidance of skin currents at all times and, in tandem with the equilibrium coils, for the simultaneous control of plasma position and current. Therefore, the OH power supply should be capable of actively controlling the OH current, during as much of the plasma discharge as possible. This implies the avoidance of passive components such as capacitors and homopolar generators with marginal economies over active supplies. The single exception is the use of an initiation resistor, because of the substantial cost savings and the short time during which active control must be lost.

A circuit which satisfies all of the above requirements is shown in Figure 7-1. A dual rectifier-inverter, driven by an ac flywheel-generator buffer, supplies power to the OH coil during coil charging before each pulse, during the latter phase of start-up, during burn and during the latter phase of shutdown. It operates as an inverter and regenerates power to the ac buffer during the beginning of start-up, during auxiliary heating and during the beginning of shutdown. Current is carried through the mechanical bypass switch, except during the initiation period. Immediately preceding plasma initiation, current is transferred from the mechanical bypass switch to a set of vacuum breakers, acting as the current interrupting switch. The current is then transferred to the plasma initiation resistor by counterpulsing a commutating circuit and opening the interrupting switch. An original mechanical load interrupter design is shown in Figure 7-2,

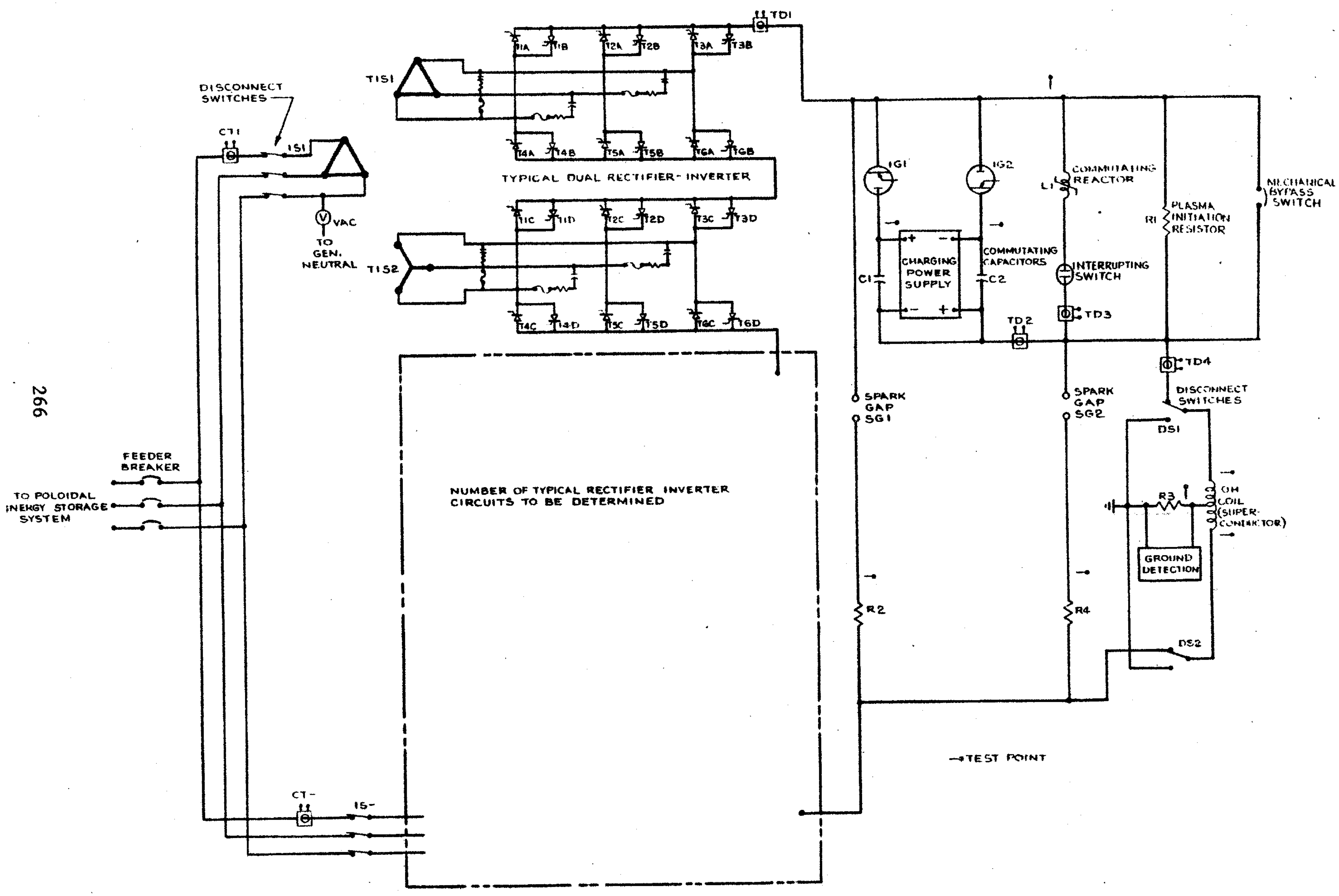

Figure 7-1 HFCTR Ohmic Heating Coil Power Conditioning System

IMPROVED MECHANICAL SWITCHING SYSTEM FOR OH INITIATION

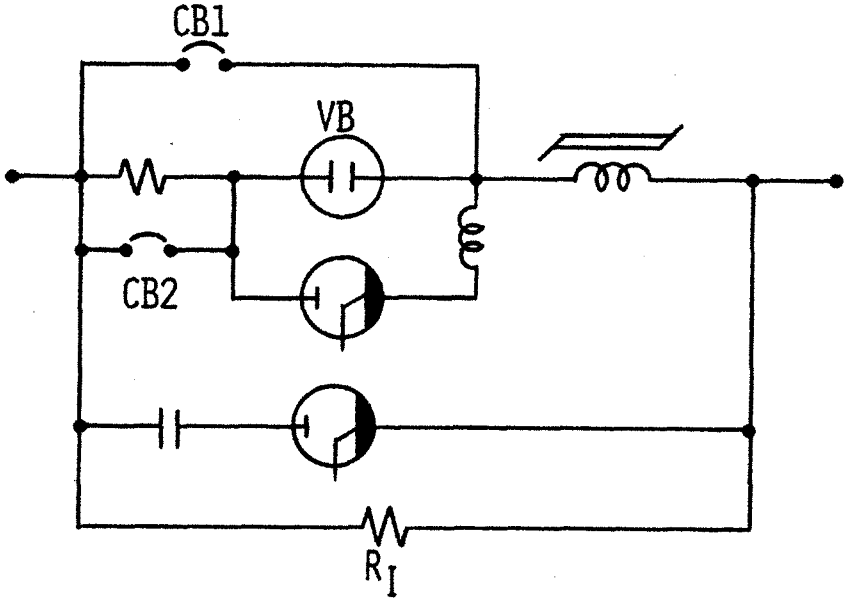

VACUUM BREAKER LOAD SWITCH WITH
TWO MECHANICAL BYPASS SWITCHES, COMMUTATING CIRCUIT
AND AUXILIARY CLOSING SWITCH

Figure 7-2

which should achieve a longer erosion-limited lifetime than previous designs (4). It should be noted that all circuit elements in each of the poloidal field power conditioning systems would actually be arranged symmetrically about the coils they are driving, which are center tapped to ground. This halves the voltage to ground for a given voltage across the coils and minimizes the coil voltages induced by charging of parasitic capacitances during coil pulsing. However, for simplicity, only one set of switching elements is shown in Figure 7-1.

7.3.2 Null Coil Power Conditioning System

The null coil is the equilibrium field coil which is actively programmed to maintain the desired plasma equilibrium position vs. time. However, because of the unique HFCTR design, the null coil current is nulling out the "final" equilibrium field at the beginning of a pulse, instead of growing from zero, along with the plasma current, as in other designs. Because of this prebiasing of the null field current its power conditioning system topologically ressembles that of a full-biased ohmic heating circuit more closely than that of a conventional equilibrium field circuit.

The requirements of the null field power conditioning circuit are listed below:

- The null field coil must only carry current of one polarity. Therefore, a single rectifier-inverter circuit is adequate.
- The null field coil regenerates a moderately high (~250 MVA) amount of power during the initiation period, which must be absorbed by the null field power conditioning system.

- The null field coil should preferably retain active control of the plasma equilibrium position at all times. As with the ohmic heating power supply, this rule is broken only during plasma initiation.

A circuit which satisfies all of the above requirements is shown in Figure 7-3. It is topologically identical to the ohmic heating circuit, except that a single, rather than a dual, rectifier-inverter is used to provide unipolar current to the null field coil. It should be noted that the null, quadrupole and dipole power conditioning systems each drive their upper and lower sets of equilibrium field coils in parallel, in order to obtain passive damping of the plasma vertical instability. The very small power supplies, which drive the upper and lower sets of equilibrium field coils differentially are not shown in these schematics.

7.3.3 Dipole Coil Power Conditioning System

The dipole and quadrupole coils are "bias" coils in the equilibrium field system. They provide the necessary equilibrium field during steady-state burn. Their net deviation from the vertical field needed for plasma equilibrium during start-up and shut-down is cancelled by the null coils. Since, in the reference design, the dipole and quadrupole coils are driven in antiseries by a single power conditioning system, only one circuit will be described. The same circuit topology would be used to drive the dipole coil independently. A different topology would be needed to drive the quadrupole coil independently, since its current is physically of a reverse polarity from that of the dipole coil, while its net terminal voltage is of the same polarity during start-up and shut-down.

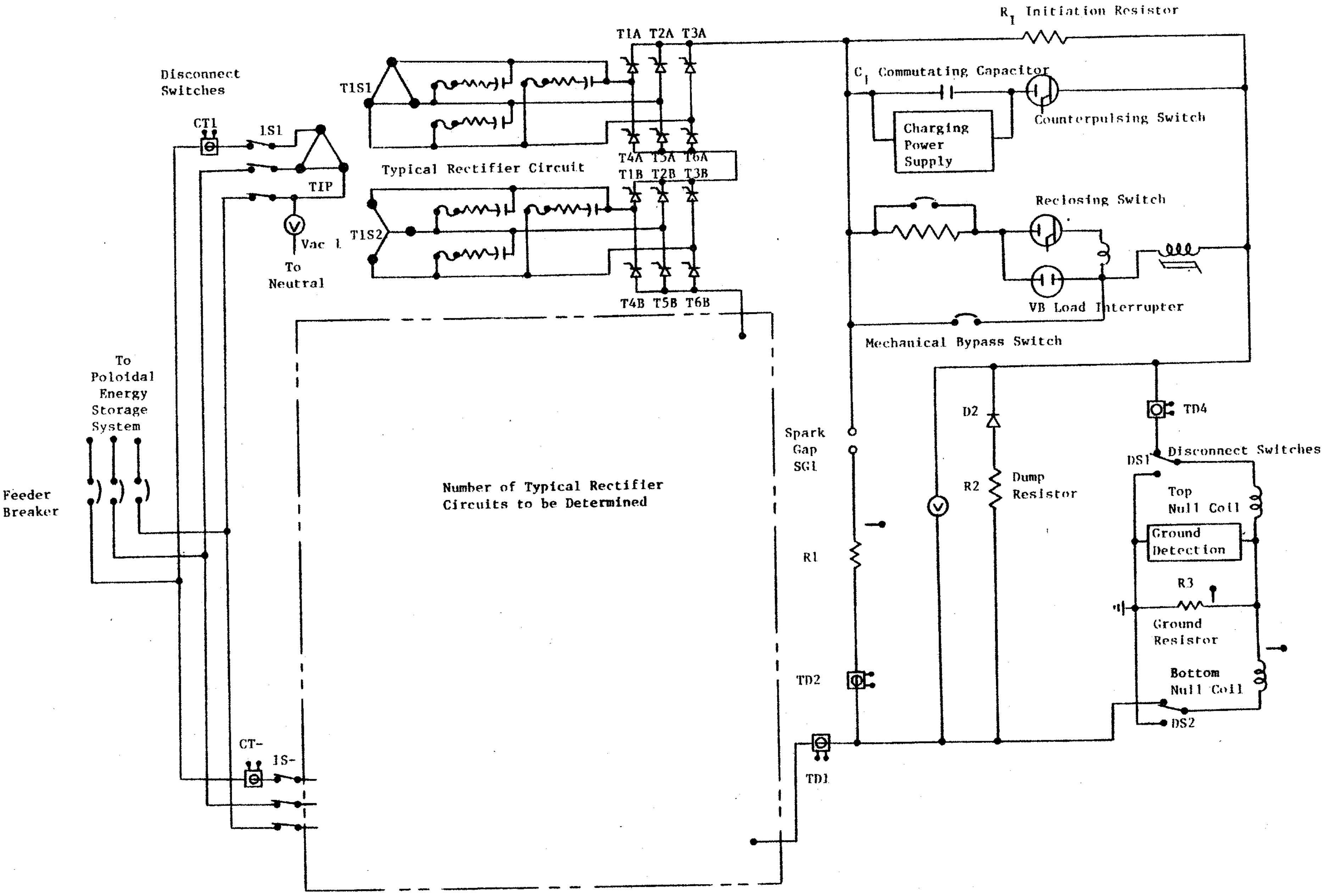

Figure 7-3 HFCTR Null Coil Power Conditioning System

The dipole and quadrupole coils are driven in antiseries and coil turn ratioes are adjusted so that the coil currents can have the same polarity and magnitude, while providing the prescribed ampere-turns of different polarity and magnitude required by the plasma. Since there are over three times as many ampere-turns in the dipole coils as in the quadrupole coils, the induced terminal voltages across the quadrupole coils will be less than a third of those across the dipole coils for equal induced volts/turn. The net combined voltages which must be provided by the power conditioning system are shown in Table 7.3-IV.

The dipole-quadrupole coil power conditioning system is characterized by the following requirements:

- Ability to sustain a constant current, against relatively high induced voltages during start-up and shut-down
- A high net power (1,522 MVA) must be supplied to the coils during initiation and a moderately high net power should be supplied in an actively controlled manner during start-up (487 MVA) and auxiliary heating (118 MVA). Equally high regenerative power flow from the coils should be expected during shut-down.
- The top and bottom (mirror image across the reactor horizontal equatorial plane) halves of the dipole and quadrupole coils should be driven in parallel, in order to provide passive damping of the plasma vertical instability.

A circuit which can achieve the above objectives is shown in Figure 7-4. A simplified schematic is shown in Figure 7-5, which illustrates the principal features of the circuit. A three-phase bridge rectifier is used for active control of plasma position during all phases of reactor operation,

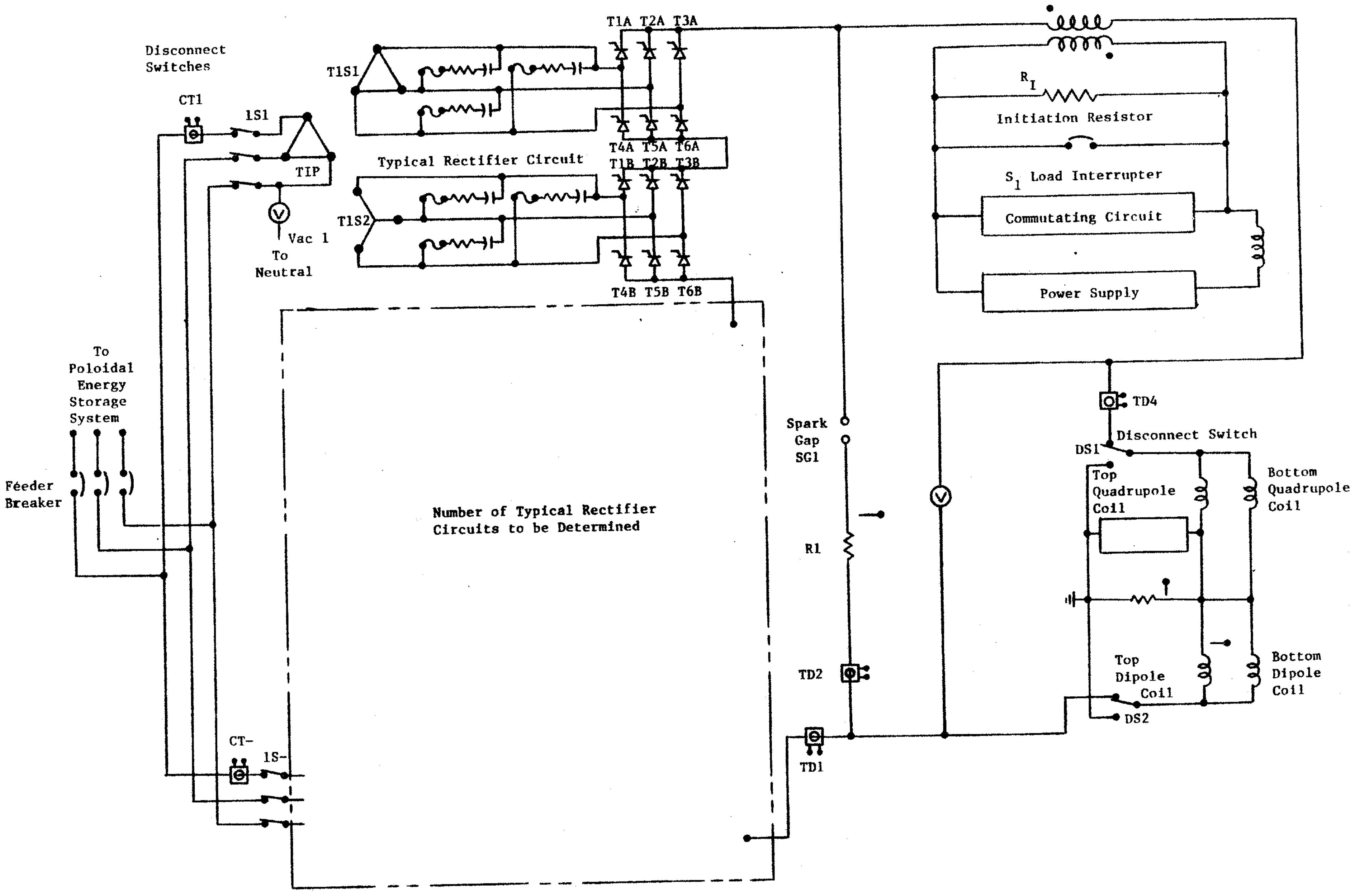

Figure 7-4 HFCTR Combined Dipole and Quadrupole Coil Power Conditioning System

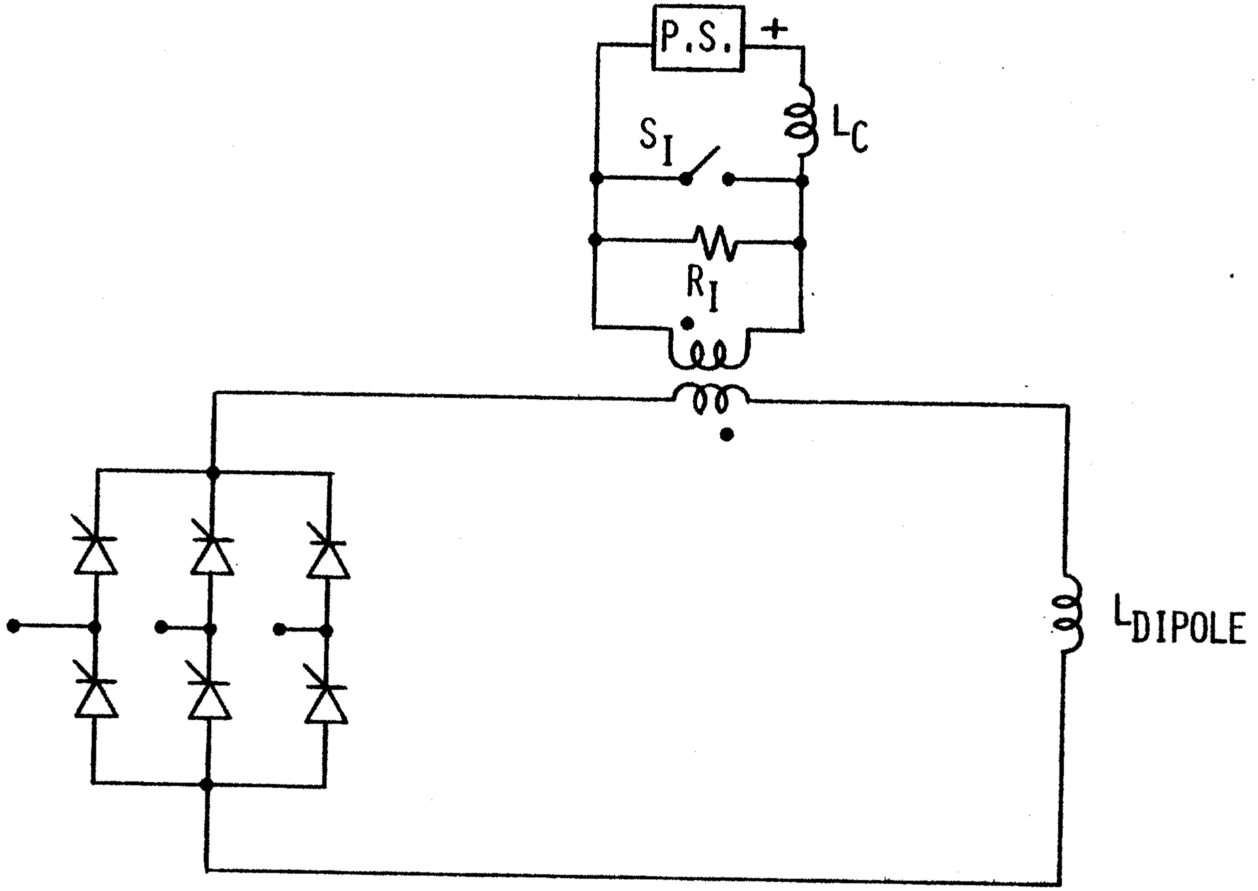

Figure 7-5 HFCTR Dipole Coil Power Conditioning System

with the exception of plasma initiation. During initiation, the magnetic energy stored in the magnetizing inductance of an air-core transformer is dumped into an initiation resistor. The voltage across the resistor is coupled through the transformer to supply power to the equilibrium field coils. The magnetizing current is adjusted between pulses to keep the current in the equilibrium field coils as nearly constant as possible, during the initiation period. Notice that this topology has never been suggested previously, because it is only desirable for coils with large prebiased steady-state currents, which absorb energy during initiation. This circuit is more complex and is projected to be more costly for a given initiation switch rating (peak voltage × peak current) than the simpler resistor switch used with conventional, unbiased EF coils. This "topological inferiority" partially cancels the cost advantage of using a null and dipole coil, as indicated in Section 7.2.2.

7.3.4 Quadrupole Power Conditioning System

In the reference design, there is no independent power conditioning system for the quadrupole coil, since it is driven by the combined dipole-quadrupole power conditioning system. It may be desirable to drive the quadrupole coils independently for the following alternative designs.

- Independent control of plasma position and elongation.
- Ease of initiation with quadrupole and null coils, instead of OH (See Section 7.2.1).
- Provision of plasma equilibrium field with pulsed dipole coil and no null coil (See Section 7.2.2).

If the quadrupole coil were driven independently, its power supply would be characterized by the following requirements:

- Regeneration of a moderately high (1,100 MVA) power during initiation.
- Ability to carry current of one polarity. A single rectifier-inverter is adequate.

The circuit topology selected for the null coil power conditioning system, shown in Figure 7-3, meets these requirements.

7.3.5 Substation and Buffer Generator

An input substation must be provided, which is separate from the output substation, associated with the plant net electrical output. This input substation is used to drive the generator-flywheel set which buffers the poloidal field coils and neutral beam sources from the utility line. With the possible exception of very stiff electrical grids, neither the poloidal field circuits nor the neutral beam sources can be pulsed from existing utility lines without causing unacceptably high line voltage transients or turbine spindle torques. Since interactions between different loads can be predicted and designed about, it is possible to benefit from the economies of feeding the poloidal field and neutral beam systems from a single generator buffer.

The substation rating can be determined from the energy inventory in Section 9. A 260 MW service should be provided by the outside electrical grid.

The generator-flywheel buffer and its charging circuit is shown in Figure 7-6. The reference design uses a rectifier-inverter set which runs the generator as a motor in order to make up its averaged losses over a cycle. There appears to be little difference in cost between a motor and a rectifier-inverter drive for the generator. Because of the complexity of the interactions between the generator, the rectifiers and the rectifier-inverter, rectifier-

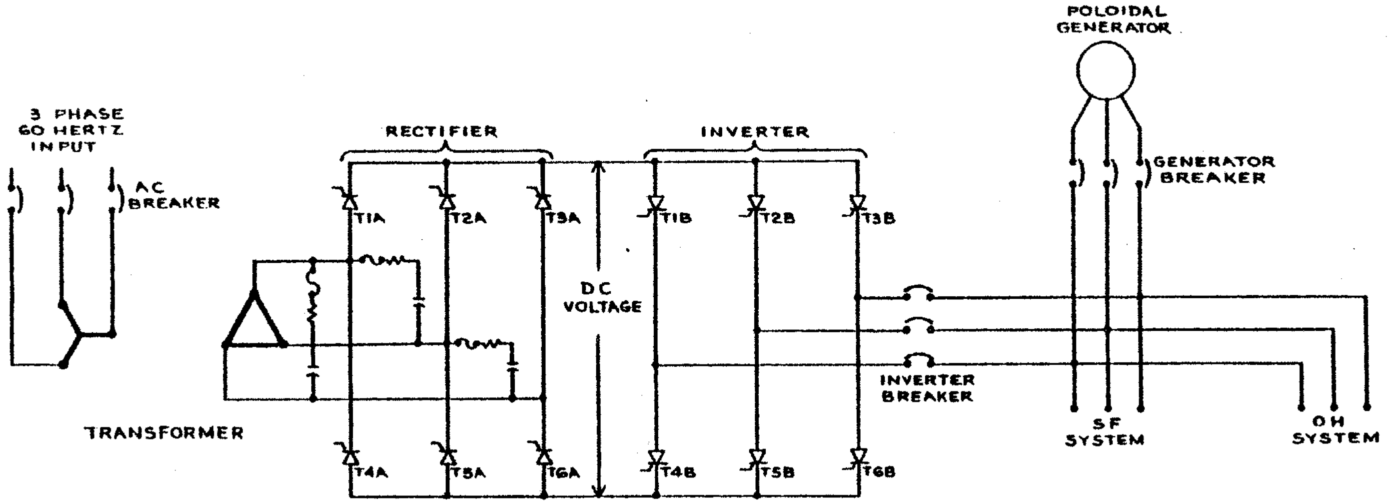

Figure 7-6 HFCTR Utility Line Buffer System

transformers are used with each poloidal field coil supply for isolation, even though the OH rectifier-transformer, which is the largest poloidal field transformer is not needed for impedance transformation.

7.3.6 Toroidal Field Coil Power Conditioning System

The toroidal field coil power conditioning system is relatively small, because its load consists of unpulsed, superconducting coils. Its design constraints are different from those of the very large coil charging power supplies which drive the normal copper TF coils in all planned and existing tokamaks. In HFCTR, the TF coils are charged to full current in half an hour. This time is long enough that the dominant factors in setting the design of the power conditioning system are the need to safely dump the coil energy in the case of a coil going normal and the need to provide a controlled voltage to balance the diamagnetic induction effect.

The constraints for safe removal of the magnetic energy in the toroidal field system when a coil is driven normal and fails to recover superconductivity are that the terminal and internal voltages in the toroidal field coils should not be high enough to cause flashover, but that the energy should be removed rapidly enough that joule heating of the TF coils does not cause melting or insupportable thermal stresses.

The two basic constraints associated with energy dumping conflict and dictate that the toroidal field system be driven by several independent power supplies. It is undesirable to split the toroidal field supply into several independently driven supplies for two reasons. It is best to drive all the toroidal field coils in series to ensure equal currents in each coil, which is particularly important in the case of an undetected fault or a failure in a coil control circuit. If the currents are not equal, there can be a large rotational force in the toroidal direction between coils. There are also diseconomies associated with breaking up the supplies in an application with superconducting TF coils, because the terminal voltages are sufficiently low that power supply costs are much more closely proportional to current than to power. Increasing the number of independently driven coils by breaking series connections between coils will increase the total current rating of the power conditioning system.

Since the TF coil plates will create a ground plane, the voltage at any point in a conductor is limited by the dielectric strength on the groundwall insulation around a single conductor jacket. For an epoxy-fiberglass ground wrap with a thickness of 0.1 cm at an integrated neutron dose of 10^9 rad, the maximum TF coil terminal voltage is constrained to be 4 kV. Since the coil current is 11.8 kA and each coil can be center-tapped, this implies dual dump resistors of 0.34 Ω. If the TF coil system is split into N independently driven systems, the peak dump power would equal $2NI_{TF}V_{MAX} = N \times 94.4$ MW and the effective L/R time constant would equal $E_{TF}/P_{TF}(0) = 4 \times 10^4$ MJ/(94.4 MW × N) = 424 s/N. The average coil resistance during the dump period is dependent on how many coils and how much of those coils have been driven normal. The energy deposited in the stainless steel structural plates should be relatively small. If the equivalent resistivity of each TF coil were 1×10^{-10} Ω - m, the instantaneous peak power deposited in the windings would equal 43.5 MW or 348 mW/cc. Breaking the TF circuit into eight independently driven supplies, one for each coil module, was selected as a reference. This would allow the coil to be substantially discharged in 55 s. The load dumping circuit consists of a mechanical circuit breaker, operated as a dc load switch with a counterpulsing circuit, and paralleled by an 0.34 Ω dump resistor (See Figure 7-7).

The peak power requirements of the bridge rectifier shown in Figure 7-7 will be determined either by the voltage required for coil charging or the control voltage needed to prevent TF coil current changes due to diamagnetic induction from the plasma. The peak coil charging voltage is $L\dot{I}$,peak. If the coil current charges linearly with time over 30 minutes, the constant coil voltage would equal

$$V_{TF} = \frac{2\ E_{TF}}{I_{TF} \times T} = \frac{2\ (4 \times 10^{10} J)}{(11.8 \times 10^{3} A)(1.8 \times 10^{4} s)} = 377\ V \quad (7.6)$$

The highest voltage induced by diamagnetic induction would probably occur during normally scheduled shut-down. The worst case that has been identified in the present plasma start-up scenario, described in 2.3, occurs between t = 4.0 s and t = 4.5 s, when plasma density is increased rapidly at the beginning of neutral beam heating. During this time, β_p increases from 0.2 to 1.2 in 0.5 s. The voltage induced in the TF coils by a rapid change in β_p is expressed by

$$1 - \beta_p = \frac{8\pi\ B_\pi\ \delta\Phi}{\mu_o^2\ I_p^2} \quad (7.7)$$

If I_p is held constant, as specified in the start-up scenario, then

$$\dot{\Phi} = \frac{\mu_o^2\ I_p^2}{8\ \pi\ B_t} = -.09\ V/turn \quad \dot{\Phi} - \frac{\mu_o^2\ I_p^2}{8\pi\beta_t}\dot{\beta}_p \quad (7.8)$$

Since the TF coil system has 18,800 turns, the voltage across a seriesed system would be 1,690 V. This is higher than the charging voltage and would, therefore, determine the rectifier rating. Each of the eight individual rectifier modules would be designed to supply 210 V. Of course, the high rate of rise

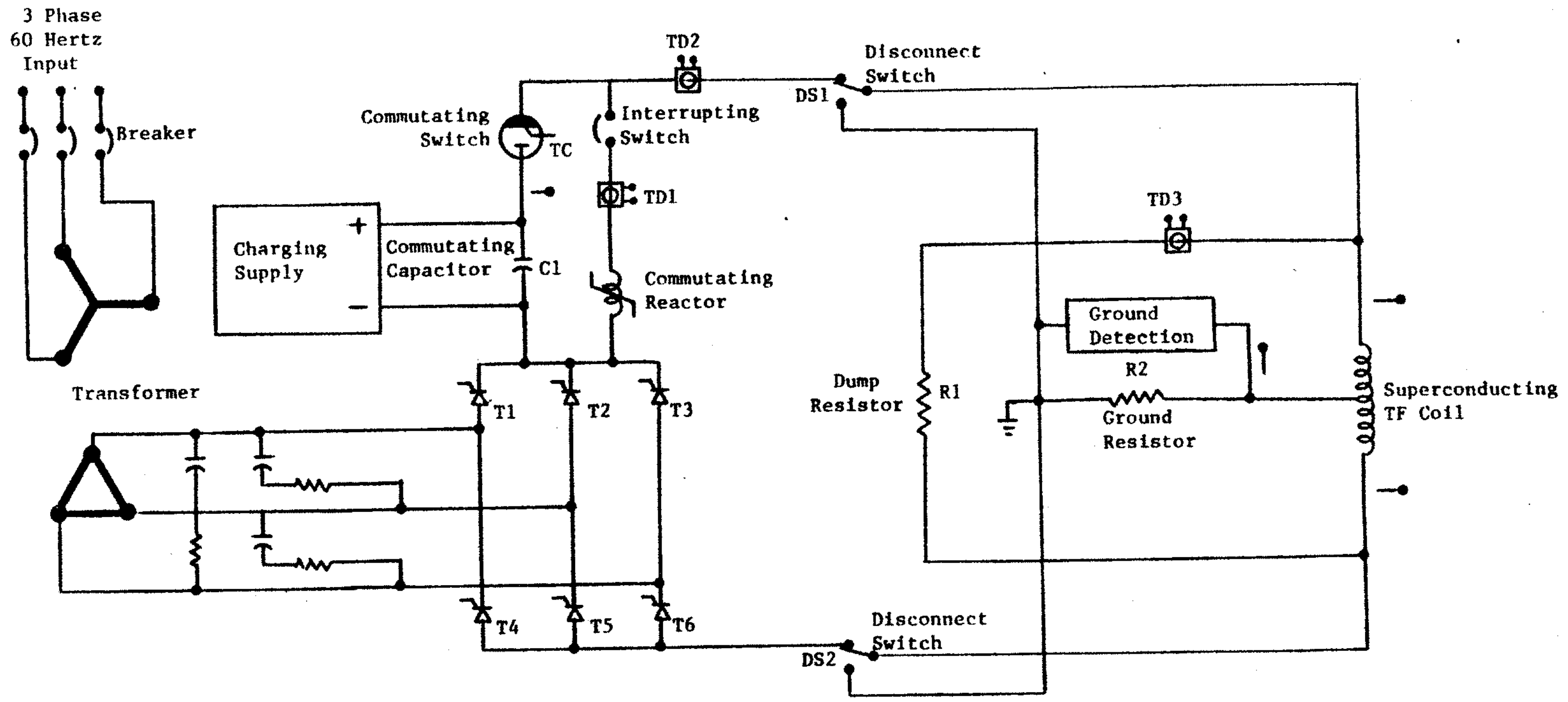

Figure 7-7 HFCTR Toroidal Field Coil Power Conditioning System

of β_p from 4.0 s to 4.5 s is not fundamentally constrained and could be reduced. However, since abort and shut-down have been ignored, this would not be a conservative approach. There is also little further cost advantage to be gained by reducing the voltage, since power supply costs will be driven by current requirements at such low voltages. Notice that the voltage from diamagnetic induction is considerably less than the dumping voltage, so this effect has no influence on insulation or dump resistance design.

7.4 ALTERNATIVE CIRCUIT CONCEPTS

7.4.1 Antitransformers

The use of antitransformers, as illustrated in Figure 7-8, was considered, to decouple the effect of pulses in the more highly pulsed poloidal field coil systems, such as the ohmic heating and null coils, from the unpulsed coils, such as the quadrupole and dipole coils. Antitransformers are used for decoupling the equilibrium field coil circuits from the ohmic heating coil in Alcators A and C and in TEXT. It was felt that antitransformers might be particularly effective in the HFCTR design, because of the presence of two coil systems (dipole and quadrupole) with relatively high steady-state current. Without decoupling, their power supplies have to supply high voltage at high current, in order to keep the coil current constant, when other poloidal field coils are pulsed. With decoupling coils, it was believed that small power supplies could be used to drive the two steady-state coils.

Power supply voltages were calculated for several cases, including decoupling all steady-state coils from all pulsed coils, decoupling all coils from the OH coil only, decoupling from the null coil only, overdecoupling and underdecoupling.

The results of the trade study were universally discouraging. No degree of decoupling could be identified which could possibly be economically competitive with no decoupling at all. The most significant results are listed below:

- When a coil with a smaller peak power rating was decoupled from a higher power coil such as the OH coil; the decrease in the power

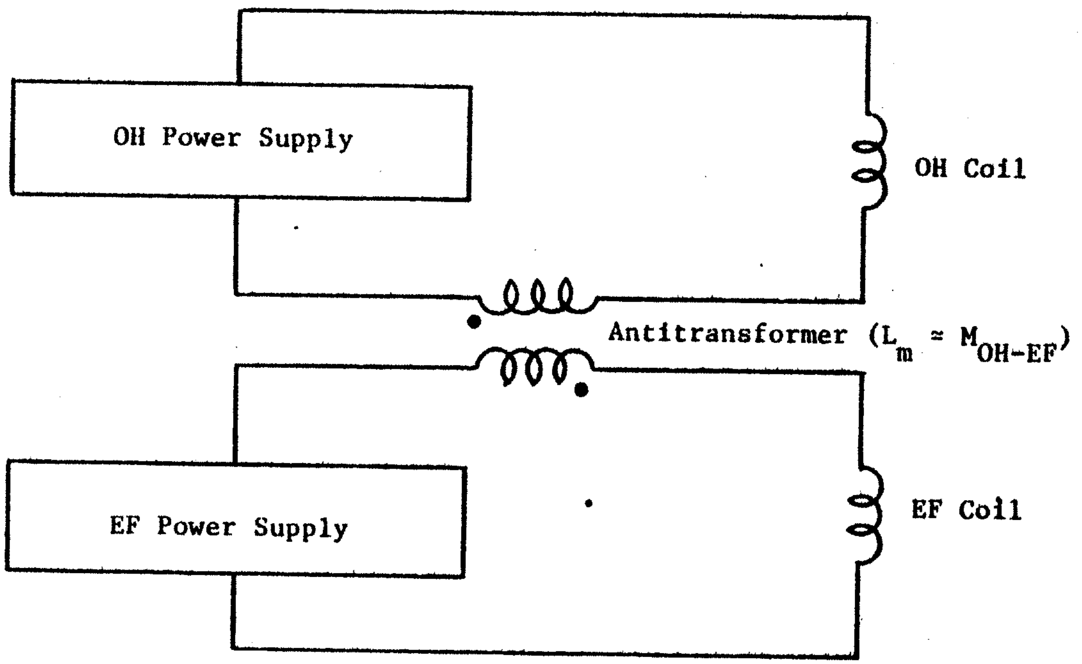

Figure 7-8 Simplified Diagram of Poloidal Field Circuits with Antitransformer

supply was always less than the increase in the power supply requirements of the high power coil.

- During auxiliary heating, when the direction of ohmic heating current change reverses sign, the decoupling coils actually added to the power supply requirements of the equilibrium and quadrupole field coils.
- Decoupling coils themselves are not inexpensive. They are not capable of greatly simplifying coil power supply operation, because none of the coils can be decoupled from the plasma, which is the least predictable of the poloidal field "coils". They inherently degrade passive stabilization of plasma vertical and radial motions by placing a relatively high impedance external to the coils. Therefore, a very dramatic improvement in power supply requirements would have to be demonstrated, before recommending any form of decoupling. It appears unlikely that antitransformers will have any place in any commercial tokamak reactor.
- However, since all forms of decoupling increased the total power supply requirements, it remains possible that power supply requirements could be reduced by reversing an antitransformer's leads and overcoupling!

7.4.2 Modularization

A large rectifier, containing hundreds or thousands of individual thyristors and firing circuits, may be broken up into any number of identical modules. The reference design uses only two series modules for each poloidal field rectifier. An alternative approach to be used in TFTR (5) breaks up each giant rectifier into as many identical modules as possible. This "total modularization" approach, specifies that each identical module have six rectifiers in a three-phase bridge configuration. The advantages of this approach are extreme flexibility in reconfiguration, ease of replacement of a failed module, the possibility of isolating a single faulty thyristor with a fuse, and a potentially high power factor.

Total modularization was not selected for HFCTR for the following reasons:

- The initial cost of a modularized design must be higher, since each module must be insulated for the highest system voltage and each module requires solid-state bypass modules.
- Relatively high power factor can be achieved by running only two series modules in a buck-boost mode.
- Extreme flexibility in reconfiguration is not nearly as important for a commercial reactor as it is for a laboratory with ambitions to apply previously acquired equipment to future experimental reactors.
- The postulated (5) ability to remove and reinstall a faulty module in one hour is somewhat less advantageous in a commercial reactor, where steam would be lost anyway and the plant would be down for about eight hours, while steam was reestablished.

- In order to let individual thyristors be bypassed, there is an additional cost of current limiting reactors to ensure 120° conduction. In a large module, a small amount of parallel and series device redundancy permits failed devices to be automatically bypassed until routine maintenance periods. For HFCTR, these periods are short, but frequent.

7.4.3 Inductive Energy Storage

Large energy storage inductors have been proposed (6) as an inexpensive alternative to motor-generator-flywheel sets as utility line buffers. The circuit shown in Figure 7-9 is the most completely analyzed of the several possible energy transfer systems that could be associated with inductive energy storage and was used as a reference for comparison with a motor-generator-flywheel set. The inductive energy transfer system was rejected for the following reasons:

- Regardless of the relative costs of the energy storage elements, the rectifiers for the inductive system require three times as many thyristors as the rectifiers for the inertial storage system. As can be seen from Figure 7-9, two equal-rating bridges are required for the inductive system versus one bridge for an inertial storage system. Also, since the voltage on the interbridge capacitors is proportional to the sum of the two coil currents, when half of the original stored energy has been transferred, the peak capacitor voltages and the peak thyristor blocking voltages will be about 1.4 times greater than the full load and no load voltages. The ratio of forward blocking voltage to dc load voltage for a rectifier fed by a

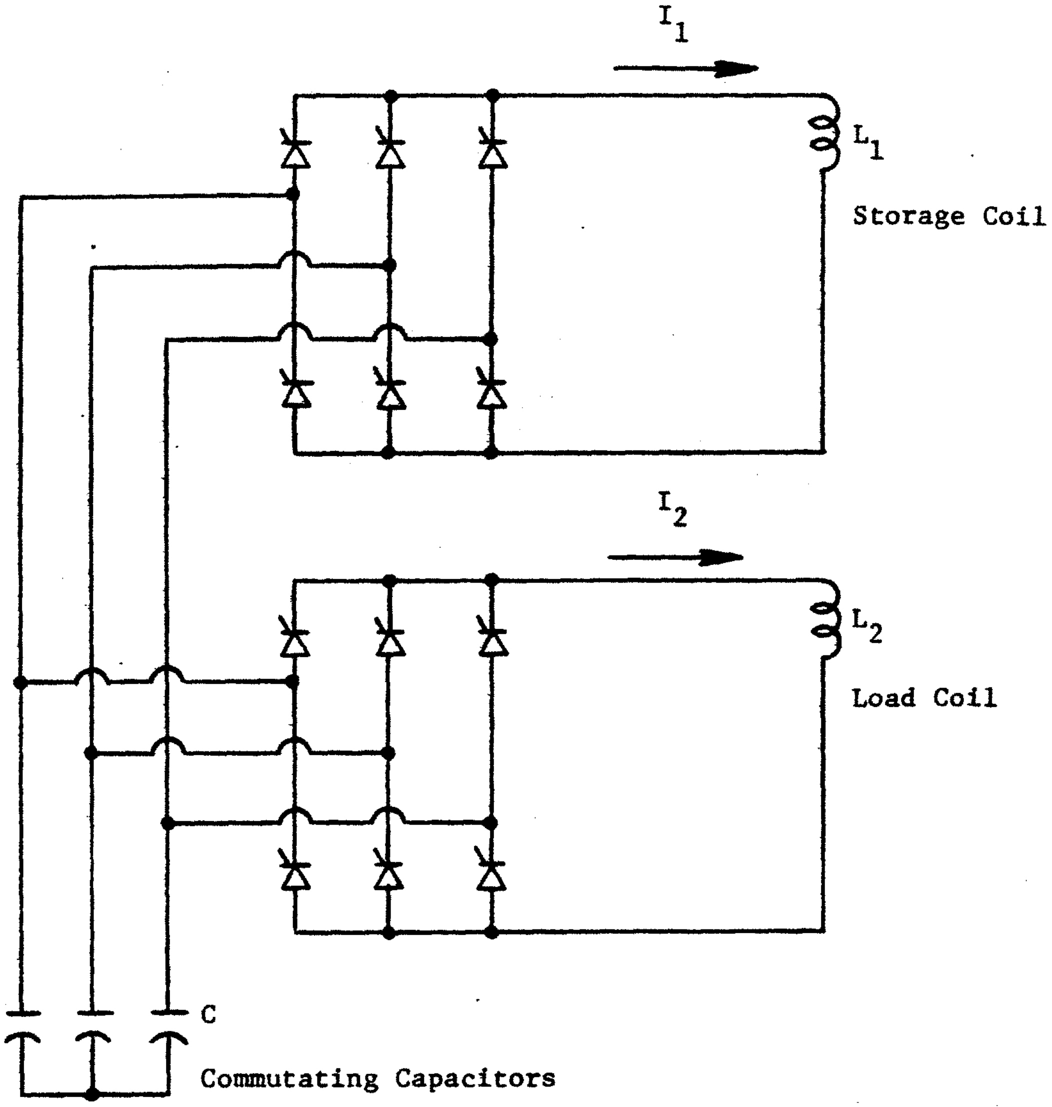

Figure 7-9 Inductive Energy Transfer System Using Bridge Rectifiers and Natural Commutating Capacitors

three-phase generator is only 1.05 : 1. The remainder of the difference arises from the different waveshapes on the ac side of the rectifiers.

- Very low energy storage costs, in the range of 0.1¢/J have been predicted for large energy storage inductors. Advanced inertial energy storage systems have even lower predicted costs for the flywheel element. Chiao (7) has proposed that E-glass/epoxy flywheels can be built for as little as $3.9/MJ and that steel flywheels can be built for less than $89/MJ or 0.01¢/J.
- Since generator costs are large, but nondominant, the proposed inductive energy storage system should not be preferable, unless the relative cost of rectifier bridges improves considerably versus the cost of synchronous generators.

7.5 THERMAL ENERGY STORAGE SYSTEM

During the twenty seconds between ignited burns in normal operation, it is necessary that the steam generator supplying the steam turbine should not lose steam. In present-day utilities, once steam is lost, it typically requires eight hours to bring the electrical generating equipment up to operating temperature and speed. It would not be acceptable for a tokamak power plant to lose steam frequently because of a moderate miscalculation of the time needed between pulses or due to temporary losses of enable, caused by the need to switch from a defective motor, valve or circuit to a spare. A thermal energy storage system which can prevent steam from being lost for over a minute is desirable.

7.5.1 Use of an Energy Storing Blanket

The University of Wisconsin NUWMAK study (8) has proposed the use of a $Li_{62}Pb_{38}$ eutectic as the blanket/breeder material. This blanket material has favorable neutronic properties and should also be useful as a source of thermal energy storage. For a blanket volume of 200 m^3 in HFCTR, the high enthalpy of phase transition (140 kJ/kg) of the eutectic, would allow a 49 s interval between ignited burns, before the primary coolant loop absorbed the entire heat of transition of the salt. If a 100 C drop in the blanket temperature were permitted, another 6.0 s of steam could be generated, which seems to be not worth the price in thermal cycling. Since this blanket material has only begun to be characterized, it was not selected over lithium. However, if it is a feasible blanket material, it should be preferable to any other known tritium breeding material as a thermal reservoir.

7.5.2 Use of Flash Steam in Steam Generator

Buchanan (10) has suggested the use of flash steam, which stores energy in the water/steam combination in the steam generator. A pressure reducer at the outlet of the steam generator lowers the vapor pressure of the steam in the steam generator significantly in order to flash water into steam and to keep the temperature of the steam supplied to the steam turbine relatively constant. Only a 25 C drop in the inlet temperature of the steam supplied to the turbine is permitted.

The reference design parameters of the boiler and turbine condenser conditions are shown in Table 7.5-I. A typical light water reactor turbine, operating off of saturated steam, was selected, along with a free-surface pressurized-water reactor boiler. It must be noted that the 343 C peak temperature of the boiler corresponds to a 32% thermal to electric energy conversion efficiency, while a high temperature boiler-turbine system can achieve up to 40% efficiency. The efficiency could be raised if a eutectic blanket were feasible, but otherwise there is little choice. The only energy storage alternative which does not appear to be prohibitively costly is a fluidized bed. Since the use of radioactive FLIBE as a primary coolant mandates the use of an intermediate heat exchanger, the use of a fluidized bed, say of graded sand, may have a low incremental cost. This approach requires considerable scaling in physical size before it can be shown to be viable.

The reference flash steam energy storage system allows 20 seconds of full electrical output from flash steam alone. The minimum quantity of water in the boiler at the beginning of the off period is $.162 \times 10^6$ kg and the fractional water level drop during the off period is 12.8%.

TABLE 7.5-I

BOILER CONDITION

	TOP	BOTTOM
	ENGLISH / SI	ENGLISH / SI
P	2200 psi / 15.1 MPa	1600 psi / 11.0 MPa
h_f	695.5 BTU·lb^{-1} / 1,616 kJ·kg^{-1}	624.2 BTU·lb^{-1} / 1,451 kJ·kg^{-1}
h_{fg}	426.7 BTU·lb^{-1} / 992 kJ·kg^{-1}	540.3 BTU·lb^{-1} / 1,256 kJ·kg^{-1}
h_g	1,122.2 BTU·lb^{-1} / 2,610 kJ·kg^{-1}	1,164.5 BTU·lb^{-1} / 2,706 kJ·kg^{-1}
V_f	0.02669 ft^{3}lb^{-1} / 1.67 × 10^{-3} m^{3}kg^{-1}	0.02387 ft^{3}lb^{-1} / 1.49 × 10^{-3} m^{3}kg^{-1}
T	649.5 F / 343 C	604.9 F / 318 C

TURBINE CONDENSER CONDITION

(English/SI)

P	10 in$_{Hg}$/33.8 kPa
h_f	129.4 BTU·lb^{-1}/300.8 kJ·kg^{-1}
V_f	0.0164 ft^3·lb^{-1}/1.03 × 10^{-3} m^{3}kg^{-1}
T	161.5 F/71.9 C

CHANGE TOP-BOTTOM

ΔP	600 psi/4.1 MPa
Δh_f	71.3 BTU·lb^{-1}/165 kJ·kg^{-1}
Δh_g	-42.3 BTU·lb^{-1}/-96 kJ·kg^{-1}
ΔV_f	.00282 ft^{3}lb^{-1}/.18 × 10^{-3}m^{3}kg^{-1}
ΔT	44.6 F/24.8 C

REFERENCES - SECTION 7

(1) J. F. Clarke, D. J. Sigmar, "Global Properties of High Pressure Flux Conserving Tokamak Equilibria," ORNL/TM-5599, Aug 1976

(2) R. J. Hawryluk, private communication

(3) K. J. Thomassen, et al, "Fusion Reactor Requirements and Systems for Energy Storage and Transfer," ANS Third Topical Meeting on the Technology of Controlled Nuclear Fusion, Santa Fe; May, 1978

(4) J. H. Schultz, "Switching Technologies for Future Tokamak Fusion Reactors," ANS Third Topical Meeting on the Technology of Controlled Nuclear Fusion, Santa Fe; May, 1978

(5) G. Karady and R. Cassel, "Design Philosophy of the 600 MW Pulsed Energy Converters for the Toroidal Field Coil of TFTR at Princeton," Proc. of Seventh Symp on Eng Prob of Fusion Research; Knoxville; Oct, 1977

(6) R. L. Kustom, et al, "Argonne National Laboratory Energy Storage and Transfer Experimental Program," Proc of Seventh Symp of Eng Prob of Fusion Research; Knoxville; Oct, 1977

(7) T. T. Chiao, "Fiber Composite Materials and their Application to Energy-storage Flywheels," Energy and Technology Review, UCRL-52000-78-6; Je 1978

(8) R. W. Conn, G. L. Kulcinski, E. W. Maynard, "NUMAK: An Attractive Reactor for the Main Line of Tokamaks," ANS Third Top Mtg on Tech of Cont Nuc Fusion; Santa Fe; May, 1978

(9) C. H. Buchanan, "Energy Storage for Tokamak Reactor Cycles,"

8. NEUTRAL BEAM HEATING SYSTEM

The neutral beam heating system is a conventional, positive-ion source auxiliary heating system, operating at a beam energy (120 keV) compatible with moderately high neutralization efficiency. This low beam energy can be achieved in a reactor with a high ignition margin of safety by the use of asymmetric ripple assisted injection. The ripple requirements for adequate penetration are discussed along with a rationale for the injection angle and the number of asymmetric ripple-creating coils. A guiding-center orbit calculation was used to demonstrate the feasibility of this idea for the HFCTR plasma. The beamline pumping and space requirements for the reference design were also calculated.

8.1 RIPPLE-TRAPPING INJECTION

The steady gradient-B drift of ripple-trapped ions can be used to advantage for increasing the effective penetration distance of injected neutral beams [1]. Figure 2.36 shows contours of peak-to-peak vacuum ripple $\delta(r)$ set up by the ripple-coil system described in Section 3.5. (For simplicity, a circular plasma is used in this analysis.) In the presence of the plasma current, the actual depth of a local magnetic well set up by the ripple decreases to $\delta_*(\bar{r})$, where δ_*/δ depends on the position within the plasma. Energetic ions with $v_{11}/v < \delta_*^{1/2}$ are trapped in local magnetic wells and drift vertically with the ∇B-drift velocity. In Figure 2.36 energetic ions formed from neutral beams injected vertically from the bottom ($v_{11} = 0$) are thus mirror-trapped in the high-ripple region at $z > 0$, so that in this region $\delta_* = 0$. Then at $z > 0$ ions with small v_{11}/v no longer have time-averaged vertical drifts, but instead follow banana orbits.

To reach the midplane ($z = 0$) before pitch-angle scattering out of its local magnetic well, an ion of atomic mass A_w must have energy

$$W_{min}(\mathrm{keV}) = 3.2 \times 10^{-9} \left[\frac{\langle n_e Z_{eff} \rangle}{\delta_o A_w}\right]^{2/5} \qquad (8\text{-}1)$$

where δ_o is the ripple at $z = 0$ (cgs units are used) [1]. Figure 8-1 shows W_{min} as a function of δ_o. For large dense plasmas, the required beam energy for ripple injection can be one order of magnitude smaller than that required by the conventional injection method.

Figure 8-2 shows a typical Monte Carlo calculation of the guiding-center orbit of a 120 keV ion injected into the HFCTR plasma at high density. The conventional injection technique would require a beam energy of about 400 keV to obtain comparable penetration. The Monte Carlo calculations and also theoretical considerations indicate that vertically asymmetric ripple gives rise to unclosed banana orbits that gradually drift outward [2]. However in the presence of Coulomb drag, ions injected in an energy range near W_{min} thermalize near the central plasma region. Nevertheless, the neoclassical diffusion rate of ions with energy exceeding about 8 keV is enhanced

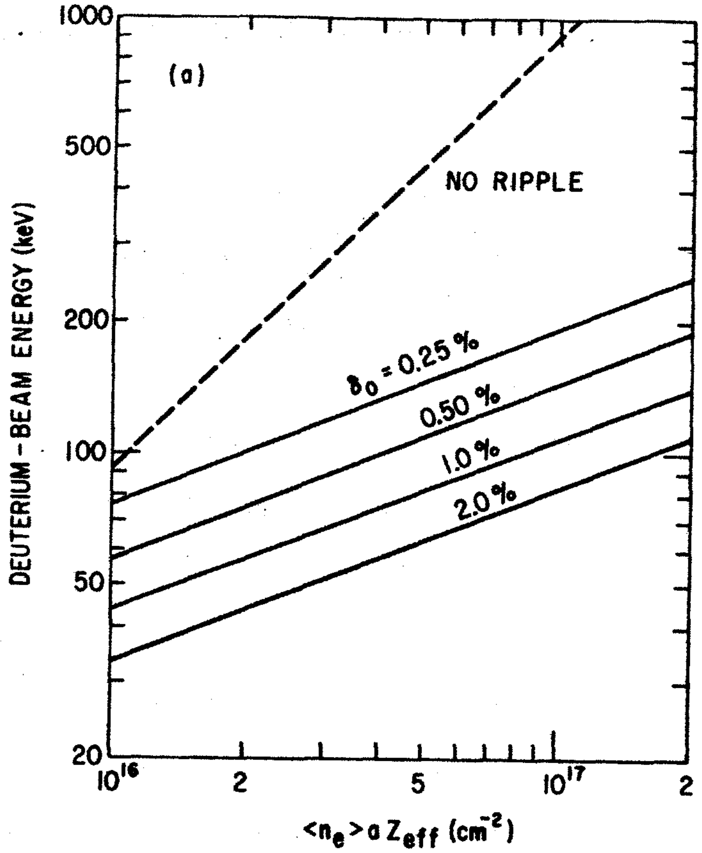

Figure 8-1 Required injection energy (D°) so that deuterons drift from the bottom of the torus to the horizontal midplane.

somewhat by the asymmetric ripple. This effect occurs only during start-up when the ripple coils are activated, but could be used to advantage in regulating the plasma temperature during the thermonuclear burn, as discussed in Section 2.5.

Strictly vertical injection is often inconvenient, because of the limited access between the TF coils at smaller major radius. The Monte Carlo calculations have demonstrated that fast-ion penetration and thermalization are adequate when the injection angle is as large as 30° from the vertical (but still in the vertical plane), provided that the outer boundary of the neutral beam intersects the magnetic axis [3]. This injection angle has been adopted for the HFCTR, as previously shown. In order to minimize the required ripple-coil current and associated power demand, the plasma is displaced 20 cm below the horizontal midplane during heating. At this stage, the plasma shape factor $S = 1.4$. The final plasma elongation of $S = 1.5$ is established during alpha-particle heating to operating temperature.

The application of vertically asymmetric ripple also produces magnetic islands when the number of ripple locations around the torus, N, is small [4].

It has been determined for the HFCTR that no magnetic islands are formed when $N \geq 4$. In fact, $N = 8$ is used to obtain sufficient access for beam injection, as discussed in Section 8.2

The first experimental test of the ripple-trapping injection is expected to take place on the ISX-B tokamak at ORNL in 1978-79 [5]. A 3 A, 15-keV neutral beam will be vertically injected from the bottom of the tokamak, and the orbits of 15-keV ions will be followed carefully by charge-exchange diagnostics. The effect on bulk-ion diffusion, and on the magnetic structure of the plasma, will also be investigated.

8.2 CHARACTERISTICS OF THE NEUTRAL BEAM SYSTEM

Since performance of the neutral beam system is critically important, a conservative approach to the choice of the system requirements has been taken. Eight beamlines, each utilizing three sources of the LLL/LBL type, have been chosen. By using asymmetric-ripple injection, the energy of the beams may be kept at 120-150 keV. These injectors are thus basically similar to the TFTR injectors [6] of which a prototype will be operating in 1979. The monatomic percentage of extracted current is assumed to be 80%. While a monatomic fraction of at least 90% seems possible in view of recent ORNL results, such improvements are not assumed in the present design.

The beam characteristics have been obtained by scaling to the TFTR beam specifications assuming constant current density. Again, this assumption is somewhat conservative since current density has continuously been increased during the beam development program. If higher current densities do become available, the present margin of safety in beam performance will become larger.

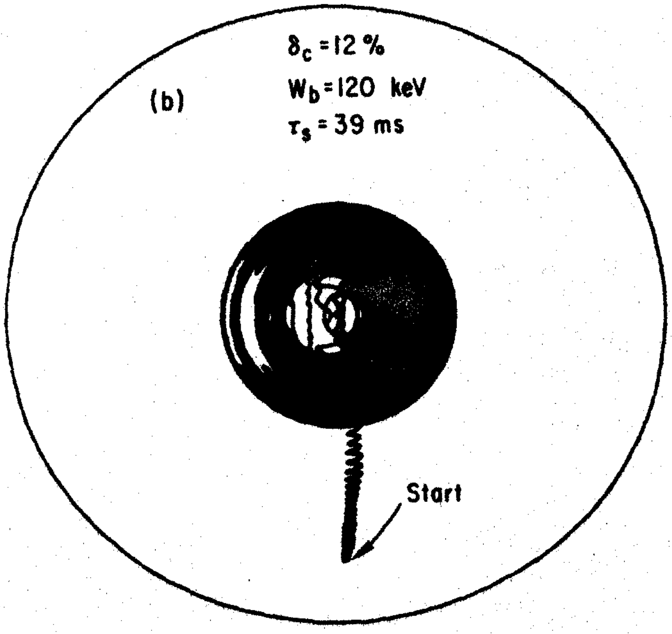

Figure 8-2 Guiding center trajectory over the slowing down time (39 ms) of a 120 keV ion.

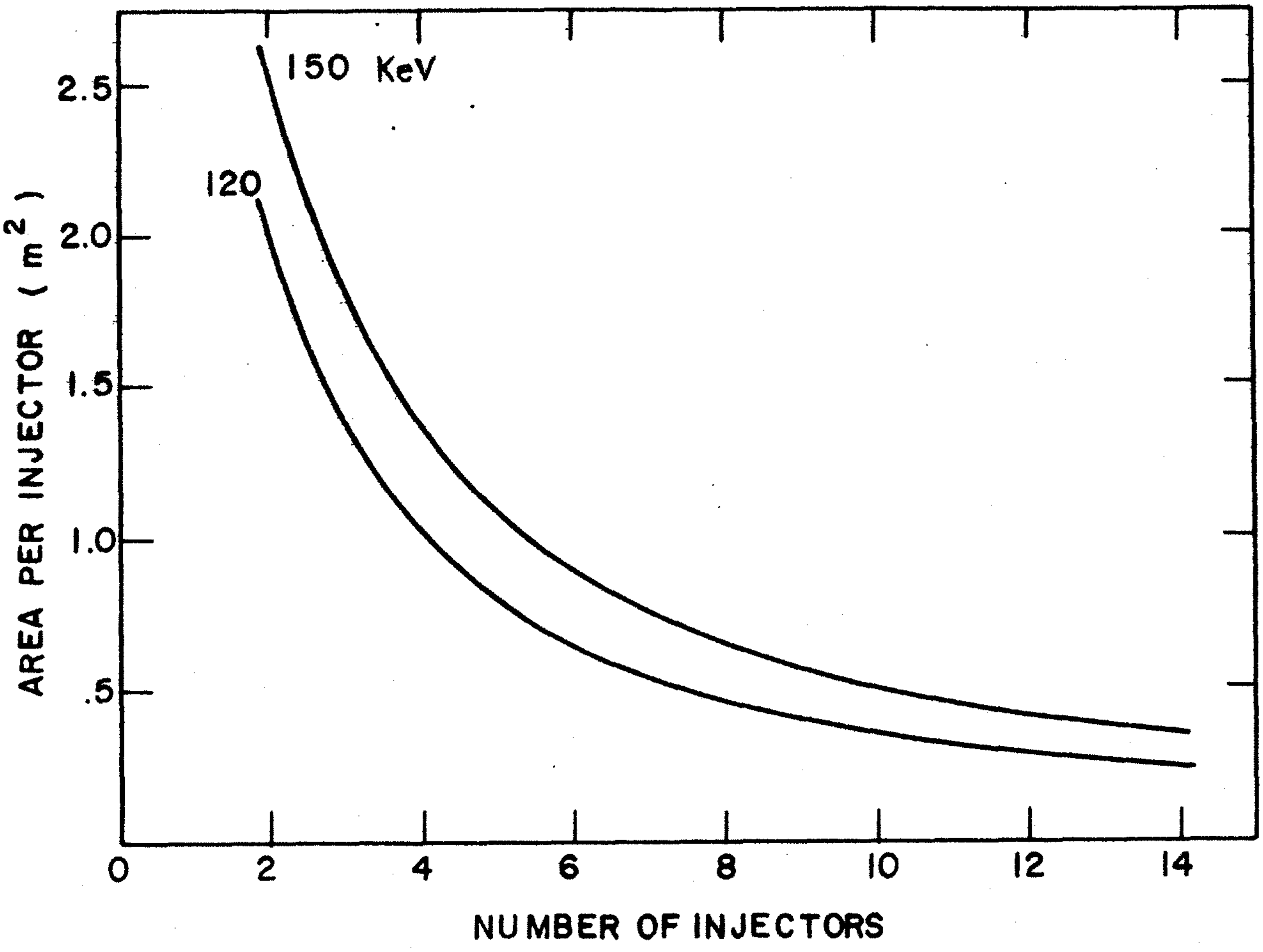

Figure 8-3 Injection area per injector

Based on constant current density scaling, injection of 100 MW of monoenergetic deuterium atoms requires 5.0 m^2 of area (667 amps, $D^o{}_{150}$) at 150 keV, and 3.7 m^2 of area (833 amps, $D^o{}_{120}$) at 120 keV. The different areas are due principally to the difference in conversion efficiency from ions to atoms at the two energies (29% @ 150 keV; 41% @ 120 keV). The power density of the 120 keV beam is somewhat higher than the 150 keV beam.

The injection area per injector is shown as a function of the number of injectors in Figure 8-3. The range of the number of injectors which could be used in a tokamak with R_o = 6 m and a = 1.2 m is probably from 4 to 16. A reasonable compromise between the number and size of injectors for a machine with a complex magnet structure and a ripple-coil system appears to be 8. With 16 TF coils and 8 beamlines, there is adequate room for injection and shielding between coils. At 150 keV, each injector requires 0.62 m^2 of injection area for injection of 83 amps D^o. At 120 keV, each injector requires 0.46 m^2 of injection area for injection of 104 amps D^o.

Half-energy neutrals resulting from accelerated D_2^+ (i.e. $D_{60}{}^o$ or $D_{75}{}^o$) enter the plasma along with the full-energy component. Because the half-energy component has a larger neutralization efficiency, it accounts for a substantial fraction of the injected power. For example, 90 amps of $D_{60}{}^o$ would be injected simultaneously with 104 amps of $D_{120}{}^o$ (assuming ~20% D_2^+ from the source). Methods are being considered to alleviate this problem (e.g. electromagnetic removal of D_2^+ before it enters the neutralization cell); however, much additional work is needed.

8.3 BEAMLINE PUMPING AND SPACE REQUIREMENTS

The largest access problem involved in the beamline design is not that of neutronic shielding of the TF coils in the vicinity of the beamport, but it is rather the problem of obtaining adequate pumping speed in the beamline to ensure the required low pressures (thus preventing beam reionization and scattering). The severity of the problem can be realized by observing that the overall gas efficiency of the beams (product of source gas efficiency, monatomic extraction efficiency, and neutralization efficiency) is only 12% @ 150 keV and 16% @ 120 keV.

The expected gas loads are given below for the 120 keV neutral injection system.

From sources	Cause	Gas load Pa-m^3/s per beam line	8 beamlines
	Flow out aperture	10	-
	D^+ not neutralized	2	-
	Total from sources and neutralizer	12	96

These gas loads are shown at their point of origin in a single 120 keV injector in Figure 8-4. Also shown is the calculated pressure required to prevent re-ionization of the beam by the cell gas. The fractional re-ionization vs. pumping speed (determined by pressure at a fixed throughout or gas load) is shown for the beamlines in Figure 8-5. In TFTR beamlines, a value of 1% re-ionization is assumed. In the HFCTR beamlines, this value (1%) requires pumping speeds of 1.7×10^7 liters/second. This speed is unacceptably large, and a re-ionization limit of 4% appears much more desirable as a

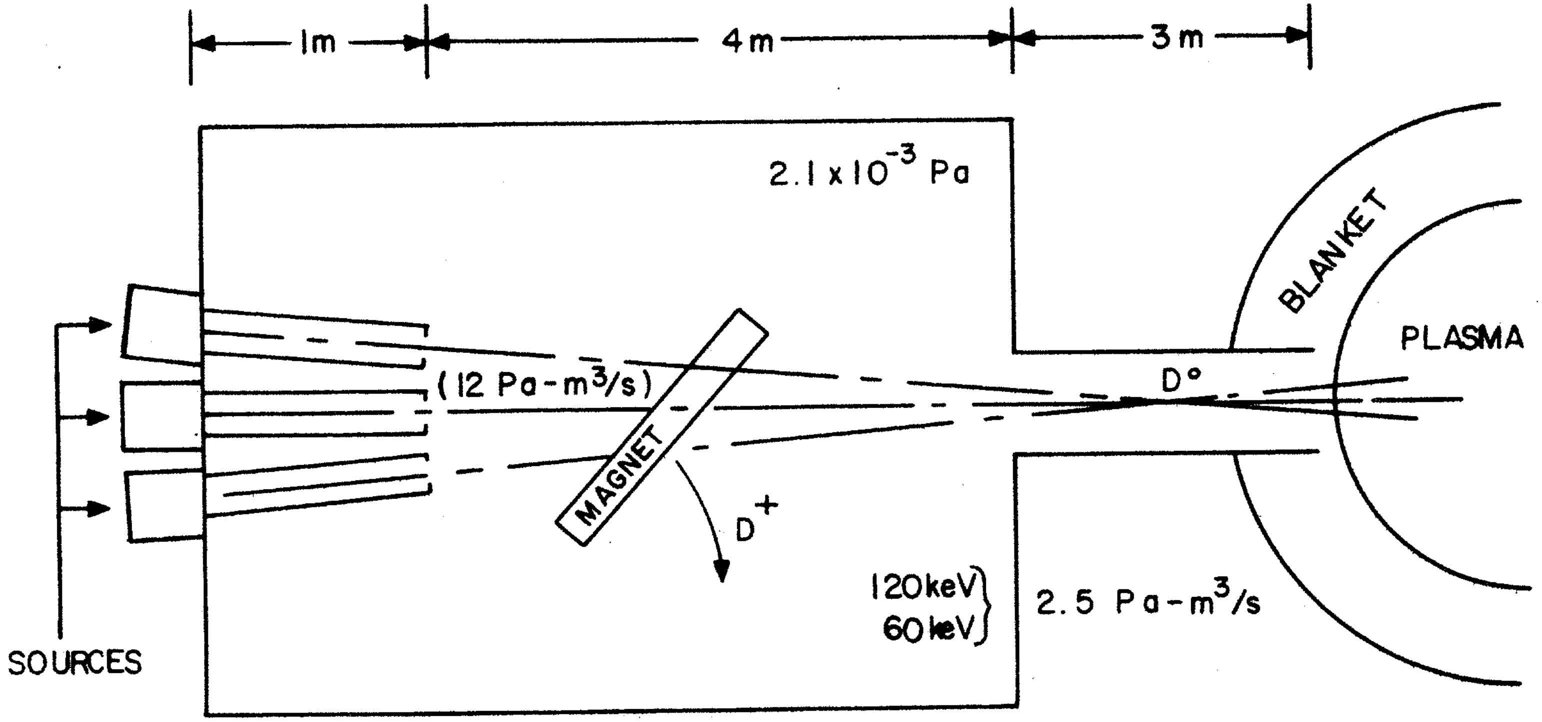

Figure 8-4 Injection gas load.

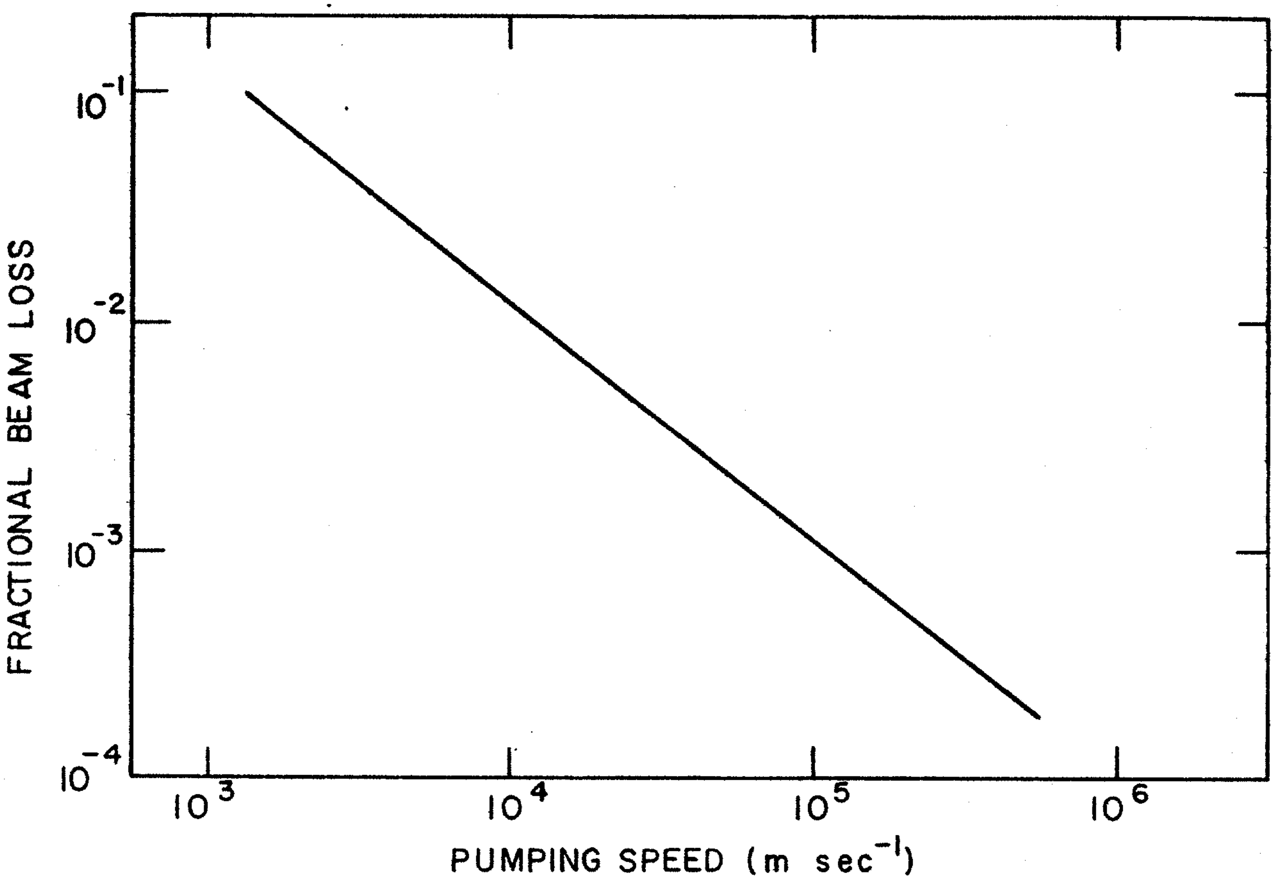

Figure 8-5 Fractional reionization vs. pumping speed.

compromise between beam loss and pumping speed.

The gas loads, required pressures, and resultant required pumping speeds for each beamline are tabulated below:

Gas load out of neutralizer ($Pa-m^3/s$)	12
Pressure (Pa)	2.1×10^{-3}
Pumping Speed (m^3/s)	5.6×10^3
Gas load to plasma ($Pa-m^3/s$)	0.02

The only methods of providing sufficient pumping speed in close proximity to the gas loads (i.e., to avoid conductance limitations) are to use cryosorption panels or gettering surfaces on the inside walls of the beamlines. Cryosorption panels are currently in use, and are planned for use in the TFTR beamlines. A typical panel design is shown in Figure 8-6. The 77 K chevron baffle does not pump deuterium, but does reduce the heat load on the 15 K baffle by a factor of 4.5. Since refrigerator efficiency is proportional to absolute temperature raised to a power higher than one at these values, operation at 77 K significantly improves efficiency. The probability of sticking on the molecular sieve at 15 K is very near unity. Efficiency is increased by approximately a factor of four by using a 15 K panel vs. a 4 K panel. Using this arrangement, desorption of the deuterium is accomplished by warming to only 30 K.

These panels pump deuterium at a speed of 10 liters/second/cm^2 [8]. Therefore, 60 m^2 of cryopanel surface area is required for each beamline.

By injecting at a 30° angle to the vertical, an injection housing that can accomodate 80 m^2 of cryopanel surface on the sides can be designed.

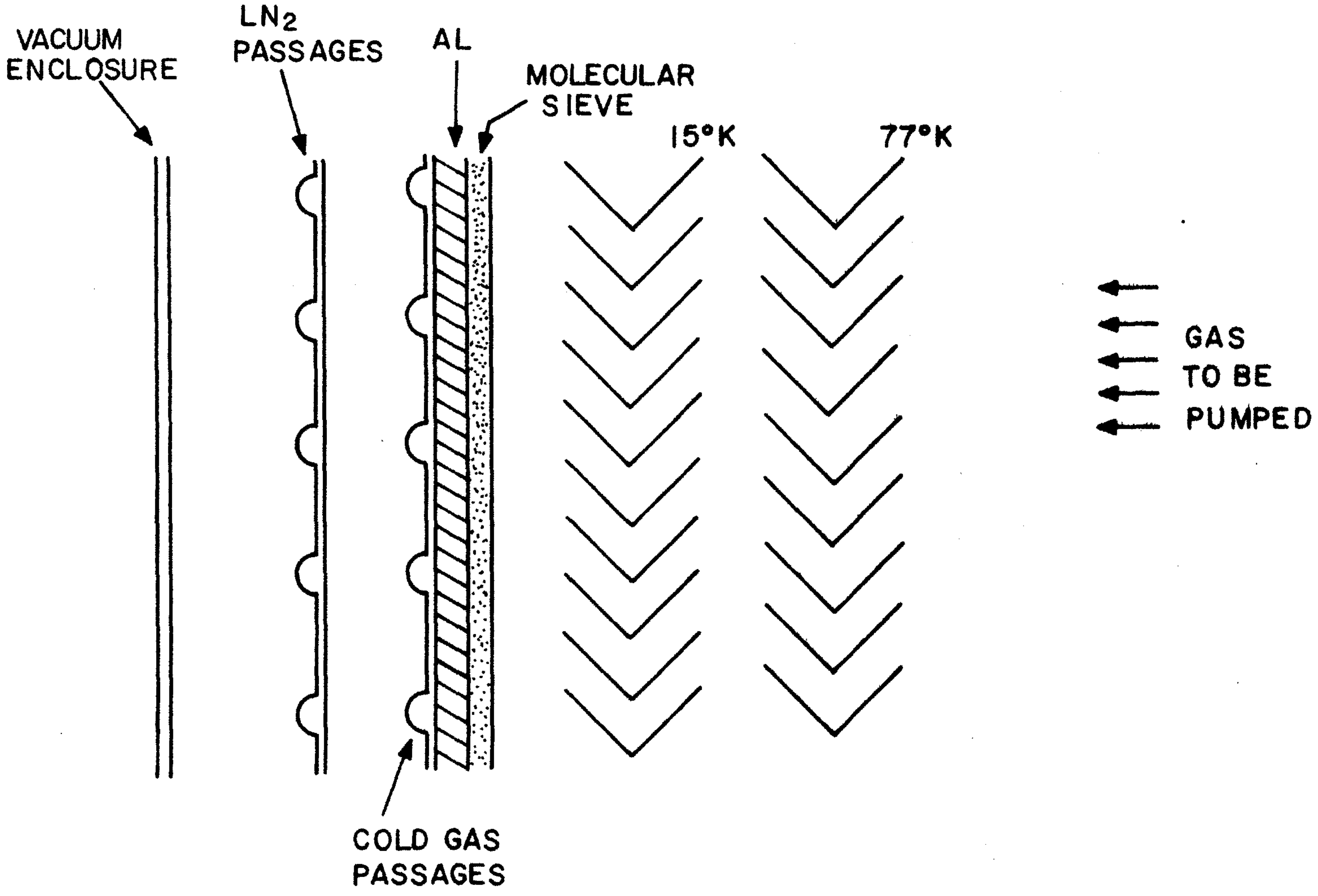

Figure 8-6 A typical cryosorption panel assembly.

Studies at ANL have resulted in a method of sliding panels with fixed vacuum jackets for cryopanel rejuvenation.

9. SYSTEM COSTING AND ENERGY INVENTORY

The HFCTR was costed, using the method for component rating and costing developed by Sink and Iwinski [1]. Special attention was given to the costing of the toroidal field system, remote maintenance equipment, and the poloidal field power conversion systems, because of their unique designs. A simpler costing method, developed by Steiner and Reid [2], was also used in order to illustrate the difference between a high field and a high beta reactor. A complete energy inventory was tabulated for the reactor and conclusions were drawn concerning the need for higher efficiency conventional electrical equipment.

9.1 SYSTEM COSTING

The HFCTR reactor system was costed by two methods. The HFCTR was costed in considerable detail, using a combination of costing methods, based on a knowledge of the actual design. A set of simple scaling relations developed by Steiner and Reid [2] was also used, in order to compare a high-field reactor with a high-beta reactor on an equal basis.

The HFCTR was costed in detail (see Table 9-I) according to the principle of using the "best" available costing technique for each system. The toroidal field coils were designed in enough detail to be costed by a manufacturing engineer. The electrical systems, poloidal field coils and remote handling systems were designed in enough detail to be costed using more general cost scaling models. Other subsystems had to be both sized and costed, using a method for sizing and costing of tokamaks developed at Westinghouse [1].

TABLE 9-I

COST OF HFCTR

System/Subsystem	Rating	Cost
1.0 Tokamak System		$688.6 M
1.1.a Vac Vessel Assemb		$ 5.5 M
1.1.b Material Limiters	7.2 m^2	$ 2.3 M
1.2.a Machine structure	1.6×10^6 kg	$ 24 M
1.2.b Central Column	10^6 kg	$ 13.6 M
1.3 TF Coils - Total		$400.0 M
1.3.a TF Coil Assy-Cond		$182.4 M
1.3.b TF Coil Assy-Struct		$108.8 M
1.3.c TF Coil Assy-Machining		$ 22.4 M
1.3.d TF Coil Assy-Winding		$ 83.2 M
1.3.e TF Coil Dewar		$ 3.2 M
1.4.a Quad + Null Coil Assy	109.5 m^3	$ 49.3 M
1.4.b Dipole + Hex Coil Assy	68.9 m^3	$ 68.9 M
1.4.c OH Coil Assy	73.3 m^3	$ 73.3 M
1.4.d Winding Stat'n		
1.5 Shield System	355 m^3	$ 16.9 M
1.6.a Blanket Assy	242 m^3	$ 23.0 M
1.6.b Lithium + FLIBE Inventory	483 m^3	$ 5.3 M
1.7 NB Duct Shield	8 beam lines	$ 2.0 M
1.8 Ripple Coils	10.1 m^3	$ 4.5 M

TABLE 9-I

COST OF HFCTR (CONT.)

	System/Subsystem	Rating		Cost
2.0	Electrical Systems			$164.6 M
2.1.a	OH PC System	Initiation	5,294 MVA	$ 33.7 M
		Start-up	3,357 MVA	
2.1.b	Null PC System	Initiation	1,029 MVA	$ 4.65 M
		Start-up	251 MVA	
2.1.c	Dipole + Quadrupole	Initiation	1,119 MVA	$ 7.88 M
		Start-up	403 MVA	
2.1.d	PF MGF System	4,000 MVA eq		$ 34.1 M
2.1	Grand Total, PF System			$ 80.3 M
2.2	TF PC System	96 KA		$ 3.2 M
2.3	NB PC System	432 MW		$ 69.0 M
2.4	IC + D System			$ 9 M
2.5	Ripple Coil System	154 MVA		$ 2.04 M
2.6	Standby and Emergency Systems			$ 1.0 M

TABLE 9-I

COST OF HFCTR (CONT.)

System/Subsystem	Rating	Cost
3.0 Tokamak Support Systems		\$164.3 M
3.1 Remote Servicing Systems		\$ 18.0 M
3.2.a Tritium Storage		\$ 5.5 M
3.2.b Deuterium Storage		\$ 0.4 M
3.2.c Fuel Fabrication-Injection		\$ 8.2 M
3.2.d Exhaust Plasma Processing		\$ 5.0 M
3.2.e Cryogenic Distillation Sys		\$ 5.0 M
3.2.f Continuous Fusile Fuel Handling		\$ 24.1 M
3.2.g Tritium Cleanup		\$ 5.3 M
3.3 Torus Vacuum Pump Sys		\$ 12.8 M
3.4.a Helium SC Refrig	20 KW, 4°	\$ 7.7 M
3.4.b LN_2 SC Refrig	20 KW, 77°	\$ 0.4 M
3.4.c H_2O Cooling, Shield	135 MW,th	\$ 0.9 M
3.4.d NB Cooling	100 MW	\$ 3.6 M
3.4.e FLIBE Cooling-Vessel	514 MW,th	\$ 7.7 M
3.4.f FLIBE Cooling, Blanket	1,600 MW,th	\$ 19.4 M
3.4.g H_2O Cooling, Plant Circ	1,630 MW,th	\$ 27.8 M
3.5.a Exp Area Ventilation		\$ 1.5 M
3.5.b Exp Area Cryopanels		\$ 8.0 M
3.6 Radioact Waste Handling		\$ 3.0 M

TABLE 9-I

COST OF HFCTR (CONT.)

System/Subsystem		Rating	Cost
4.0	Struct. and Site Services		$ 78.5 M
4.1	Site Improve. and Services		$ 5.8 M
4.2	Reactor Operations Bldg		$ 33.3 M
4.3	Reactor Support Struct		$ 7.3 M
4.4	Elect Plant Struct		$ 23.5 M
4.5	Other Structures		$ 2.5 M
4.6	Misc. Plant Equipt.		$ 6.1 M
5.0	Neutral Beam Systems		$ 99.0 M
5.1	Neutral Beam Arms	100 MW	$ 30.0 M
5.2	NB Power Supplies (see 2.3)	432 MW	$ 69.0 M
6.0	Balance of Electrical Generation Equipment		$136.9 M
6.1	Substation	870 MW	$ 13.0 M
6.2	Turbine Generator	870 MW	$ 45.5 M
6.3	Steam Generator	330°C, 870 MW	$ 69.3 M
6.4	Accessory Elec. Equip.	2,470 MW	$ 9.1 M
Grand Total, Building and Equipment Cost			$1,263.0 M

The total system cost of \$ 1,263 M is slightly higher than that predicted by the Oak Ridge code. The uncertainties in fusion reactor costing are too great to determine systematic optimism of one costing technique versus another, at this time. Certain features of the more detailed costing should be noted, however.

- The cost of the high-field reactor is the most "magnet driven" of all demonstration reactor designs. The cost of the toroidal and poloidal coils are almost half of the system cost. Balance of plant costs do not dominate. However, it should be noticed that the toroidal field coil system was the only major subsystem which was costed by a manufacturing engineer, and it is probably the most conservatively costed. This is because the cost is that of building the coils today and much of the cost is the currently high price of the niobium-tin superconductor. Since it is expected (4) that in a fusion economy, the cost of Nb_3Sn superconductor will be no higher than that of NbTi, the cost of Nb_3Sn toroidal field coils should be less in constant dollars than the amount predicted here.
- The cost of remote handling equipment has been costed in detail and is only \$ 20 M. If the approximate cost of replacement power is \$500 K per day and a single module replacement required 40-60 days (5), using manipulators, then the cost of automation would be repaid by a single module replacement. Similarly, in comparison to the interesting and viable approach developed for the Culham Mark II demonstration reactor (6), which automates the removal of a blanket and shield module only, the cost of the additional

automation in the HFCTR would be repaid after the occurrence of a single unanticipated fault in a module's coils or structure. The cost, compared to the Culham approach, would also be repaid by a single scheduled, but infrequent, replacement of a toroidal field coil module; either temporary, for annealing of defects in the superconductor matrix, or permanent, because of groundwall insulation damage.

- The trade studies used to lower the poloidal field electrical system cost were successful, as shown in Table 9-I. It is less than 10% of the total system cost, despite the compactness of the reactor, which necessitates a relatively high field (5.5 T) and, therefore, high energy in the OH bore.
- Since the fabricability of the reference blanket and first wall designs are open to serious question, their costing can not be taken too seriously and is included only for the sake of completeness. A better cost estimate will have to await a mechanical design of these systems in future work.

Using a simple cost scaling method [2], the HFCTR was costed and compared with the Oak Ridge National Laboratory representative tokamak power reactor [2,3]. The specific cost of the HFCTR in $/kWe is only 2.5% higher than that of the higher beta reactor (6% lower than the cost calculated in Table I). The explanation is that, by using high force-density construction of the TF coils, the overall reactor dimensions and power output were kept about the same as those of the higher-beta device. Thus, all the major subsystems of both reactors fit within similarly sized envelopes and had similar costs, with the significant exception of the toroidal field coils. The toroidal field coils are costed in the Oak Ridge code as a function of their total stored energy, so that the high energy density of the toroidal field system led to a predicted high cost, despite their small size. This is not unfair to HFCTR, since it was necessary to use a higher-cost superconductor (Nb_3Sn), structural material outside of the coil volume and a more expensive two-sided winding technique in order to achieve high energy density. However, since the toroidal field coils are less than 25% of the total system cost in this model, the overall system cost was relatively insensitive to their higher cost. The ability of high energy-density TF coils to allow all other parts of a tokamak reactor system to compete identically with higher-beta systems is a dramatic indication of the value of high force-density design.

9.2 SYSTEM ELECTRICAL ENERGY BALANCE

A listing of all significant electrical loads in the HFCTR is shown in Table 9-II. Energy balances are shown for the reference scenario of a 500 second burn and the conservative case of a 100 second burn, in the case of 100% recycling of impurities and alpha ash. In this design, the energy expended in the neutral beams is not a significant limitation on the Q of a 500 second cycle. The power required for cryogenic refrigeration, blanket and shield cooling, and the secondary water coolant loop (assumed to be necessary because the primary FLIBE loop is radioactive), are all comparable. Over half of the system losses are the transformer excitation, armature and transformer winding, buswork and generator friction and windage losses, associated with the poloidal field power conversion systems. With the possible exception of generator and flywheel windage, which ought to be significantly reduced by operation in a low-pressure hydrogen environment, the high losses in the poloidal field system are believed to be a fundamental problem associated with conventional electrical equipment. The relatively high circulating power, even in a long-pulse tokamak reactor, is a strong motivation for the development of superconducting generators, transformers and buswork.

TABLE 9-II

ELECTRICAL ENERGY INVENTORY FOR HFCTR

System	Peak Power	Energy/ 500s Cycle	Energy/ 100s Cycle	Avg. Power/ 500s Cycle	Avg. Power/ 100s Cycle
Neutral Beam Supply				4.44 MW	22.2 MW
(NB Power to Plasma)	100 MW				
(Accel Grid Power)	432 MW				
Accel Input Power	540 MW	2,160 MJ	2,160 MJ	4.32 MW	21.6 MW
Filament Power	2.6 MW	10.4 MJ	10.4 MJ	.02 MW	.1 MW
Arc Power	8.5 MW	34.0 MJ	34.0 MJ	.07 MW	.34 MW
Decel Power	3.5 MW	14.0 MJ	14.0 MJ	.03 MW	.14 MW
Poloidal Field System					
Null Coil	62.2 MW	400 MJ	400 MJ	0.8 MW	4.0 MW
Quadrupole Coil	22.1 MW	11,050 MJ	2,210 MJ	22.1 MW	22.1 MW
Null Coil Bus	5.8 MW	40 MJ	40 MJ	0.1 MW	0.4 MW
Dipole and Quadrupole Bus	5.8 MW	2,900 MJ	580 MJ	5.8 MW	5.8 MW
Thyristor Losses					
OH Supply	6.2 MW	1,550 MJ	310 MJ	3.1 MW	3.1 MW
EF Supply	2.6 MW	1,050 MJ	210 MJ	2.1 MW	2.1 MW

TABLE 9-II (Cont.)

ELECTRICAL ENERGY INVENTORY FOR HFCTR

System	Peak Power	Energy/ 500s Cycle	Energy/ 100s Cycle	Avg. Power/ 500s Cycle	Avg. Power/ 100s Cycle
OH Initiation Resistor	6,600 MW	198 MJ	198 MJ	.4 MW	2.0 MW
Dipole Initiation Resistor	1,120 MW	40 MJ	40 MJ	.1 MW	0.5 MW
Plasma I^2R Loss		250 MJ	90 MJ	0.5 MW	0.9 MW
Generator, Total		26,000 MJ	5,500 MJ	52 MW	55 MW
Friction + Windage	124 MW	20,000 MJ	4,000 MJ	40 MW	40 MW
I^2R, Field + Armature	24 MW	6,000 MJ	1,500 MJ	12 MW	15 MW
Rectifier-Tranformers					
OH, I^2R	48.4 MW	8,400 MJ	2,000 MJ	16.8 MW	20 MW
OH, Excitation	16.8 MW	8,400 MJ	1,680 MJ	16.8 MW	16.8 MW
Dipole + Quadrupole, I^2R	6.0 MW	1,000 MJ	250 MJ	2.0 MW	2.5 MW
Dipole ± Quadrupole, Excitation	2.0 MW	1,000 MJ	200 MJ	2.0 MW	2.0 MW
Rectifier-Inverter		550 MJ	200 MJ	1.1 MW	2.0 MW
Tritium Processing	1.5 MW	750 MJ	150 MJ	1.5 MW	1.5 MW
Cooling System, Total	74.3 MW	37,150 MJ	7,430 MJ	74.3 MW	74.3 MW

TABLE 9-II (Cont.)

ELECTRICAL ENERGY INVENTORY FOR HFCTR

System	Peak Power	Energy/ 500s Cycle	Energy/ 100s Cycle	Avg. Power/ 500s Cycle	Avg. Power/ 100s Cycle
Water, Gen Plant	24.7 MW	12,350 MJ	2,470 MJ	24.7 MW	24.7 MW
FLIBE (Blanket Shield)	19.6 MW	9,800 MJ	1,960 MJ	19.6 MW	19.6 MW
Helium Refrig, Total	28.5 MW	14,250 MJ	2,850 MJ	28.5 MW	28.5 MW
TF Coils	20 MW	10,000 MJ	2,000 MJ	20 MW	20 MW
OH Coils	2 MW	1,000 MJ	200 MJ	2 MW	2 MW
EF Coils	.5 MW	250 MJ	50 MJ	.5 MW	.5 MW
NB Cryopanels	2 MW	1,000 MJ	200 MJ	2 MW	2 MW
Schivel Pumps	4 MW	2,000 MJ	400 MJ	4 MW	4 MW
Nitrogen Refrig, Total	1.5 MW	750 MJ	150 MJ	1.5 MW	1.5 MW
TF Coils	1.0 MW	500 MJ	100 MJ	1.0 MW	1.0 MW
OH Coils	.05 MW	——	——	——	——
EF Coils	.01 MW	——	——	——	——
NB Cryopanels	.05 MW	——	——	——	——
Schivel Pumps	.1 MW	——	——	——	——

TABLE 9-II (Cont.)

ELECTRICAL ENERGY INVENTORY FOR HFCTR

System	Peak Power	Energy/ 500s Cycle	Energy/ 100s Cycle	Avg. Power/ 500s Cycle	Avg. Power/ 100s Cycle
Ripple Coils	128 MW	512 MJ	512 MJ	1.0 MW	5.1 MW
Ripple Coil Bus	1.0 MW	—	—	—	0.1 MW
Exp. Area Ventilation	5.5 MW	2,750 MJ	550 MJ	5.5 MW	5.5 MW
Miscellaneous	10.0 MW	5,000 MJ	1,000 MJ	10.0 MW	10.0 MW
Grand Total		111,000 MJ	25,800 MJ	222 MW	258 MW

REFERENCE - SECTION 9

[1] D. A. Sink and E. Iwinski, "COAST, A Code for Costing and Sizing of D-T Burning Tokamaks," Westinghouse Fusion Power Systems Department, TME-062; Oct., 1977.

[2] D. Steiner et al, ORNL Fusion Power Demonstration Study: Interim Report, ORNL/TM-5813; Mar., 1977.

[3] D. Steiner and J. F. Clarke, "The Tokamak: Model T Fusion Reactor," Science, 31 Mar., 1978, Vol. 199, p. 1395.

[4] J. R. Powell, "Design and Economics of Large DC Fusion Magnets," Applied Superconductivity Conf., 1972; Annapolis, Md.

[5] M. Sniderman, "Fusion Reactor Remote Maintenance Study - Final Report," EPRI Contract No. RP1044-1.

[6] J. T. D. Mitchell and J. A. Hollis, "A Tokamak Reactor with Servicing Capability," Proceedings of the 9th Symposium on Fusion Technology, p. 429, Pergamon Press, 1976.

ACKNOWLEDGMENTS

The authors wish to give special thanks to C. A. Flanagan, D. Klein, T. C. Varljen, G. Gibson and F. M. Heck for helpful comments and for editing the manuscript. The assistance of the PPPL computational group in running the MHD codes is gratefully acknowledged. The authors would further like to thank R. R. Parker and D. B. Montgomery for helpful suggestions and comments. They are also indebted to Martin Wilson and Carl Weggel for their contributions to the magnet design during the early stages of this project. The responisbility for the various sections of this report was divided as follows: MIT was responsible for sections 2., 3.1, 3.3, 3.4, 3.5, 4. and 8. and Appendices A, B, C, D, F, and I. The Westinghouse Electric Corporation was responsible for sections 3.2, 5., 6., 7. and 9. and Appendices G, H, J and K. MIT and Westinghouse were jointly responsible for section 1. The Charles Stark Draper Laboratory was responsible for section 2.5 and Appendix E.

APPENDIX A - DEFINITIONS AND UNITS

τ_E	global energy confinement time (seconds)
τ_P	particle confinement time (seconds)
τ_{nc}	neoclassical energy confinement time (seconds)
τ_{emp}	empirical energy confinement time (seconds)
$\bar{n}_L$	line-averaged ion density (m^{-3})
q	safety factor at $r = a$
a	minor radius (of halfwidth of noncircular plasma) (m)
R	major radius (m)
z	vertical coordinate with $z = 0$ at the mid-plane (m)
B_T	toroidal magnetic field on axis (Tesla)
B_P	poloidal magnetic field (Tesla)
I	current (Amperes)
T_j	temperature of j^{th} specie (all species at same temperature) (keV)
n_j	densities of j^{th} specie (m^{-3})
σ_f	fusion cross section (m^2)
Z_I	impurity charge (here = 42 due to molybdenum wall)
r	distance from plasma geometric center (m)
$\bar{T}$	density-averaged temperature of plasma(keV)
S	shaping factor. For ellipse, perimeter = $2\pi aS$
κ	$[2S^2 - 1]^{1/2}$. For ellipse, area = $\pi a^2\kappa$
A	aspect ratio
p_{sA}	pressure term due to supra-thermal alpha (keV/m^3)
β_T	toroidal beta

β_P	poloidal beta
β_c	maximum toroidal beta
d	distance from plasma axis to inner side of toroidal field coil
B_{To}	toroidal field at the coil
P_{th}	total thermal output (including blanket multiplication) (watts)
P_w	neutron wall loading (watt/m^2)
P_f	fusion power density (watt/m^3)
P_B	bremsstrahlung power (watt/m^3)
P_L	line radiation power (watt/m^3)
P_{Rad}	total radiation power (watt/m^3)
MS	margin of safety in reaching ignition
$n_{\tau_{max}}$	density at which peak energy confinement occurs (m^{-3})
C	unitless measurement of collisionality
W_b	neutral beam energy (keV)
V_{loop}	applied loop voltage (volts)
η	resistivity (Ω - cm)
J	current density
Q	energy multiplication factor
F_α	fraction of fusion alpha energy deposited in the plasma
$\delta(r)$	peak-to-peak vacuum ripple

Subscripts: e = electron, i = Deuterium plus tritium, α = alpha, I = impurity,

p = plasma

X => local value of X

X_o => peak value of X

$\bar{X}$ => area-averaged value of X

APPENDIX B: CYCLOTRON RADIATION IN HIGH-FIELD TOKAMAKS

The cyclotron radiation emitted from a plasma increases with increasing magnetic field strength, electron density, and electron temperature. In previous demonstration reactor designs, the magnetic field has been relatively low (B_o ~ 4-6 Tesla), the density moderate ($\bar{n} \sim 1\text{-}2 \times 10^{20}\ m^{-3}$), and the cyclotron radiation negligible. In the present design both the field (B_o ~ 8 Tesla) and the density ($n_{max} \sim 5 \times 10^{20}\ m^{-3}$) are larger, making it necessary to estimate the cyclotron power loss in order to determine its effect on the power balance.

B.1 Determination of Power Loss with Wall Reflection

Drummond and Rosenbluth [1] have calculated emission and absorption of cyclotron radiation for a cylindrical plasma and have given an equation for the last black harmonic (m*) with reflection. The result is

$$m^{*3} = 10^3 K\ (\beta_e BL^*)^{1/2}$$

where

$$\beta_e^* \equiv \frac{n_e kT}{B_o^2} (2\mu_o),$$

$$L^* \equiv L/(1-R),$$

R is the average reflectivity of the vacuum chamber, K is a function of T_e, and L is the cylinder diameter in meters.

From the curves of m^{*3} vs. BL^*, values for K appear to be:

T_e (keV)	K
100	0.98
75	0.72
60	0.55
50	0.40
25	0.24
15	0.15
7.5	0.20

Drummond and Rosenbluth then estimate the power per unit area lost (S) as

$$S = \frac{\omega_e^3 kT_e}{12 \; {}^2 c^2} (1-R)(m^*)^3$$

where

$$\omega_c \equiv \frac{eB}{m} = \text{cyclotron frequency.}$$

This is the blackbody loss integrated up to $\omega = m^*\omega_c$ multiplied by the vacuum vessel absorptivity. For the case of no reflection the limit is simply the blackbody loss integrated to the last black harmonic. The discrete nature of the cyclotron emission spectrum is neglected here.

B.2 Effect of Wall Reflection

The effect of reflection on the value of m* is determined to be

$$\frac{m^*_{\text{with reflection}}}{m^*_{\text{without reflection}}} = \frac{\left(K \left(\beta_e B_o \frac{L}{1-R}\right)^{1/2}\right)^{1/3}}{\left(K \left(\beta_e B_o L\right)^{1/2}\right)^{1/3}} = \left(\frac{1}{1-R}\right)^{1/6}$$

and the effect on the total power loss is therefore

$$\frac{S_{\text{with reflection}}}{S_{\text{without reflection}}} = (1-R) \left(\frac{1}{1-R}\right)^{1/2} = (1-R)^{1/2}$$

For example, the total power loss for R = 0.9 is about a factor of 3 less than the noreflection case.

B.3 Estimating Average Reflectivity

The average reflectivity is given by

$$R = \frac{R_w A_w}{A_w + A_H}$$

where R_w is the wall reflectivity, A_w is the total wall area, and A_H is the hole (or part) area.

The wall reflectivity is

$$R_w = 1 - \frac{8\omega\eta}{\mu c}$$

where μ is the magnetic permeability, and η is the wall material resistivity.

A couple of typical examples are:

(1) niobium at 1000 C, $R_w \simeq 0.994$

(2) graphite at 600 C, $R_w \simeq 0.963$

In addition, since $\frac{A_w}{A_H + A_w} \simeq 90\%$,

$$R \simeq 0.9$$

B.4 Estimating the Effect of Cyclotron Losses for Various Reactor Designs

The importance of the cyclotron power loss depends on how much alpha power is available to counter the loss. Three different parameterized designs are shown in Table B-I, along with their corresponding alpha power production, cyclotron power loss, and bremsstrahlung power loss (for $Z_{eff} = 1.5$). These calculations assume that R = 0.9.

In conclusion, cyclotron power loss is very small for a wide range of reactor parameters and must be taken into account in the alpha heating energy balance only when $T_e > 15$ keV and $n_e > 5 \times 10^{20}$ m^{-3} simultaneously.

TABLE B-I

	Design 1	Design 2	Design 3
$n_e (m^{-3})$	1×10^{20}	5×10^{20}	3.5×10^{20}
kT(KeV)	10	7.5	15
B (Tesla)	4.5	8.0	10.00
L (m)	4.2	2.4	4.0
$\omega_c (sec^{-1})$	8.0×10^{11}	1.42×10^{12}	1.78×10^{12}
m^*_{DR}	6.15	5.97	7.58
F	1.8 Kw/m^2	6.9 Kw/m^2	55.3 Kw/m^2
β_e	0.0199	0.0236	0.0211
K	0.12	0.1	0.15
alpha	129 Mw	376 Mw	1000 Mw
Bremsstrahlung	18.6 Mw	118 Mw	566 Mw
cyclotron	0.9 Mw	1.8 Mw	61 Mw
Bremsstrahlung/alpha	14%	31%	57%
Cyclotron/alpha	0.7%	0.5%	6.1%

REFERENCES - APPENDIX B

[1] Drummond, W. E. *et al.*, Phys. Fluids *6* (1963) 276

APPENDIX C: START-UP CODE

A zero-dimensional time dependent code is used to investigate the HFCTR start-up. The start-up sequence must satisfy the set of constraints described in Section 2.3. Several assumptions implicit in the code are presented below.

(1) The temperature, density, and current density profiles are flat, causing the alpha power production to be underestimated.

(2) Flux is not conserved, at least during the early stages of start-up.

(3) An initially small plasma is produced, which gradually increases to full size.

(4) Neutral beam ripple injection allows 100% of the beam power to be distributed uniformly throughout the plasma.

(5) When the ripple coils are on, 30% of the alpha power is lost; otherwise 100% of the alpha power is deposited in the plasma.

(6) A controllable fueling mechanism is available (perhaps the method discussed in Section 2.4).

(7) The alpha and beam particle energy transfer to the plasma ions and electrons is instantaneous.

(8) Throughout start-up the ion energy confinement time follows neoclassical scaling and the electron energy confinement time follows empirical scaling.

With the exception of temperatures and particle energies, MKS units are used throughout. The temperatures and particle energies are in keV.

C.1 Independent Variables

The independent variables in the code are the neutral beam current, the fueling rate, the plasma size, and the plasma current. The plasma current is specified, rather than the applied loop voltage, reducing the number of differential equations by one and thus making it easier to find a combination of controllable inputs that satisfy the constraints. The applied loop voltage is then found by using

$$V_{loop} = 2\pi R\eta J + \frac{d(LI)}{dt}$$

where [1]

$$\eta = 2.97 \times 10^{-8}\, Z_{eff}/T_e^{1.5} \text{ for low } Z_{eff},$$

$$L = \mu_o R\left(\ln\frac{8R}{a\delta^{1/2}} + \frac{l_i}{2} - 2\right)$$

and R is the plasma major radius.

C.2 Power and Particle Balance Equations

The zero-dimensional power balance equations are:

$$\frac{1}{V_p}\frac{d1.5n_iT_iV_p}{dt} = (f_i + g_iQ_b)P_B + \frac{n_i^2}{4}<\sigma v>_{DT}(E_\alpha g_i - 3T_i)$$

$$- P_{ei} - \frac{1.5n_iT_i}{\tau_{nc}}$$

$$\frac{1}{V_p}\frac{d1.5n_iT_iV_p}{dt} = \left[(1-f_i) + (1-g_i)\right] Q_b\, P_B + \frac{n_i^2}{4}\langle\sigma v\rangle_{DT}\, E_\alpha(1-g_i)$$

$$+ \eta J^2 + P_{ei} - \frac{1.5n_eT_e}{\tau_e} - P_{rad}$$

where n_i is the D-T density, V_p is the plasma volume, Q_b is the energy multiplication factor from beam-target fusions, P_B is the beam power per V_p, and f_i and g_i are the fractions of beam energy and alpha energy deposited on the ions. The other symbols are self-evident.

The zero-dimensional particle balance equations are:

$$\frac{1}{V_p}\frac{dV_pn_i}{dt} = S_F - I_B - \frac{n_i}{\tau_{pi}} - \frac{n_i}{2}\langle\sigma v\rangle_{DT}$$

$$n_e = n_i + \sum_I Z_In_I$$

where S_F is the fueling rate per V_p, I_B is the beam current per V_p, n_I is the density of the I^{th} impurity, and Z_I is its average charge state.

C.3 Details of Some of the Terms

plasma volume

$$V_p = 2\pi^2Rab$$

Here the plasma D cross section is approximated as an ellipse with a the plasma half-width and b the plasma half-length.

fraction of beam and alpha energies deposited with the ions [2]

$$f_{B,\alpha} = \frac{2}{x}\left[\frac{1}{6}\ln\left[\frac{1-\sqrt{x}+x}{(1+\sqrt{x})^2}\right] + \frac{1}{\sqrt{3}}\tan^{-1}\left[\frac{2\sqrt{x}-1}{\sqrt{3}}\right] + .3023\right]$$

where $x = \frac{W_B}{E_{cB}}$ for the beams, $x = \frac{E_\alpha}{E_{c\alpha}}$ for the alphas, W_B = 120 keV, and E_c is the critical energy for the appropriate slowing down particle.

energy multiplication from beam-target fusions

$$Q_B = E_\alpha \frac{\int_o^{t_s} n_T \sigma(v) v \, dt}{W_B}$$

The results of Q_B were taken from Ref. [3], adjusted for the case of $n_T = \frac{n_e}{2}$. Also E_α is used instead of the 17.6 MeV used in Ref. [3]. Throughout start-up Q_B remains small, reaching a maximum of ∿.14 at the end of start-up.

fusion reaction rate

$$<\sigma v>_{DT} = \frac{2.97 \times 10^{-17}}{T_i^{.886}} e^{\frac{-22.591}{T_i^{1/3}}} \quad \text{for } T < 10 \text{ kev}$$

electron-ion power transfer [4]

$$P_{ei} = 1.83 \times 10^{-34} n_e n_i (T_e - T_i)/T_e^{1.5}$$

electron confinement time [5]

$$\tau_e = 0.5 \, \tau_{emp}$$

ion confinement time (with $Z_{eff} = 1.2$) [5]

$$\tau_{nc} = 3.8 \times 10^8 T^{1/2} I_p^2/n \qquad \text{collisional regime}$$

$$\tau_{nc} = 1.68 \times 10^{-6} \frac{I_p a}{T_e^{1.5}} \qquad \text{plateau regime}$$

$$\tau_{nc} = 1.85 \times 10^7 T^{1/2} I_p^2/n \qquad \text{banana regime}$$

Throughout start-up $\tau_{nc} >> \tau_{emp}$.

radiation

Bremsstrahlung and heavy metal line radiation losses are described in Section 2.1. As discussed in Appendix B, cyclotron radiation is negligible.

simplified energy containment time

If $Z_{eff} \simeq 1.0$ and $T_i \simeq T_e$, then the energy containment time becomes

$$\tau_E \simeq 3.2 \times 10^{-21} \bar{n}_L q^{1/2} a^2$$

REFERENCES - APPENDIX C

[1] Spitzer, Jr., L., Physics of Fully Ionized Gases, Interscience Publisher's Inc., N.Y. (1956).

[2] Stix, T. H., Plasma Phys. 14 (1972) 367.

[3] Jassby, D. L., Nucl. Fusion 17 (1977) 309.

[4] Sivukhim, D. V., Reviews of Plasma Physics, - Leontovich, M. A. ed., Consultants Bureau, N.Y. 1965.

[5] Stacey, W. M., et al, Tokamak Experimental Power Reactor Conceptual Design, ANL/CTR-76-3, August, 1976.

APPENDIX D. PLASMA-GAS BLANKET IN ALCATOR A†

D.1 Fueling: Experimental Observations

Alcator discharges are produced by first establishing a low density equilibrium ($\bar{n} \lesssim 5 \times 10^{13}$ cm^{-3}) and subsequently puffing gas so as to produce an increase in density up to operating levels of $\bar{n} = 6 \times 10^{14}$ cm^{-3}. This is shown in Figure D-1.

The rate of plasma increase is, within a factor of 2, equal to the throughput of the gas valve used for admitting gas to the plasma volume. The exact correspondence depends on wall conditions; the higher the recycling coefficient, the larger the rate of density rise for a given gas admission rate. Under low recycling conditions, most of the recycled gas comes from the limiter; with high recycling, most of the recycled gas comes from the wall. These conclusions are based on the relative intensity of Lyman alpha (H_α) light at each of the four toroidal locations allowed by the port configuration; more quantitative evaluation is difficult because it is not possible to measure H_α (ϕ,θ) where ϕ and θ are the toroidal and poloidal angles.

The first question to be asked concerning the plasma buildup is whether the central density rise could be due to direct ionization of neutral gas. Numerical simulations (which are discussed below) show that this is not possible since the central neutral density drops to very low levels in the high density regime. This conclusion is supported by direct experimental evidence, which shows that the energetic neutral flux drops by about 2 orders of magnitude as the plasma density increases from $\bar{n} = 1.5 \times 10^{14}$ cm^{-3} to $n = 5 \times 10^{14}$ cm^{-3}. At the same time the rate of density rise remains unaffected.

Consequently, we must look for other plasma ingestion mechanisms.

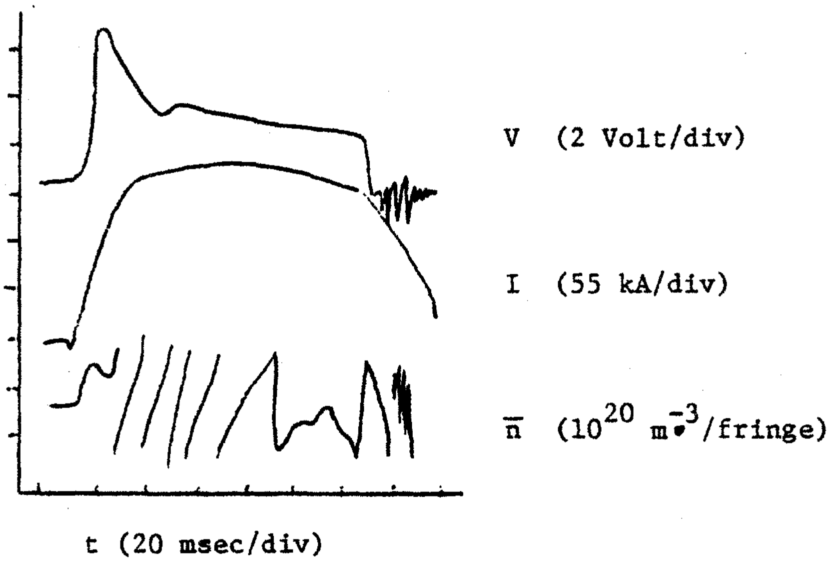

Figure 1. An ultra-high density discharge in Alcator showing loop voltage, current and density. The discontinuities in the density trace are due to resets in the fringe counter and should be ignored.

By locating valves at different angles away from the limiter, it has been determined that there is no dependence on toroidal or poloidal angle.

Also, by reversing the toroidal field, no dependence (less than 5%) on the direction of the gradient drift relative to the gas valve location has been found, although this has been shown to have an effect on the diffusion of light impurities. The only parameter which has been found to have an effect on the ingestion efficiency is dI/dt. There is also a related broadening and contracting of the temperature profile according to the sign of dI/dt; this may place more particles in trapped collisionless regimes, making them susceptible to inward convection by the Ware pinch.

D.2 Fueling: Theoretical Modeling

The computer model consists of a one dimensional (radial) plasma transport code and a Monte Carlo algorithm for calculating the neutral density. These can be run concurrently.

The plasma code [1] evolves the usual transport equations for density, electron and ion temperatures, poloidal magnetic field, and toroidal electric field using the neoclassical fluxes plus anomalous contributions from current driven drift wave fluctuations. The neoclassical coefficients used are accurate throughout the banana and plateau regimes, which covers the parameters explored experimentally. Since the experimental observations show transport in excess of neoclassical (except possibly at the extreme upper limit of density), some type of anomaly must be included if reasonable agreement is to be expected. The current driven drift wave contributions we have used are dominant at all plasma radii for average densities below $\bar{n} \sim 1.5 \times 10^{14}$ cm^{-3}, and at all densities in the radius range $0.75 < r/a < 1$. Because of the achievement on Alcator of substantially pure, $Z_{eff} \sim 1$, plasmas, we exclude any consideration of impurity transport.

The neutral algorithm [1] uses a numerical Monte Carlo scheme to compute the neutral profiles, given the plasma density, temperature profiles, and the incident neutral flux. Ionization of the pulsed gas (molecular hydrogen) near the plasma edge provides an isotropic, source of 3 eV hydrogen atoms. The profile of these is determined from the Monte Carlo scheme. A second source of neutrals due to recycling is treated separately. Our recycling model is as follows. It is assumed that lost plasma ions acquire an electron on the limiter or the wall and return to the plasma as a neutral. The energy and angular distributions of the reflected neutrals are taken from Behrisch [2]. Emergent charge exchange neutrals behave similarly. All particles are returned to the plasma; there is some degradation of their energy.

The combined code is run using the experimental values of toroidal field, current and pulsed gas. It begins from a previously computed low density, $\bar{n} = 0.64 \times 10^{14}$ cm^{-3}, equilibrium. If the inward Ware pinch effect is turned off in the code, one finds that on a very short, 20 msec time scale the density profile inverts (which is not seen experimentally) and even after 100 msec the central plasma density has not changed appreciably. This is simply due to the small ionization rate resulting from the plasma's opacity. The implication is that some kind of inward plasma flow accounts for the observed density risc. Including the Ware pinch does result in density build-up in the center. Peak densities exceeding 8×10^{14} cm^{-3} have been obtained computationally without profile inversions. However, the time to achieve this peak value is 112 msec as compared to the observed 60 msec. Also the final density profile obtained is broader than those seen in the experiment.

It is important to note that although in these high densities the transport coefficients are predominantly neoclassical over most of the radius, the outer anomalous region nonetheless plays a significant role. The basic difficulty in accounting for the inward flow is that the region where both the Ware pinch and the plasma source (neutrals) exist is very small. The Ware pinch speed falls to the outside due to an increased collisionality. At some point the flux changes sign and is outward. The neutral density decays exponentially toward the center. In fact a negligible number of the 3 eV neutrals from the pulsed gas can penetrate to points of inward flow.

One thus arrives at a picture in which the pulsed gas atom is ionized at the edge, heated as an ion to the edge temperature, lost to the wall by diffusion and finally, now as a hot ($\sim$ 50 eV) neutral, penetrates to a radius where the pinch can operate. It is accordingly necessary to have high (anomalous) loss rates at the edge to provide a large recycled neutral flux.

With this comes the suggestion that modifying the assumed edge anomaly to increase the recycling rate might reproduce the observed density rise rates while maintaining the Ware pinch as the principal mechanism. Such a modification is also suggested by the computed density profiles which are broader than those observed.

D.3 Neutral Flux Cutoff: Experimental Observations

As the density is increased in Alcator, the emitted neutral flux with the energies greater than 200 eV first increases up to the density $\bar{n} = \bar{n}_C \simeq 1.5 \times 10^{14}\ \mathrm{cm}^{-3}$, and then decreases abruptly as n is raised above n_C. This is shown in Figure 2. This effect is due to the shortening of the neutral mean free path, which results in a simultaneous reduction in the central neutral density and attenuation of the emitted neutral charge-exchanged flux. Since the density at which the neutral signals first decrease is independent of energy, it is believed that the effect is initially due to a decrease in central neutral density. At higher densities, the emitted flux is also severely attenuated and the energy spectrum is then no longer characteristic of the central ion distribution function.

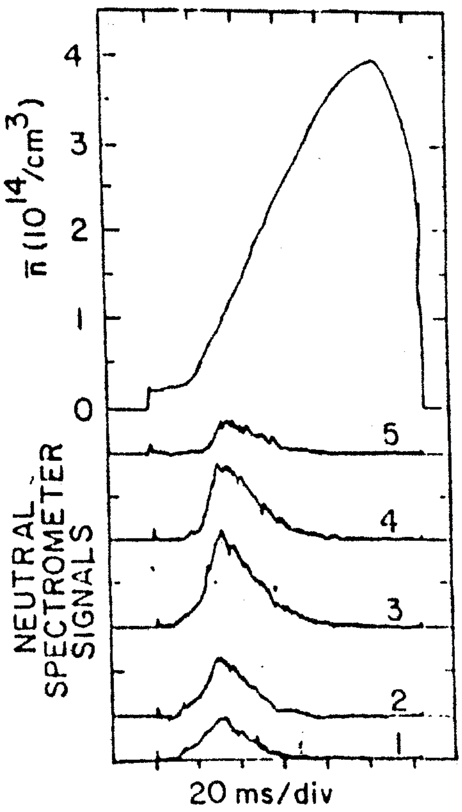

Figure 2. Cutoff of energetic neutral flux during a high density discharge. The top trace is line average electron density obtained from the 119 μm laser. The lower traces are unnormalized signals from the 5 analyzer channels: 1) 500 eV, 2) 685 eV, 3) 974 eV, 4) 1321 eV and 5) 1947 eV. Note the decrease in the flux for average densities in excess of 1×10^{14} cm^{-3}.

D.4 Neutral Flux Cutoff: Theoretical Calculations

As expected, the code results show that the flux of high energy neutrals attenuates as the density increases to values in excess of about 1×10^{20} m^{-3}. Figure 3 shows a plot of the average energy of emitted neutrals as a function of the central plasma density. Two cases are shown: one for a central ion temperature of 1 keV and plasma radius of 100 cm. In the first case the average energy drops by nearly an order of magniture, as the central density is increased from 1×10^{20} to 1.6×10^{21}. The flux of heavy impurities

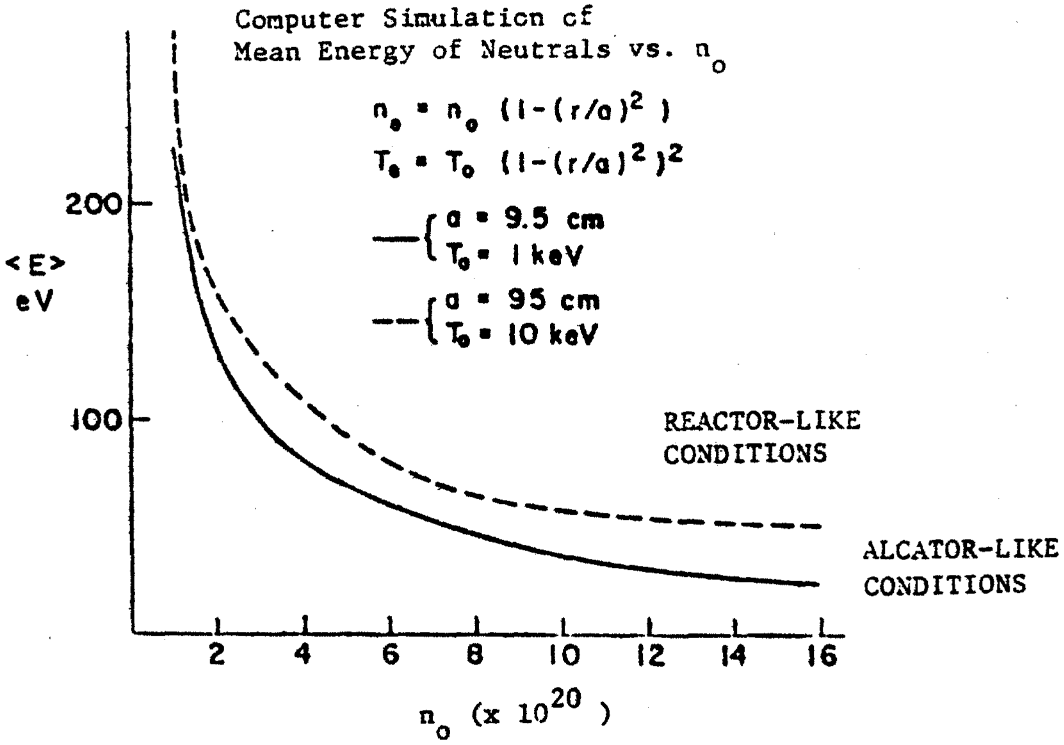

Figure 3. Mean Energy of effluent, charge-exchanged neutral flux vs. central plasma density, n_o. (M. H. Hughes, private communication)

sputtered from a stainless steel wall by this neutral flux drops by a factor of 50. The case of 10 keV central temperature and 1 m radius shows that an equivalent reduction in neutral flux capable of sputtering a stainless steel wall occurs even under reactor conditions. Consequently the effect of impurity production by physical sputtering due to charge-exchanged neutrals does not appear to be serious in sufficiently opaque plasma regimes. Two words of caution should be added; this calculation does not include the effects of recombination. The latter effect has been estimated to give a central neutral density $n^{\circ} \sim 10^{13}\ m^{-3}$, whereas the code used here allows the neutral density to drop to arbitratliy low values.

The edge neutral density has been estimated to be 1-3 × 10^{17} m^{-3} by measurement of H_α emission using a calibrated monochromater. It would be difficult to support an edge neutral density significantly larger than this since influx of neutral gas would then be larger than the plasma outflux. The neutral particle calculation then shows that at $n_o \sim 10^{21}$, the average energy of neutral outflux is 40 eV and the flux is 0.6-2 × 10^{21} m^{-2} sec^{-1}, resulting in a power flow of 1.5-5 kW/m^2. The tentative conclusion is that power flow to the wall by low energy charge-exchanged neutrals is a negligible part of the total power flow. A more definitive measurement of the actual neutral edge density is required to confirm this assertion.

REFERENCES AND FOOTNOTES - APPENDIX D

† Parts of this work were presented in a paper by R. Parker, K. Molvig and L. Scaturro in the Workshop on Fusion Fueling, Princeton, N.J. (1977)

[1] Hughes, M. H. and D. E. Post, Princeton Plasma Physics Laboratory, Report No 1335 (1977).

[2] Behrisch, R. *et al.*, in Proc. of 5th International Conf. on Atomic Collisions in Solids, Gatlinburg, Tn (1975), p 315.

APPENDIX E: MAGNETIC FIELD RIPPLE AND GAS REFUELING CONTROLS

E.1 Introduction

The following is a summary of the methodology developed for the control of temperature after plasma ignition. A general nonlinear plasma computer simulation and the peripheral computer programs developed for feedback controller design, have been adapted to model the dynamics of the HFCTR plasma and to study the magnetic field ripple concept and neutral gas modulation as possible effectors to control thermal runaway. The analytical models associated with these two effectors are described in Section E.2. Sections E.3 and E.4 outline the controls development programs and the basic methodology used in the analysis.

E.2 Physics Models

a. Ripple Coil Dynamics

The fraction of alpha particles (F_α) lost as a function of the peak to peak ripple on the magnetic axis (δ_0) is obtained through a cross plot of Figure 2-37. Such a plot is shown in Figure E-1 for two ripple locations. An analytical fit to Figure E-1 takes the form,

$$F_\alpha = C_1 \left(1 - e^{-C_2(\delta_0 - C_3)}\right) \tag{1}$$

where:

$$C_1 = 0.26 \quad , \tag{2}$$

$$C_2 = 12.566 \tag{3}$$

and

$$C_3 = 0.0035 \quad . \tag{4}$$

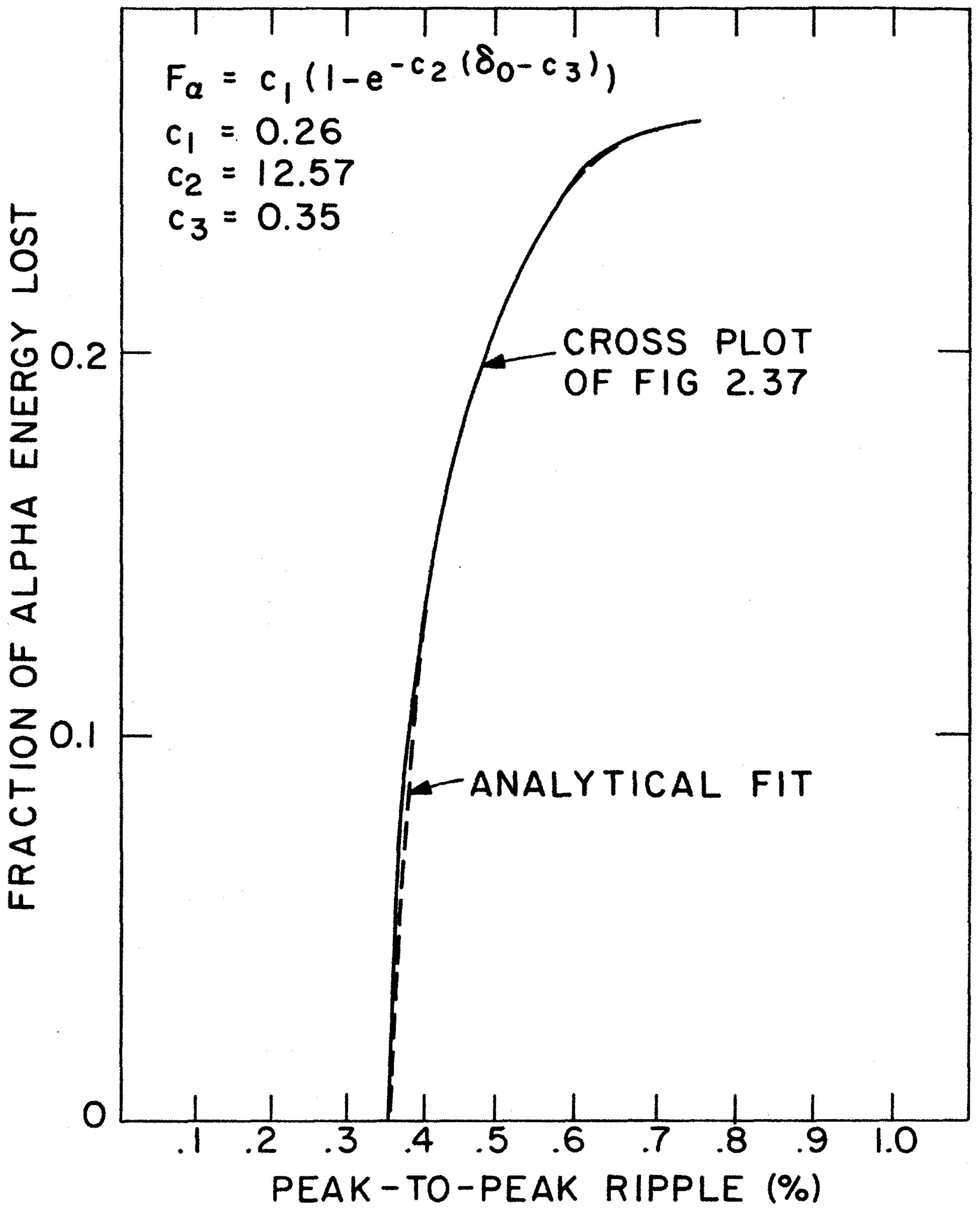

Figure E-1 Alpha Energy Loss vs.
Peak-to-Peak Ripple in HFCTR Plasma

the effect of magnetic diffusion is modeled by a first order delay,

$$\frac{\partial}{\partial t}\,\delta_0 = \frac{\left(.004\,\frac{I_R}{I_{RMAX}} + .0035\right) - \delta_0}{\tau_B}\,, \qquad (5)$$

where τ_B is the characteristic magnetic diffusion time for penetration through the blanket, first wall, and plasma.

From Equation (5) it is seen that when the ripple coils are turned off (i.e., $\dot{\delta}_0 = I_R = 0$), $\delta_0 = 0.35\%$. This assumes a "natural" on-axis ripple of 0.35%.

The power supply for the ripple coil sets used for the equilibrium burn control must be actively controlled because the desired field level is proportional primarily to the temperature and density variations from their desired equilibrium values. Probable designs for the controlled power supply include a multiphase thyristor-controlled rectifier, driven either through a flywheel-generator buffer or directly from a utility line.

Nonlinear regulators of the type likely to be used in this control application can be modeled approximately by linear equations for perturbations about a nominal operating point. This has been done to explore the control of the equilibrium burn involving modulation of the ripple field and neutral gas injection rate. Because the unstable eigenvalue of the thermal response dynamic system is approximately 10 $\sec^{-1}$, the coil current regulator should have a response time five to ten times faster for adequate overall control response. Consider the linear coil current regulator shown in Figure E-2. The transfer function relating input to output is given by

$$\frac{I}{I_{cmd}} = \frac{(K/L)}{s + \left(\frac{R + K}{L}\right)}\,, \qquad (7)$$

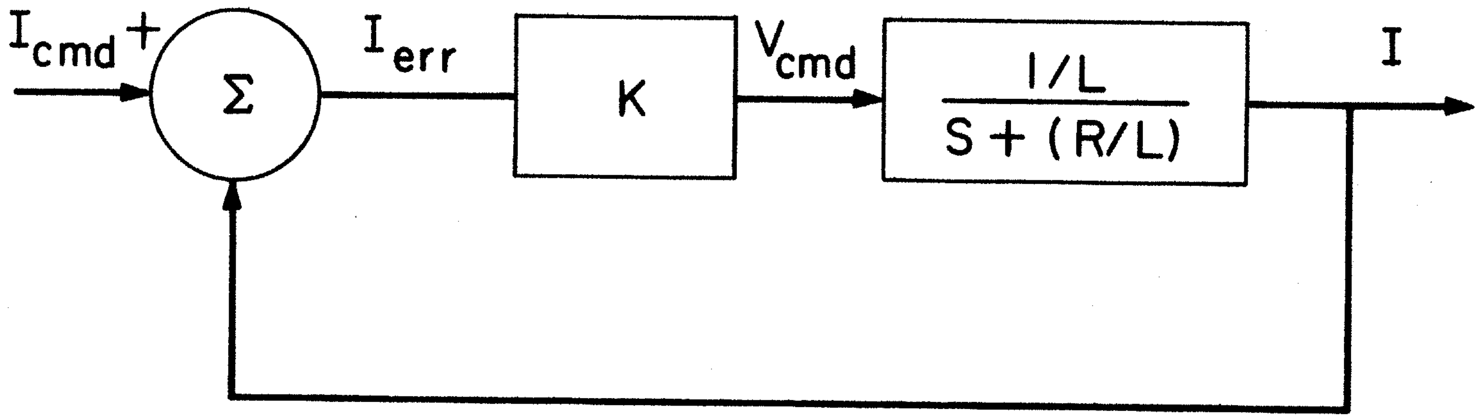

Figure E-2 Linear coil current regulator model.

where L and R are the ripple coil inductance and resistance, respectively, and K is the controller gain. A low-order representation of the current regulator is used to simplify the control analysis. An acceptable steady-state error for a first-order system is something less than 10%. A criterion of 3% is used as an allowable steady-state error. This gives a low-frequency gain of the controller, deduced from equation (7), of

$$\frac{K}{R + K} = 0.97 \ , \tag{8}$$

which results in a controller gain of

$$K = 3.22 \times 10^{-4} \text{ V/A} \tag{9}$$

and a regulator time constant of

$$\tau_R = 0.0112 \text{ sec} \ , \tag{10}$$

which is acceptable. Based on this, a linear current regulator model of the form

$$\dot{I}_R = \frac{(I_{RC} - I_R)}{\tau_R} \tag{11}$$

has been implemented in the computer simulation.

b. Refueling Control Dynamics

An additional control built into the system consists of modulating the neutral gas refueling rate R_F. A model for this controller must encompass the dynamics of the gas flowing through long and narrow ducts. This problem has been investigated by Moy [2] and Burrell [3]; from their work, the delay in transferring gas from the source to the edge of the plasma is 10-20 ms. The gas dynamics are appropriately described here by a second order model of the form:

$$\frac{d^2R_F}{dt^2} = 2\rho_F \omega_F \frac{dR_F}{dt} + \omega_F^2(R_{FC} - R_F) . \qquad (12)$$

c. System of Equations

Except for the ripple and gas refueling dynamics outlined above, the remaining equations follow the physics as described in Ref. 1. These equations are highly nonlinear. In order to develop the feedback controller, it is necessary to linearize the full set of nonlinear rate equation. In summary, the computer code keeps track of seven state variables as they evolve in time, following a small perturbation in any one of them. The state variables are listed in Table E-I. The nonlinear set of equations is linearized numerically using a computer program which is described in the next section. The end result is a set of seven coupled first order linear differential equations of the following form:

$$\begin{aligned}\frac{dn}{dt} &= a_{11}n + a_{12}T + a_{13}E_\alpha + a_{14}R_F + a_{15}\dot{R}_F \\ &\quad + a_{16}\delta + a_{17}I_R + B_{11}R_{FC} + B_{12}I_{RC} \\ \frac{dT}{dt} &= a_{21}n + a_{22}T + a_{23}E_\alpha + a_{24}R_F + a_{25}\dot{R}_F \\ &\quad + a_{26}\delta + a_{27}I_R + B_{21}R_{FC} + B_{22}I_{RC}\end{aligned}$$

Table E-I

STATE VARIABLES FOR THE HFCTR

VARIABLE	DETAIL
n	Plasma density ions and electrons in m^{-3}
T	Plasma temperature ($T_e = T_i = T$) in keV
E_α	Alpha particle energy density in keV/m^{-3}
R_F	Neutral gas refueling rate in m^{-3} s^{-1}
$\dot{R}_F$	Time derivative of R_F in m^{-3} s^{-2}
δ	Local magnetic field ripple ($\Delta B/B$) dimensionless
I_R	Current in ripple coil windings in MA

$$\frac{dE_\alpha}{dt} = a_{31}n + aT + a_{33}E_\alpha + \dots.$$

and similarly for the derivatives of the remaining state variables. The system can be written in the matrix form:

$$\dot{x} = \underline{\underline{A}}\ \underline{x} + \underline{\underline{B}}\ \underline{u} \quad , \tag{19}$$

where the matrices $\underline{\underline{A}}$ and $\underline{\underline{B}}$ are given by

$$\underline{\underline{A}} = \begin{bmatrix} a_{11} & a_{12} & a_{13} & a_{14} & a_{15} & a_{16} & a_{17} \\ a_{21} & & & & & & \vdots \\ a_{31} & & & & & & \vdots \\ a_{41} & & & & & & \vdots \\ a_{51} & & & & & & \vdots \\ a_{61} & & & & & & \vdots \\ a_{71} & \cdot & \cdot & \cdot & \cdot & \cdot & a_{77} \end{bmatrix}$$

and

$$\underline{\underline{B}} = \begin{bmatrix} B_{11} & B_{12} \\ B_{21} & B_{22} \\ B_{31} & B_{32} \\ B_{41} & B_{42} \\ B_{51} & B_{52} \\ B_{61} & B_{62} \\ B_{71} & B_{72} \end{bmatrix} , \qquad (21)$$

and $\underline{x}$ and $\underline{u}$ are the vectors

$$\underline{x} = \begin{bmatrix} n \\ T \\ E_\alpha \\ R_F \\ \dot{R}_F \\ \delta \\ I_R \end{bmatrix} \quad \text{and} \quad \underline{u} = \begin{bmatrix} R_{FC} \\ I_{RC} \end{bmatrix} \qquad (22a,b)$$

representing the state and control variables respectively. Since the controls affect only the refueling and current regulator equations (4th and 7th elements in the state vector) all the terms in the $\underline{\underline{B}}$ matrix will be zero except for B_{41} and B_{77}; they have the dimensions of frequency, and represent the inverse of the delay times τ_F and τ_R, respectively.

E.3 Controls Development Programs

In this section specific digital programs used in the design, analysis and evaluation of a reactor control system are described. In general the plasma system can be defined by a set of nonlinear differential equations. These equations are linearized about a nominal operating (or equilibrium) point. Thus the type of control problem investigated is the perturbation control of a linear system. A control strategy is devised which seeks to minimize perturbations about the equilibrium point. The methodology used involves three main steps:

(a) Determine the plasma burn (temperature, density, etc.) equilibrium values consistent with given reactor parameters;

(b) Linearize the plasma dynamics about the determined equilibrium point; and

(c) Determine the matrix of optimal gains which meet the control objectives.

A CSDL developed set of digital computer programs was used to perform the above design procedures. A summary of these programs and their functions is given in Table E-II.

Once the burn and radial position controllers are designed they need to be evaluated in a realistic (nonlinear) reactor model environment. A

CSDL developed nonlinear digital simulation program was used to exhibit all of the important nonlinearities of the reactor model. A block diagram of this modular, structured program is shown in Figures E-3a, b and c. The program which includes plasma dynamics and effector (cold gas, magnetic ripple, etc.) is structured in such a way that the "simulation program" code (containing the program for numerically solving differential equations, plotting and printing, etc.) is completely separated from the "reactor to be simulated" code (which contains the plasma physics, sensor and effector models). The two blocks of code "talk" to each other through a common data pool. The utility of such a structure is that the same reactor code and data used in the simulation is also used in the equilibrium and linearization programs.

Following the methodology outlined above one arrives at a closed loop system with feedback to the ripple current regulator and the neutral gas injection system. The feedback control laws are linear functions of the system state variables. The preliminary design assumes perfect state information; a schematic of this controller is shown in Figure E-4. In order to complete step (c) above one needs to generate a "cost function" which reflects the design criteria that the controller must meet. Such a function takes the form:

$$J = \lim_{(t_o - t_f) \to 0} \int_{t_o}^{t_f} (\underline{x}^T \underline{\underline{Q}}\, \underline{x} + \underline{u}^T \underline{\underline{R}}\, \underline{u})dt \, , \qquad (23)$$

where $\underline{x}^T$ and $\underline{u}^T$ are transposed vectors $\underline{x}$ and $\underline{u}$. The matrices $\underline{\underline{Q}}$ and $\underline{\underline{R}}$ represent the weights on the states ($\underline{x}$) and controls ($\underline{u}$) respectively. The ratio of $\underline{\underline{Q}}$ to $\underline{\underline{R}}$ is a measure of how much control one is willing to spend to minimize a particular disturbance in $\underline{x}$. When $\underline{\underline{R}}$ is large compared to $\underline{\underline{Q}}$ the

Figure E-3a. Nonlinear Reactor Digital Simulation Program Structure

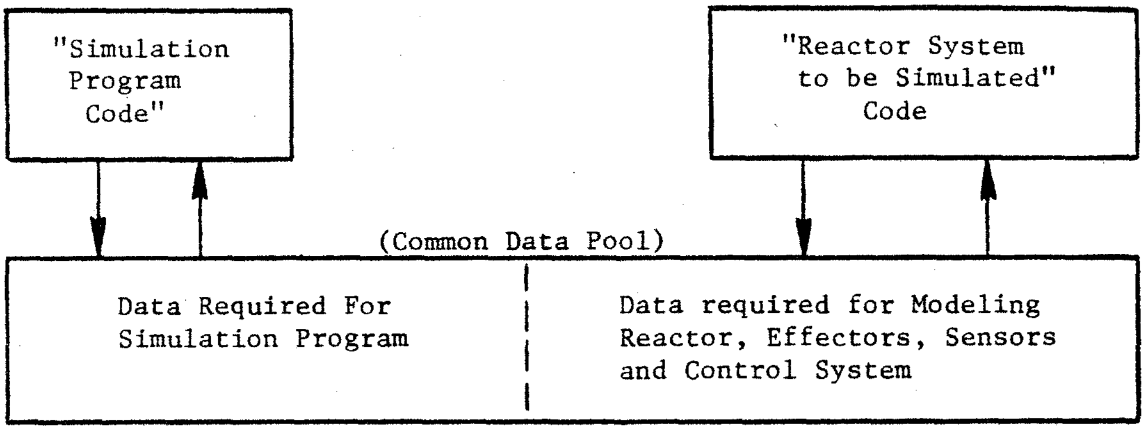

Figure E-3b. Nonlinear Reactor Digital Equilibrium Program Structure

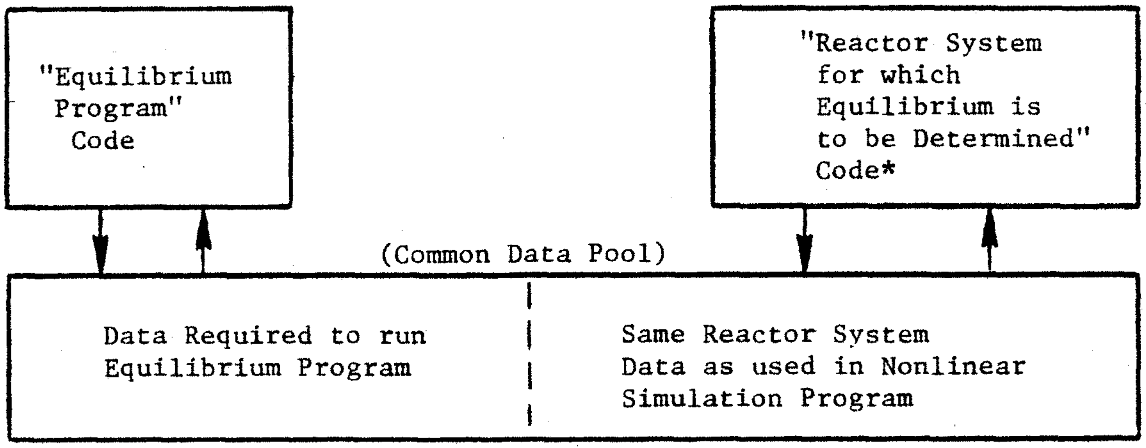

Figure E-3c. Digital Linearization Program Structure

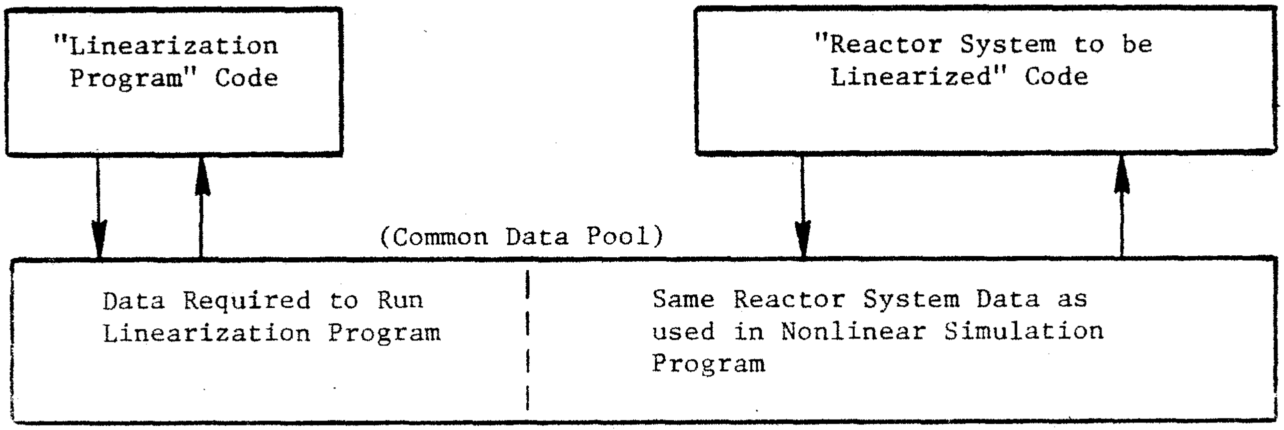

*Same code as used in "Reactor System to be simulated" code

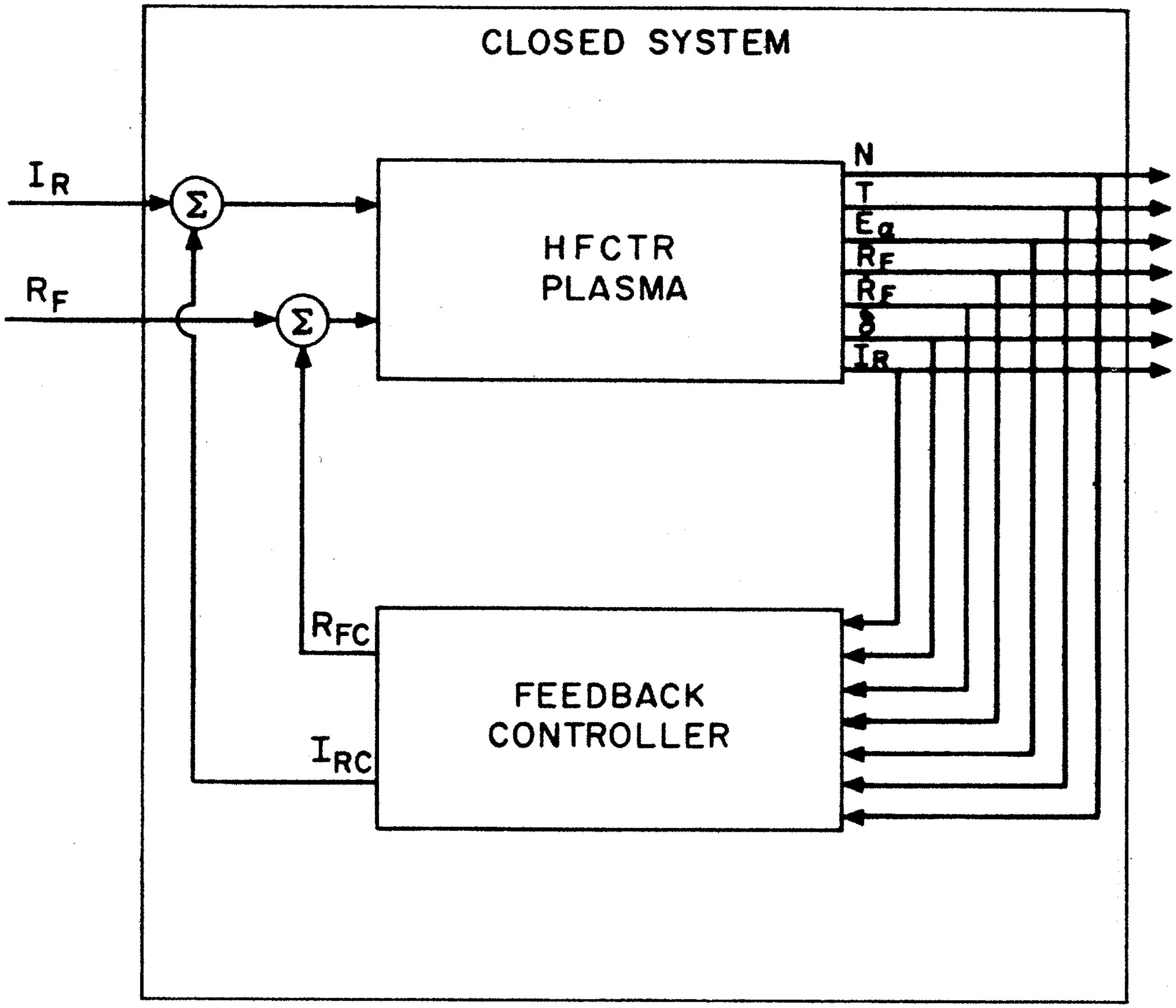

Figure E-4 HFCTR with ripple and gas feedback.

controller is penalized, whereas when $\underline{\underline{Q}}$ is larger the penalty is more heavily weighed on the states. In this preliminary study weight Q_{11} and Q_{22} have been assigned to the state variables n and T only, and weights R_{11} and R_{22} to the control variables R_{FG} and I_{RC} respectively; so that our specialized cost function takes the form:

$$J = \lim_{(t_o - t_f) \rightarrow 0} \int_{t_o}^{t_f} (n^2 Q_{11} + T^2 Q_{22} + R_{FC}^2 R_{11} + I_{RC}^2 R_{22}) dt \ . \quad (24)$$

Equation (23) is by no means the only cost function possible, nor is the integrand in Equation 24 the only choice of weights and variables; for example, one could have chosen to control n and nT instead of n and T independently; a proper choice necessitates an indepth study of economical and engineering tradeoffs. However, these are issues that are beyond the scope of this control study.

REFERENCES - APPENDIX E

[1] Cohn, D. R., et al., "High Field Compact Tokamak Reactor (HFCTR) Conceptual Design", Interim Report, MIT Plasma Fusion Center Report RR-78-2, March, 1978.

[2] Moy, D., "Plasma Density Control in Fusion Reactors: Modelling Gas Flow Transients", MIT Thesis, September, 1978.

[3] Burrell, K. H., "Fast Hydrogen Gas Injection System for Plasma Physics Experiments", Rev. Sci. Instrum. 48 (7), July, 1978.

APPENDIX F: TRITIUM BREEDING RATIO REQUIREMENT

The neutronics code ANISN is a one-dimensional code and required input in the form of a one-dimensional blanket.

Several characteristics of the actual blanket/shield configuration are two and three-dimensional in nature, and must be considered when using the results of ANISN. In particular, factors such as penetrations of the blanket (e.g., beamports, vacuum lines) and poloidal variations of blanket thickness and composition must be taken into account. Any non-uniformity in wall loading should also be considered. Only when all of these effects have been estimated can an accurate evaluation of the net tritium-breeding ratio be made.

In this section, the required breeding ratio of the large, outboard blanket is specified such that the net breeding ratio of the entire blanket is one when all necessary corrections for blanket thickness, penetrations, and neutron wall loading variations are taken into account.

F.1 Assumptions

(1) The blanket and shield are divided into quadrants for the purpose of this calculation. (Four 90° Poloidal Sectors)

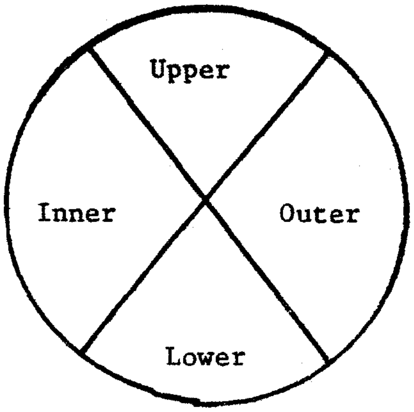

The inner blanket/shield is restricted to a thickness of 60-70 cm while the other 3 quadrants may have thicknesses up to 1.2-1.3 meters.

(2) The breeding ratio of the inner 90° is assumed to be 75% of the breeding ratio of the outer 90° quadrant. This is simply a result of early ANISN runs. The breeding ratios of the upper, lower, and outer quadrants are assumed equal before penetrations and neutron flux profiles are considered.

(3) The fraction of first wall area used for neutral beamlines, beamline shielding, vacuum ports, diagnostic ports, etc. is assumed to be ~7%. This means that for near-vertical injection, about 28% of the lower quadrant will be used as ports, giving only 72% of the nominal breeding ratio for that quadrant.

F.2 Neutron Flux Profiles

Although neutrons are born isotropically in fusion reactions, the effect of toroidal geometry is to shift the current profile, magnetic flux surfaces, and density profiles toward the outside (large major radius) of the torus. The reaction rate profile for neutron production is therefore also shifted to the outside, resulting in a higher neutron wall loading at the outer quadrant, and a lower loading at the inner quadrant because of the 1/r dependence, where r is the distance from the neutron source to the wall.

F.3 Cases Examined

The effects of blanket thickness variation, penetrations, and neutron flux shift on the breeding ratio have been examined for three cases:

(1) Circular Plasma - no flux shift

(2) Circular Plasma - with flux shift

(3) Non-circular Plasma - with flux shift

For each case, the required outboard breeding ratio which gives net breeding equal to unity has been calculated.

Case 1: Circular Plasma - No Flux Shift

The nominal wall load distribution in this case (i.e., fraction of 1 neutron which strikes each quadrant) is uniform:

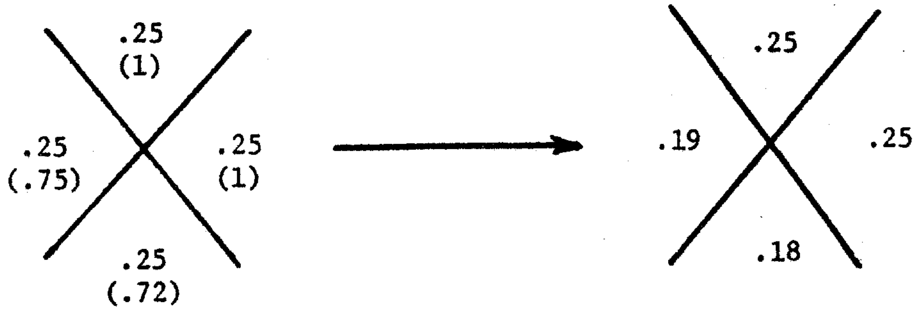

Therefore, 1/4 neutron strikes each quadrant. Normalized to the outer quadrant, the numbers in parentheses give the relative breeding in each quadrant and produce the distribution shown at the right. In this case, and in the following ones, the inner quadrant breeds at 75% of the value of the outer and upper quadrant while the lower quadrant is composed of 40% port area and only 60% of outside breeding is obtained.

The required outer quadrant breeding ratio for net breeding of unity is then

$$K_o(.25 + .25 + .19 + .18) = 1$$

$$K_o = 1.15$$

If no breeding could be obtained on the inner quadrant, the required outer

$$K_{o_{3/4}} = \frac{1}{.25+.25+.18} = 1.47$$

Case 2: Circular Plasma - With Flux Shift

The effect of the neutron flux shift on the poloidal dependence of the neutron wall load has been estimated for both circular and non-circular cross-section tokamaks by Chapin and Price (1). Their results are used for the nominal wall load in each quadrant for Cases 2 and 3. For the circular plasma, the distribution is the following:

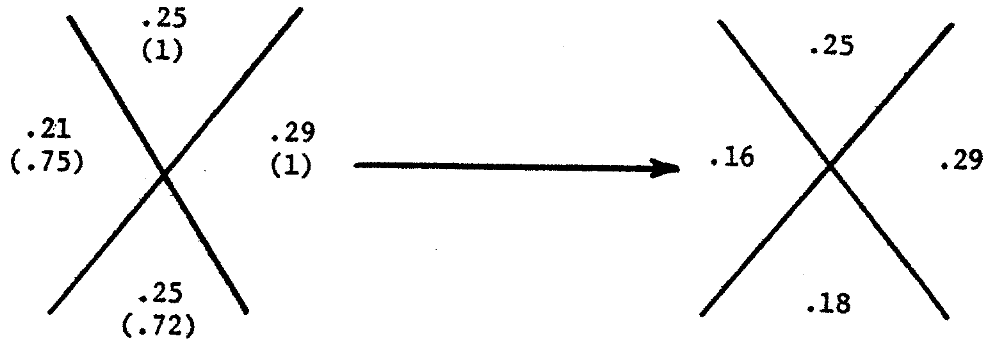

For net breeding of unity, the outer breeding ratio must be

$$K_o = \frac{1}{.25 + .29 + .18 + .16} = 1.14$$

With no breeding on the inner quadrant, the required outboard breeding is

$$K_o = \frac{1}{.25 + .29 + .18} = 1.39$$

Case 3: Non-Circular Plasma - With Flux Shift

For this case, the neutron wall load distribution is approximately

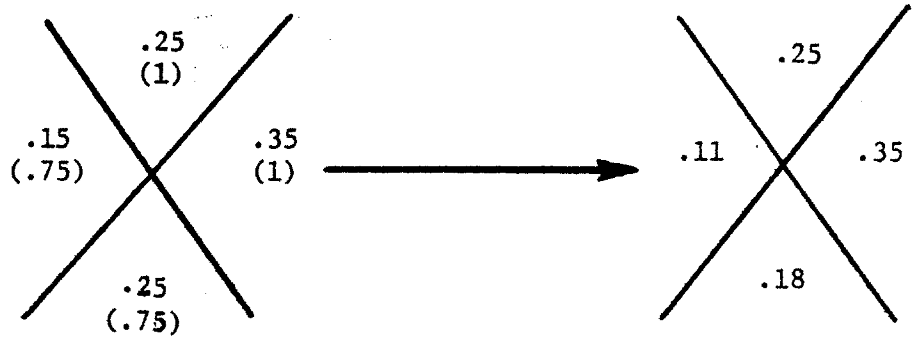

For net breeding of unity, the outside breeding ratio must be

$$K_o = \frac{1}{.25 + .35 + .18 + .11} = 1.12$$

With no breeding on the inner quadrant, the required outboard breeding is

$$K_{o_{3/4}} = \frac{1}{.25 + .35 + .18} = 1.28$$

F.4 Discussion

The table on the following page shows the required outboard breeding ratio which provides net unity breeding when the inside quadrant breeds at 75% of the outer value (K_o) and at 0% of the outer value ($K_{o_{3/4}}$)

	K_o	$K_{o_{3/4}}$	ΔK_o
Case 1 - Circular Plasma - No Shift	1.15	1.47	.32
Case 2 - Circular Plasma - With Shift	1.14	1.39	.25
Case 3 - Non-Circular Plasma - With Shift	1.12	1.28	.16

The difference, ΔK_o, is also shown. The effect of the flux shift is to decrease the contribution to the net breeding ratio of the inside 90° quadrant. This is seen in the large variation (16%) of $K_{o_{3/4}}$, the required outside breeding ratio for net breeding of unity when the inboard quadrant does not breed at all. The reason for this is that as the neutron flux shifts outward fewer neutrons are lost through the inboard quadrant while more neutrons are lost in penetrations in the lower quadrant, and more neutrons are also used effectively in the upper and outer quadrants. These effects tend to cancel each other in determining K_o.

F.5 Conclusion

Based on the assumption that 7% of the first-wall surface is used for purposes (i.e., injection, pumping, piping, etc.) which preclude breeding of tritium, and the analytical observation that the inboard quadrant can breed at 75% of the value of the outer quadrant, we find the required breeding of the outboard blanket to be 1.12-1.15. This gives net tritium breeding equal to unity. This range is relatively insensitive to the neutron flux poloidal profile, but would be significantly higher (perhaps 1.20-1.25) if the neutral injection were not carried out vertically. For a slightly elongated plasma employing near-vertical injection, the required outboard breeding ratio is about 1.12 for a net breeding ratio of 1 for the total blanket.

APPENDIX G: BUCKING CYLINDER FABRICATION PLAN

G.1 DESCRIPTION OF BUCKING CYLINDER

The bucking cylinder for the HFCTR design will be a large welded and machined structure. The cylinder will be constructed of 24 vertical plates surrounded by 148 horizontal annular plates. These plates are held together by bolting 4 end plates on the top and bottom of the cylinder to all of the vertical plates and the end horizontal plates. The cylinder will be insulated at plate interfaces in order to reduce eddy current losses.

The assembled cylinder will have a vertical height of 11.6 m (38.3 ft), a bore diameter of 4.8 m (15.8 ft) and an end plate diameter of 5.4 m (17.8 ft) as shown in Figures G.1-1 and G.1-2. The approximate assembled weight is 1475 metric tons (1625 tons).

G.2 STRUCTURAL MATERIAL

The bucking cylinder will be fabricated from an austenitic stainless steel 310 S. This material was selected because of its desirable mechanical and physical properties, availability, moderate cost and excellent fabricability.

Bolts will be made from A-286 stainless steel material. A-286 was selected primarily for its extremely high yield strength.

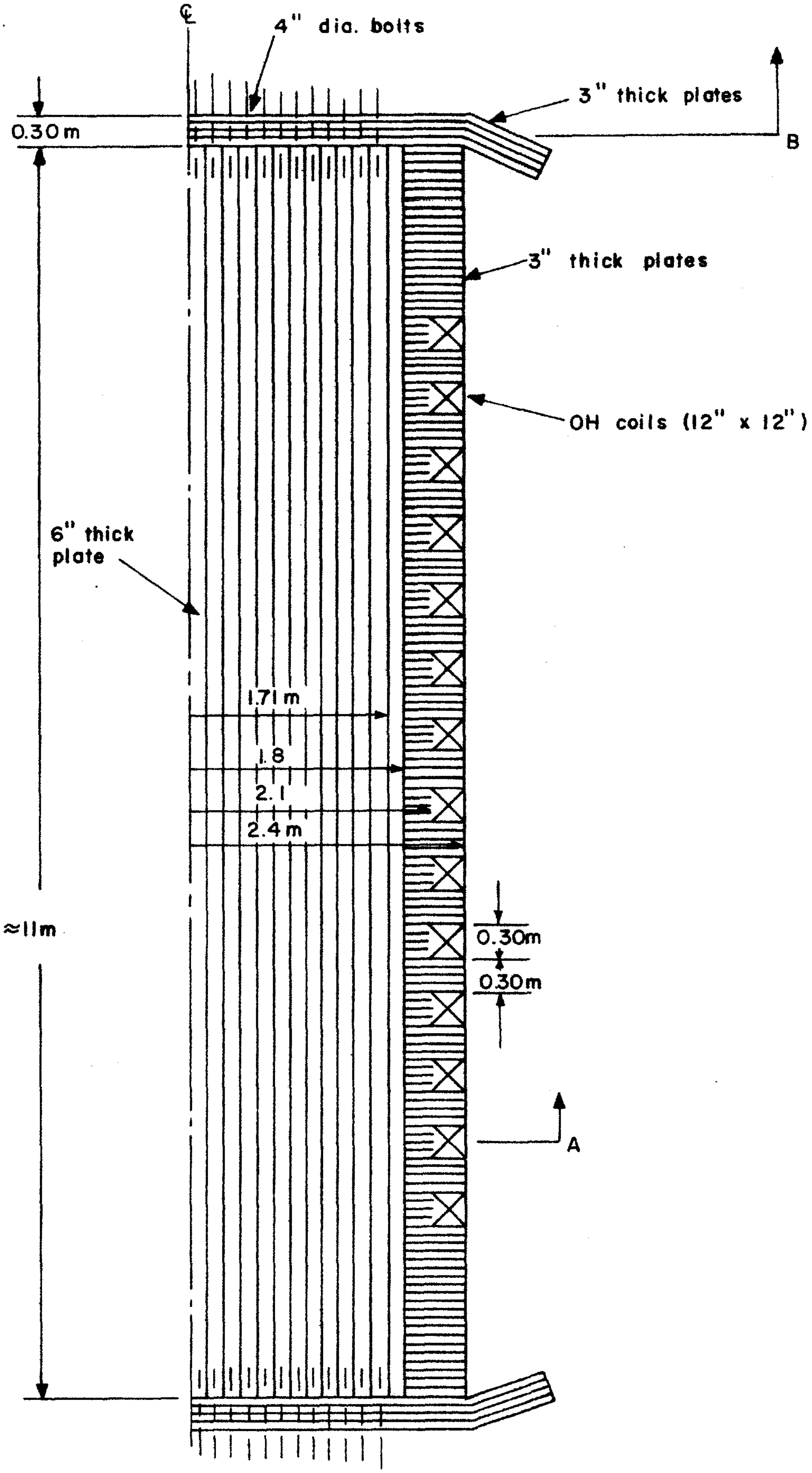

℄
4" dia. bolts
3" thick plates
B
0.30 m
3" thick plates
OH coils (12" x 12")
6" thick plate
1.71 m
1.8
2.1
2.4 m
≈11m
0.30m
0.30m
A

Figure G.1—1

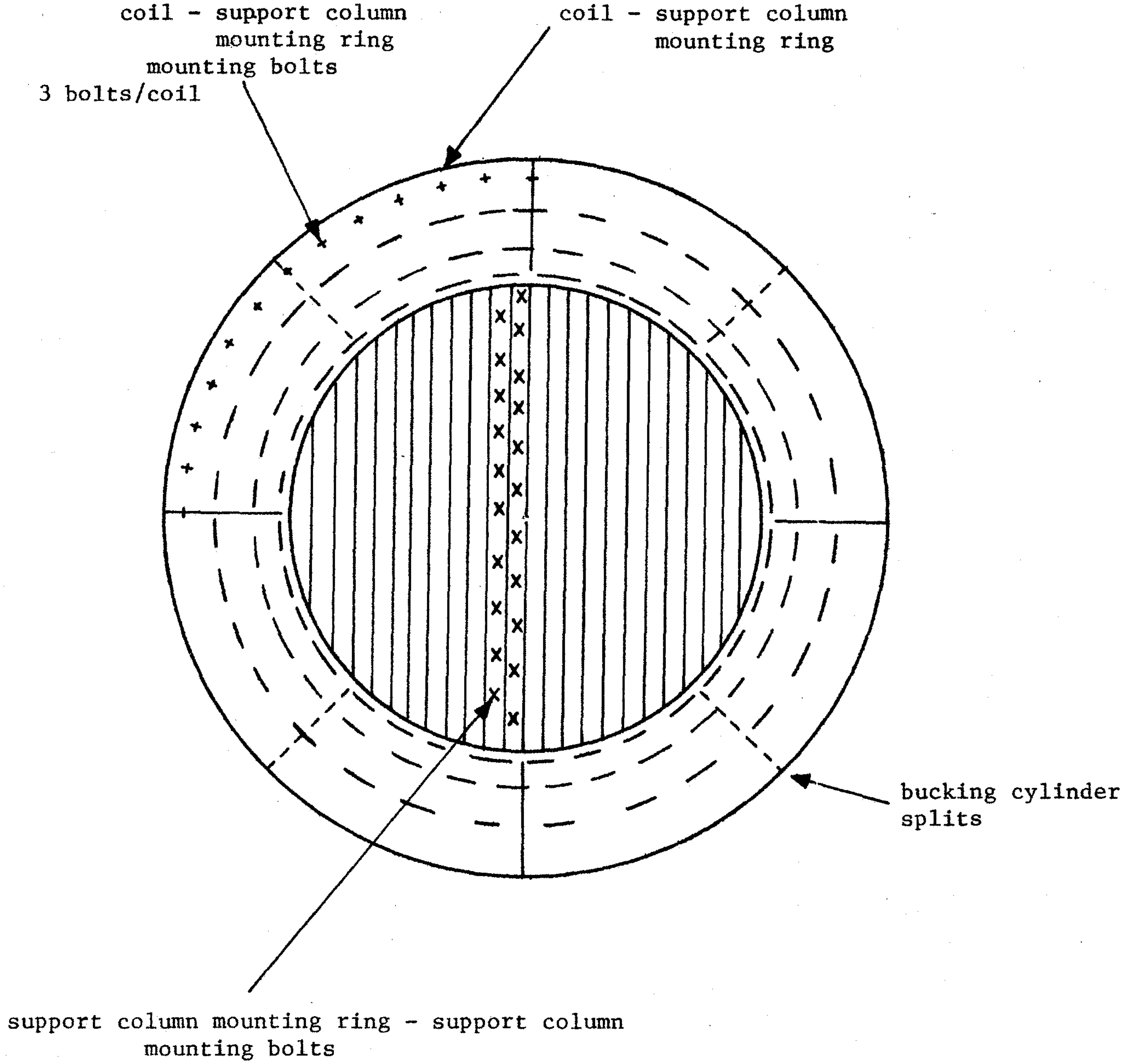

4" dia. bolts
total 212 bolts

Section B

Figure G.1-2

G.3 FABRICATION OPERATION SEQUENCE

Step 1 Purchase Slabs

Stainless steel 310 S will be purchased in accordance with a written material specification. It is impossible to obtain any of the vertical support column or coil support rings in a solid slab. Consequently the vertical support slabs will be obtained in 1/2 of their full length 6.0 m (19.8 ft) with a full width of 3.42 m (11.3 ft) from a 0.15 m (6 in) thick material. The coil support column rings will each be composed of 1/8 circumference segments. These segments will be cut from slabs 2.44 m (8 ft) by 3.64 m (12 ft) and 0.15 m (6 in) thick material. The end rings will consist of four sections cut from slabs 2.74m (9 ft) by 2.74 m (9 ft) of 0.075 m (3 in) thick material.

Step 2 Receiving Inspection

Upon receipt of the material the mill test report will be checked to ensure compliance with the material specification. At this time, the material will be identified with the appropriate shop order, drawing and item number.

Step 3 Weld Slabs to Required Length

It is not possible to purchase the slabs for the required length of 11 meters needed for the support column. It will therefore be necessary to weld together two slabs, each slab 5.5 m (18.1 ft) in length.

The slabs will be welded, utilizing the electroslag process. In this process, the longitudinal axis of the weld is in a vertical plane. Water-cooled copper shoes are fit tightly against the base metal and act as a dam that confines the liquid weld metal. A starting and finishing metal block is fitted and manually tack welded at the bottom and top of the weld joint.

Filler wires are automatically fed into the weld joint. As the wires melt, the liquid puddle continues to rise until the weld reaches the level of the finishing block. At this time the welding is stopped, the copper shoes removed, and the starting and finishing blocks are removed by carbon arc gouging. Figure G.3-1 shows the set-up that will be used to electroslag weld the slabs to the required length.

Step 4 Ultrasonic Inspection of Electroslag Weldments

The completed welds will be ultrasonically inspected to ensure acceptable weld quality.

Step 5 Mill Edges of Welded Slabs

In preparation for welding, both edges of all welded slabs will be faced and tapered in a gantry planer mill. The splice area of the vertical plate has three different locations over a length of 1 m (39.37 in).

Step 6 Clean and Inspect

The machined edges will be deburred and cleaned of machining lubricants. The edges will also be inspected to insure plumb, parallelism, and taper angle.

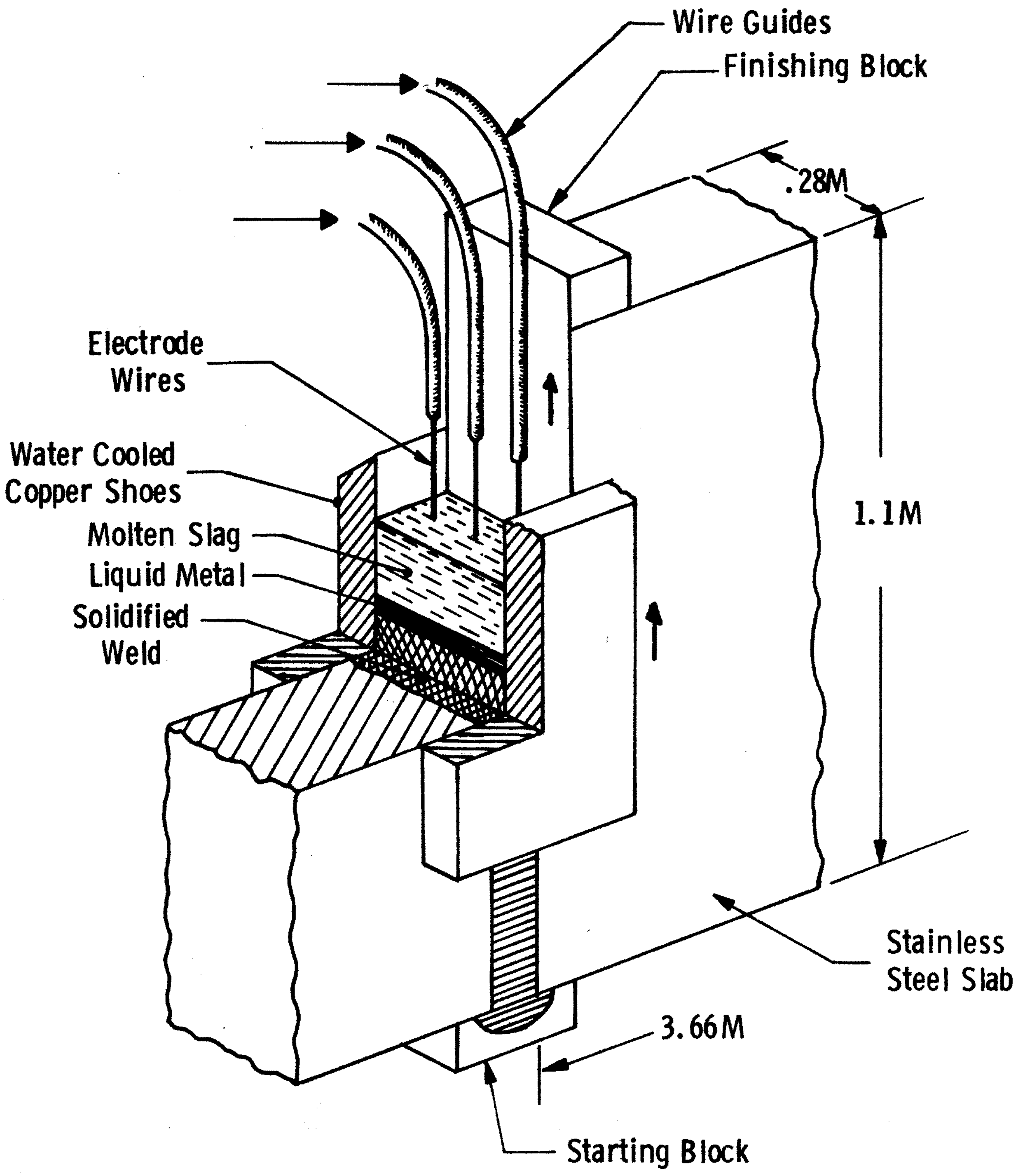

Figure G.3-1 Electroslag Welding Process

Step 7 Weld Slabs to Form Half Cylinder Shape

The slabs will be fitted in a vertical plane and prepared for welding. The 0.15 m (6 in) thick by approximately 3.42 m (11.2 ft) long welds will be made with the electroslag welding process as shown in Figure G.3-1.

Step 8 Inspect Weldments

The completed welds will be ultrasonically inspected to ensure acceptable weld quality.

Step 9 Anneal Cylinder Plates

Each welded support plate, consisting of two halves, will be treated in order to refine the grain structure and relieve welding stresses. It is necessary to relieve stresses in order to maintain dimensional tolerances during subsequent machining operations.

Step 10 Machine Cylinder Plates

All required machining operations for each support plate will be done in a horizontal boring mill. Both faces will be machined to ensure that the support plates are plumb when assembled. The edge surfaces will then be tapered to the proper dimensions to obtain the proper curvature.

Step 11 Clean and Inspect

Each support plate will be cleaned and inspected for plumb, parallelism, slot dimensions, hole location, hole size, threads and finish.

Step 12 Cutting Horizontal Bucking Cylinder and End Support Plates

The segments of the plates, 8 for the bucking cylinder support layer and 4 for the end plates, will be plasma burned for slab material.

Step 13 Machining of Horizontal Plates

The segments will be surface milled and then edge machined and contoured to obtain the desired periphery shape. The locating bolt holes will then be drilled as shown in Figure G.3-2.

Step 14 Inspect and Clean

The finished machined horizontal plates will be inspected and then degreased.

Step 15 Assembly

The bottom horizontal plates will be layed on a flat surface and bolted together. The vertical plates will then be placed on top of the bottom horizontal plates and bolted. Shim stock will be placed between all plates to simulate insulation thickness. The horizontal bucking cylinder support plates will then be assembled around the vertical support plates. The top horizontal plates are then bolted to the top of the center support column and bucking cylinder plates.

Step 16 Disassemble the Cylinder

The assembly bolts will be removed and the cylinder will be disassembled.

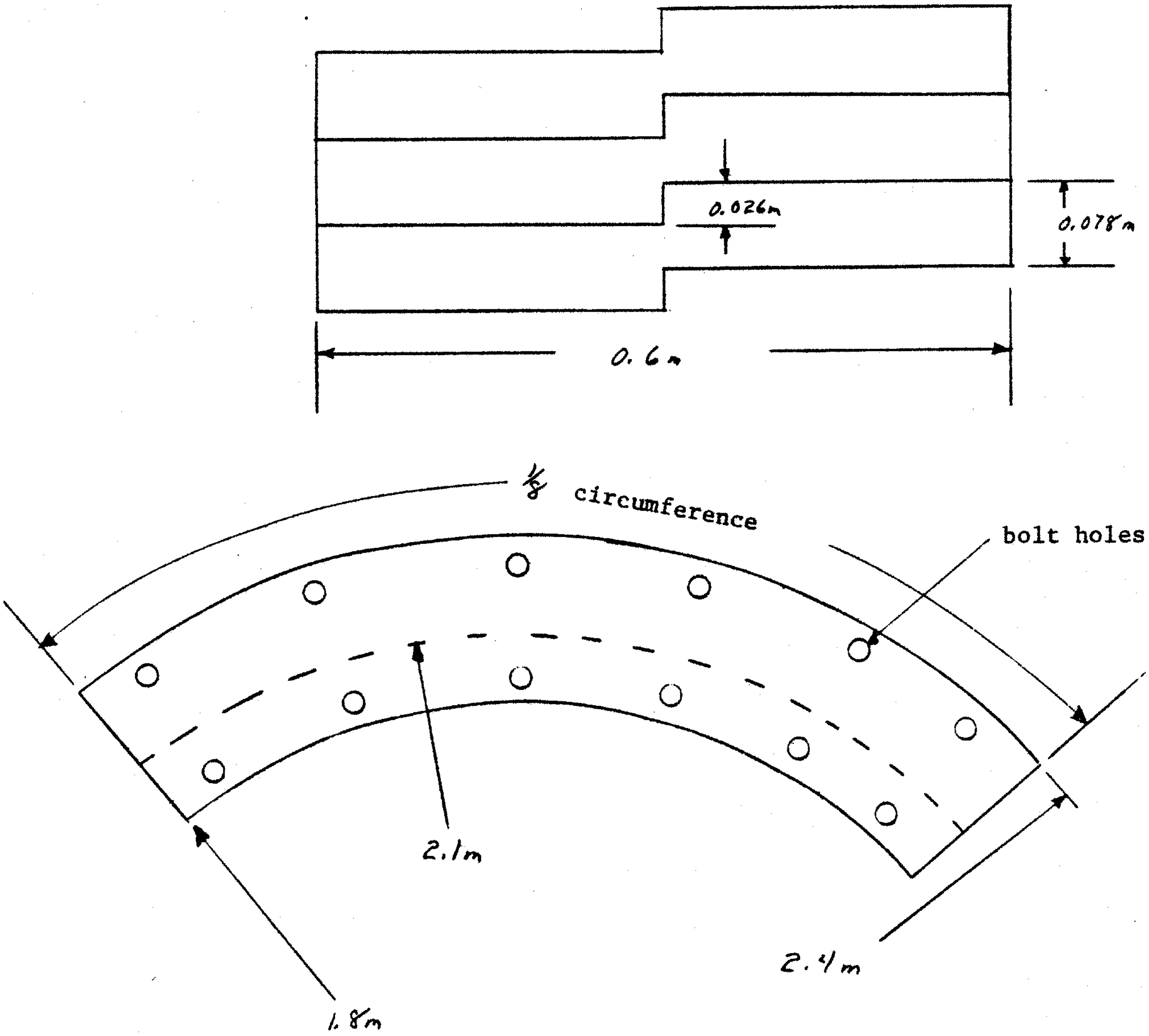

Figure G.3-2 Bucking Cylinder Support Plates

Step 17 <u>Ship to Erection Site</u>

The bolts and plates will be identified and packaged. All components will be shipped to the erection site.

APPENDIX H: METHOD FOR CALCULATING TOTAL TIME OF REACTOR MODULE REPLACEMENT

H.1 Introduction

H.2 Groundrules and Assumptions

H.3 Total Octant Replacement

H.4 Individual Operations

H.5 Typical Procedure

H.1 INTRODUCTION

This appendix presents the details of an evaluation of the time necessary to remove and replace one octant module in HFCTR. A previously developed timing method [1], which allows every one of the thousands of individual operations involved in a module replacement to be quickly assembled and tabulated, was used in this study.

The philosophy which was used to develop the time estimates for the removal and replacement of an octant module was based on the general assumption that the devices and operations were designed with the goal of maximum utilization of automatic functions. It was also assumed that the equipment and procedures had been used numerous times before and that the personnel involved were well trained and fully familiar with the operations being performed. The resultant time estimates purposely reflect this optimistic approach.

Specific elementary operations such as the joining of standard water connection occurred numerous times during each major operation and typical procedure steps are included for these types of functions, so that the time needed for an elementary operation need not be recalculated in detail every time it recurs.

H.2 GROUNDRULES AND ASSUMPTIONS

H.2.1 Utility Joints Connections and Disconnections

Assumptions

All the utility joint connections will be designed and installed so that they can automatically be joined and/or separated. The mechanism to perform this function will be built into the movable half of each joint so that pressing a button or moving a lever will start the series of actions required to join and/or separate the utility joint. These actions would include, but not be limited to, the unlocking of the joint from its temporary unjoined storage position, the start of the movement of the movable-joint half toward the stationary half, the placement of the alignment feature to assure proper joining, the final mating, the proper sealing and seating in the operating position and the confirmation that the joint has been properly made. As an example, a cryogenic-type joint could have a male fitting (approximately 15" long) which would be inserted into a sheath. A pair of alignment pins would be incorporated to assure proper guidance during assembly and disassembly. The cold end will contain a sealing surface and the hot end will have a compression ring seal. Once the bayonet insertion is completed, a V-groove type clamp (such as a Marman clamp) will exert the force to pull the joints together to develop the seals. This clamp could be actuated by means of hydrualic or pneumatic pressure causing the movement of a lever arm. A visual indication by different colored lights could be used to indicate the activation of the mechanism to uncouple the cryogenic joint; the breaking of the main seal, and the complete separation of the two parts of the joint. Supply lines will be valved closed prior to joint separation and a shut-off valve at the joint would automatically be actuated and the joint region purged before joint separation during disassembly. The joint would open upon complete sealing after assembly.

Provision for a backup or redundant system would be made to assure that a malfunction would not cause an excessive slowdown.

H.2.2 Power Supply for the Superconducting Toroidal Field Coils

Assume that the joint to be broken is not in the superconductor, but rather in the normal copper portion of the line at room temperature. The connection joint will be similar to that used for power connectors to switch gears with possibly four or five large contacts being made simultaneously.[2]. The contacts are forced into and out of position by rotating a threaded shaft which will be aligned and fed into a nut which engages a stationary power screw pulling the connectors into the proper contact position. The threaded shaft on the joint is spinfree at the end of joint travel to assure proper engagement and to prevent overtightening.

This connection is visualized as being approximately 46 cm × 46 cm × 60 cm deep with bottom support rollers on the floor. Once the connection is broken, the joint assembly is pulled back out of the way. It will have a firmly established position on the floor to start the assembly. The power joint will be moved back to the outer wall location about 12 meters back. Cables will have sufficient flexibility to be able to be sprung to the required position or else the complete section must be moved by breaking the second joint. One inlet and one outlet are required for each octant module.

H.2.3 Move Old Octant Module Out of Position

Assumptions

A track system is provided which connects the reactor room to other parts of the facility. The tokamak reactor is located in the center of a circular array of tracks. Eight individual sets of spur tracks (one for each modular octant) emanate from the center of the reactor outward to the circumferential tracks.

The complete module will be positioned on a support structure which rests on closely machined guide rollers sitting in a machine track or way. This track arrangement with associated rollers would be designed such that very fine locational guidance will be possible. The load can be jacked off the rollers during normal machine operation, so that the probability of the rollers operating properly will be better assured. The load could be transferred back to the rollers prior to moving the complete module. A jacking arrangement would be built in so that the complete assembly can be moved very slowly and accurately during the first (approximate) 25 cm of movement. A tractor located on the circumferential track and connected by a pulley arrangement could be utilized to pull the complete assembly the remaining 10 meters in a straight radial line away from the center of the torus and then around an outside perimeter track.

The radial track systems (rollers mounted parallel to the long axis of the vehicle) could be installed in pairs of two and positioned to fit the span of the radial rail system. By providing two retractable roller assemblies at each suspension point, the transporter will be able to negotiate the break in the radial rails at the intersection with the circular track without causing excessive deflection in the transporter frame. The radial track roller system will have the capability of being retracted or adjusted vertically to provide a constant vertical position of the octant module regardless of minor deviations in the floor and rail system.

The circular track roller system would consist of tapered rollers for following a circular track. The support frame for the rollers will be mounted in a retractable carriage located on the sides of the transporter. When the modular segment transporter is operating on the radial tracks the carriage mounted wheels would be retracted. In transferring the transporter from the radial track system to the circular track, the unit would be moved out radially until the carriage mounted rollers are aligned with the circular tracks. At this point, the carriages would be lowered to engage the circular track roller system with the circular track and the radial roller system would be raised, completing the transfer of the transporter from the radial track system to the circular track system.

A portable refrigeration system will be included with the modular segment transporter so that the octant module can be disconnected from the permanent refrigeration system and kept cold while being moved. This portable refrigeration system will either be housed on a separate vehicle along with the transporter or connected by flexible lines. With flexible lines, the same system would be used while bringing the new modular segment into position.

H.2.4 Move the New Octant Module into Position at the Torus

Assume that the new module has previously been brought into the reactor room, along the radial rails to the periphery track. The load is transferred to the periphery rollers (radial rollers retracted) and the module moved around to a position beyond the radial track leading to the replacement slot. This permits the old module to be taken out toward the air lock and the new unit to be inserted. The unit hooked up to its temporary refrigeration system so that it is maintained close to the required operating temperature.

H.2.5 Connect the Vacuum Vessel to Adjacent Modules

The faces of the adjacent vacuum vessel module sections are assumed to be flanges with a mechanism for sealing the two flanges together and verifying that the vacuum seal is proper. Only the flange on one side of the module would contain the sealing mechanism, so that the modules would be standardized and the number of spare parts minimized. The two flanges could be locked together by the activation of a group of power clamps around the perimiter of the flange. The clamps would be moved, latched and locked by the automatic action of a control device. The vacuum closure is made by pressurizing a tube to deform the sealing faces. Both right and left seals would be tightened simultaneously. After the joint has been tightened, the seal would be checked for vacuum tightness. If a leak is found, the seal would be remade and rechecked.

The clamping device would have to have a power source connected to perform the locking and unlocking. This would not remain connected to the clamps during plant operation.

The various connections for the coolant, vacuum, etc., will be performed at the same time as the utilities will be connected for the blanket shield, TF coils, etc.

H.2.6 Structural Core Flanges (Center Column Hold Down)

One of the basic design objectives is to assure that the toroidal field coils are kept at operating (4 K) or close to operating temperatures during the time that octant modules are being exchanged. To accomplish this goal, the design features a dewar which completely encompasses two toroidal field coils. This dewar has a bellows arrangement built into the areas where structural forces or loads must be taken against the dewar such as at the vertical face in contact with the bucking cylinder, the adjacent side vertical surfaces where modules mate with each other and the top and bottom support flange area. This results in having three bellows surfaces coming together at the inner top and bottom intersections between adjacent octant modules. Small actuators are installed on the inside dewar faces which cause the bellows to expand the required distance of approximately 0.635 cm when the octant is separated and provide a vacuum behind the dewar. An alternative approach is to place a passive spring system between the structural plates and moveable cryostat walls. Prior to moving an octant module out of the seating position, it is necessary to release the tension load on the core vertical plate structure. This can be accomplished by loosening the 188 tension bolts holding the individual vertical plates in the center column. Loosening of these bolts will release any holding forces at the upper and lower field coil center column flanges and will permit the outward radial movement of the octant.

The loosening of the 188 vertical tension bolts will be accomplished by a computer-controlled device; which, after being properly positioned on the center column, will proceed to loosen the tension bolts. This may be accomplished on individual bolts or on a group of bolts at a time. This device will be stored on the center column while the old module is removed and then used to apply the proper tension to the bolts, after the new module is positioned. The device will not be stored on the device while the reactor is being operated.

H.2.7 Neutral Beam Injector

There are eight neutral beam injectors located around the perimeter of the tokamak. One is located in the space between each octant module. The main connection to the tokamak vacuum vessel is assumed to be a bolted flange approximately 95 cm in diameter with 78 bolts securing the injector to the vessel. A computer-controlled torquing device is visualized for this operation in which the bolts are progressively loosened and retracted. The bolts as well as the seal will be captive in the flange to minimize the assembly problems. Staggered tightening of the bolts to provide a good vacuum seal and provisions will be made to confirm proper sealing.

In addition to the main flange connection, it is assumed that the following utilities which are similar to those used in other parts of the tokamak will be required:

a. Cooling water inlet and outlet header.
b. Liquid helium and liquid nitrogen inlet and outlet headers.
c. Gas-handling inlet and outlet headers.
d. Electric power inlet and return lines.
e. Vacuum connections.

Any shielding which is required for the neutral beam injector will not have to be removed prior to moving the injector.

Once all the connections are broken the complete neutral beam injector along with its support structure will be retracted below the floor level by means of an automatic elevator-type structure. A cover plate will automatically be positioned so that the floor and any track area will be ready to move the octant module.

H.2.8 Poloidal Field Coils External to Toroidal Field Coils

There are four sets of poloidal field coils which are located external to the toroidal field coils. Two sets are located above the equator and two sets below the equator. These coils are supported between the octant modules. These supports have incorporated devices to move the coils above or below the tokamak when the octant module is being replaced.

The coils located above the equator will be raised sufficiently to provide clear movement of the module. It is assumed that this movement is small enough so that the utility connections (vacuum, electric power, cryogenic) do not have to be broken.

The coils located below the equator must be moved down below the track area to assure that the module movement radially outward is possible. This is a larger movement, but it is still assumed that the utility joints will not have to be disconnected for this movement.

The automatic control action will require the unlocking of the coils from the support, the actual movement of the coils, the locking in the stored position and, in the case of the lower coils, the movement of the rail section and replacement of the floor sections.

H.2.9 Vacuum Pump Removal

It is assumed that each octant module will require one vacuum pump penetration into the vacuum vessel. There will be two flanged joints in the high-vacuum duct which must be disconnected for the octant module to be moved: one into the vacuum vessel and one down to the roughing pumps in the high-vacuum pump foreline. An electric power line will also have to be disconnected. No shielding will be required around the vacuum pump. The flange joints will be joined and sealed by the use of clamps around the periphery, similar to those described for the vacuum vessel parting joints.

H.2.10 Instrumentation

All the instrument leads for each octant module will be routed so that the leads, electric, pneumatic, etc., come together into one flexible compact connector. This connector will be a flanged joint held together by approximately 8 clamps which will keep the male and female portions joined together. Alignment pins will be used to properly orient the two parts of the instrument junctions. One part of the joint will be firmly attached to a support so that it does not move when the mating joint is forced into contact with it.

The routing of all the instrumentation for a modular segment into one connector is recognized to be a serious design problem. If it proves not feasible to accomplish this, then two or more instrument joints for each modular segment could be handled. Since the time element for this operation is not very great, this would not present a severe penalty.

H.3 TOTAL OCTANT MODULE REPLACEMENT TIME

TABLE 1

SCENARIO OF PROCEDURES FOR EXCHANGE OF AN OCTANT MODULE

Major Procedure Steps	Performance Time (Minutes)
1. Loosen and disconnect toroidal field coils from center column	212
2. Disconnect and move the neutral beam injector	186
3. Move external poloidal field coils vertically away from the toroidal field coils	16
4. Disconnect utility services and vacuum vessel attachments	179
5. Move old octant module out	200
6. Move new octant module into position	132
7. Connect and tighten toroidal field coil to center column	205
8. Connect utility services and vacuum vessel attachments	400
9. Reposition external poloidal field coils	16
10. Reposition neutral beam injector	401
11. 40% Contingency	774
	2709 min (45.2 Hr)

H.4 INDIVIDUAL OPERATIONS

1. OPERATION - LOOSEN AND DISCONNECT TOROIDAL COIL FROM CENTER COLUMN (APPROXIMATELY 188 BOLTS) *

Procedure Steps	Performance Time (Minutes)
(1) With the overhead crane (operated and controlled at the main control room), lift the torquing device from its storage rack and move it over the top of the center column. Benchmarks are utilized for gross alignment and locating dowels provide final alignment.	10
(2) Lower the torquing device onto the center core column so that it is properly positioned and aligned and release the crane lifting device from the torquing device.	7
(3) Depress the control mechanism to activate the torquing device for loosening the first tension bolt.	—
(4) Move the torquing device in position to loosen the first bolt. Loosen the first bolt.	8
(5) Move the torquing device to the next tension bolt and proceed to loosen it and the remaing 187 bolts.	187
	212

*Note: If there are any additional tasks required to disconnect the top and bottom flanges at the center column, they will be performed in parallel with this task.

2. OPERATION - DISCONNECT AND MOVE THE NEUTRAL BEAM INJECTOR BELOW THE RAILS

Procedure Steps	Performance Time (Minutes)
(1) Uncouple the utility connections	
(a) Water inlet and outlet header (See typical water disconnection procedure #A).	12
(b) Liquid helium - unlock and remove the insulation around the inlet and outlet header and disconnect the liquid helium inlet and outlet fittings (See typical cryogenic insulation and fitting procedure #C and #A).	22
(c) Liquid nitrogen - unlock and remove the insulation around the inlet and outlet header and disconnect the liquid nitrogen inlet and outlet fittings. (See typical cryogenic insulation and fitting procedures #C and #A).	22
(d) Gas handling inlet and outlet fitting. (See typical gas handling header procedure #A).	12
(e) Vacuum (See typical vacuum connection procedure #G).	11
(f) Electric inlet and outlet bus (See typical electric connection procedure #E).	6

2. OPERATION - DISCONNECT AND MOVE THE NEUTRAL BEAM INJECTOR BELOW THE RAILS (Cont.)

Procedure Steps	Performance Time (Minutes)
(2) Depress the control mechanism to activate the mechanism which unlocks and moves the bolt torquing device into the proper position for loosening and retracting the main flange bolts.	5
(3) Loosen and retract the first flange bolt.	1
(4) Loosen and retract each of the remaining 77 bolts.	77
(5) Activate the mechanism to move the torquing device away from the vacuum flange to its storage position and lock it there.	5
(6) Operate the mechanism to retract the complete neutral beam injector to its temporary storage location below the rails.	10
(7) Raise the floor cover plate over the floor opening.	4
	186

3. OPERATION - MOVE THE EXTERNAL POLOIDAL FIELD COILS VERTICALLY AWAY FROM THE TOROIDAL FIELD COILS

Procedure Steps	Performance Time (Minutes)
(1) Activate the mechanism to unlock the hold-down for the poloidal field coils both above and below the equator.	1
(2) The locking devices move out of their locking position and a light indicates that all locks are open.	2
(3) Automatically move the poloidal field coils away from this support structure. (Coils move up or down depending on their location in relationship to the tokamak equator.)	10
(4) Lock the coils in their storage position.	2
(5) Confirm that all coils are moved and locked in storage position.	1
	16

4. OPERATION - DISCONNECT THE UTILITY SERVICES AND THE VACUUM VESSEL ATTACHMENTS

Procedure Steps	Performance Time (Minutes)
(1) Toroidal Field Coils	
(a) Disconnect the superconductor power supply leads. (See typical procedure #K).	28
(b) The liquid helium and nitrogen fittings will be disconnected in operation #7 after the temporary refrigeration is connected for the TF dewar.	—
(c) Disconnect the vacuum to the dewar. (See typical procedure for vacuum connection #G).	11
(2) Blanket and Shield	
(a) Disconnect the FLIBE inlet and outlet. (See typical procedure to disconnect FLIBE #I).	18
(b) Disconnect the lithium inlet and outlet. (See typical procedure to disconnect lithium #I).	18
(c) Disconnect the coolant water inlet and outlet joints for the structural supports. (See typical procedure to disconnect water coolant, #A).	12
(3) Poloidal Field Coils located inside the toroidal field coils.	
(a) Disconnect the water coolant inlet and outlet. (See typical procedures to disconnect water coolant joints #A).	12

4. OPERATION - DISCONNECT THE UTILITY SERVICES AND THE VACUUM VESSEL ATTACHMENTS (Cont.)

Procedure Steps	Performance Time (Minutes)
(4) Vacuum Vessel	
(a) Disconnect the secondary vacuum containment located outside the shield. (See typical procedure for disconnecting vacuum wall #M).	14
(b) Disconnect the vacuum walls from the adjacent modules. (See typical procedure for disconnecting vacuum wall #M).	14
(c) Disconnect the two vacuum pump connections one for each vacuum enclosure. (See the procedure for vacuum pump disconnection #O).	24
(5) Disconnect the instrumentation. (See typical instrumentation disconnection procedure #Q).	10
(6) Ripple Coil	
(a) Disconnect the inlet and outlet coolant water. (See typical procedure to disconnect coolant water joints #A).	12
(b) Disconnect the feed and return electric power. (See procedure for disconnecting electric power #E).	6
	179

5. OPERATION - MOVE OLD OCTANT MODULE AWAY FROM THE TORUS

Procedure Steps	Performance Time (Minutes)
(1) Move the tractor into the reactor room and attach it to the transporter which supports the module. (This involves the remote movement of the tractor into the air lock, then to the reactor room and around the periphery of the room to the final radial positioning and attaching to the module transporter. This can all be accomplished in approximately ten minutes, while Step 6 is being performed so that no critical path time is used.)	—
(2) Connect the temporary refrigeration lines from the tractor unit to the octant module. There are two separate sets of inlet and outlet lines for this refrigeration-- one set for the liquid helium and one for the liquid nitrogen. (See typical procedure #B for connecting the liquid helium and nitrogen joints.)	32
(3) Position and lock the insulation over the liquid helium and nitrogen joints. (See typical procedure #D for positioning the insulation.)	20
(4) Change the coolant flow from the permanent refrigeration unit to the temporary coolant system by opening and closing the proper valving at the main control room.	2

5. OPERATION - MOVE OLD OCTANT MODULE AWAY FROM TORUS (Cont.)

Procedure Steps	Performance Time (Minutes)
(5) Remove the insulation from the four permanent refrigeration lines. (See typical procedure #C for removing the insulation.)	20
(6) Disconnect the four permanent refrigeration coolant lines from the TF dewar. (See typical procedure #A for disconnecting the cryogenic joints.)	24
(7) Perform a computer check that all joints, fixtures, clamps, etc., which are required to be loosened or released have in fact been properly performed.	3
(8) Connect the two electric joints to the connectors for heating the nose and adjacent plates so that it will be possible to break any freeze joint between the mating surfaces. (See typical procedure #F for connecting an electric joint.)	8
(9) Turn the heat on and unfreeze the contact plates.	8
(10) Activate the mechanism to move the octant module approximately 1/4" to allow the dewar bellows to expand and have a vacuum space inside the dewar wall at the nose and the walls directly adjacent to it.	5

5. OPERATION - MOVE OLD OCTANT MODULE AWAY FROM TORUS (Cont.)

Procedure Steps	Performance Time (Minutes)
(11) Move the complete module assembly approximately 10", after releasing the clamping pressure on the internal poloidal field joints. This will release the electric joints for the poloidal field coils internal to the toroidal field coils.	30
(12) Move the complete octant module away from the torus toward the periphery track approximately 10 meters.	30
(13) Lower the periphery wheels and transfer the load to these wheels and retract the radial wheels.	3
(14) Move the octant module around the outside periphery toward the air lock until it is clear of the radial spur, so that the new octant module can be moved in.	10
	195

6. OPERATION - MOVE NEW OCTANT MODULE INTO POSITION

Procedure Steps	Performance Time (Minutes)
(1) Move the octant module to line up with the radial rail spur leading into the torus.	5
(2) Lower the radial wheels, transfer load and retract the periphery wheels.	3
(3) Move the octant module radially inward toward the torus (approximately 10 meters). It will stop about 10 inches before the seating position.	30
(4) Activate the jacking device to move the module to within 1/4" of final seating. This operation will couple the internal poloidal field coils. Alignment will be provided to assist in the proper orientation and close fits.	30
(5) Operate the actuators to retract dewar walls against TF coil support plates in nose region.	5
(6) Jack the module in the additional 1/4" to collapse the dewar bellows and gain firm contact with the bucking cylinder.	5
(7) Connect the permanent refrigeration lines to the module. There are two separate sets of inlet and outlet lines for the refrigeration: one set for the liquid helium and one set for the liquid nitrogen. (See typical procedure #B for connecting the liquid helium and nitrogen joints.)	32

6. OPERATION - MOVE NEW OCTANT MODULE INTO POSITION (Cont.)

Procedure Steps	Performance Time (Minutes)
(8) Position and lock the insulation over the permanent liquid helium and nitrogen joints. (See typical procedure #D for positioning the insulation.)	20
(9) Change the coolant flow from the temporary refrigeration unit to the permanent refrigeration system by opening and closing the proper valving at the main control room.	2
(10) Disconnect the tractor from the transporter and move it out to the air lock. (This will be performed in parallel with other operations and will therefore not have any critical path time associated with it.)	—
	132

7. OPERATION - CONNECT THE UTILITY SERVICES AND THE VACUUM VESSEL ATTACHMENTS

Procedure Steps	Performance Time (Minutes)
(1) Vacuum Vessel	
(a) Connect the secondary vacuum containment located outside the shield. (See typical procedure for connectin vacuum wall #N).	67
(b) Connect the vacuum walls from the adjacent modules. (See typical procedure for connecting vacuum wall #N).	67
(c) Connect the two vacuum pump connections--one for each vacuum enclosure. These are performed in parallel with each other and do not take double time. (See procedure for vacuum pump connection #P).	59
(2) Poloidal Field Coils located inside the toroidal field coils.	
(a) Connect the water coolant inlet and outlet. (See typical procedure for water coolant joints #B).	16
(3) Blanket and Shield	
(a) Connect the FLIBE inlet and outlet. (See typical procedure to connect FLIBE #J).	22
(b) Connect the lithium inlet and outlet. (See typical procedure to connect lithium #J).	22
(c) Connect the coolant water inlet and outlet joints for the structural supports. (See typical procedure for water coolant joints #B).	16

7. OPERATION - CONNECT THE UTILITY SERVICES AND THE VACUUM VESSEL ATTACHMENTS (Cont.)

Procedure Steps	Performance Time (Minutes)
(4) Toroidal Field Coils	
(a) Connect the superconductor power supply leads. (See typical procedure #L).	36
(b) The liquid helium and nitrogen fittings will be connected in operation #8 before the temporary refrigeration is disconnected from the TF dewar.	---
(c) Disconnect the vacuum to the dewar. (See typical procedure for vacuum connector #H).	56
(5) Connect the instrumentation. (See typical instrumentation connection procedure #R).	15
(6) Ripple Coil	
(a) Connect the inlet and outlet coolant water. (See typical procedure for coolant water joints #B).	16
(b) Connect the feed and return electric power bus. (See procedure for connecting electric power #F).	8
	400

8. OPERATION - CONNECT AND TIGHTEN TOROIDAL FIELD COIL SUPPORT PLATES TO CENTER COLUMN (APPROXIMATELY 188 BOLTS) *

Procedure Steps	Performance Time (Minutes)
(1) Lift the torquing device from its storage location and move it over the center core column so that it is properly positioned and aligned for the first tension bolt.	4
(2) Depress the control mechanism to activate the torquing device for tightening the first tension bolt and tighten it.	1
(3) Move the device to the next tension bolt and proceed to tighten each of the remaining 187 bolts.	187
(4) Deactivate the torquing device.	1
(5) Operate the overhead crane and move it in position to attach it to the torquing device.	4
(6) Attach the crane lifting device to the torquing device. Lift the torquing device off the center column.	2
(7) Move the crane carrying the torquing device to the floor storage area and discharge it into a support stand for future removal from the reactor cell.	5
	204

*Note: If there are any additional tasks required to connect the top and bottom flange at the center column they will be performed in parallel with this task.

9. OPERATION - REPOSITION THE EXTERNAL POLOIDAL FIELD COILS

Procedure Steps	Performance Time (Minutes)
(1) Activate the device to move the module transporter rails back out of the way to permit the movement of the poloidal field coils stored below the rails, to their normal operating position. (This operation is performed during the tensioning of the center column bolts so no critical path time is expended.)	—
(2) Lock the rails in the retracted position.	—
(3) Depress the button which actuates the mechanism to unlock the stored poloidal field coils.	1
(4) The locking devices move out of their locking position and a light indicates that the locks are open.	2
(5) Automatically move the poloidal field coils from the storage position to their normal operating position.	10
(6) Lock the coils in their operating position.	2
(7) Confirm that all coils are properly located and locked in place.	1
	16

10. OPERATION - REPOSITION THE NEUTRAL BEAM INJECTOR

Procedure Steps	Performance Time (Minutes)
(1) Operate the mechanism which will lift the floor plate covering and them raise the neutral beam injector on its elevator from the storage position to the proper height for connection to the vacuum vessel.	10
(2) Activate the mechanism which unlocks and moves the bolt torquing device into position to connect and tighten the first vacuum flange bolt.	5
(3) Connect the other 77 bolts for the vacuum flange.	77
(4) Tighten the 78 bolts in the proper sequence to assure a good seal. (This will require that each bolt be tightened in two separate sequences as a check that proper sealing is being obtained.)	156
(5) Activate the device to move the torquing device away from the flange to its storage location and lock it in place.	5
(6) Connect the utility connections	
(a) Water inlet and outlet header (See typical water connection procedure #B).	16
(b) Liquid helium - position and lock the insulation around the inlet and outlet header and connect the liquid helium inlet and outlet fittings. (See typical cryogenic insulation and fitting procedures #D and #B).	26

10. OPERATION - REPOSITION THE NEUTRAL BEAM INJECTOR (Cont.)

Procedure Steps	Performance Time (Minutes)
(6) Cont.)	
(c) Liquid nitrogen - position and lock the insulation around the inlet and outlet header and connect the liquid nitrogen inlet and outlet fittings. (See typical cryogenic insulation and fitting procedures #D and #B).	26
(d) Gas handling inlet and outlet fitting. (See typical gas handling header procedure #B).	16
(e) Vacuum (See typical vacuum connection procedure #H).	56
(f) Electric inlet and outlet bus (See typical electric connection procedure #F).	8
	401

H.5 TYPICAL ELEMENTARY OPERATION PROCEDURES

A. TYPICAL PROCEDURE TO DISCONNECT WATER COOLANT, CRYOGENIC AND GAS FITTINGS

Procedure Steps	Performance Time (Minutes)
(1) Shut or confirm shut the cryogenic flow.	2
(2) Activate mechanism to release locking bar of the V-groove type clamp.	1
(3) Activate device to start the movable portion of the joint to traverse away from the stationary section until the alignment pins are clear.	1
(4) Lock the movable joint section in the retracted position away from the stationary joint half.	1
(5) Light goes on to indicate that joint has been properly disconnected and locked in storage position.	1
	6

B. TYPICAL PROCEDURE FOR CONNECTING WATER COOLANT, CRYOGENIC AND GAS FITTINGS

Procedure Steps	Performance Time (Minutes)
(1) Start operation. Light will indicate start of operation.	—
(2) Lock on movable side of joint is unfastened and joint half moves toward stationary joint.	1
(3) Alignment pins engage and light indicates initiation of alignment.	—
(4) Movable joint continues until the end of the fitting has entered its final seating position and stops moving.	1
(5) Locking lever is activated to seat flange and provide seal.	1
(6) Proper sealing is confirmed.	5
(7) Joint is determined properly mated.	—
	8

C. TYPICAL PROCEDURE FOR UNLOCKING AND MOVING CRYOGENIC INSULATION AWAY FROM CRYOGENIC JOINTS

Procedure Steps	Performance Time (Minutes)
(1) Start the mechanism which separates two locking bars and opens the insulation section to form clearance around the joint.	2
(2) Start the mechanism to move and support the insulation section approximately 10" away from the cryogenic joint toward the permanent half of the joint.	1
(3) Start the mechanism attached to the locking bars which will retain the insulation section away from the joint.	1
(4) Confirmation signal received that the task has been completed.	1
	5

D. TYPICAL PROCEDURE FOR MOVING INSULATION INTO POSITION OVER A CRYOGENIC JOINT AND LOCKING IT IN PLACE

Procedure Steps	Performance Time (Minutes)
(1) Depress button to activate the mechanism which unlocks the two locking bars and opens the insulation section to form clearance around its storage location.	2
(2) Depress the button to move the insulation section approximately 10" from its storage location to encompass the cryogenic joint.	1
(3) Activate the mechanism attached to the locking bars to close the insulation section around the cryogenic joint and lock it in position. Evacuate insulation space.	1
(4) Confirmation signal received that the task has been completed.	1
	5

E. TYPICAL PROCEDURE FOR DISCONNECTING
STANDARD ELECTRIC POWER JOINT

Procedure Steps	Performance Time (Minutes)
(1) Push control button to release the joint and the V-groove clamp locking lever arm is released.	—
(2) Movable joint half starts to move away from stationary joint half.	1
(3) Joint half separates from mating joint half and clears alignment pins.	1
(4) Light indicates that joint is free.	1
	3

F. TYPICAL PROCEDURE FOR CONNECTING STANDARD ELECTRIC POWER JOINTS

Procedure Steps	Performance Time (Minutes)
(1) Push control button and light goes on indicating start of operation.	—
(2) Movable joint section starts to move toward stationary joint.	1
(3) Alignment pins engage and light indicates start of alignment.	—
(4) Movable joint half moves until tapered male lead contacts stationary joint half and seats.	1
(5) Locking lever is actuated to seat joint halves and to provide seal.	1
(6) Check made to assure joint has proper contact.	1
	4

G. TYPICAL PROCEDURE FOR DISCONNECTING VACUUM FLANGE JOINT

Procedure Steps	Performance Time (Minutes)
(1) Activate the mechanism for releasing the clamping action.	—
(2) Unlock the clamp operating device from its storage position and move it into location to operate the clamp.	6
(3) Start the unclamping action and confirm that all the clamps are free and pulled away from the flanges.	3
(4) Move the movable half of the vacuum joint away from the stationary half and secure it in its storage location.	2
	11

H. TYPICAL PROCEDURE FOR CONNECTING VACUUM FLANGE JOINT

Procedure Steps	Performance Time (Minutes)
(1) Activate the device to permit the movable half of the vacuum line to move from its storage location.	——
(2) Movable half section starts to move toward stationary joint half.	1
(3) Alignment pins engage and visual light signals the start of alignment.	——
(4) Movable half continues to move until it is fully seated.	1
(5) Depress control button to activate the mechanism for operating the off-set clamps.	——
(6) Unlock the clamp operating device from its storage position and move it into location to operate clamps.	6
(7) Start the clamping action of one-half of the clamps.	2
(8) Repeat the clamping action for the second group of clamps.	2
(9) Repeat clamping action for final tightening of clamping force.	4

H. TYPICAL PROCEDURE FOR CONNECTING VACUUM FLANGE JOINT (Cont.)

Procedure Steps	Performance Time (Minutes)
(10) Test the vacuum seal to assure that the joint is proper and not leaking:	
(a) Hook-up test fixture automatically	5
(b) Pressurize	5
(c) Confirm that seal is not leaking by monitoring	20
(d) Remove test fixture.	5
(11) Disconnect the control mechanism for the off-set clamps and move device to storage position.	5
	56

I. TYPICAL PROCEDURE TO DISCONNECT LITHIUM AND FLIBE FITTINGS

Procedure Steps	Performance Time (Minutes)
(1) Shut or confirm shut the fluid flow. Purge joint volume.	2
(2) Activate mechanism to release locking bar to the V-groove type clamp.	1
(3) Attempt to move flanges apart.	1
(4) Apply heat to permanent flange face to unfreeze the joint.	3
(5) Move flange faces apart far enough to clear alignment pins.	1
(6) Lock movable flange in place.	1
(7) Light indicates that the joint is free.	—
	9

J. TYPICAL PROCEDURE FOR CONNECTING LITHIUM AND FLIBE FITTINGS

Procedure Steps	Performance Time (Minutes)
(1) Push control button and light will indicate start of operation.	—
(2) Lock on movable side of joint is unfastened and joint half moves toward stationary joint.	1
(3) Alignment pins engage and light indicates initiation of alignment.	—
(4) Movable joint continues until the end of the fitting has entered its final seating position and stops moving.	1
(5) Heat turned on to melt any frozen lithium at contact.	3
(6) Locking lever is activated to seat flange and provide seal.	1
(7) Button pushed to check proper sealing.	5
(8) Joint is determined to be properly mated.	—
	11

K. DISCONNECT POWER SUPPLY FROM THE TOROIDAL FIELD COILS

Procedure Steps	Performance Time (Minutes)
(1) Confirm that power has been turned off from the supply lines.	2
(2) Push control button to start the removal operation. Light goes on, indicating operation is starting.	—
(3) Lever shaft starts to rotate in proper direction to withdraw the power joint.	—
(4) Power joint is pulled out of contact with all four or five connecting surfaces simultaneously. This movement is approximately six inches of travel.	6
(5) Change of light color indicates that full retraction from TF coil has occured.	—
(6) Power joint assembly continues to move away at faster speed to its storage position at outer wall area approximately 10 meters away.	5
(7) Power joint assembly is locked into retracted location.	1
	14

L. CONNECT POWER SUPPLY TO THE TOROIDAL FIELD COIL

Procedure Steps	Performance Time (Minutes)
(1) Push control button and light will indicate start of operation.	—
(2) Lock on movable side of joint is unfastened and joint half is free to move toward stationary joint.	1
(3) Move power joint assembly from storage position to start of close alignment position (10 meters).	10
(4) Power joint assembly is moved into contact with stationary receptacle on TF coil.	6
(5) Joint is seated and locked in position.	1
	18

M. TYPICAL PROCEDURE FOR DISCONNECTING VACUUM WALL JOINTS

Procedure Steps	Performance Time (Minutes)
(1) Activate the mechanism for releasing the clamping action.	——
(2) Unlock the clamp operating device from its storage position and move it into location to operate the clamps.	6
(3) Start the unclamping action and confirm that all the clamps at both the wall joints are free and pulled away from the flanges.	4
(4) Confirm that the clamps have all been released.	2
	12

N. TYPICAL PROCEDURE FOR CONNECTING VACUUM WALL JOINTS

Procedure Steps	Performance Time (Minutes)
(1) Activate the mechanism which will operate the clamping devices.	—
(2) Unlock the clamp operating device from its storage position and move it into location to operate the off-set clamp.	6
(3) Start the section to have the off-set clamps contact the locking surface and slowly pull the clamping flanges together while engaging the alignment pins for position control.	5
(4) Tighten 1/4 of the clamps at a time and repeat complete operation twice for a total of eight separate clamping actions.	16
(5) Test the vacuum seal to assure that the joint is proper and not leaking.	
(a) Hook-up test future automatically	5
(b) Pressurize	5
(c) Confirm that seal is not leaking by monitoring	20
(d) Remove test fixture	5
(6) Disconnect the control mechanism for the off-set clamps and move device to position.	—
	67

O. TYPICAL PROCEDURE FOR DISCONNECTING VACUUM PUMP

Procedure Steps	Performance Time (Minutes)
(1) Activate the mechanism for releasing the clamping action for the roughening pump.	—
(2) Unlock the clamp operating device from its storage position and move it into location to operate the clamps.	6
(3) Start the unclamping action and confirm that all the clamps are free and pulled away from the flanges.	3
(4) Repeat steps 1, 2 and 3 for the main vacuum pump connection. (This can be performed in parallel with the roughening pump so that no time is added.)	--
(5) Disconnect the electric power supply for the vacuum pump.	3
	12

P. TYPICAL PROCEDURE FOR CONNECTING VACUUM PUMP

Procedure Steps	Performance Time (Minutes)
(1) Activate the mechanism which will operate the clamping devices for the roughening pump.	—
(2) Unlock the clamp operating device from its storage position and move it into location to operate the off-set clamp.	6
(3) Start the action to have the off-set clamps contact the locking surface, and slowly pull the clamping flanges together while engaging the alignment pins for position control.	5
(4) Tighten the clamps and repeat complete operation twice.	4
(5) Test the vacuum seal to assure that the joint is proper and not leaking.	
(a) Hook-up test future automatically	5
(b) Pressurize	5
(c) Confirm that seal is not leaking by monitoring	20
(d) Remove test fixture	5
(6) Disconnect the control device for the clamp activator.	5
(7) Repeat steps 1, 2, 3, 4 and 5 for the main vacuum pump. (This can be performed simultaneously with	

P. TYPICAL PROCEDURE FOR CONNECTING VACUUM PUMP (Cont.)

Procedure Steps	Performance Time (Minutes)
(7) Cont.) the roughening pump connection so that time is not added.)	—
(8) Connect the electric power supply.	4
	59

Q. TYPICAL PROCEDURE TO DISCONNECT AN INSTRUMENT JOINT

Procedure Steps	Performance Time (Minutes)
(1) Activate the mechanism for releasing the clamps securing the instrument joint.	——
(2) Unlock the clamp operating device from its storage position and move it into location to open the clamps.	5
(3) Start the unclamping action and move the movable half of the instrument joint until it clears the alignment pins.	2
(4) Confirm that all clamps have been unlatched and that the joint halves have properly separated from each other.	1
(5) Lock the movable joint in its temporary storage position.	2
	10

R. TYPICAL PROCEDURE FOR CONNECTING INSTRUMENT JOINT

Procedure Steps	Performance Time (Minutes)
(1) Activate the device to unlock the latch and to permit the movable half of the instrument joint to move from its storage location.	—
(2) Movable half-section starts to move toward stationary joint half.	1
(3) Alignment pins engage and visual light signal start of alignment.	—
(4) Movable half continues to move until fully seated.	1
(5) Depress control button to activate the mechanism for operating the off-set clamps.	—
(6) Unlock the clamp operating device from its storage position and move it into location to operate clamps.	6
(7) Start the clamping action to grasp and lock the flanges together.	2
(8) Disconnect the control mechanism for the off-set clamps and move device to position.	5
	15

REFERENCES

[1] Sniderman, M., "Fusion Reactor Remote Maintenance Study", Final Report, EPRI Contract No. RP1044-1, 1978.

[2] Westinghouse Descriptive Bulletin 32-252

APPENDIX I: FIRST WALL COOLING TUBES

The surface heat flux seen by a first wall cooling tube can be approximated by a cosine distribution on the side facing the plasma and by an adiabatic rear half. The solution to Laplace's equation for the annular region is symmetric about $\theta = 0$, where the $\theta = 0$ axis points radially away from the plasma, and can be represented as [1]:

$$T(r,\theta) = \sum_{n=0}^{\infty} F_n(r) \cos(n\theta) \qquad (1)$$

where $$F_n(r) = \frac{C_n}{r^n} + D_n r^n$$

The appropriate boundary conditions are:

$$\left.\frac{\partial T}{\partial r}\right|_{a_1} = \begin{cases} \dfrac{q''(a_1)}{k}\cos\theta, & \text{for } 0 \leq \theta \leq \frac{\pi}{2} \\ 0, & \text{for } \frac{\pi}{2} < \theta < \pi \end{cases} \qquad (2)$$

$$k \left.\frac{\partial T}{\partial r}\right|_{a_2} = h(T(a_2) - T_F) \qquad (3)$$

where a_1 is the outer radius, a_2 the inner radius, h the heat transfer coefficient, T_F the bulk coolant temperature, k the thermal conductivity, and q" the heat flux.

The boundary conditions given by (2) can be expressed as a Fourier Series, so that

$$\frac{\partial T}{\partial r} = b_o + \sum_{n=1}^{\infty} b_n \cos n\theta$$

where $b_o = q''/\pi k$, $b_1 = q''/2k$, and for $n \geq 2$

$$b_n = \begin{cases} \dfrac{2q''}{\pi k} \dfrac{(-1)^{\frac{n}{2}+1}}{n^2 - 1} & \text{, for n even} \\ 0 & \text{, for n odd} \end{cases}$$

The solution for C_n and D_n is then found to be

$$C_1 = \frac{q'' a_1^2 a_2^2}{2k} \frac{k - ha_2}{k\,(a_1^2 - a_2^2) + ha_2(a_1^2 + a_2^2)}$$

$$D_1 = \frac{q'' a_1^2}{2k} \frac{k + ha_2}{k\,(a_1^2 - a_2^2) + ha_2(a_1^2 + a_2^2)} \quad ,$$

for $n = 2, 4, 6, \ldots \infty$

$$C_n = \frac{q''}{\pi\, k\, m} \left\{ \frac{(-1)^{m+1}}{(2\,m)^2 - 1} \right\} \frac{a_1^{2m+1}\,(2mk - ha_2)}{[2\,m\,k\,(C^{4m} - 1) + ha_2(C^{4m} + 1)]}$$

$$D_n = \frac{1}{2^{4m}} \frac{[2m + ha_2]}{[2m - ha_2]} C_m$$

and for $n = 1, 3, 5, \ldots \infty$

$$C_n = D_n = 0$$

where $$C = a_1/a_2$$

The complete temperature distribution, for a uniform q''' is given by

$$T\ (r,\theta) = \frac{a_1}{k}\left(\frac{q''}{\pi} + \frac{q'''a_1}{2}\right) \ell n\ \frac{r}{a_1} - \frac{q'''}{4k}\left(r^2 - a_2^2\right)$$

$$+ \frac{(a_1^2 - a_2^2)q''' + 2a_1\ q''/\pi}{2a_2h} + T_F$$

$$+ \sum_{n\,=\,1}^{\infty} \left(\frac{C_n}{r^n} + D_n\ r^n\right) \cos n\ \theta$$

The average temperature is given by

$$\bar{T} = \frac{a_1}{k}\left(\frac{a_1^2}{a_1^2 - a_2^2}\ \ell n\ \frac{a_1}{a_2}\right)\left(q'' + \frac{q'''a_1}{2}\right) - \frac{(a_1^2 + a_2^2)}{8k}\ q'''$$

$$+ \frac{\pi(a_1^2 - a_2^2)q''' + 2aq''}{2\pi a_2h} + T_F$$

The stress due to a uniform q''' for a long tube that is not axially restrained is given by [2]. The result is

$$\sigma_{r_3} = q'''\ \frac{Ka_1^2}{4k}\left[(1 - \rho^2)\left\{\frac{\ell nC}{1 - 1/C^2} - \frac{1}{4C^2} - \frac{3}{4}\right\} - \ell n\ \rho + \frac{1}{2}\right.$$

$$\left. - \frac{1}{2\rho^2} + \frac{1}{4C^2}\left(\rho^2 - \frac{1}{\rho^2}\right)\right]$$

$$\sigma_{\theta_3} = q''' \left[\frac{Ka_1^2}{4k} \left(1 - \rho^{-2}\right) \left\{ \frac{\ell n C}{1 - -/C^2} - \frac{1}{4C^2} - \frac{3}{4} \right\} - \frac{1}{2} + \frac{1}{2\rho^2} + \frac{1}{4C^2} \left(3\rho^2 + \frac{1}{\rho^2}\right) \right]$$

where $\rho = r/a_2$ and $K = \alpha E(1 - \nu)$.

To calculate the stress due to the surface heat flux it is assumed that the tube is completely constrained against all bending but that it is free to expand axially. A uniform axial tension equal to $\alpha\ E\ \bar{T}$ is then added to the plain strain solution of reference [1]. The result is:

$$\sigma_r = \sigma_{r_3} + \frac{ET_o}{2(1 - \nu)} \left\{ \left(\frac{a}{r}\right)^2 \frac{r^2 - a_2^2}{a_1^2 - a_2^2} \ \ell n \frac{a_1}{a_2} - \ell n\ (r/a_2) \right\}$$

$$+ \frac{\alpha E r}{2(a_1^2 + a_2^2)(1 - \nu)} \left(1 - \frac{a_2^2}{r^2}\right)\left(1 - \frac{a_1^2}{r^2}\right) C_1 \cos\theta$$

$$\sigma_\theta = \sigma_{\theta_3} + \frac{\alpha E T_o}{2(1 - \nu)} \left\{ \left(\frac{a_1}{r}\right)\left(\frac{r^2 + a_2^2}{a_1^2 - a_2^2}\right) \ell n \frac{a_1}{a_2} - \ell n \frac{r}{a_2} - 1 \right\}$$

$$+ \frac{\alpha E r}{2(a_1^2 + a_2^2)(1 - \nu)} \left(3 - \frac{a_1^2 + a_2^2}{r^2} - \frac{a_1^2 a_2^2}{r^4}\right) C_1 \cos\theta$$

$$\sigma_{r\theta} = \frac{\alpha E r}{2(a_1^2 + a_2^2)} \left(1 - \frac{a_1^2}{r^2}\right)\left(1 - \frac{a_2^2}{r^2}\right) C_1 \sin\theta$$

$$\sigma_Z = \nu(\sigma_r + \sigma_\theta) - \alpha E(T - \bar{T})$$

where $T_o = \frac{aq''}{\pi k}$

APPENDIX J. GENERAL AND SPECIFIC CASES OF KIRCHOFF'S VOLTAGE LAW FOR TOKAMAKS WITH TIME-VARYING RADIUS, ELONGATION AND INDEX OF CURVATURE

The MIT High-Field Compact Tokamak Reactor enjoys a very well-defined plasma scenario which specifies plasma current, beta-poloidal, major radius, minor radius, elongation and vertical field index of curvature as a function of time. In order to model the plasma as an electrical load, the plasma could be modeled as a fixed-dimension solid torus with uniform current density, as a first approximation. However, the clear definition of the plasma scenario invites the development of a more general set of plasma voltage equations, which could also be used in other systems studies. The specific cases of fixed-radius initiation, constant-J growth off of a limiter, constant-radius current increase and FCT auxiliary heating, which are used in the HFCTR scenario, are modeled and worked examples are given. Adiabatic radial compression is also modeled. Eddy currents are modeled, but not included in the worked HFCTR examples. The specific cases of scheduled shutdown and unscheduled abort are not modeled, despite their probable importance to power supply specification, because the authors do not yet know how to model these cases. Some conclusions will be drawn concerning the possibly beneficial effects on power supply ratings of deliberately shaping the plasma inductance as a function of time.

J.1 Derivation of the General Expression for Kirchoff's Voltage Law for a Toroidal Plasma

The expression of Kirchoff's voltage law for a tokamak plasma is:

$$0 = \frac{d}{dt}(L_p I_p) + R_p I_p + \sum_k \frac{d}{dt}(M_{p-k} I_k) \tag{1}$$

The equilibrium equation for a toroidal plasma is :

$$B_V = \frac{-\mu_o I_p}{4\pi R}\left[\ln\frac{8R}{a\delta} + \frac{l_i}{2} + \bar{\beta}_\theta - \frac{3}{2}\right] \tag{2}$$

The inductance of a toroidal conductor is taken to be :

$$L_p = \mu_o R \left(\ln\frac{8R}{a\delta^{1/2}} + \frac{l_{i,L}}{2} - 2\right) \tag{3}$$

The index of curvature of the vertical field is defined as:

$$n = -\frac{R_o}{B_{V,R_o}}\frac{\partial B_V}{\partial R} \tag{4}$$

If n is constant along the horizontal midplane, then

$$B_{V,R} = B_{V,R_o}\left(1 - \frac{n\Delta R}{R_o}\right) \tag{5}$$

All derivations of poloidal field voltages are based on equations 1 - 5. Notice that a distinction is made between

$$\frac{l_i}{2} \equiv \frac{2\pi}{\mu_o^2}\,\frac{\int_o^a B_\theta(r)^2\, 2\pi\delta r\, dr}{I_p^2} \tag{6}$$

the usual, energy-related definition of internal inductance, and

$$\frac{l_{i,L}}{2} \equiv \frac{2\pi \int_{0}^{a} B_{\theta} \, (R_o + r) \, dr}{\mu_o R_o I_p} \tag{7}$$

the flux-related definition of internal inductance. Several investigators have apparently been unaware that these two terms are distinct and have used the same symbol for both.

The key assumption is that only one coil or equivalent set of coils will be servoed to the equilibrium equation. In the case of the MIT HFCTR, this coil is the null coil. Other coils may be used to provide volt-seconds, plasma curvature or reduce total power requirements. Eddy currents induced in toroidally continuous structures will also form a set of equivalent poloidal field coils. Once the net field of all the other equivalent coils is measured or accounted for, one EF coil set is adjusted to provide equilibrium. The equilibrium equation is restated as:

$$B_V = \frac{-\mu_o I_p}{4\pi R} \left[\ln \frac{8R}{a\delta} + \frac{l_i}{2} + \bar{\beta}_{\theta} - \frac{3}{2} \right] = \sum_{k} K_{BV-k}{}^{-1} I_k \left(\frac{R_o - n_k \Delta R}{R_o} \right)$$

where

$$K_{BV-k} B_{V,k} = I_k \quad \text{at } R = R_o$$

The current field of the EF coil is labeled K_{BV} and the index of curvature of EF field as n. Then the current in the EF coil is expressed as:

$$I_{EF} = K_{BV} \left(\frac{R_o}{R_o - n\Delta R} \right) \left(B_V - \sum_{k,\text{excl EF}} K_{BV-k}{}^{-1} I_k \left(\frac{R_o - n_k \Delta R}{R_o} \right) \right)$$

Let $\frac{R_o - n\Delta R}{R_o} = b_V^{-1}$, indicating a normalized correction for vertical field. Then

$$I_{EF} = K_{BV}\, b_V \left(\frac{-\mu_o\, I_p}{4\pi R} \left[\ln \frac{8R}{a\delta} + \frac{l_i}{2} + \bar{\beta}_\theta - \frac{3}{2} \right] - \sum_{k,\mathrm{excl\ EF}} K_{BV-k}^{-1}\, b_{V-k}^{-1}\, I_k \right)$$

The total derivative of I_{EF} with respect to time can then be expressed as:

$$\frac{d\, I_{EF}}{dt} = K_{BV}\, b_V\, \dot{B}_V + K_{BV}\, B_V\, \dot{b}_V - K_{BV}\Big(b_V \sum_k K_{BV-k}^{-1} \dot{I}_k\, b_{V-k}^{-1} + \dot{b}_V \sum_k K_{BV-k}^{-1}\, I_k\, b_{V-k}^{-1} + b_V \sum_k K_{BV-k}^{-1}\, I_k\, (\dot{b}_{V-k}^{-1})\Big)$$

If the plasma self and mutual inductances and position are functions of major radius, minor radius, elongation, $l_i/2$ and $\bar{\beta}_\theta$, then a set of partial derivatives is needed to compute the total derivatives of current and flux linkages vs. time. These partial derivatives are tabulated in Table 1.

The general expression of Kirchoff's voltage law for the plasma is then:

$$0 = \frac{d}{dt}(L_p I_p) + R_p I_p + \sum_k \frac{d}{dt}(I_k M_{p-k})$$

TABLE 1

PARTIAL DERIVATIVES OF PF PARAMETERS WITH RESPECT TO R, a, δ, $l_i/2$ AND $\bar{\beta}_\theta$

Partial derivative of / With respect to	$L_{p,ext}$	$L_{p,int}$	B_V	b_V	b_V^{-1}
R	$\mu_o(\ln \frac{8R}{a\delta^{1/2}} - 1)$	$\mu_o l_i/2$	$\frac{\mu_o I_p}{4\pi R^2}\left[\ln \frac{8R}{a\delta} + \frac{l_i}{2} + \bar{\beta}_\theta - \frac{5}{2}\right]$	$\frac{nb_V^2}{R_o}$	$-\frac{n}{R_o}$
a	$-\mu_o \frac{R}{a}$	0	$\frac{\mu_o I_p}{4\pi aR}$	0	0
δ	$-\frac{\mu_o R}{2\delta}$	0	$\frac{\mu_o I_p}{4\pi\delta R}$	0	0
S	—	0	—	0	0
$l_i/2$	0	$\mu_o R$	$-\frac{\mu_o I_p}{4\pi R}$	0	0
$\bar{\beta}_\theta$	0	0	$-\frac{\mu_o I_p}{4\pi R}$	0	0
I_p	—	—	$\frac{-\mu_o}{4\pi R}\left[\ln \frac{8R}{a\delta} + \frac{l_i}{2} + \bar{\beta}_\theta - \frac{3}{2}\right]$		

or

$$
\begin{aligned}
0 = {} & L_p \dot{I}_p + I_p \frac{\partial L_p}{\partial R} \dot{R} + I_p \frac{\partial L_p}{\partial a} \dot{a} + I_p \frac{\partial L_p}{\partial \delta} \dot{\delta} + I_p \frac{\partial L_p}{\partial l_i/2} \dot{l}_i/2 \\
& + R_p I_p + \sum_{k,\mathrm{excl\ EF}} (M_{p-k} \dot{I}_k + I_k \dot{M}_{p-k}) + I_{EF} \dot{M}_{p-EF} \\
& + M_{p-EF} \Big(K_{BV} b_V \dot{B}_V + K_{BV} B_V \dot{b}_V - K_{BV} \Big(b_V \sum_k K_{BV-k}{}^{-1} \dot{I}_k b_{V-k}{}^{-1} \\
& + \dot{b}_V \sum_k K_{BV-k}{}^{-1} I_k b_{V-k}{}^{-1} + b_V \sum_k K_{BV-k}{}^{-1} I_k (\dot{b}_{V-k}{}^{-1})\Big)\Big)
\end{aligned}
$$

In all cases, $I_k \dot{M}_{p-k} = B_{V-k,R} 2\pi R\dot{R} = K_{BV-k}{}^{-1} I_k b_{V-k}{}^{-1} 2\pi R\dot{R}$

In most cases, the Kirchoff law for the plasma loop will be used to find $\dot{I}_{OH}$, after I_p vs time has been specified by plasma engineers and I_{EF} has been determined from the equilibrium equation.

Several special cases of interest can be defined.

(A) No change in coupling from OH coil to plasma.

No vertical field from OH coil.

No current changes in any PF coil other than plasma, EF and OH.

We will use this model for all the time periods in the HFCTR scenario.

$$K_{BV-OH}^{-1} = 0$$

$$\dot{I}_{k,\text{excl EF,OH}} = 0$$

$$
\begin{aligned}
0 = {} & \mu_o R \left(\ln \frac{8R}{a\delta^{1/2}} + \frac{l_{i,L}}{2} - 2\right)\dot{I}_p + I_p \mu_o \left(\ln \frac{8R}{a\delta^{1/2}} + \frac{l_{i,L}}{2} - 1\right)\dot{R} \\
& - I_p \mu_o A\dot{a} - I_p \mu_o \frac{R}{2\delta}\dot{\delta} + I_p \mu_o R \frac{l_{i,L}}{2} + R_p I_p \\
& + \sum_{k,\text{excl EF,OH}} K_{BV-k}^{-1}\, I_k\, b_{V-k}^{-1}\, 2\pi R\dot{R} + M_{P-OH}\dot{I}_{OH} \\
& - \frac{\mu_o I_p}{2}\left(\ln \frac{8R}{a\delta} + \frac{l_i}{2} + \bar{\beta}_\theta - \frac{3}{2}\right)\dot{R} - 2\pi R \sum_{k,\text{excl EF,OH}} \\
& K_{BV-k}^{-1}\, I_k\, b_{V-k}^{-1}\,\dot{R} + M_{P-EF}(K_{BV} b_V \Bigg[- \frac{\mu_o}{4\pi R}\left(\ln \frac{8R}{a\delta} + \frac{l_i}{2} + \bar{\beta}_\theta - \frac{3}{2}\right) \\
& \dot{I}_p + \frac{\mu_o I_p}{4\pi R^2}\left(\ln \frac{8R}{a\delta} + \frac{l_i}{2} + \bar{\beta}_\theta - \frac{5}{2}\right)\dot{R} + \frac{\mu_o I_p}{4\pi a R}\, a + \frac{\mu_o I_p}{4\pi\delta R}\dot{\delta} - \frac{\mu_o I_p}{4\pi R}\frac{l_i}{2} \\
& - \frac{\mu_o I_p}{4\pi R}\dot{\bar{\beta}}_\theta \Bigg] - K_{BV}\frac{\mu_o I_p}{4\pi R}\left[\ln \frac{8R}{a\delta} + \frac{l_i}{2} + \bar{\beta}_\theta - \frac{3}{2}\right]\frac{n b_V^2}{R_o}\dot{R}
\end{aligned}
$$

$$- K_{BV} \left(\frac{nb_V{}^2}{R_o} \sum_{k,\text{excl EF}} K_{BV-k}{}^{-1} I_k b_{V-k}{}^{-1} \dot{R} - b_V \sum K_{BV-k}{}^{-1} \right.$$

$$\left. I_k \frac{n_k}{R_o} \dot{R} \right)$$

This equation can be reduced to:

$$0 = \mu_o R I_p \left[\left(\ln \frac{8R}{a\delta^{1/2}} + \frac{l_{i,L}}{2} - 2 \right) \frac{\dot{I}_p}{I_p} + \left(\ln \frac{8R}{a\delta^{1/2}} + \frac{l_{i,L}}{2} - 1 \right) \frac{\dot{R}}{R} \right.$$

$$\left. - \frac{\dot{a}}{a} - \frac{\dot{\delta}}{2\delta} + \frac{\dot{l}_{i,L}}{2} \right] + R_p I_p + M_{P-OH} \dot{I}_{OH}$$

$$- \frac{\mu_o R I_p}{2} \left(\ln \frac{8R}{a\delta} + \frac{l_i}{2} + \bar{\beta}_\theta - \frac{3}{2} \right) \frac{\dot{R}}{R}$$

$$+ M_{P-EF} K_{BV} b_V \left\{ \frac{\mu_o I_p}{4\pi R} \left[- \left(\ln \frac{8R}{a\delta} + \frac{l_i}{2} + \bar{\beta}_\theta - \frac{3}{2} \right) \frac{\dot{I}_p}{I_p} \right. \right.$$

$$+ \left(\ln \frac{8R}{a\delta} + \frac{l_i}{2} + \bar{\beta}_\theta - \frac{5}{2} \right) \frac{\dot{R}}{R}$$

$$\left. + \frac{\dot{a}}{a} + \frac{\dot{\delta}}{\delta} - \frac{\dot{l}_i}{2} - \dot{\bar{\beta}}_\theta - \left(\ln \frac{8R}{a\delta} + \frac{l_i}{2} + \bar{\beta}_\theta - \frac{3}{2} \right) \frac{nb_V}{R_o} \dot{R} \right].$$

$$- \frac{nb_V}{R_o} \sum_{k,\text{excl EF}} K_{BV-k}{}^{-1} I_k b_{V-k}{}^{-1} \dot{R}$$

$$\left. + \sum_{k,\text{excl EF}} K_{BV-k}{}^{-1} I_k \frac{n_k}{R_o} \dot{R} \right\}$$

(B) Stationary plasma (all subsequent special cases derived include the restrictions in case A)

$$0 = \dot{R} = \dot{a} = \dot{\delta} = \dot{M}_{p-k}$$

$$0 = \mu_o R \left(\ln \frac{8R}{a\delta^{1/2}} + \frac{l_{i,L}}{2} - 2\right) \dot{I}_p$$

$$+ I_p \mu_o R \frac{\dot{l}_{i,L}}{2} + R_p I_p + M_{P\text{-}OH} \dot{I}_{OH}$$

$$- M_{P\text{-}EF} \Big(K_{BV} b_V \Big[\frac{\mu_o}{4\pi R} \left(\ln \frac{8R}{a\delta} + \frac{l_i}{2} + \bar{\beta}_\theta - \frac{3}{2}\right) \dot{I}_p$$

$$+ \frac{\mu_o I_p}{4\pi R} \frac{\dot{l}_i}{2} + \frac{\mu_o I_p}{4\pi R} \dot{\bar{\beta}}_\theta \Big]$$

$$\dot{I}_{EF} = -K_{BV} b_V \Big[\frac{\mu_o}{4\pi R} \left(\ln \frac{8R}{a\delta} + \frac{l_i}{2} + \bar{\beta}_\theta - \frac{3}{2}\right) \dot{I}_p$$

$$+ \frac{\mu_o I_p}{4\pi R} \frac{\dot{l}_i}{2} + \frac{\mu_o I_p}{4\pi R} \dot{\bar{\beta}}_\theta \Big]$$

and

$$\dot{I}_{OH} = -M_{P\text{-}OH}^{\;\;-1} \Big[\mu_o R \left(\ln \frac{8R}{a\delta^{1/2}} + \frac{l_{i,L}}{2} - 2\right) \dot{I}_p$$

$$+ I_p \mu_o R \frac{\dot{l}_{i,L}}{2} + R_p I_p + M_{P\text{-}EF} \dot{I}_{EF}\Big]$$

(C) Growth off of a limiter

$\dot{R} = -\dot{a}$

$\dot{l}_i/2 = 0$, since we design for no skin currents

$\dot{\beta}_\theta = 0$, since β_θ is low during this period

$$0 = \mu_o R \left(\ln \frac{8R}{a\delta^{1/2}} + \frac{l_{i,L}}{2} - 2\right)\dot{I}_p + I_p \mu_o \left(\ln \frac{8R}{a\delta^{1/2}} + \frac{l_{i,L}}{2} - 1 + A\right) \dot{R}$$

$$- I_p \mu_o \frac{R_o}{2\delta} \dot{\delta} + R_p I_p + M_{P-OH} \dot{I}_{OH}$$

$$- \frac{\mu_o R I_P}{2} \left(\ln \frac{8R}{a\delta} + \frac{l_i}{2} + \bar{\beta}_\theta - \frac{3}{2}\right) \frac{\dot{R}}{R} + M_{P-EF} \dot{I}_{EF}$$

where

$$\dot{I}_{EF} = K_{BV} b_V \left\{ \frac{-\mu_o}{4\pi R} \left[\left(\ln \frac{8R}{a\delta} + \frac{l_i}{2} + \bar{\beta}_\theta - \frac{3}{2}\right) \dot{I}_p \right. \right.$$

$$\left. - \left(\ln \frac{8R}{a\delta} + \frac{l_i}{2} + \bar{\beta}_s - A - \frac{5}{2}\right) \frac{\dot{R}}{R} - \frac{\dot{\delta}}{\delta} \right]$$

$$- \frac{\mu_o I_p}{4\pi R} \left(\ln \frac{8R}{a\delta} + \frac{l_i}{2} + \bar{\beta}_\theta - \frac{3}{2}\right) \frac{n b_V}{R_0} \dot{R}$$

$$- \frac{n b_V}{R_o} \sum_{k,\ \mathrm{excl\ EF}} K_{BV-k}^{-1} I_k b_{V-k}^{-1} \dot{R}$$

$$\left. + \sum_{k,\mathrm{excl\ EF}} K_{BV-k}^{-1} I_k \frac{n_k}{R_o} \dot{R} \right\}$$

(D) FCT Heating

The key assumptions for modeling FCT heating with no change in major radius are that toroidal and poloidal flux are conserved

$$0 = L_{p,int} \dot{I}_{p,int} + I_{p,int} \dot{L}_{p,int} \quad \text{and}$$

$$0 = L_{p,ext} \dot{I}_{p,total} + I_{p,total} L_{p,ext} + \sum \frac{d}{dt} (M_{p-h} I_k)$$

where $I_{p,total} = I_{p,int} + I_{p,skin}$. As a design goal we add the further constraint that

$$I_{p,skin} = 0$$

Assume that $\dot{R} = \dot{a} = \dot{\delta} = 0$

$$\dot{L}_{p,int} = \mu_o R \dot{l}_{i,L} /2$$

Clarke and Sigmar (1) derived an asymptotic approximation to plasma current during FCT heating

$$I(\psi_o) = \begin{cases} \dfrac{\psi_o}{R_o} & \text{(low } \beta) \\[2ex] \dfrac{\psi_o}{R_o} (1 - d^2)^{-1/2} \simeq \dfrac{\psi_o}{R_c} \left(\dfrac{\bar{\beta}_\theta}{A}\right)^{1/3} & \text{(high } \beta), \end{cases}$$

where d is a complex flux function < 1.

From conservation of internal flux,

$$\frac{l_{i,L}}{2} \propto \left(\frac{\bar{\beta}_\theta}{A}\right)^{-1/3} \qquad \text{(high } \beta).$$

For circuit modelling, the following approximation may be adequate.

$$\frac{\dot{l}_{i,L}}{2} = 0 \qquad\qquad \bar{\beta}_\theta < A$$

$$\frac{\dot{l}_{i,L}}{2} = \frac{l_{i,L}}{6}\left(\frac{\dot{R}}{R} - \frac{\dot{a}}{a} - \frac{\dot{\bar{\beta}}_\theta}{\beta_\theta}\right) \qquad \bar{\beta}_\theta > A$$

If the further condition of no skin currents is imposed, then $\dot{I}_p = 0$, which corresponds to the MIT HFCTR scenario. The expressions of Kirchoff's voltage law are then:

$$\dot{I}_{EF} = -K_{BV}\, b_V \frac{\mu_o I_p}{4\pi R}\, \dot{\beta}_\theta \qquad \text{and}$$

$$\dot{I}_{OH} = -\, M_{P-OH}^{\;-1}\, M_{P-EF}\, \dot{I}_{EF}$$

(E) Adiabatic Radial Compression

The assumptions for adiabatic radial compression are conservation of toroidal and poloidal flux and of the rotational transform

$$0 = L_{p,int} \, \dot{I}_{p,int} + I_{p,int} \, \dot{L}_{p,int}$$

$$0 = L_{p,ext} \, \dot{I}_{p,total} + I_{p,total} \, \dot{L}_{p,ext} + \sum \frac{d}{dt} (M_k I_k)$$

$$0 = \frac{a^2 \delta}{a_o^2 \delta_o^2} - \frac{R}{R_o} \qquad \text{and}$$

$$0 = \frac{d}{dt}\left(\frac{\mu_o I_p R}{a^2 S^2 B_t}\right) = \frac{d}{dt}\left(\frac{2\pi I_p R^2}{a^2 S^2 \ NI_{TF}}\right)$$

If flux is frozen, then:

$$\int_o^a B_\theta \ 2\pi \ R \ dr = \text{const}$$

Since
$$\frac{l_{i,L}}{2} = \frac{2\pi \int_o^a B_\theta \ R \ dr}{\mu_o R_o I_p} \quad ,$$

the numerator is a constant. For a circular plasma, $R_o \propto a^2$, giving the familiar result that $I_p \propto R_o^{-1}$ and $l_{i,L}/2$ is a constant. For an elongated plasma,

$$R_o \propto a^2 \delta$$

$$I_p \propto a^2 S^2 / R_o^2$$

and
$$I_p R_o \propto S^2 \delta^{-1}$$

Therefore,
$$\frac{\dot{l}_{i,L}}{2} = \frac{l_{i,L}}{2} \left(-2 \frac{\dot{S}}{S} + \frac{\dot{\delta}}{\delta}\right)$$

Since $$\beta_\theta = \frac{16\,\pi^2 a^2 S^2}{I_p^2}\,(\overline{n_e kTe})$$

and $$\beta_\theta \simeq \beta_\theta \left(\frac{2\dot{a}}{a} + \frac{2\dot{S}}{S} + \frac{\dot{\overline{n}}_e}{\overline{n}_e} + \frac{\dot{\overline{T}}_e}{\overline{T}_e} - \frac{2\,\dot{I}_p}{I_p} \right),$$

$$\text{if } \frac{d}{dt}\,(\overline{n_e kT_e}) \simeq k\,\bar{T}_e \frac{d}{dt}\,\bar{n}_e + k\,\bar{n}_e \frac{d}{dt}\,\bar{T}_e \quad .$$

During adiabatic radial compression,

$$a^2 \delta \propto R$$

$$\bar{n}_e \propto V^{-1} \propto R^{-1}\,a^{-2}\,\delta^{-1} \propto R^{-2}$$

$$I_p \propto a^2\,S^2\,R^{-2} \propto S^2\,\delta^{-1}\,R^{-1} \quad \text{and}$$

$$\bar{T}_e \propto R^{-4/3}$$

Then,

$$\bar{\beta}_\theta = \bar{\beta}_\theta\,\left(\frac{\dot{\delta}}{\delta} - \frac{2\dot{S}}{S} - \frac{\dot{R}}{3R}\right) \quad .$$

REFERENCES - APPENDIX J

(1) J. F. Clarke, D. J. Sigmar, "Global Properties of High Pressure Flux Conserving Tokamak Equilibria," ORNL/TM-5599; Aug., 1976

Appendix K: TOROIDAL FIELD COIL MANUFACTURING PLAN

K.1 Manufacturing Plan Objectives

The following groundrules were established for the manufacturing plan:

- Minimize labor and expense costs.
- Utilize existing manufacturing processes and technology where possible.
- Identify all required check points.
- Adopt a realistic production schedule by identifying bottleneck operations where possible.
- Minimize the need for large, expensive capital equipment which is not presently available.
- Prefabricate component parts to the maximum possible extent, in order to minimize handling and field erection costs.

In accordance with the above manufacturing objectives and the desire to construct a modular, rigid, integrated support structure, the following manufacturing plan was developed for the toroidal field coils.

K.2 Toroidal Field Coil Support Structure Fabrication Plan

K.2.1 Description of Support Structure

The support structure for the toroidal field coil will be a modular, pancake construction with a total of 32 pancakes per coil. Individual pancakes are made of machined plate segments which, when assembled, overlap the segments of adjacent pancakes as shown in Figure 3-3.

The entire coil support structure is assembled using bolted construction.

Shear bolts extend completely through the support structure thickness. In addition to providing structural integrity, the bolts serve as building posts or guides during the assembly of the segmented plates.

The support structure of the assembled toroidal field coil will measure 6.5 meters horizontal bore and 10.5 meters vertical bore. The cross section will have a 1.0 meter build on the inner coil leg and a 1.37 meter build on the outer leg, with a maximum coil width of 1.353 meters. The "nose" section of the coil will be trapezoidal. The total weight of the coil support structure will be 358 tons. (See Figure K-1)

K.2.2 Structural Materials

The support structure segments will be fabricated from 310 S stainless steel plate. This material was selected because of its availability, mechinability and good mechanical properties. A-286 stainless steel in a 40% cold worked condition will be used as the bolting material.

K.2.3 Fabrication Operation Sequence - Structure Support

The fabrication operation sequence of the TF coil support structure is described below.

Step 1 Purchase Plate

Pancake segments will be made from 310 S stainless steel plate. The plate will be purchased in accordance with a written specification that will delineate composition, minimum mechanical properties, dimensional tolerances, testing requirements and mill test report requirements.

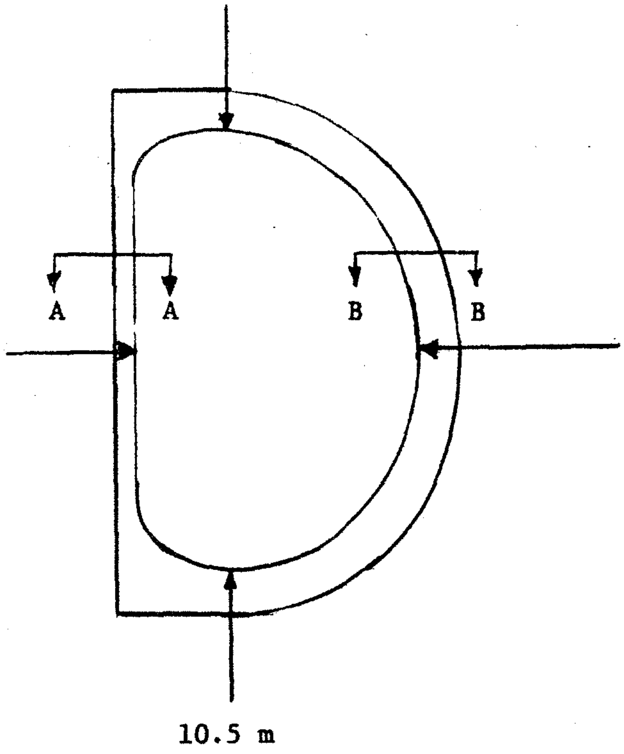

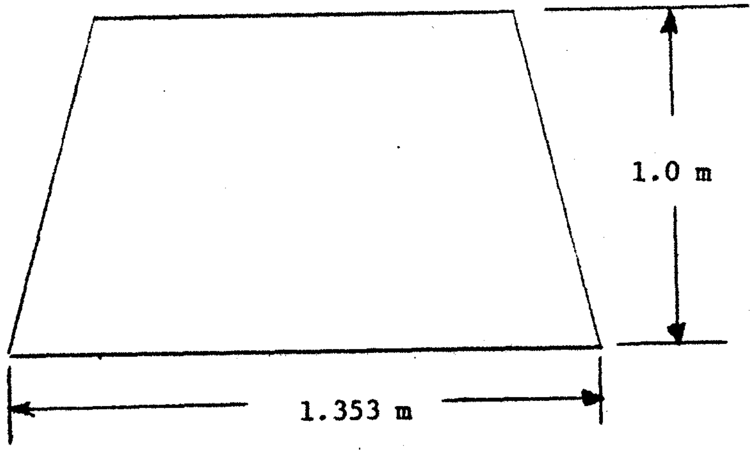

Sec A-A

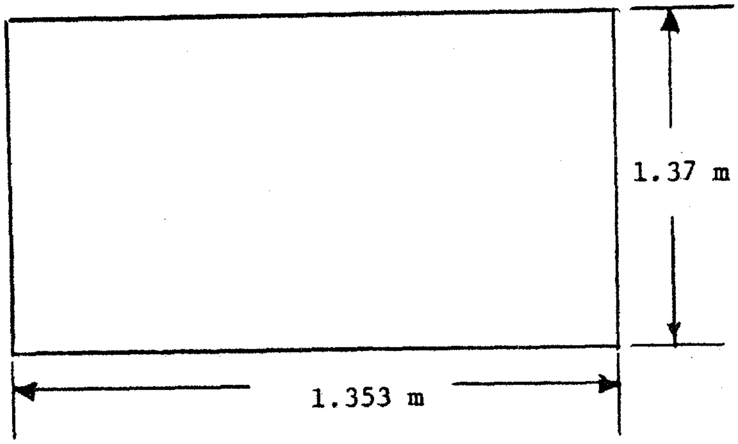

Figure K-1 Toroidal Field Coil Structure Dimensions

Step 2 Receiving Inspection

Upon receipt of the plate and bolt material, the mill test report will be checked to insure compliance with the material specification. At this time, the material will be identified with the appropriate shop order number.

Step 3 Cutting of Pancake Segments

The pancake segments will be burned from the plate, utilizing a plasma cutting machine. A computer program will be used to determine the plate layout. In this manner, maximum plate utilization will be realized. Segments will be burned oversize to insure adequate stock for subsequent machining operations.

Step 4 Identification, Cleaning and Inspection

The pancake segments will then be identified with the appropriate shop order, drawing and item number. Segments will be cleaned of burning dross, and subsequently inspected for size and burning gashes.

Step 5 Flatten Segments

Segments will then be flattened in a straightening press.

Step 6 Ship

All segments will be shipped to a numerically controlled drill press.

Step 7 Drill and Top Assembly Holes - Drill and Counterbore Assembly Holes

Segments will be placed in a locating fixture and all assembly holes will be located and drilled on a numerically controlled drilling machine.

Auxiliary assembly holes will be tapped at this time. The remaining assembly holes will be counterbored. All segments which constitute the first pancake layer are drilled and tapped only. (See Figures K-2 and K-3)

Step 8 Drill Through Bolt Holes

All segments will be placed in a locating fixture and all through bolt holes will be located and drilled on a numerically controlled drilling machine, allowing stock for final reaming at assembly. Through bolt holes will be drilled along the same D-shaped bolt circle as the assembly holes. (See Figure K-4)

Step 9 Clean and Inspect

Drill burrs will be removed and bolt holes will be inspected for location, dimensions, and thread.

Step 10 Slab Grind Segment Faces

Faces of segments will be slab ground to 5.18 cm (2.04 in) thickness.

Step 11 Clean and Inspect

Remove burrs and inspect segments for flatness and thickness.

Step 12 Machine Partings

All parting segments (ends of segments) will be milled.

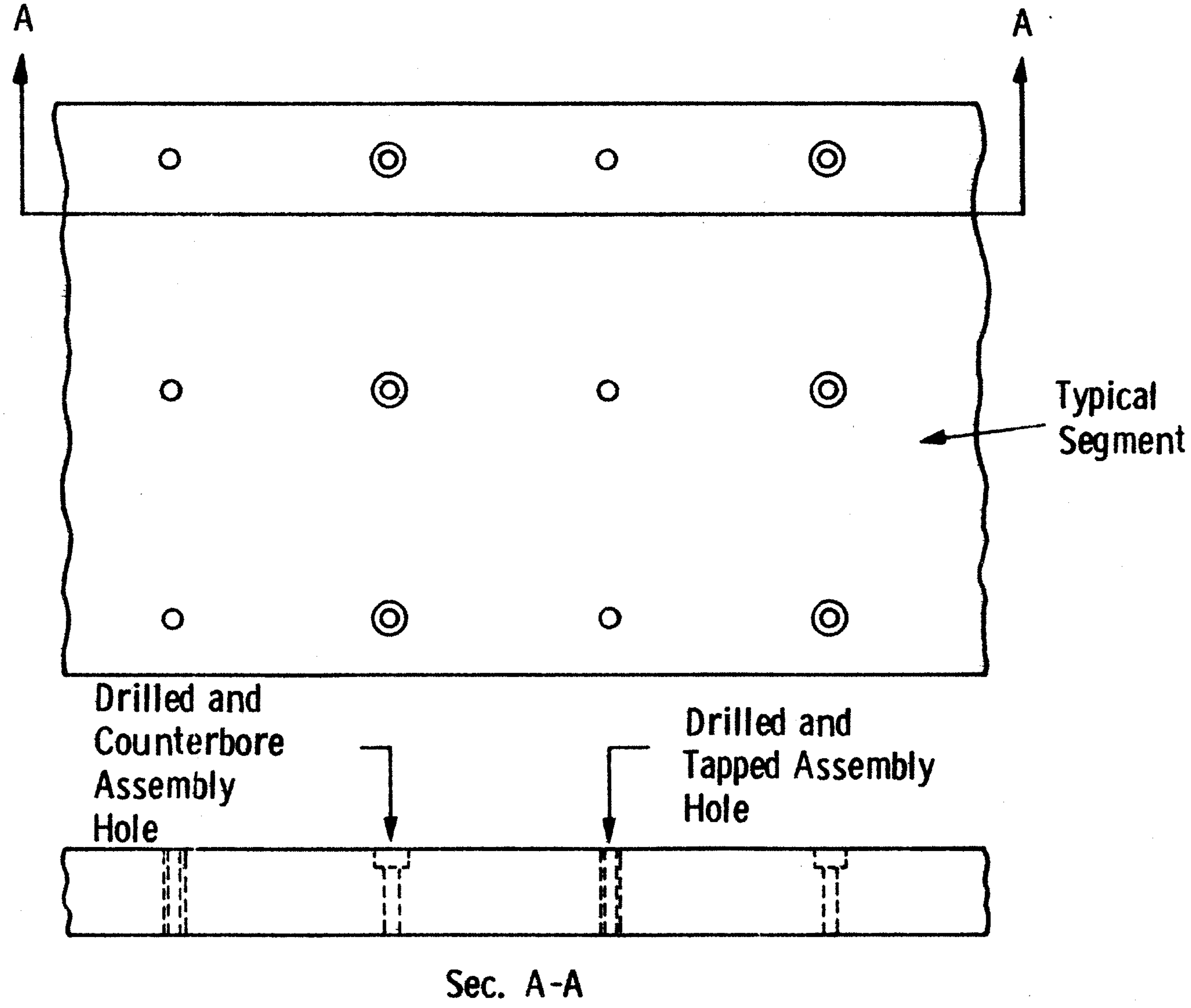

Figure K-2 Assembly Holes in Typical Support Segment

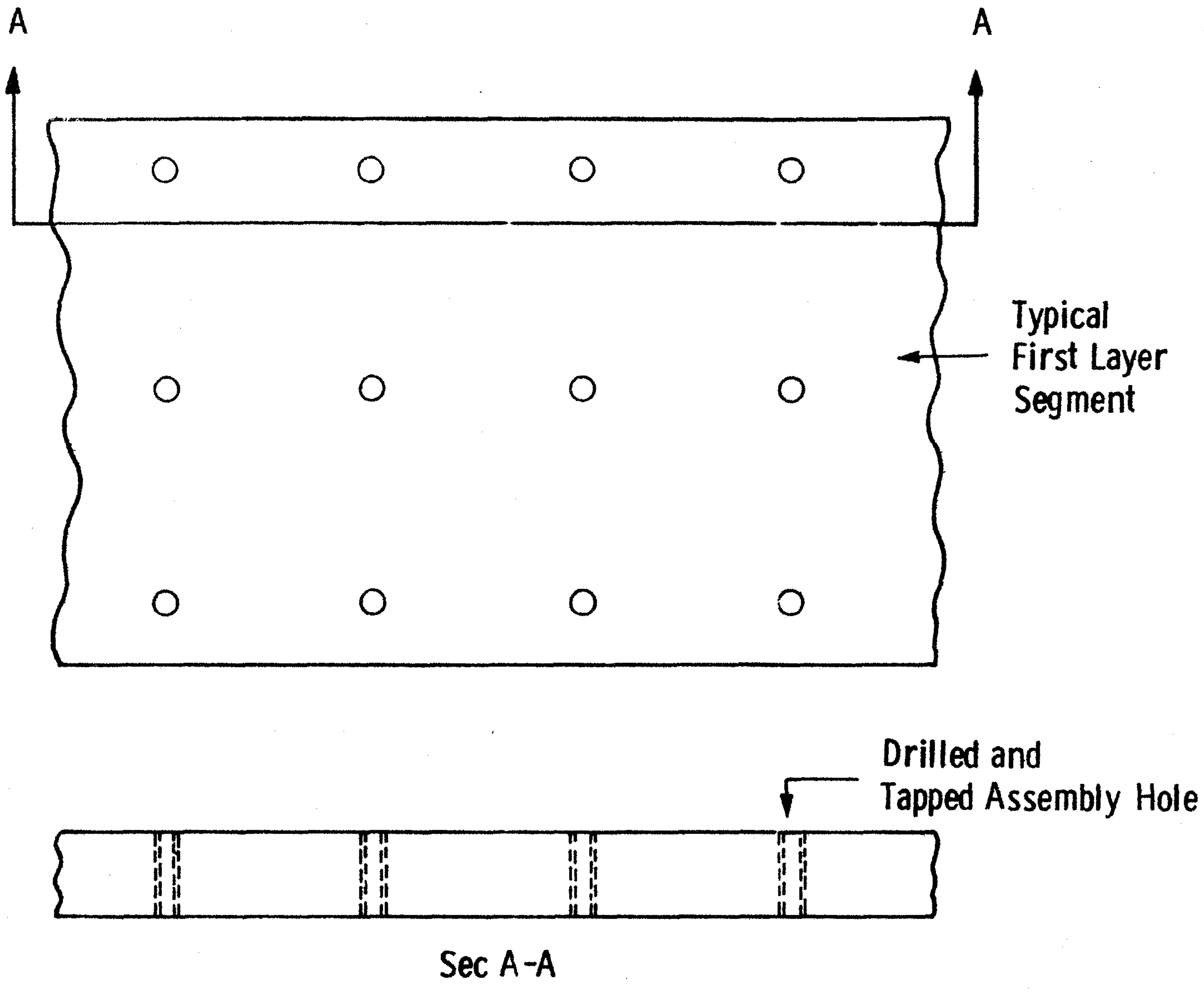

Figure K-3 Assembly Holes in Typical First Pancake Layer Segment

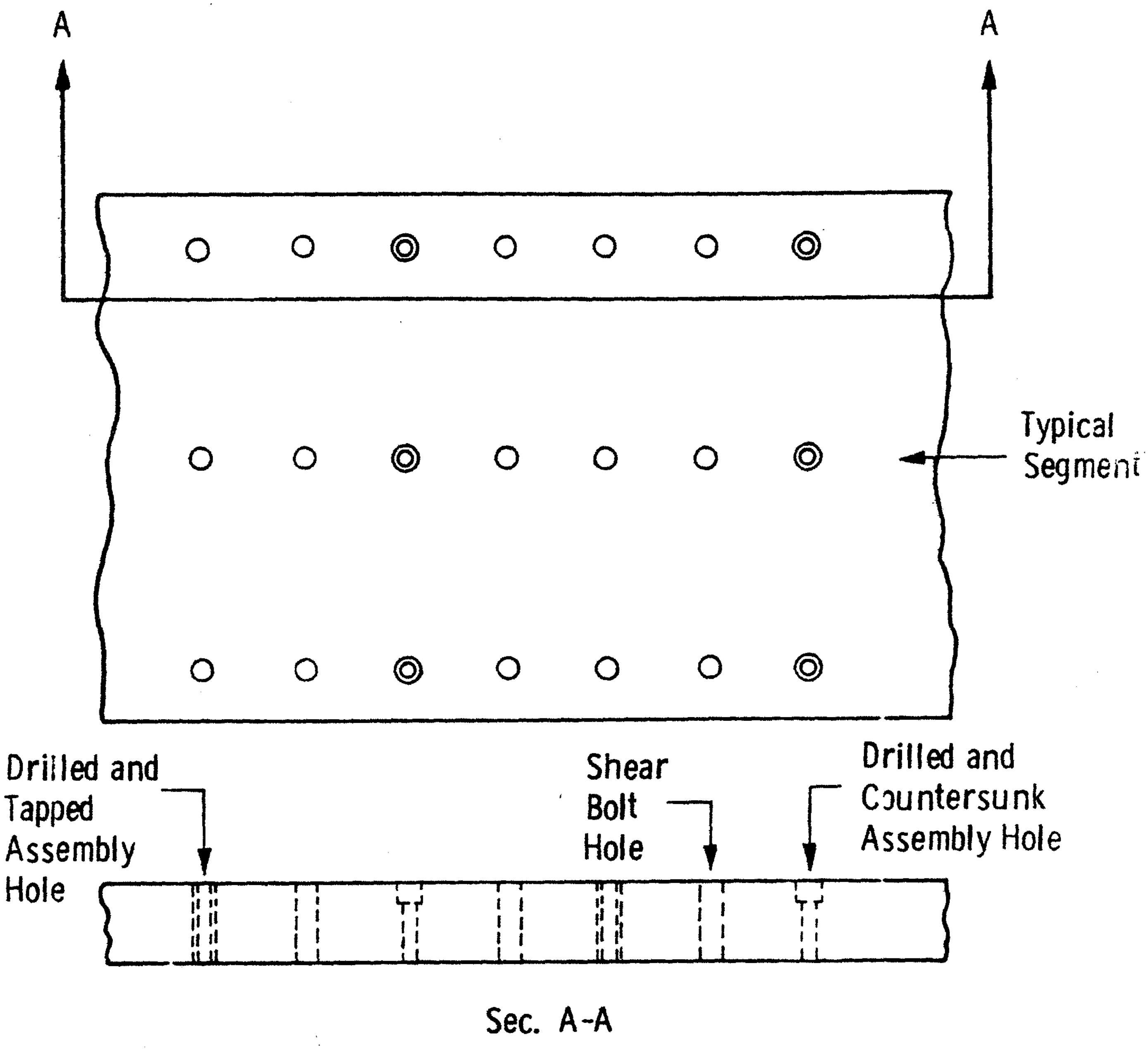

Figure K-4 Shear and Assembly Holes in Typical Support Structure Segment

Step 13 Clean and Inspect

Remove machining burrs and inspect for appropriate chordal dimensions.

Step 14 Bore and Turn

The inside and outside radii of the curved segments will be machined on a vertical boring mill.

Step 15 Machine Conductor Slots

Conductor slots in the plate segments will be machined on a numerically controlled vertical milling machine. This includes the slots in straight segments, segments of constant radii, segments of variable radii and transition segments. (See Figures K-5 and K-6) The width and depth tolerance of all conductor slots will be ±0.0075 cm (±0.003 in).

Step 16 Clean and Inspect

Remove burrs and inspect conductor slots for required dimension tolerance and finish. All measurements will be taken from the same reference points in order to minimize cumulative errors. (See Figure K-7)

Step 17 Clean

Clean all segments in a vapor degreasing tank to remove machining lubricants.

Step 18 Insulate

Apply insulation to both sides of all segments. The insulation will be applied by spraying. The segments will be subsequently heated to

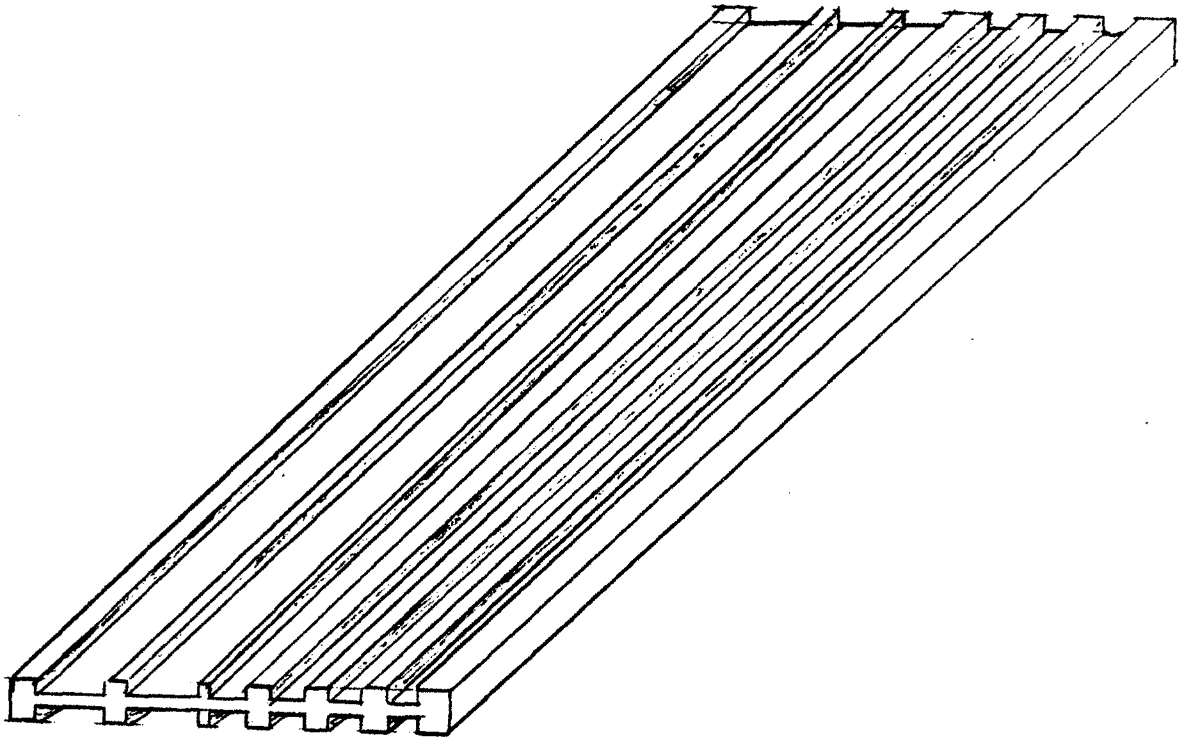

Conductor Slots Straight Segment

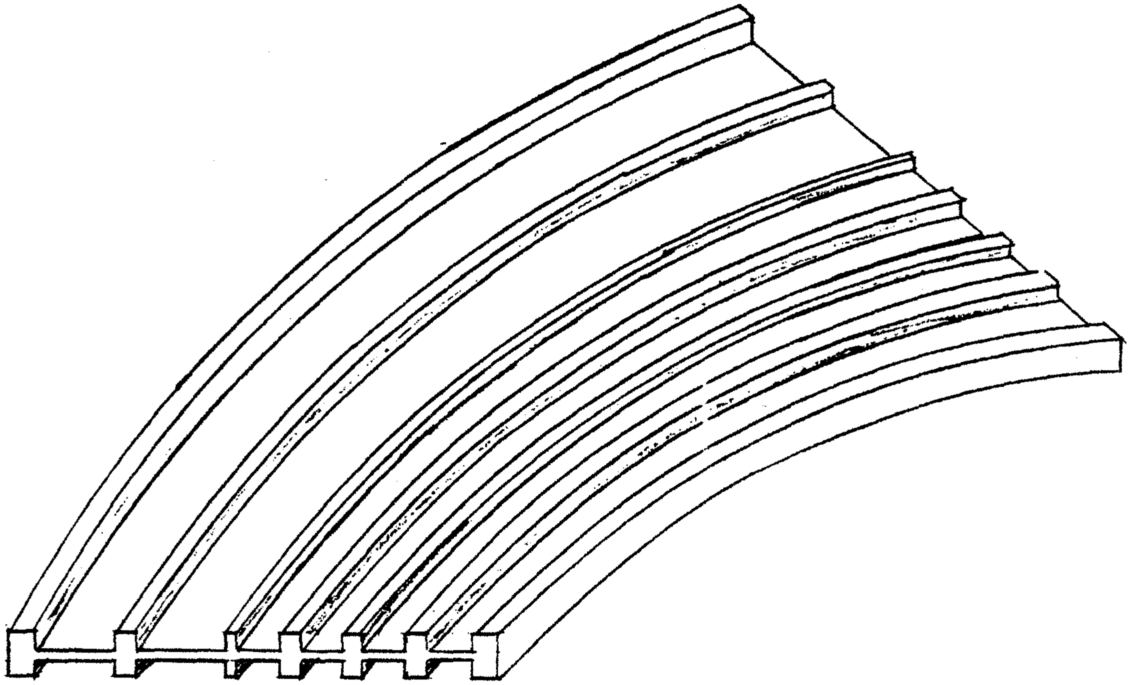

Conductor Slots Curved Segment

Figure K-5 Schematic Showing Conductor Slots Machined in Straight and Curved Segments

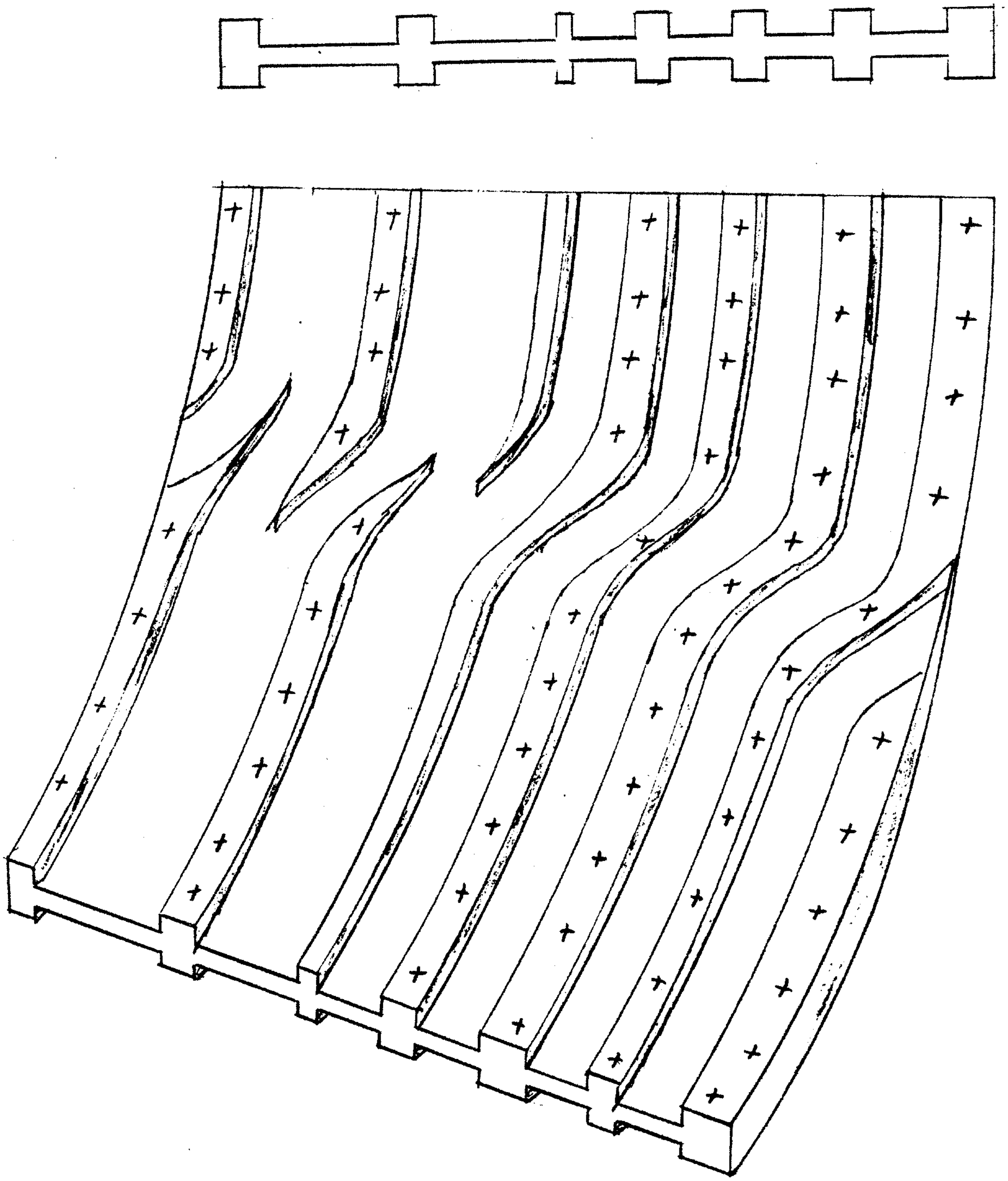

Figure K-6 Schematic Showing Conductor Slots in Transition Segment

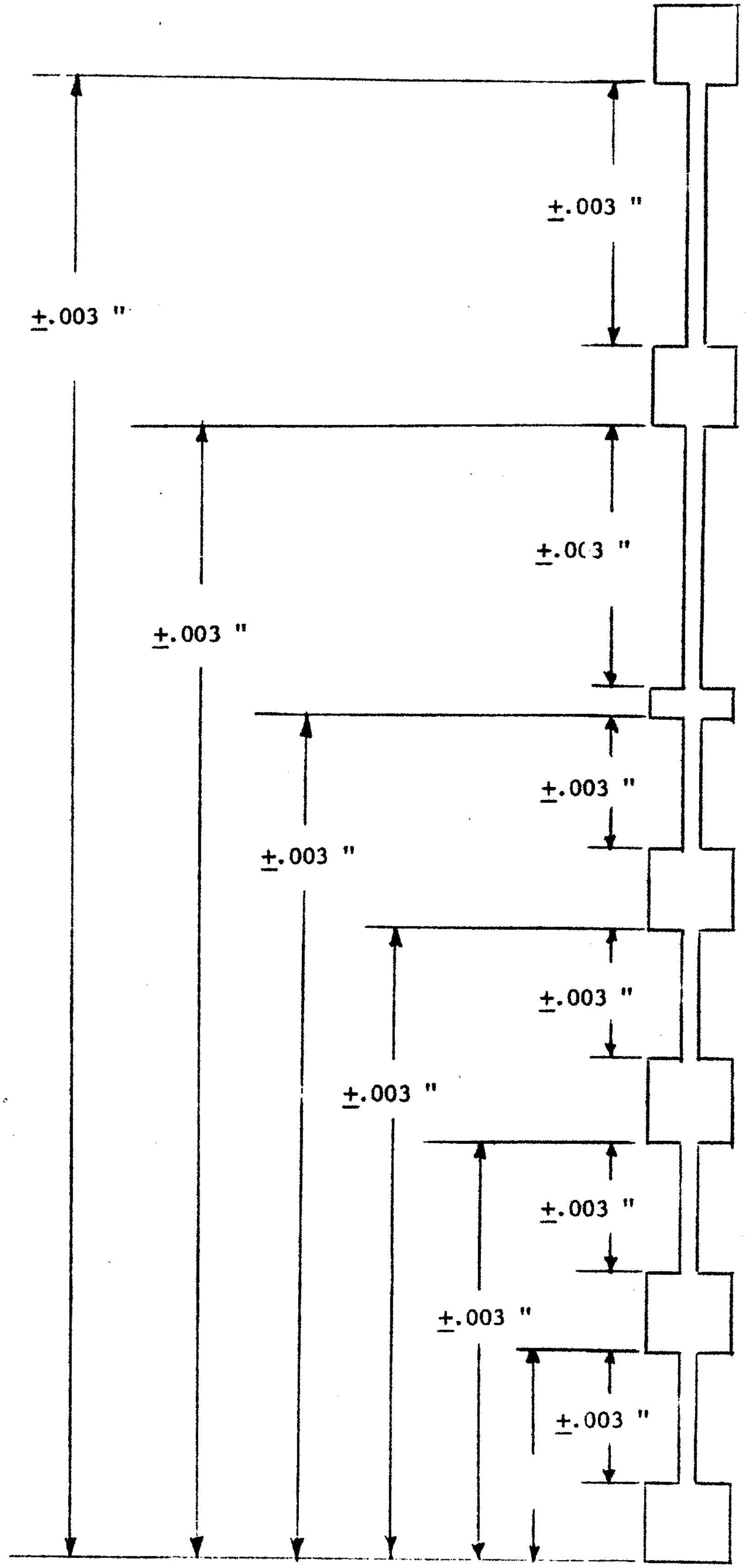

Figure K-7 Showing Conductor Slots Machining Tolerances and Measurement Reference Point

93°C (200°F) in order to cure the insulation. The insulation coating thickness will be less than 0.0025 cm (0.001 in).

Step 19 Inspect

An electrical resistivity test will be applied to check the quality of the insulation.

Step 20 Assemble Coil Segments

All segments will be assembled to form a complete support structure assembly. This operation will be performed by utilizing an assembly fixture and building bolts. The building bolts are threaded into the fixture and act as guide pins for the assembly operation. The segments, containing holes previously drilled for the through bolts, are then stacked in their proper position. When the first pancake layer is in position, short assembly bolts are used to tighten each segment flat against the assembly fixture. (See Figures K-8 and K-9)

Conductor grooves will be inspected at this time for alignment. The alignment tolerance will be ±0.010 cm (±0.004 in).

The second layer is assembled in a simialr manner. Each pancake segment is lowered over the building bolts and then bolted to the segment beneath it. Each assembly bolt is tightened to 170 N-m (120 ft-lb) torque. The segments comprising the second layer overlap the first layer segments forming a laminated support structure assembly. (See Figure 3-3)

Step 21 Line Ream Through Bolt Holes

When all layers of segments are assembled, the building bolts are removed,

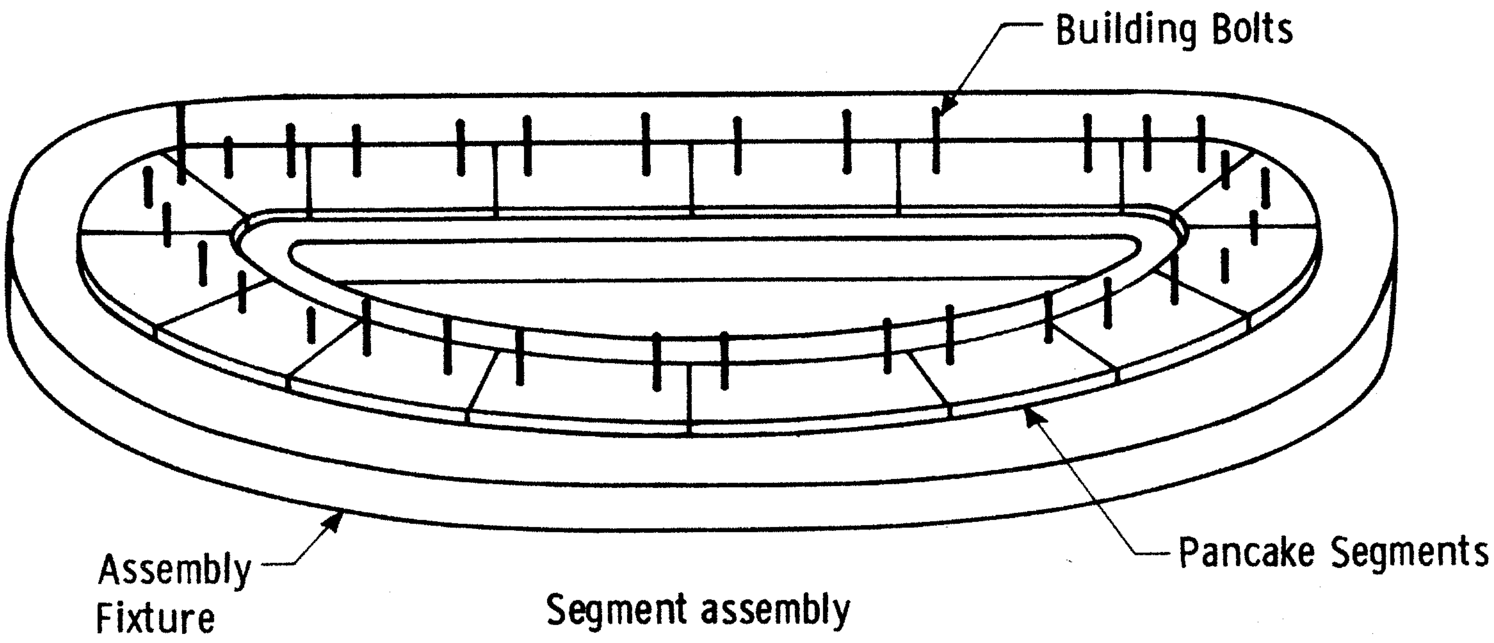

Figure K-8 Schematic of Segment Assemble on Assenbly Fixture

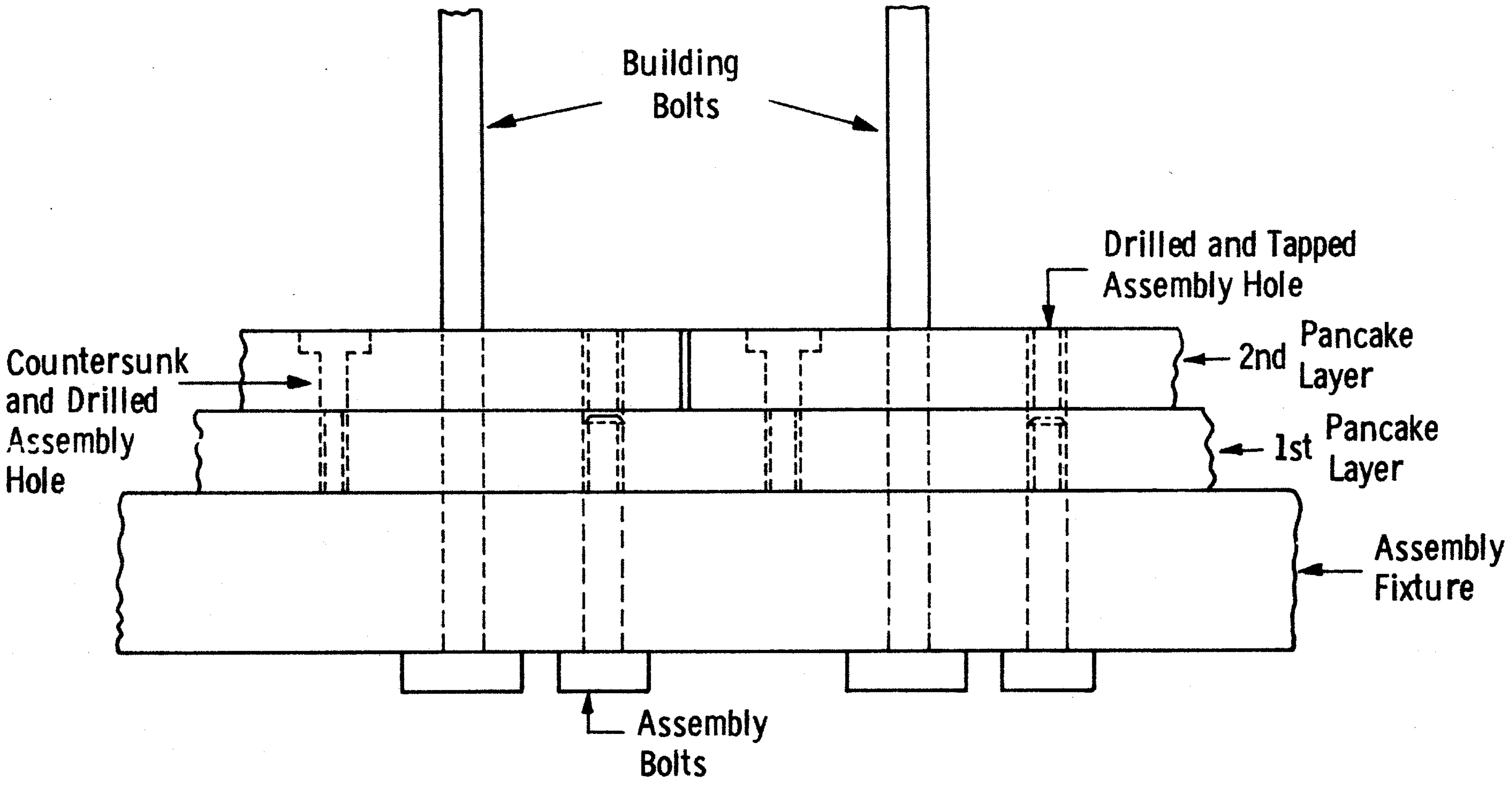

Figure K-9 Schematic of Assembly and Building Bolts in Place During Assembly of First and Second Pancake Layers the coil structure is removed from the fixture and all through bolt holes are line reamed.

Step 22 Disassemble Coil Support Structure

After all through bolts are line reamed, the support structure is disassembled. All segments are deburred and identified as to location during the winding and final assembly operation.

Step 23 Assemble Nose Section

All segments which constitute the nose or trapezoidal shaped portion of the coil will be reassembled using the building bolts as guides. Reassembly is necessary because a fully assembled coil is too large for the available gantry planer mill used in Step 24.

Step 24 Machine Nose Section

The nose section of the coil is set up in a gantry-type planer mill and the trapezoidal sides and nose (that surface which contacts the bucking cylinder) will be machined. (See Figure K-10)

Step 25 Inspect

The tapers and nose will be inspected for dimensions, plumb, and parallelism.

Step 26 Disassemble Nose Section

The nose section will be disassembled. All segments will be cleaned, deburred and checked for identification.

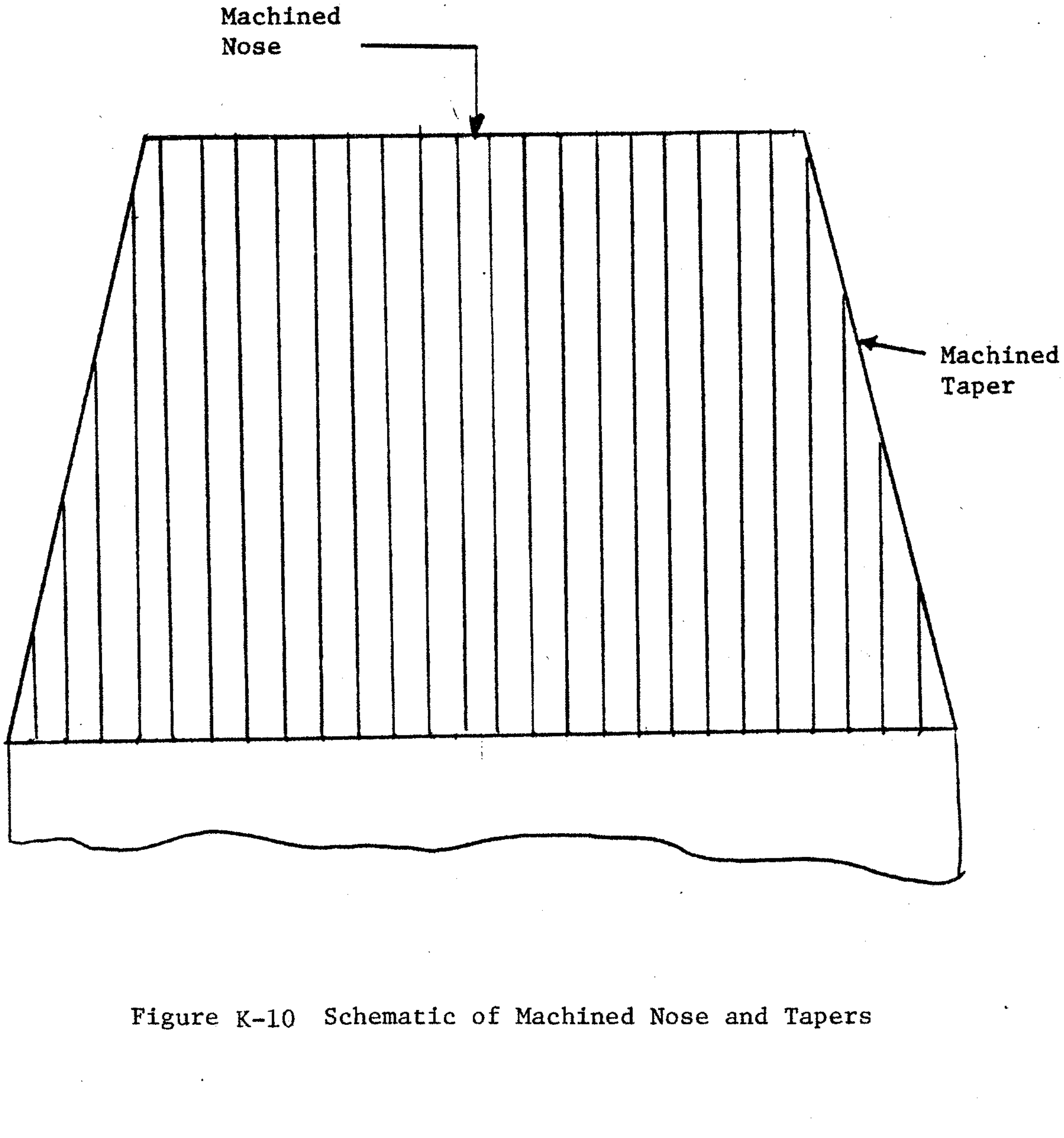

Figure K-10 Schematic of Machined Nose and Tapers

Step 27 Package and Shipment

All segments, assembly bolts, and through bolts will be packaged in protective boxes, identified and shipped to the erection site.

3.2.4.2.4 Major Equipment Requirements for Fabrication of the Toroidal Field Coil Support Structure

The major equipment required to fabricate the support structure for the toroidal field coils is as follows:

(1) Plasma Cutting Equipment
(2) Straightening Press
(3) Numerically Controlled Drill Press
(4) Drill Fixtures
(5) Slab Grinding Machine
(6) Vertical Boring and Milling Machine
(7) Gantry Planer Mill
(8) Numerically-Controlled Vertical Milling Machine
(9) Degreasing Tank
(10) Assembly Fixture
(11) 150 Ton Overhead Crane

All of the above equipment is presently commercially available except for the fixtures.

K.3 Winding Plan - Toroidal Field Coil

The plan for winding a toroidal field coil in the structural support plates is described below.

K.3.1 Winding Operation Sequence

Step 1 Fit and bolt the first plate segments of the coil support structure to the winding fixture.

Step 2 Conductor is received on a reel. The conductor strands are circumferentially tied approximately every two feet of conductor length. (See Figure K-11)

Step 3 A pulling cable from the jacketed conductor reeling mechanism is attached to the conductor end to begin pulling the cabled conductor from the reel.

Step 4 As the cabled conductor de-reels, the ties are removed and the conductor is inspected for damage resulting from transportation and handling. Provisions may be required for detecting broken strands and lost continuity.

Step 5 The conductor passes through the jacketing station where the steel jacket is applied and welded shut.

Step 6 The required jacketed conductor length is then reeled onto appropriately sized reels for reaction and helium leak testing.

Step 7 The conductor jacket is helium leak tested.

Step 8 The reel is then placed in a furnace for the required reaction time and temperature (approximately 30 hrs. at 700°C).

Step 9 The jacketed conductor is again helium leak tested.

Step 10 Reels consisting of reacted conductor are then transported to the winding site of the pancakes.

Step 11 A pulling cable from the pancake rotating table mechanism is attached to the conductor end to begin pulling the conductor from the reel.

Step 12 As the conductor de-reels, the conductor is inspected for damage resulting from transportation and handling.

Step 13 The reacted conductor is passed through straightening rolls and cleaned. Straightening rolls will remove any jacket set which may have occurred due to the reeling and de-reeling operation.

Step 14 The conductor passes through an incremental bender which is programmed to advance and bend the conductor the required amount.

Step 15 The insulation, consisting of three half-lapped layers of resin rich mica tape, is applied by an automatic taping head. The final protective layer, consisting of epoxy impregnated glass fiber, is also applied by the taping head.

Step 16 Winding of the pancake commences with the smaller radius first. The automatic bender (Step 14) must be programmed to change the bend radius as the conductor turn length increases.

Step 17 When the complete pancake is wound, a continuity and short circuit test will be required.

Step 18 After cure of the insulation, extra resin is applied to the slot and teflon-coated segmented plates are positioned over the conductor grooves. These plates ensure a smooth surface plane with the pancake surface.

Step 19 The stainless steel jacket is then heated by passing current through the jacket to cure the epoxy resin.

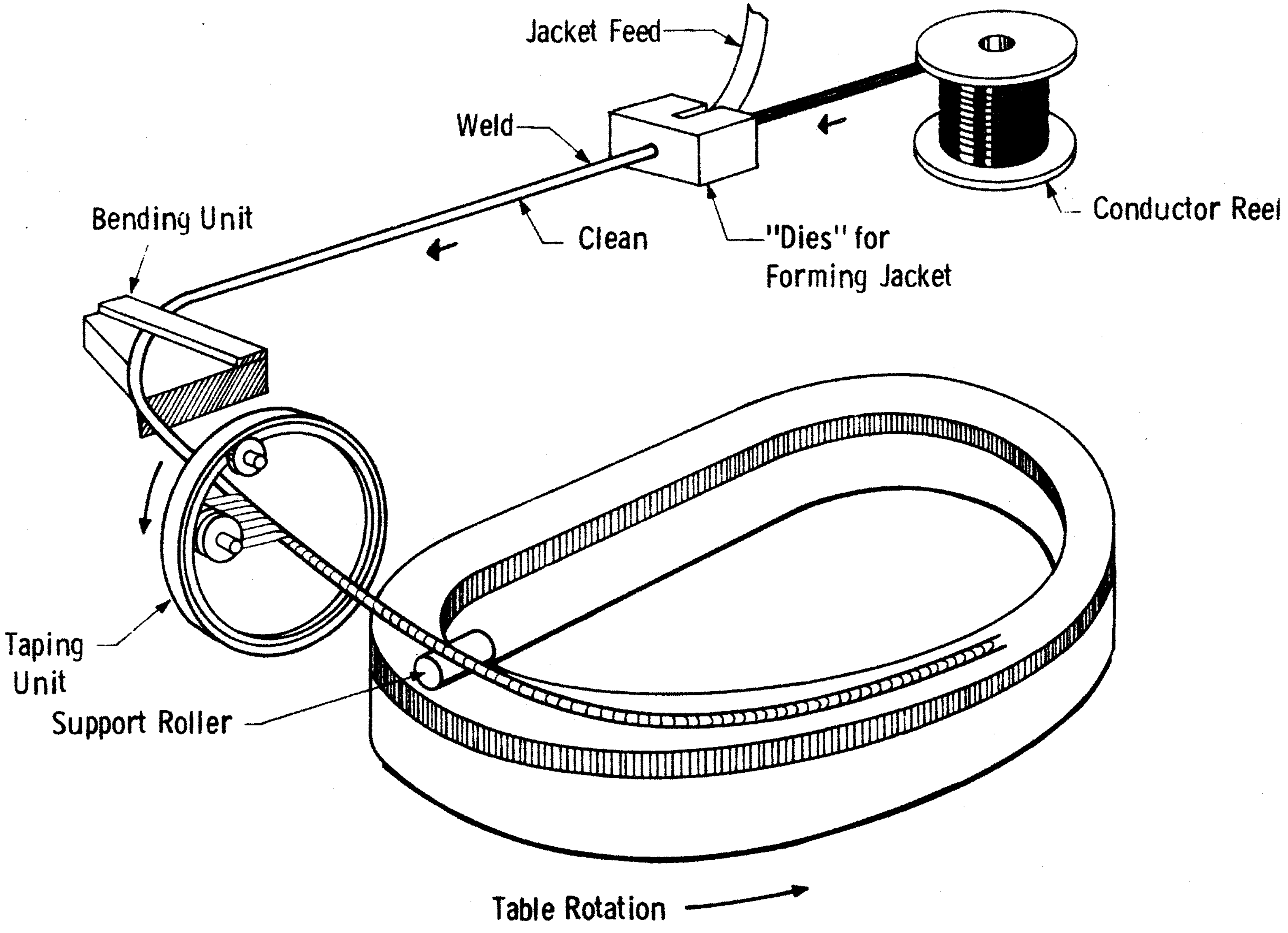

Figure K-11 Schematic of Field Coil Winding Station

Step 20 After resin cure, remove plates and inspect.
Note: Between stations, the conductor can be supported on "free wheeling" roller stands, to avoid overstraining the conductor.

Step 21 After inspection of the first wound side of the pancake (pancakes have conductors on both sides) an external lifting plate is mounted on the top of the pancake by means of the assembly holes. The entire pancake and lifting plates are then turned over exposing the opposite side of the pancake. Winding of this side of the pancake then proceeds in a similar manner to that described in Steps 16 through 20.

Step 22 After completion of Step 21, for the opposite side of the pancake, the lifting plate-winding fixture plus the wound pancake is moved to the adjacent coil assembly location.

Step 23 The initial pancake of the coil is placed on an assembly form which accounts for both the coil nose taper and through bolt locating pins.

Step 24 Remove lifting plate-winding fixture and return it to the winding area for use on the next pancake.

Step 25 Bolt holes, header locations and edges of the coil locations are checked for alignments and adjustments started.

Step 26 The pancakes are then externally clamped to the assembly form to minimize shifting.

Step 27 Final alignment adjustments are made and preparation for electrical and coolant joints are started.

Step 28 Make electrical and coolant joints by the following procedure:

(a) Strip insulation from the cable ends
(b) Crimp cable within a copper sleeve

(c) Resistance weld conductor ends together to form electrical joint

(d) Fit the coolant header jacket and weld to the conductor jacket

(e) Insulate the header jacket by hand

(f) Attach coolant piping.

Step 29 Repeat steps 11 through 28 until the entire coil is stacked, aligned and joints connected.

Step 30 Insert through bolts and tighten to the prescribed torque and order as specified by the design specification.

K.3.2 Major Equipment Required to Wind the Toroidal Field Coils

(1) Jacket fitting and forming unit

(2) Tig welding unit for jacket seams

(3) Programmable auto-taping unit

(4) Programmable auto-bending unit

(5) Adjustable rotating platform for the pancake assembly.

(6) Hydraulic tooling for coil winding assist

(7) Winding assembly fixture

(8) Furnace for reaction of cable

Although none of the above equipment is presently available, similar equipment has been used in the past. This type of equipment will be designed, constructed and tested during the manufacture of the Westinghouse/Airco LCP coil.

APPENDIX L: THE RELATION OF J × B IN THE TF SYSTEM TO PLASMA FIGURES OF MERIT

In the Executive Summary (Section 1.2) it was stated that $\bar{J} \times B_{MAX}$, the product of the average current density in the TF coil envelope and the maximum flux density at the coil, was a fundamental figure of merit for tokamak reactor designs. This appendix will attempt to demonstrate that this is indeed the case and to indicate the direction to be taken for further improvement in tokamak reactor designs.

The product $\bar{J}_{TF} \times B_{MAX,TF}$ can be related to plasma parameters through the following two identities:

$$\bar{J} = 2\pi R_o B_T / \mu A_{TF} \tag{1}$$

and

$$B_{MAX} = B_T \frac{R_o}{R_o - a - \Delta} \tag{2}$$

where Δ is the sum of the radial builds associated with the blanket, shield, plasma scrape-off layer and assembly gaps. Δ is a very slow function of other reactor parameters and typically equals 1.4 m.

Then, $\bar{J} \times B_{MAX}$, henceforth called (JB) is

$$(JB) = \frac{2\pi R_o^2 B_T^2}{\mu A_{TF}(R_o - a - \Delta)} \tag{3}$$

In order to reveal the physical significance of (JB), the case where

$$A_{TF} = \pi(R_o - a - \Delta)^2 \tag{4}$$

is used as an example. The use of this simplifying case is justified, because

(1) it is completely true for a few proposed reactor designs [1,2].

(2) it is nearly true (A_{TF} correct to within 25%) for all designs where

$$\frac{R_{OUT}}{R_{IN}} > 2 \tag{5}$$

where R_{OUT} is the outer radius of the inside leg of the TF coil and R_{IN} is the inner radius.

(3) the use of correction terms obscures but in no way alters the fundamental significance of (JB).

Defining

$$C = \frac{R_o - a - \Delta}{R_o} \tag{6}$$

as a factor indicating the relative closeness of the TF coil to the plasma magnetic axis and using the assumption in equation (4), we get

$$(JB) = \frac{2}{\mu_o} \frac{B_t^2}{C^3 R_o} \tag{7}$$

Any figure of plasma performance which has an analytic proportional relationship to major plasma parameters can now be expressed as a function of (JB). Proportionalities for seven important figures of performance follow:

(1) $n\tau_{EMP} \sim a^2 B_T^4$

$$a^2 B_T^4 \sim (JB)^2 C^3 \varepsilon R_o^2 \tag{8}$$

where ε is the inverse aspect ratio.

(2) Fusion power density P_f with β_T fixed ~ B_T^4 (β_t fixed corresponds to the flux-conserving model for which the maximum achievable β_T becomes a weak function of the reactor shape)

$$B_T^4 \sim (JB)^2 C^6 R_o^2 \tag{9}$$

(3) Fusion power density P_f with ($\beta_T \sim \varepsilon$) ~ $B_T^4 \varepsilon^2$ (corresponding to either ballooning or equilibrium limits on β_T)

$$B_T^4 \varepsilon^2 \sim (JB)^2 C^6 \varepsilon^2 R_o^2 \tag{10}$$

(4) Gross electric power P_e, with β_T fixed ~ $B_T^4 R_o a^2$

$$B_T^4 R_o a^2 \sim (JB)^2 C^6 \varepsilon^2 R_o^5 \tag{11}$$

(5) Gross electric power P_e with ($\beta_T \sim \varepsilon$) ~ $B_T^4 \varepsilon^2 R_o a^2$

$$B_T^4 \varepsilon^2 R_o a^2 \sim (JB)^2 C^6 \varepsilon^4 R_o^5 \tag{12}$$

(6) Wall loading P_w with ($\beta_T \sim \varepsilon$) ~ $B_T^4 \varepsilon^2 a$

$$B_T^4 \varepsilon^2 a \sim (JB)^2 C^6 \varepsilon^3 R_o^3 \tag{13}$$

(7) Alpha containment ~ $I_p \varepsilon^{-1}$ ~ $B_T a q^{-1}$

$$B_T a q^{-1} \sim (JB)^{1/2} C^{3/2} \varepsilon q^{-1} R_o^{3/2} \tag{14}$$

Notice that all seven expressions have a term with the form $C^n \varepsilon^m$, where n and m are positive. Since $C = 0$ when $\varepsilon = 1$ and $\varepsilon = 0$ when $C = 1$, each of these expressions has an optimum value for any given major radius. If Δ is either constant or an analytic function of major plasma parameters, then each optimum is analytically determinable.

For a given major radius, the only way to increase plasma performance is to maximize $C^n\varepsilon^m$, optimize elongation, or to increase JB. Similarly, for a given plasma output power, the only way to decrease plasma major radius is to maximize $C^n\varepsilon^m$, optimize elongation or to increase JB. Optimization of elongation is expected to be achieved by the current generation of plasma experiments (Doublet III, ISX-B, PDX, JET, JT-60). Maximization of $C^n\varepsilon^m$ for different figures of performance has essentially been accomplished numerically by various computerized reactor cost studies (3,4). However, the significance of (JB) escaped the notice of the trade studies because their method was to specify a fixed design approach while varying major parameters. The method suggested here is to continually attempt to improve the design approach for the toroidal field coils.

It can be seen from the above simple scaling relationship that, so long as the cost of the toroidal field coils does not grow in a highly nonlinear manner with (JB), that there is always adequate motivation for promoting more advanced toroidal field coil designs. This is true, whether or not the reactor is considered to be an embodiment of high field, the doublet, flux conservation or any other approach. Arguments that "low field" or niobium-titanium TF coils are "good enough", while perhaps true for certain specified goals, are misleading when applied to the problem of the commercialization of tokamak fusion power.

We propose as a basis for thought that there are three basic reactor figures of merit for commercial tokamaks:

(1) $\bar{J} \times B_{MAX}$ in the toroidal field coils

(2) P_W, (MW/m^2) in the first wall, and

(3) $P_W \times$ plant availability

The simultaneous increase of these three parameters from one conceptual design to the next is an unambiguous step toward the commercialization of fusion power. The improvement of any two without the third is not necessarily an overall improvement in conceptual reactor design.